

# From the Kondo box problem to the physics of the Kondo-lattice box

Dissertation  
zur Erlangung des Doktorgrades  
des Fachbereiches Physik  
der Universität Hamburg

vorgelegt von  
Andrej Schwabe  
aus Berlin

Hamburg  
2013

Gutachterin/Gutachter der Dissertation:	Prof. Dr. Michael Potthoff Prof. Dr. Alexander Lichtenstein Prof. Dr. Kevin Beach
Gutachterin/Gutachter der Disputation:	Prof. Dr. Michael Potthoff Prof. Dr. Frank Lechermann
Datum der Disputation:	19. Dezember 2013
Vorsitzende/Vorsitzender des Prüfungsausschusses:	Prof. Dr. Michael Thorwart
Vorsitzende/Vorsitzender des Promotionsausschusses:	Prof. Dr. Peter Hauschildt
Dekanin/Dekan des Fachbereichs Physik:	Prof. Dr. Heinrich Graener

## Abstract

The Kondo effect, the screening of the spin of an impurity by the conduction electrons of a metallic host system, is a standard problem in solid state physics. At weak coupling strengths between the host system and a group of impurities, the Kondo effect competes with indirect (RKKY) exchange, mediated by the conduction electrons, which promotes magnetic order among the impurities.

This work deals with the physics emerging in impurity systems with spatially confined metallic host materials, relevant to the quantum dots and artificial nanostructures created by scanning tunnelling techniques. It is shown that (i) the finite system size leads to an unconventional reentrant Kondo-vs.-RKKY competition, where the Kondo effect prevails at weak couplings in contradiction to the standard Doniach picture. (ii) A novel mechanism is proposed which ferromagnetically correlates the impurities' magnetic moments without any indirect exchange. (iii) In case of degenerate Fermi levels, a "multi-channel finite-size Kondo effect" is observed. (iv) In the regime of strong couplings magnetic ordering is shown to be driven by a novel inverse indirect magnetic exchange (IIME), which is mediated by magnetically inert Kondo singlets.

The evolution of this physics is studied from the "single-impurity Kondo box" limit via the "Kondo-vs.-RKKY quantum box" to the regime of the "Kondo-lattice box". Key insights are gained analytically by deriving effective low-energy Hamiltonians in the respective regimes by perturbation theory, and numerically by means of density-matrix renormalisation group (DMRG), dynamical mean-field theory (DMFT), and full diagonalisation calculations.

The presented theoretical concept is robust against weak environmental influences. The predicted effects await an experimental confirmation and exploration.

## Zusammenfassung

Der Kondo-Effekt, die Abschirmung eines Störstellen-Spins durch Leitungselektronen eines metallischen Wirtssystems, ist ein Standardproblem in der Festkörperphysik. Bei schwachen Kopplungen zwischen dem Wirtssystem und einer Gruppe von Störstellen konkurriert er mit dem indirekten, durch die Leitungselektronen vermittelten (RKKY) Austausch, der magnetische Ordnungen der Störstellen begünstigt.

Die vorliegende Arbeit behandelt die Physik von Störstellensystemen mit räumlich eingeschränkten metallischen Wirtsmaterialien, die von großer Bedeutung ist für Quantenpunkte und künstliche Nanostrukturen, die mit Rastertunneltechniken erschaffen werden können. Es wird gezeigt, dass (i) die endliche Systemgröße zu einem unkonventionellen Kondo-vs.-RKKY Wettstreit führt, in dem der Kondo-Effekt sich entgegen den Standardvorstellungen nach Doniach bei kleinen Kopplungen durchsetzt.

(ii) Ein neuartiger Mechanismus wird vorgeschlagen, der die magnetischen Momente von Störstellen ohne jeglichen indirekten Austausch ferromagnetisch korreliert. (iii) Im Fall von entarteten Fermikanten-Zuständen wird ein „multi-channel finite-size“ Kondo-Effekt beobachtet. (iv) Magnetische Ordnung im Regime großer Kopplungen wird durch einen neuartigen inversen indirekten magnetischen Austausch (IIMA) verursacht, der durch magnetisch inerte Kondo-Singlets vermittelt wird.

Die Entwicklung dieser Physik wird untersucht von der „Eine-Störstelle-Kondo-Box“, über die „Kondo-vs.-RKKY-Quantum-Box“, bis hin zum Regime der „Kondo-Gitter-Box“. Schlüsselerkenntnisse werden analytisch gewonnen durch die störungstheoretische Ableitung von effektiven Niedrigenergie-Hamiltonoperatoren in den entsprechenden Grenzfällen und numerisch mithilfe von Dichtematrix-Renormierungsgruppe (DMRG), dynamischer Meanfield-Theorie (DMFT) und voller Diagonalisierung.

Das vorgestellte Konzept ist robust gegen schwache Umgebungseinflüsse. Die vorhergesagten Effekte sehen einer experimentellen Bestätigung und Erforschung entgegen.



# Contents

<b>1</b>	<b>Introduction</b>	<b>9</b>
1.1	Motivation from experiments . . . . .	11
1.2	Structure of the work . . . . .	12
<b>2</b>	<b>The Kondo Effect</b>	<b>15</b>
2.1	Introduction . . . . .	15
2.2	Local-moment formation . . . . .	16
2.3	The Kondo problem . . . . .	21
2.4	Model Hamiltonians, conventions, and notations . . . . .	28
2.5	The Kondo box . . . . .	31
2.6	Outlook . . . . .	37
<b>3</b>	<b>Methods and theorems</b>	<b>39</b>
3.1	Introduction . . . . .	39
3.2	Origin of DMRG . . . . .	40
3.3	Density-matrix renormalisation group . . . . .	40
3.4	Real-space dynamical mean-field theory . . . . .	48
3.5	Generalised Lieb theorem . . . . .	51
<b>4</b>	<b>Off-resonant models</b>	<b>55</b>
4.1	Introduction . . . . .	55
4.2	Review of multi-impurity and two-impurity models in the literature . . . . .	57
4.3	Two-impurity models—effective RKKY models . . . . .	61
4.4	Magnetic response and spin correlations . . . . .	62
4.5	Distance dependence . . . . .	66
4.6	Dependence on the local exchange coupling . . . . .	69
4.7	Different distances between the impurities . . . . .	71
4.8	Summary . . . . .	72
<b>5</b>	<b>On-resonant models</b>	<b>75</b>
5.1	Introduction . . . . .	75
5.2	Perturbation theory in the weak-coupling regime . . . . .	77
5.3	The "bad-good-bad" configuration . . . . .	83
5.4	Uncovering the RKKY regime . . . . .	85
5.5	The screening process . . . . .	88

## Contents

5.6	Summary . . . . .	92
<b>6</b>	<b>Resonant enhancement</b>	<b>93</b>
6.1	Introduction . . . . .	93
6.2	Apparent inconsistencies of the concept of the finite-size Kondo effect .	94
6.3	A mechanism generating ferromagnetically correlated impurities . . . .	97
6.4	Finite-size RKKY interaction . . . . .	101
6.5	Evidencing the different energy scales . . . . .	103
6.6	Summary . . . . .	105
<b>7</b>	<b>Periodic chains</b>	<b>107</b>
7.1	Off-resonant models . . . . .	109
7.2	On-resonant models . . . . .	110
7.3	Summary . . . . .	115
<b>8</b>	<b>Coupling to the environment</b>	<b>117</b>
8.1	Introduction . . . . .	117
8.2	Influence on the local density of states . . . . .	118
8.3	Influence on the Kondo physics . . . . .	120
8.4	How correlations change . . . . .	124
8.5	Details of the screening process . . . . .	127
8.6	Influence on the RKKY physics . . . . .	129
8.7	Summary . . . . .	132
<b>9</b>	<b>Large systems</b>	<b>133</b>
9.1	Phase transition between Kondo and RKKY regime . . . . .	133
9.2	Multi-stage Kondo screening . . . . .	136
9.3	Summary . . . . .	140
<b>10</b>	<b>Strong-coupling regime</b>	<b>141</b>
10.1	Introduction . . . . .	141
10.2	From RKKY to inverse exchange . . . . .	142
10.3	Low-energy model . . . . .	143
10.4	Perturbation theory in the strong-coupling regime . . . . .	147
10.5	Correlation functions and Kondo effects . . . . .	158
10.6	Indirect inverse exchange and adiabaticity . . . . .	166
10.7	Summary . . . . .	169
<b>11</b>	<b>Depleted Kondo lattice model</b>	<b>171</b>
11.1	Introduction . . . . .	171
11.2	Magnetic order . . . . .	172
11.3	Charge fluctuations . . . . .	174
11.4	Low-energy spin and charge excitations . . . . .	176

11.5 Higher dimensions . . . . .	177
<b>12 Doped conduction-electron systems</b>	<b>179</b>
12.1 Introduction . . . . .	179
12.2 Transitions between finite-size Kondo and RKKY regime . . . . .	181
12.3 Transitions between RKKY and Kondo regime . . . . .	183
<b>13 Exhaustion problem and heavy fermions</b>	<b>187</b>
<b>14 Summary and outlook</b>	<b>191</b>
14.1 Summary . . . . .	191
14.2 Outlook . . . . .	193



# 1 Introduction

It was nobel laureate P. W. Anderson [1, 2], amongst others, who pointed out that "emergence" plays a fundamental, constitutive role for our surrounding world. Opposed to the point of view of reductionism—a complementary major paradigm of physics—the emergence of new phenomena and effects is intimately linked to complexity of many-body systems, which permits organising principles which are not obvious from or dependent on the building blocks of a particular theory.

Condensed matter physics may be regarded as a prime example. While the physical laws dictating the microscopic electronic and atomic behaviour are known for decades, theoreticians are not able to readily explain all new effects observed by experimentalists, overwhelmed by the sheer complexity. In this regard, we might for example think of unconventional superconductors whose physics is apparently determined by many competing energy scales, posing a yet intractable challenge.

History reveals that new experimental discoveries and theoretical concepts may lead to "revolutionary" Kuhnian paradigm shifts [3], changing the way physicists view and understand their subject. Among remarkable examples due to emergence are that the single-electron excitations may become impossible in one-dimensional materials due to spin-charge separation (Tomonaga-Luttinger liquid [4, 5]), that seemingly indivisible quanta such as electron charges can be broken into pieces due to the fractional quantum Hall effect [6], or that Cooper pairs seem to condense from the nowhere without being explicitly mentioned by microscopic theory [7].

The Kondo liquid [8], a low-temperature state of matter in multi-impurity systems, is another preeminent example. In fact, the field of Kondo physics played an important role in the development of ideas of emergence. The Kondo problem (Fig. 1.1), unsolved for a decade, triggered the development of renormalisation group ideas and techniques [9, 10], which reveal that a system may show different physical behaviour, when probed at different energy or length scales, respectively. Doubtlessly, these concepts can be considered to be of fundamental significance; with implications not only in physics but also on a human scale.

The Kondo model [8] represents a typical strongly-correlated system as it generates a small energy scale; smaller than any other coupling in the Hamiltonian. This scale is related to the Kondo effect [11], which occurs due to screening of the spin of a single impurity surrounded by a metallic host system with a local antiferromagnetic exchange coupling  $J$  between impurity and electrons (Fig. 1.1). In real space, the screening takes

## 1 Introduction

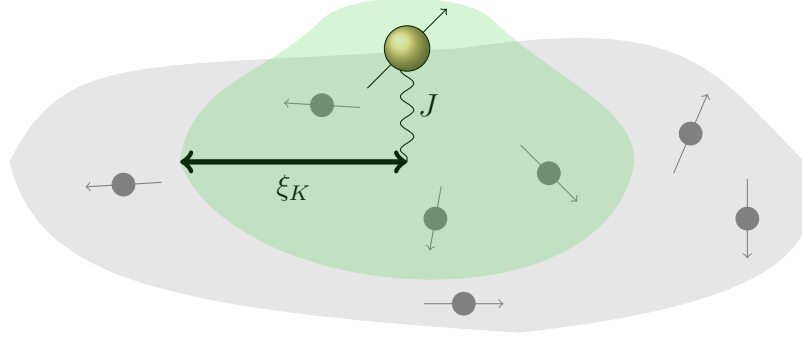


**Figure 1.1:** A magnetic impurity (yellow circle), immersed in a metallic host system (antiferromagnetic exchange coupling  $J$ ), is screened by itinerant electrons (grey) below the Kondo temperature  $T_K$ , resulting in the Kondo effect. In real space, the screening occurs at a specific length scale—the Kondo cloud size  $\xi_K \sim \frac{v_F}{T_K}$  (green cloud), where  $v_F$  denotes the Fermi velocity.

place on a length scale of mesoscopic size, denoted as the Kondo screening cloud. A competition arises for sufficiently large impurity concentrations; that is when Kondo clouds would start to overlap and impurities are provided the possibility to indirectly interact with each other via the conduction electrons (RKKY exchange [12, 13, 14]).

With the advent of low-temperature, nano-scale experimental techniques [15, 16, 17], the realisation of Kondo models of nanoscopic or mesoscopic size came into reach. While the physics of impurity models is itself fascinating enough due to the correlation of localised magnetic moments with itinerant electrons [18], it rapidly became clear that this experimental progress adds a new dimension to the problem: the system size plays a crucial role when the Kondo cloud is too large to match it [19, 20]. However, we will demonstrate that also the interplay between Kondo effect and indirect impurity interactions may be fundamentally changed by finite-size and boundary effects. For example, we observe an unexpected reentrant competition, where the Kondo effect prevails even for weak couplings, in contradiction to conventional belief [21].

This constitutes the starting point for our work. Our objective is the detailed study of the physics of impurity systems in *finite* host systems. We will develop a conclusive and comprehensive picture of finite-size effects in multi-impurity models, which goes beyond existing theories and demonstrates that such impurities can be correlated with one another and with the conduction electrons in basically different ways as compared to traditional considerations. First, we turn to models with few impurities coupled to a spatially confined host system [22, 21]. An important aspect is that open boundary conditions induce Friedel oscillations in the host system [23], determining the spatial variation of finite-size effects. Stimulated by the success of our picture, we turn to multi-impurity systems of large size, where the emergence of magnetic order becomes possible. We reveal that ordering in the strong-coupling regime is provided by the

novel "inverse indirect magnetic exchange" (IIME) [24]. Furthermore, we motivate that the presented physics is accessible by experiments. The key to understand our results is provided by perturbation theory, which permits to derive the effective low-energy Hamiltonians in the weak and strong-coupling regime. Our concept is evidenced by numerical results obtained mainly from density-matrix renormalisation group [25] (DMRG) but also from real-space dynamical mean-field theory [26, 27] (R-DMFT) and full diagonalisation calculations.

However, our work is not only important from a point of view of physics on nano-size length scales, but we may also understand it as studying the transition from few-particle systems to many-particle systems, allowing for emergent phenomena such as the conventional Kondo effect or magnetic ordering. Furthermore, it permits to characterise finite-size effects with which numerical methods such as DMRG are typically plagued.

## 1.1 Motivation from experiments

As already suggested in the preceding section, systems may behave differently when relevant (correlation) length scales are cut off by the system size, e.g. the exponential Kondo cloud size  $\xi_K$  (see section 2.3). Kondo models of nanoscopic size—"Kondo boxes"—have been realised as an individual grain [28, 29], as a single metallocene molecule [30], or as a small quantum dot which acts as a spin-half impurity and which is coupled to a large quantum dot with a finite level spacing [31]. The ratio between the Kondo scale and the spectral gap, induced by the finite system size, can be tuned by varying the voltage on the gates separating the two dots. One-dimensional Kondo boxes can be realised by small Co clusters in short carbon nanotube pieces [32] or by a carbon nanotube exchange coupled to a localised electron [33].

Recent developments in the experimental techniques to investigate properties of magnetic adatoms on non-magnetic surfaces, allow for direct probing and analysis of fundamental magnetic exchange mechanisms on an atomic scale. A prominent example for this challenge represents the competition between the indirect magnetic exchange of the adatoms via conduction electrons of the substrate and the screening of the magnetic moment of the adatoms by the conduction electrons. The scanning-tunnelling microscope (STM) [15] has been used to study the Kondo physics of single magnetic adatoms [16, 34, 35] and the magnetic properties of individual magnetic islands on non-magnetic substrates [36, 37]. Even atomically precise maps of the inter-impurity coupling between individually pairs on metallic surfaces can be recorded [17, 38, 39, 40]

With progress in manipulation and characterisation of magnetic systems on mesoscopic and nanoscopic scales, studies of the interplay between Kondo screening and indirect exchange in a quantum box seem possible in the near future, e.g., in artificial and tunable double quantum-dot systems [41]. STM techniques nowadays allow

## 1 Introduction

the bottom-up construction of tailored magnetic nanostructures with atomic control [42, 43]. Our work will reveal the relevant basic mechanisms which can be employed for this purpose, along with many intriguing phenomena.

### 1.2 Structure of the work

In the first place, we present a compact overview of the knowledge about the Kondo effect in chapter 2, to become familiar with historical and conceptual aspects [44]. In particular, we want to understand the conventional ideas about its competition with indirect exchange mediated by the conduction electrons [45, 46] (sections 2.2 and 2.3, continued in section 4.2) in order to contrast them with the results of our work. In section 2.5, we discuss the physics of the Kondo box [19, 20], i.e. the influence of the finiteness of the host system and open boundary conditions on the single-impurity Kondo effect. We want to demonstrate that the traditional picture of the Kondo resonance breaks down in a Kondo box at weak couplings and that it has to be replaced in return by a suitable theory of finite-size effects to be developed in this work.

In chapter 3, the main numerical methods, density-matrix renormalisation group [25] (DMRG) (section 3.3) and real-space dynamical mean-field theory [26, 27] (R-DMFT) (section 3.4), are introduced as well as the generalised Lieb theorem [47, 48] (section 3.5), which permits exact analytical statements of great significance at half-filling.

In the following chapters 4-9, we turn our attention to the detailed discussion of finite-size and boundary effects in multi-impurity models, i.e. the "Kondo-vs.-RKKY-exchange quantum box" [21]. Our aim is to acquire a broader understanding of how this competition is modified. An important step represents the derivation of the effective low-energy Hamiltonian at weak couplings by perturbation theory (section 5.2). Furthermore, we illustrate the diverse and sometimes counterintuitive consequences of these finite-size effects, along with effects from the open boundaries.

We discuss two models for which finite-size effects occur at weak couplings in basically different ways. The "off-resonance case" (chapter 4), using the example of a two-impurity model [22], is in line with the conventional considerations about the competition between RKKY exchange and Kondo effect, whereas the "on-resonance case" (chapter 5) is in contradiction to them by leading to an unconventional reentrant competition. The consequences are explicated by using a three-impurity model [21].

As chapter 6 demonstrates, "on-resonance cases" have unexpected implications such as "resonant enhancement", found in several quantities: enhanced RKKY couplings and special inter-impurity correlations. These appear at first glance to be contradictory to the conclusions of chapter 5, but they turn out to be consistent with our picture. In chapter 7 we investigate the corresponding influences in periodic host systems.

So far we studied somehow artificial models, perfectly isolated from any environmental



influences. This condition is relaxed in chapter 8 in order to mimic experimental situations and to contrast our concept with the results of previous works [49, 50]. It is shown that the discussed finite-size physics is stable against weak coupling to the environment at energy scales larger than the induced spectral broadening of conduction-electron states [21].

In chapter 9 we make contact to conventional ideas by studying systems of large size. The recovery of established paradigms of Kondo physics such as the number of screening channels in the RKKY regime or phase transitions between Kondo and RKKY regime [51, 52] is analysed as a function of system size.

Our analysis also motivates questions related to the strong-coupling regime (chapter 10) in terms of adiabatic connection to the weak-coupling regime. We derive an effective low-energy Hamiltonian for multi-impurity models at strong couplings, describing the weak interactions among the remaining electrons which are not trapped in Kondo clouds. These interactions are provided by virtual excitations of magnetically inert Kondo clouds, constituting a novel "inverse indirect magnetic exchange" (IIME) [24].

After elaborating all integral parts of our concept, we make the leap to models of large size with a large number of impurities, discussed in chapter 11 using the example of a depleted Kondo lattice model [53]. The macroscopic number of impurities gives rise to instabilities of the remaining Fermi liquid against magnetic ordering.

The broad understanding of weak and strong-coupling regime allows us to extend our concepts to systems away from half-filling (chapter 12). In the end, we derive a qualitative magnetic phase diagram for the depleted Kondo lattice model discussed in chapter 11.

We conclude our work with a brief survey of the physics of dense Kondo lattice models [44] (chapter 13) and relate it to our results.



## 2 The Kondo Effect

### 2.1 Introduction

In the first half of the twentieth century the recently developed low-temperature experimental techniques brought a great deal of new fascinating evidences for unconventional behaviour in solid state materials. However, they challenged the theoreticians for decades. As prominent example the conventional superconductivity may be regarded, which needed almost sixty years to be satisfyingly explained by BCS theory [7].

Another collective phenomenon is the Kondo effect, first described in 1934 [8]. Measurements of Au with Fe impurities showed a puzzling resistance minimum at low temperatures. It appeared contradicting that the resistance increases when the temperature is lowered, since familiar mechanisms such as electron-phonon scattering or electron-electron interaction vanish or remain constant for vanishing temperatures  $T \rightarrow 0$  [44].

In this chapter we want to give an idea of the obstacles that theory had to overcome to understand the Kondo effect and which concepts evolved in consequence. At the heart of the Kondo effect is the screening of an impurity spin by a set of otherwise non-interacting electrons. Screening effects are also known in classical contexts such as the screening of electrical charges and electromagnetic fields. However, the Kondo effect is inaccessible by weak-coupling perturbation theory [8] owing to low-temperature divergencies of perturbatively calculated system quantities. This makes the problem theoretically intractable at first sight [54].

Before tackling these divergencies, the formation and role of magnetic impurities needed to be clarified. In 1961, Anderson figured out that local moments can be obtained in incompletely filled atomic electron shells, whose wave functions exhibit a very localised behaviour [55]. This includes 4f (rare earth, for example Ce), 5f (actinide, e.g. U), and 3d (transition metals, e.g. Fe) shells. If the corresponding energy levels lie in the conduction bands of the host materials, hybridisation due to tunneling becomes possible. On the other hand, the presence of strongly repulsive interactions among the localised electrons leads to the formation of local moments.

The discovery of an effective antiferromagnetic spin exchange, which couples the impurity moment to the conduction electrons, led Jun Kondo to derive his famous perturbative results in 1964 [11]. The generation of the associated exponential energy scale  $T_K$ , known as the Kondo temperature, and the corresponding low-temperature

physics could later be convincingly explained by the development of renormalisation group ideas in the early 1970s [9, 10]. For his distinguished contributions to this field, Kenneth Wilson was recognised with a Nobel prize in 1982.

Nowadays, the Kondo effect attracts interest also as playground to develop and test new theoretical concepts and numerical tools. The study of finite-size systems, in which the level spacing of the conduction-electron system is a non-negligible energy scale, has become an important branch, which will cover a large fraction of this work [19, 20, 21, 21, 24]. It may govern the physics at weak couplings with profound consequences.

## 2.2 Local-moment formation

### Mean-field theory of local-moment formation

We may think of the host materials under consideration conceptually as simple metals with broad conduction bands. The Coulomb interaction between electrons is described by the Hamiltonian

$$H_C = \frac{e^2}{8\pi\epsilon_0} \sum_{i,j}^{i \neq j} \frac{1}{|\mathbf{r}_i - \mathbf{r}_j|}, \quad (2.1)$$

where  $e$  denotes the elementary charge and  $\mathbf{r}_i$  the electron positions.<sup>1</sup> The interaction is found to be screened in typical materials for distances of the order of magnitude larger than  $1\text{\AA}$  [18]. Thus, the conduction band is composed of quasi-particles—electrons with their (charge) screening clouds—whose short-range interactions should be negligible due to their delocalised nature.

Friedel and Blandin worked out the consequences of a non-magnetic impurity without interactions [8], which is coupled to the conduction band, amounting to the screening of the impurity's excess charge by the electrons. Though their considerations led to the development of the concept of resonant bound states (also known as virtual bound states), the ideas are inadequate for the physical situation in rare earth materials or transition metals. They cannot explain, e.g., the resistance minimum at low temperatures, which is due to screening of local moments.

An important step further in understanding the reasons for the formation of local magnetic moments is provided by the mean-field theory of the Anderson model [55], which incorporates interactions between localised electrons into Friedel's picture of resonant bound-states [56, 44]. Although the Coulomb interaction experienced by the

---

<sup>1</sup>In the following, we will work in natural units with  $\hbar = 1$  and  $k_B = 1$ .

delocalised conduction electrons is strongly screened, it can take large values in the inner d or f shells of a solute atom. In the following, we will refer to the impurity states as "f states" or "f levels" for simplicity. Neglecting any orbital degeneracy, these impurity sites possess the atomic basis states  $|\uparrow\downarrow\rangle$  (doubly occupied),  $|0\rangle$  (empty),  $|\uparrow\rangle$ , and  $|\downarrow\rangle$  (singly occupied with spin up or down). In its simplest version the Anderson model contains a single impurity site and is given by the Hamiltonian [57]

$$H = \sum_{\mathbf{k}\sigma} \varepsilon_{\mathbf{k}} c_{\mathbf{k}\sigma}^\dagger c_{\mathbf{k}\sigma} + V \sum_{\sigma} (c_{i_1\sigma}^\dagger f_{\sigma} + \text{H.c.}) + \varepsilon_f \sum_{\sigma} n_{f\sigma} + U n_{f\uparrow} n_{f\downarrow}, \quad (2.2)$$

where the first term describes the conduction-electron sea, to which the f level couples locally at site  $i_1$ .  $c_{\mathbf{k}\sigma}^\dagger$  creates a conduction electron with momentum  $\mathbf{k}$  and spin  $\sigma$ , while  $c_{i_1\sigma}^\dagger$  creates an electron with spin  $\sigma$  at site  $i_1$ .  $f_{\sigma}$  denotes an annihilation operator for electrons at the impurity site and  $\varepsilon_f$  the on-site energy of the f level. The interaction term  $U$ , the remainder of the Coulomb interaction, is only active at the impurity site between up and down electrons.

If  $V = 0$ , the f level shows atomic behaviour. A magnetic (singly occupied) ground state  $|\uparrow\rangle$  or  $|\downarrow\rangle$  is obtained for  $\frac{U}{2} > |\varepsilon_f + \frac{U}{2}|$ , i.e.  $U$  must be positive. A symmetric Anderson model is obtained for  $\varepsilon_f = -\frac{U}{2}$ , i.e. mixed-valence states are avoided. Throughout the whole work, we will exclusively consider symmetric Anderson models with positive  $U$ .

When  $V$  is finite but weak compared to  $U$  and  $|\varepsilon_{\mathbf{k}}|$ , we may assume that the f ground state is changed adiabatically and is only weakly influenced by the hybridisation, resulting in energetically broadened resonances of width  $\tilde{\Delta}$ .

This is supported by the results of Anderson's mean-field treatment of the Anderson Hamiltonian (Eq. (2.2)). A single resonance centered at  $\varepsilon_f$  is obtained at weak  $U$ , whereas it splits into two resonances for sufficiently large  $U$ , i.e.  $U > U_c \sim \pi\tilde{\Delta}$ . The spin resolved density of states of the f orbital  $\rho_{f\sigma}(E)$  is given by a Lorentzian with position at  $\varepsilon_{f\sigma}$

$$\rho_{f\sigma}(E) = \frac{\tilde{\Delta}}{(E - \varepsilon_{f\sigma})^2 + \tilde{\Delta}^2}. \quad (2.3)$$

One finds  $\varepsilon_{f\sigma} = \varepsilon_f + U n_{f,-\sigma}$ , where the occupancy of the impurity site  $n_{f\sigma}$  has to be self-consistently determined.

Another important finding consists in the Friedel sum rule,  $n_{f\sigma} = \frac{1}{\pi} \delta_{\sigma}$ .  $\delta_{\sigma}$  is the phase shift for scattering of electrons with spin  $\sigma$  off the f resonance. The sum rule says that the charge bound in an atomic potential is equal to the number of nodes  $\sum_{\sigma} \frac{\delta_{\sigma}}{\pi}$  added to the scattering wave function [56].

However, Anderson's approach turns out to be incomplete in situations in which quantum fluctuations are important. As we will see below, the formed impurity spin becomes highly correlated with the conduction electrons below  $T_K$  in form of the Kondo effect.

## 2 The Kondo Effect

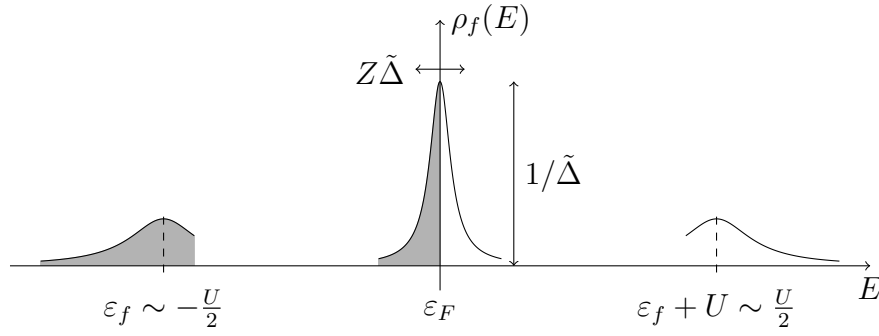


**Figure 2.1:** Impurity density of states  $\rho_f(E)$  in the single-impurity Anderson model for large  $U$  in the particle-hole symmetric case,  $\varepsilon_f = -\frac{U}{2}$ . Two peaks are found at  $E \sim \pm\frac{U}{2}$  with weights of almost  $1/2$  each. The "Kondo resonance" builds up at low energy scales; its peak height is fixed by  $1/\tilde{\Delta}$ . Consequently, its width  $Z\tilde{\Delta}$  is small, and thus  $Z \ll 1$ . The shaded area shows the filled fraction. Figure adapted from Ref. [56].

How does the Kondo effect manifests in the impurity density of states? Based on Anderson's mean-field results, we may assume two peaks in  $\rho_f(E)$  for large  $U \gg |\varepsilon_k|, V$ . Due to adiabatic connection to the states at weak  $U$ , they are expected to have weights of almost  $\frac{1}{2}$ .

However, one can find that  $\rho_f(E)$  at  $E = 0$  is fixed at a particular value, namely

$$\rho_f(E = 0) = \frac{1}{\tilde{\Delta}}, \quad (2.4)$$

suggesting a third peak at the Fermi energy. The pinning of  $\rho_f(E = 0)$  is a consequence of the adiabatic connection to  $U = 0$ , where we can think of the system as a collection of non-interacting electrons. We may assume the usual one-to-one correspondence of (low-energy) quasi-particles and their (low-energy) excitations for  $U = 0$  to finite  $U$ , as established by Landau's Fermi liquid concept. In the single-impurity model, adiabaticity is ensured by the absence of instabilities for any finite  $U$  [56].

The central peak is called "Kondo resonance" or "Abrikosov-Suhl resonance" and can be shown to possess a width of  $Z\tilde{\Delta} \ll 1$ .  $Z$  denotes the Fermi liquid parameter, describing the strength of the "wave function" renormalisation. The narrow width is enforced by the large weights of the two outer Hubbard peaks at  $\pm\frac{U}{2}$  and leads to a rather small  $Z \ll 1$ . It is astonishing that quasi-particles with such a small weight can be nevertheless of such importance for the determination of low-energy properties. Fig. 2.1 shows the resulting three-peak structure of  $\rho_f(E)$  [8, 56].

We will come back to the Fermi liquid concept later again in the case of multi-impurity models (chapter 13), where this approach allows to understand the peculiar low-energy properties of this system.

## Schrieffer-Wolff transformation

Anderson's approach has the typical drawbacks of a mean-field theory, in that it shows symmetry breaking in form of the magnetisation of the impurity, what could be justified only for a macroscopic number of degrees of freedom. This is definitely not the case for a single spin. We would rather assume quantum mechanical tunneling between  $|\uparrow\rangle$  and  $|\downarrow\rangle$  configurations of the impurity spin, which is determined by quantum fluctuations due to the interaction with the conduction electrons, especially below the Kondo temperature  $T_K$ .

Anderson ventured heuristic arguments that the spin exchange between formed impurity spin and conduction electrons may lead to a quench of the local moment [55]. The reason is that the total spin cannot be changed by the action of  $V$ , which consists in mixing conduction-electron states with f states. To lowest order, spin exchange occurs in two ways; intermediate states contain a doubly occupied or empty impurity site

$$\begin{aligned} c_\uparrow + f_\downarrow^1 &\longleftrightarrow f^2 \longleftrightarrow c_\downarrow + f_\uparrow^1 & \Delta E &\sim U + \varepsilon_f \\ c_\uparrow + f_\downarrow^1 &\longleftrightarrow c_\uparrow + c_\downarrow \longleftrightarrow c_\downarrow + f_\uparrow^1 & \Delta E &\sim -\varepsilon_f. \end{aligned} \quad (2.5)$$

$f_\sigma^1$  stands for a singly occupied f level with spin  $\sigma$  and  $f^2$  for a doubly occupied f level. The reasoning was as follows: the intermediate states are total singlet states (with respect to the considered electrons) due to the intermediate doubly occupied impurity site or site  $i_1$ , respectively. Thus, scattering is only possible if c and f electron are in a mutual singlet state, amounting to an antiferromagnetic<sup>2</sup> spin exchange [56].

In the following, we want to derive the antiferromagnetic exchange in a more quantitative way, taking the Schrieffer-Wolff transformation as basis [58]. Schrieffer's and Wolff's method makes use of canonical transformations. It should be remarked that it belongs to the first applications of renormalisation group techniques, i.e. finding an effective Hamiltonian for the low-energy degrees of freedom. The idea is to regard the above processes (2.5) as high-energetic valence fluctuations at the impurity site, which occur as virtual fluctuations when a local moment has formed. We start again from the Anderson model Eq. (2.2) and decompose the Hamiltonian into two parts

$$H = H_1 + \lambda H_{\text{mix}} \quad (2.6)$$

$$H_1 = \begin{bmatrix} H_L & 0 \\ 0 & H_H \end{bmatrix} \quad (2.7)$$

$$H_{\text{mix}} = \begin{bmatrix} 0 & V^\dagger \\ V & 0 \end{bmatrix}. \quad (2.8)$$

---

<sup>2</sup>As Anderson remarks in Ref. [55], this was quite unexpected, since intra-atomic Coulomb exchange was usually expected to be ferromagnetic. However, it can be exceeded by the antiferromagnetic contributions due to hybridisation processes.

## 2 The Kondo Effect

The block structure of the Hamiltonian matrices in the above equations refers to the separation into low-energy and high-energy subspaces ( $H_L$  and  $H_H$ , respectively), which are mixed by the hybridisation  $V$ . The low-energy subspace consists of states in which the impurity is singly occupied, while the high-energy subspace contains only states with an empty or doubly-occupied impurity site [56].

We seek for a canonical transformation  $\tilde{U}$  that brings  $H$  into block-diagonal form

$$\tilde{U} \begin{bmatrix} H_L & \lambda H_{\text{mix}}^\dagger \\ \lambda H_{\text{mix}} & H_H \end{bmatrix} \tilde{U}^\dagger = \begin{bmatrix} H^* & 0 \\ 0 & H' \end{bmatrix}. \quad (2.9)$$

The right-hand side of the above equation can be regarded as a renormalised Hamiltonian, whose low-energy part  $H^*$  is the effective Hamiltonian which describes the low-energy physics of the model.

We assume  $\tilde{U} = e^S$ , where  $S$  is the antihermitian generating function ( $S = -S^\dagger$ ), and expand  $\tilde{U}$  in a power series of  $\lambda$

$$S = \lambda S_1 + \lambda^2 S_2 + \dots \quad (2.10)$$

Comparing coefficients, one obtains after some algebra up to second order in  $\lambda$

$$H^* = H_L + H_{\text{int}} = H_L + \frac{1}{2} P_L [S_1, H_{\text{mix}}]_- P_L, \quad (2.11)$$

where  $P_L$  denotes the projector of the low-energy subspace of the unperturbed Hamiltonian.  $H_{\text{int}}$  is the additional interaction term, generated by virtual excitations into the high-energy subspaces of the unperturbed Hamiltonian. Its matrix elements are given by

$$(H_{\text{int}})_{ab} = \frac{1}{2} \sum_{|\lambda\rangle \in P_H} \left( \frac{H_{\text{mix},a\lambda}^\dagger H_{\text{mix},\lambda b}}{E_a^L - E_\lambda^H} + \frac{H_{\text{mix},a\lambda}^\dagger H_{\text{mix},\lambda b}}{E_b^L - E_\lambda^H} \right), \quad (2.12)$$

where  $P_H$  is the projector of the high-energy subspace of the unperturbed Hamiltonian.  $E^{L,H}$  are energies of states in the corresponding subspaces [56].

Employing the identity  $\delta_{ab}\delta_{cd} + \boldsymbol{\sigma}_{ab} \cdot \boldsymbol{\sigma}_{cd} = 2\delta_{ad}\delta_{bc}$ , which is valid for the vector of Pauli matrices  $\boldsymbol{\sigma}$ , and assuming a large interaction  $U \gg |\varepsilon_{\mathbf{k}}|$ , we find for the Anderson model

$$H_{\text{int}} = \frac{1}{2} \sum_{\sigma\sigma'} J c_{i_1\sigma}^\dagger \boldsymbol{\sigma}_{\sigma\sigma'} c_{i_1\sigma'} \cdot \mathbf{S}_1 - \frac{1}{2} \sum_{\sigma} V^2 \left( \frac{1}{\varepsilon_f + U} + \frac{1}{\varepsilon_f} \right) c_{i_1\sigma}^\dagger c_{i_1\sigma} + \frac{V^2}{\varepsilon_f} \quad (2.13)$$

$$J = 2V^2 \left( \frac{1}{\varepsilon_f + U} - \frac{1}{\varepsilon_f} \right) \quad (2.14)$$

$$\mathbf{S}_1 = \frac{1}{2} \sum_{\alpha\beta} f_\alpha^\dagger \boldsymbol{\sigma}_{\alpha\beta} f_\beta. \quad (2.15)$$



The suppression of charge fluctuations at the impurity site for large  $U$  indeed produces a local moment  $\mathbf{S}_1$  with spin  $S = \frac{1}{2}$ . The exchange coupling  $J$  can be seen to be a nonnegative quantity; hence antiferromagnetic, as already anticipated from Anderson's arguments. In case of particle-hole symmetry, i.e.  $\varepsilon_f = -\frac{U}{2}$ , we obtain  $J = 8\frac{V^2}{U}$ , and the second term in Eq. (2.13), describing potential scattering at the site below the impurity, disappears. However, it does not influence the dynamics of the local moment in general [56].

One can check that terms, involving higher orders in  $V$ , do not lead to basically new contributions [58]. Furthermore, if applied to a multi-impurity model, the transformation does not generate new terms up to second order in  $V$  which would for example involve two impurities.

Summarising, we figured out how local moments evolve under the action of a strongly repulsive interaction  $U$  between localised electrons at the impurity site. If  $U$  is sufficiently large (i.e.  $U \gg |\varepsilon_{\mathbf{k}}|$  and  $|V| \ll |\varepsilon_{\mathbf{k}}|$ ), the impurity valence is frozen at single occupancy and we can restrict our considerations to spin exchange between the impurity spin  $\mathbf{S}_1$  and conduction electrons, provided we are interested in the low-energy physics. We will refer to this situation as the "Kondo limit". It should be remarked that more generally, electron models with local interactions  $U$  at each lattice site ("Hubbard models") represent a typical example of a correlated electron system in which quasi-particles can be destroyed and replaced by, e.g., local moments [59].

The effective Hamiltonian, Eq. (2.13), can be slightly reformulated, resulting in the Kondo model [11] with the following Hamiltonian

$$H = \sum_{\mathbf{k}\sigma} \varepsilon_{\mathbf{k}} c_{\mathbf{k}\sigma}^\dagger c_{\mathbf{k}\sigma} + J \mathbf{s}_{i_1} \mathbf{S}_1. \quad (2.16)$$

$\mathbf{s}_{i_1} = \frac{1}{2} \sum_{\sigma\sigma'} c_{i_1\sigma}^\dagger \boldsymbol{\sigma}_{\sigma\sigma'} c_{i_1\sigma'}$  is the conduction-electron spin at site  $i_1$ , to which the  $S = \frac{1}{2}$ -impurity is coupled. The Kondo effect is obtained for antiferromagnetic  $J$  as we will see below, but  $J$  can be also set ferromagnetic to mimic other exchange interactions.

Thereby, the stage is set for the study of the Kondo effect, which initiated a dramatic change of concepts in solid state physics.

## 2.3 The Kondo problem

### Orthogonality catastrophe

In 1967, Anderson pointed out that the ground states of the Kondo model Eq. (2.16) with and without the Kondo impurity are orthogonal to each other [54]. It is the direct consequence of the "infrared catastrophe" occurring in Fermi gases when local scattering potentials such as the local Kondo coupling  $J$  are turned on. The scattering

## 2 The Kondo Effect

phase shift  $\delta$  modifies the wave function of scattered electrons in such a way that the overlap  $\tilde{S}$  between wave functions of the unperturbed and perturbed problem near the Fermi surface becomes

$$\tilde{S} \leq \tilde{N}^{-\sin^2 \delta / 3\pi^2}, \quad (2.17)$$

where  $\tilde{N}$  is the volume of the considered system<sup>3</sup> and  $\delta$  is taken at  $\varepsilon_F$ . Since  $\tilde{N} \rightarrow \infty$ , we obtain  $\tilde{S} \rightarrow 0$  for any small but finite phase shift  $\delta$ . The result is understandable if we think of emerging bound states or provoked phase transitions, when the local potential is switched on. However, it is remarkable that orthogonality is predicted even for small  $\delta$ .

The orthogonality catastrophe has profound implications on the low-energy properties of the Kondo model ( $\delta = \frac{\pi}{2}$ ). The vanishing overlap between ground states of the unperturbed and the perturbed system renders standard perturbation theory impossible because of the missing adiabaticity [61]. This corroborates the conclusions from Kondo's results from perturbation theory [8] and suggests the formation of some sort of bound state.

The situation was disturbing, since experiments provided only evidences for Fermi liquid states at low temperatures, while the theory was plagued by divergencies. Though Kondo was able to reproduce adequate results for the high-temperature regime ( $T \gg T_K$ ), the "Kondo problem" of the nature of the low-temperature regime remained unsolved. However, it can be tackled in an elegant way, as Anderson showed by his "poor man's scaling approach" [9], which can be regarded as some kind of "refined perturbation theory". The essential idea is to iteratively follow the evolution of specific model quantities such as couplings, in order to understand their qualitative changes, when considering excitations of decreasing energy.

### Poor man's scaling approach

For this purpose we assume a weak coupling  $J \ll |\varepsilon_{\mathbf{k}}|$  and rewrite the Kondo model, Eq. (2.16), in momentum space

$$H = \sum_{|\varepsilon_{\mathbf{k}}| < D, \sigma} \varepsilon_{\mathbf{k}} c_{\mathbf{k}\sigma}^\dagger c_{\mathbf{k}\sigma} + \frac{1}{2} J(D) \frac{1}{L} \sum_{|\varepsilon_{\mathbf{k}}|, |\varepsilon_{\mathbf{k}'}| < D, \sigma} c_{\mathbf{k}\sigma}^\dagger \boldsymbol{\sigma}_{\sigma\sigma'} c_{\mathbf{k}',\sigma'} \mathbf{S}_1, \quad (2.18)$$

taking the density of conduction-electron states  $\rho(E)$  to be constant for simplicity.  $D$  ( $-D$ ) is the upper (lower) band edge of the effective conduction-electron band, while

---

<sup>3</sup>The overlap  $\tilde{S}$  is largely determined by the number of possible transitions from the unperturbed states to states of the perturbed system (close to the Fermi energy) [60]. Thus, in finite systems one may expect an avoided catastrophe and a finite overlap.

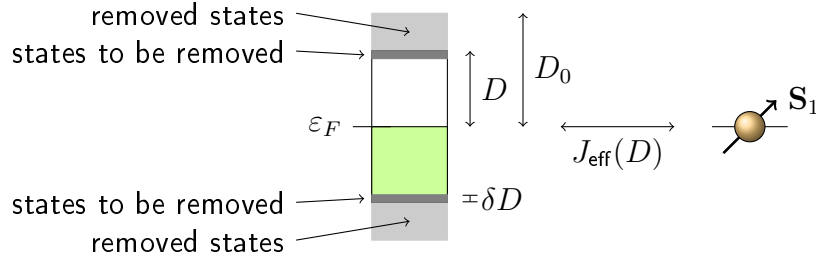


**Figure 2.2:** Illustration of the "poor man's scaling approach". At each iteration, the contributions to perturbation theory are calculated, which are produced by intermediate high-energy conduction-electron states in a thin energy shell  $\delta D$  at the band edges  $D$  and  $-D$  (dark grey). The contributions are absorbed in the local Kondo coupling  $J$ , leading to an effective coupling  $J_{\text{eff}}(D)$ . Subsequently, states in the interval  $\delta D$  at the effective band edges  $\pm D$  are removed from the system, and the procedure is repeated, until  $J_{\text{eff}}$  becomes too large to be treated by perturbation theory. The greenish area shows the filled fraction of the effective conduction-electron system. Figure adapted from Ref. [8].

the original band edge is  $D_0$  ( $-D_0$ ). The poor man's scaling procedure consists in "integrating out" the high-energy electron states in a thin energy shell  $\delta D$  at the band edges  $D$  and  $-D$ , e.g. by using the Schrieffer-Wolff transformation, Eq. (2.11), as sketched in Fig. 2.2. After some algebra, that we skip here for simplicity (see Refs. [8] and [56] for details),<sup>4</sup> we obtain an additional interaction term of the form

$$(\delta H_{\text{int}})_{\mathbf{k}'\sigma',\mathbf{k}\sigma} \approx \frac{1}{2} \frac{1}{L} J^2 \rho \frac{\delta D}{D} \boldsymbol{\sigma}_{\sigma\sigma'} \mathbf{S}_1. \quad (2.19)$$

In Eq. (2.19) we take into account the contributions stemming from initial and final low-energy electron states of energy  $|\varepsilon_{\mathbf{k}}|, |\varepsilon_{\mathbf{k}'}| \approx \varepsilon_F$  with intermediate high-energy states of energy  $D$ .  $\delta H_{\text{int}}$  can be added to the original Kondo interaction term (Eq. (2.18)), resulting in the following recursive relation for the effective Kondo coupling

$$J_{\text{eff}}(D') = J_{\text{eff}}(D) + J_{\text{eff}}^2(D) \rho \frac{\delta D}{D}. \quad (2.20)$$

$D' = D - \delta D$  denotes the effective band width ("cutoff scale") of the next iteration step. In the following, we omit the index of  $J_{\text{eff}}$  in situations in which a confusion with the "bare" coupling  $J$  can be excluded [56].

We want to pause for a moment and analyse the result. The effect of spin fluctuations associated to high-energy electrons is to enhance the local Kondo coupling, thus to

<sup>4</sup>Only results in second order in  $J$  are taken into account. The linear-in- $J$  term is energy-scale independent (Sec. 5.2) and is therefore omitted in our considerations. However, it may have substantial effects in a finite-size system, see chapter 5.

## 2 The Kondo Effect

"antiscreeen" the antiferromagnetic exchange [56] and thereby degrading the reliability of perturbation theory iteration by iteration. However, this is not the case for a ferromagnetic exchange coupling  $J$ , which effectively decreases when we decrease the cutoff  $D$ . In fact,  $J$  can be found to vanish for cutoffs approaching the Fermi surface (Eq. (2.22)). One may think of the impurity as essentially being decoupled from the conduction electrons at small energy scales. We will see in the sections 2.5 and 5.2 that the described low-energy behaviour is changed in finite-size systems.

The above equation (2.20) can be rewritten in terms of the dimensionless coupling  $g = \rho J$ , defining the so-called  $\beta$  function of  $g$

$$\frac{\partial g}{\partial \ln D} = \beta(g) = -g^2. \quad (2.21)$$

It is an explicit ordinary differential equation of first order and can be integrated without difficulty

$$g(D') = \frac{g_0}{1 - 2g_0 \ln(D_0/D')} \quad (2.22)$$

with the boundary condition  $g(D_0) = g_0$ . Introducing the scale-invariant parameter  $T_K$ , the Kondo temperature,

$$T_K = D_0 \exp\left(-\frac{1}{g_0}\right) = D_0 \exp\left(-\frac{1}{\rho J(D_0)}\right), \quad (2.23)$$

we obtain

$$g(D) = \frac{1}{\ln(D/T_K)}, \quad (2.24)$$

where  $g(D)$  depends only on  $T_K$  and the energy scale  $D$  at which  $g$  is measured. There is no reference to the original (ultraviolet) cutoff energy scale  $D_0$  left, signaling the irrelevance of the high-energy properties of the Kondo model for the low-energy degrees of freedom.

An important feature of Eq. (2.21) is that it represents an example of "asymptotic freedom", since the effective coupling  $J_{\text{eff}}$  is weak at large energy scales, i.e. at the beginning of the poor man's scaling procedure, and grows beyond unity at low energy scales. This is quite similar to quark confinement, where we find the same low-energy scaling behaviour for weak bare coupling strengths between gluons and between gluons and quarks [62]. Probed at high-energy scales, the quarks appear free, whereas confinement occurs at low-energy scales. The characteristic energy scale  $\Lambda_{\text{QCD}} = 1 \text{ GeV}$ , the mass of the proton. The corresponding length scale is of the order of 1 fm. In contrast, the Kondo length scale  $\xi_K \sim \frac{v_F}{T_K}$  is typically of the order of  $10^{-6} \text{ m}$ , i.e. of mesoscopic order of magnitude. Except of some pitfalls, one may generally switch between energy

dependent (temperature, excitation energies) and distance dependent picture<sup>5</sup> [62, 63]. For example, the low-temperature regime  $T \ll T_K$  is then (physically) identified with the behaviour at large distances  $r \gg \xi_K$ . Let us also remark the difference to charge screening, which exhibits a large effective interaction potential at small length scales due to the essentially free charge. Conversely, it is exponentially damped at large length scales [61].

According to Eq. (2.24), the effective Kondo coupling  $J_{\text{eff}}$  diverges for  $D = T_K$ . However, we must question this result, since it is derived from a perturbative approach, which is basically unreliable for large  $J_{\text{eff}}$ . Nevertheless, it is reasonable that  $J_{\text{eff}}$  can be extrapolated to large values at energy scales at and below  $T_K$  and that the system reaches a strong-coupling fixed point in terms of the scaling procedure. Hence,  $T_K$  might be rather thought of as a characteristic energy scale indicating a crossover instead of a phase transition.

For  $T \gg T_K$  we can be certain of the scaling behaviour of  $J$  and find it reflected in physical quantities, i.e. they can be written as universal functions of  $\frac{T}{T_K}$ . This concerns, e.g., the magnetic susceptibility or the resistance  $\tau^{-1}(T)$

$$\tau^{-1}(T) = \tau_0^{-1} F\left(\frac{T}{T_K}\right). \quad (2.25)$$

$F\left(\frac{T}{T_K}\right)$  can be specified by weak-coupling perturbation theory, leading to Jun Kondo's result

$$\tau^{-1}(T) = \tilde{n}_i \frac{2\pi}{\rho} S(S+1) \left( J\rho + (J\rho)^2 \ln \frac{D}{T} \right)^2, \quad (2.26)$$

where  $\tilde{n}_i$  is the density of impurities and  $S = \frac{1}{2}$  the impurity spin. When the temperature is lowered  $T \rightarrow T_K$ , the spin scattering of electrons at the magnetic impurity increases, resulting in the Kondo resistance minimum—the famous signature of the Kondo effect [56, 11].

At the strong-coupling fixed point  $J_{\text{eff}} \gg |\varepsilon_{\mathbf{k}}|$  and the impurity is strongly bound to the conduction electrons by antiferromagnetic exchange. A paramagnetic "Kondo singlet" is established and decouples from the system. The remaining (low-energy) conduction electrons at length scales larger than  $\xi_K$  would then represent a special kind of Fermi liquid, since moving to the Kondo cloud sites is accompanied by a large energy cost. This setting is the starting point of Nozières' "local Fermi liquid" picture [64]. He

---

<sup>5</sup>Keeping with the usage of natural units (footnote 1),  $T_K$  is converted by the Fermi velocity  $v_F$  to length scales,  $\xi_K \sim v_F/T_K$ . Further, it corresponds to time scales  $\tau_K \sim 1/T_K$ .

## 2 The Kondo Effect

found that the remaining Fermi liquid<sup>6</sup> in case of  $J \gg |\varepsilon_{\mathbf{k}}|$  is only weakly interacting and characterised by a phase shift of  $\delta = \frac{\pi}{2}$ . The phase shift can be understood as a boundary condition on the otherwise (comparatively) free electrons, owing to the exclusion of them at the Kondo singlet site  $i_1$ . It is in agreement with the Friedel sum rule, which states that the number of electrons bound in the Kondo singlet is  $2\frac{1}{\pi}\delta$ . It is remarkable, that many-body interactions induced by  $J$  lead to a simple phase shift at low energy scales, showing that the Kondo singlet resembles a non-magnetic scatterer. An indication of Fermi liquid properties is the specific heat, which turns out to be a linear function of temperature [56, 65].

### Further developments of the concept of scaling

Although the poor man's scaling approach clarified the physical behaviour of the Kondo model at energy scales above  $T_K$  by introducing the idea of scaling, it still did not (fully) solve the Kondo problem (i.e. the physics below  $T_K$ ). This was achieved by the further development of the "renormalisation group"<sup>7</sup> (RG) methodology and especially by Wilson's numerical renormalisation group method, which put Anderson's approach on a numerically exact basis [10].

The aim is to describe only the relevant low-energy physics of the system, for which only specific features of the high-energy physics matter. As we already did for the Kondo model, we may generally parameterise a considered Hamiltonian as a function of the cutoff energy scale  $D$ , i.e.  $H(D)$ . Decreasing  $D \rightarrow D' = \frac{1}{b}D$  with  $b > 1$ , requires to integrate out the excitations in the interval  $[D', D]$ . The resulting Hamiltonian  $H'_L$  describes the remaining low-energy degrees of freedom. In a last step, the Hamiltonian is rescaled  $H(D') = bH'_L$  [56]. Iterating these steps generates a whole trajectory of Hamiltonians  $H(D)$ , which becomes continuous as a function of  $D$  when  $b \rightarrow 1$ . If we understand the Hamiltonians as dependent on couplings  $\{g_i\}$  (in analogy to the local Kondo coupling  $g = \rho J$ ), we can characterise the trajectories by scaling equations or

---

<sup>6</sup>Another fascinating property of the Kondo model is that it has conformal symmetry [65]. The strict locality of the coupling leads to an effective one-dimensional description, which permits the application of the concepts of one-dimensional field theory in terms of left and right movers, and particularly the techniques of conformal field theory. We also know that the strong-coupling fixed point must describe a scale-invariant (and conformally invariant) situation at low energies, since it is effectively a Fermi liquid at length scales larger than  $\xi_K$ . After bosonisation of the conduction electrons in terms of spin and charge bosons, one finds indeed that the strong-coupling fixed point has conformal symmetry. The Hamiltonian is determined by spin currents which obey a Kac-Moody algebra, the infinite-dimensional generalisation of the  $SU(2)$  Lie algebra, with central charge  $k = 1$ .

<sup>7</sup>Actually, it is more a semigroup due to the missing inverses.

$$g \ll 1, H_{\text{LM}}^* \longrightarrow g \gg 1, H_{\text{SC}}^*$$

**Figure 2.3:** Renormalisation group flow from the weak-coupling fixed point to the strong-coupling fixed point. At weak couplings  $J \ll |\varepsilon_{\mathbf{k}}|$ , the local moment is essentially free and the system is described effectively by the "local-moment fixed point" Hamiltonian  $H_{\text{LM}}^*$ . Due to the flow equation Eq. (2.21) the effective coupling grows, until one approaches the strong-coupling fixed point, described by the Hamiltonian  $H_{\text{SC}}^*$ : the impurity becomes highly correlated with the conduction electrons in form of the emerging Kondo singlet. We remark that in an Anderson model, one additionally finds the "free-orbital fixed point" ( $H_{\text{FO}}^*$ ), where valence fluctuations are dominant and prevent the local moment formation at the impurity site [8, 63]. Figure adapted from Ref. [56].

renormalisation group flow equations, respectively,

$$\frac{\partial g_j}{\partial \ln D} = \beta_j(\{g_i\}). \quad (2.27)$$

If  $\beta$  is negative, as in case of the Kondo model (Eq. (2.21)), the coupling constant  $g$  is called "relevant" and increases with decreasing the cutoff. Conversely, a positive  $\beta$  leads to an "irrelevant" coupling. The renormalisation group flow of the Kondo model is depicted in Fig. 2.3.

In general, two different situations may be expected in the course of the scaling procedure [56]. If the cutoff  $D$  drops below the energy scale of a certain group of high-energy excitations, these become virtual. Thus, a crossover occurs, where additional interaction terms emerge in the transformed Hamiltonian  $H(D')$  which absorb the corresponding effects on the low-energy degrees of freedom. A prominent example is the crossover from the Anderson model to the Kondo model for  $V \ll |\varepsilon_{\mathbf{k}}|$  and  $U \gg |\varepsilon_{\mathbf{k}}|$ . Charge fluctuations at the impurity sites become virtual, leading to an effective spin exchange.

If the iterated low-energy Hamiltonian does not change any longer,  $H(D') = H(D)$  (i.e.  $\beta = 0$ ), we arrive at a fixed point of the scaling procedure. From the physical point of view, the cutoff  $D$  is then smaller than the lowest energy scale of the problem.

The development of the numerical renormalisation group (NRG [10]) was a milestone for the quantitative analysis of the Kondo model, as it does not rely on a perturbative determination of the influence of the high-energy states. Instead, the effective Hamiltonian is numerically diagonalised and only a small set of low-energy states are kept for the next iteration. Another essential feature is the logarithmic discretisation of the conduction-electron system, allowing for further improvements in the applicability but also to cover a broad range of energy scales—important to resolve exponentially dependent Kondo scales, Eq. (2.23). A basic requirement for an efficient renormalisation group treatment is the clear separation of energy scales. Nonetheless, there

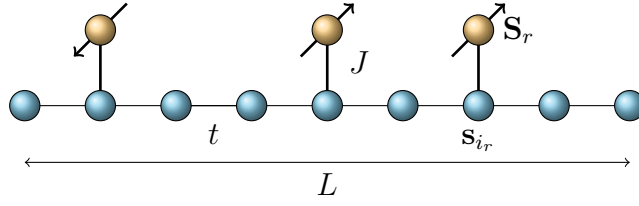


**Figure 2.4:** *The multi-impurity Kondo model discussed in this work. Local moments  $S_r$  with spin  $S = \frac{1}{2}$  are locally, antiferromagnetically exchange coupled to a non-interacting conduction-electron system of size  $L$  ( $i = 1, 2, \dots, L$ ). The electron hopping  $t = 1$  sets the energy scale. We assume open boundary conditions.*

are extensions such as the "functional renormalisation group" (fRG [66]), arguing to more effectively treat situations with competing energy scales, arising for example in multi-orbital models. Over the decades, NRG gained the status of a reliable tool for the numerical investigation of few-impurity systems. Its accuracy is confirmed by exact analytical results for the Kondo model which are based on the Bethe approach [67].

## 2.4 Model Hamiltonians, conventions, and notations

Before proceeding with the question related to effects of spatial confinement of single-impurity systems in section 2.5, we want to clarify notations and the setup of our numerical calculations. We already introduced the Anderson model (Eq. (2.2)) and the Kondo model (Eq. (2.16)). In both cases, the system can be subdivided into an impurity system, which is composed of  $R$  impurity sites, and a conduction-electron system containing a finite number of lattice sites  $L$  ( $i = 1, 2, \dots, L$ ); see Fig. 2.4 for the case of the Kondo model. Keeping in mind the applicability to surface systems, the subsystems will be sometimes also referred to as "adatoms" and "substrate". The energy scale is set by the conduction-electron hopping  $t := 1$  between nondegenerate orbitals of nearest-neighbouring sites. The electron number is denoted as  $N$ .

If not stated differently, we consider one-dimensional conduction-electron systems with open boundaries at zero temperature, in order to be able to apply DMRG (Sec. 3.3)—the default numerical method in this work. We usually employ one-dimensional systems also for simplicity, but our conclusions are similarly valid for higher dimensions (see e.g. Sec. 11.5). Impurities are placed at positions which are as symmetrical as possible with respect to the chain center. The systems are investigated at half-filling.

Practical DMRG calculations are performed in the subspace with the smallest total magnetisation  $M_{\text{tot}}$  possible (i.e.  $M_{\text{tot}} = 0$  or  $M_{\text{tot}} = \frac{1}{2}$ , respectively) to in principle permit ground states of all possible total spins  $S_{\text{gs}}$ .



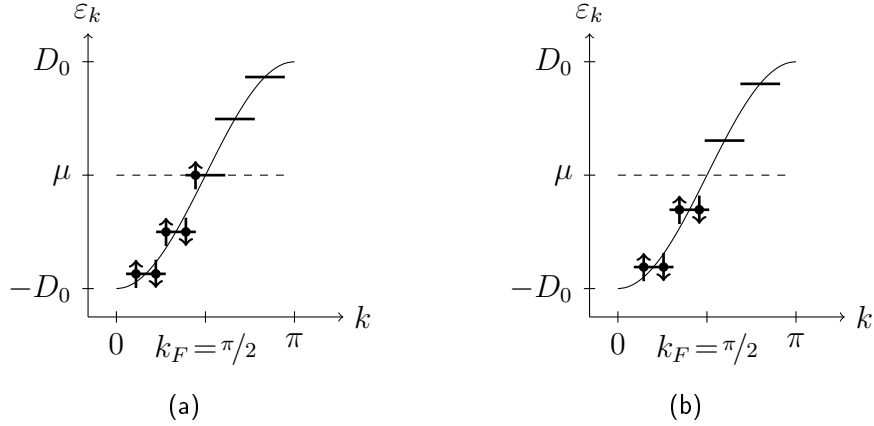


**Figure 2.5:** Energy levels  $\varepsilon_k$  of the non-interacting one-dimensional conduction-electron system ( $J = 0$  or  $V = 0$ , respectively) with open boundary conditions as functions of the momentum  $k$ . Solid lines: the electronic dispersion for  $L \rightarrow \infty$ .  $\pm D_0$  denote the band edges. Left: on-resonance case ( $L = 5$ ). An odd number of conduction electrons leaves one electron at the Fermi level resulting in a twofold spin degeneracy of the ground state. Right:  $L = 4$ . In an off-resonance case the number of conduction electrons is even. Hence, the chemical potential  $\mu$  lies within the finite-size gap between doubly occupied and empty levels.

The nondegenerate conduction-band eigenenergies of the models under consideration can be found by an analytical diagonalisation [68]

$$\varepsilon_k = -2t \cos k \quad (2.28)$$

$$k = \pi \frac{n}{L+1} \quad (2.29)$$

$$n = 1, 2, \dots, L. \quad (2.30)$$

The corresponding unitary transformation of the conduction-electron operators is given by

$$c_{i\sigma}^\dagger = \sum_k U_{ik} c_{k\sigma}^\dagger \quad (2.31)$$

$$U_{ik} = \sqrt{\frac{2}{L+1}} \sin(ik). \quad (2.32)$$

The local density of states at substrate site  $i$  is then

$$\rho_{ii}(E) = \rho_i(E) = \sum_k U_{ik}^2 \delta(E - (\varepsilon_k - \mu)), \quad (2.33)$$

where  $\mu = 0$  for a system at half-filling. If  $L$  is odd, the Fermi energy  $\varepsilon_F = 0$  and the energy-level spacing  $\Delta = 2t \sin(\pi/(L+1))$  at half-filling. Considering the filling, two

## 2 The Kondo Effect

different situations possible: when the number of conduction electrons is even, the Fermi energy lies exactly between two conduction-electron states what is termed "off-resonance case" (Fig. 2.5(b)). By contrast, in an "on-resonance case", i.e. for an odd conduction-electron number, a single electron occupies the level at the Fermi energy (Fig. 2.5(a)). Both cases cause basically different types of finite-size effects at low-energy scales as we will see in chapters 4-9. To ensure an integer total spin of the full system, we usually fix the total number of conduction electrons and localised spins  $N + R$  to be an even number. Off-resonant models then correspond to even  $R$  and on-resonant models to odd  $R$ .

The multi-impurity Kondo Hamiltonian is defined by

$$H = -t \sum_{\langle i,j \rangle, \sigma} c_{i\sigma}^\dagger c_{j\sigma} + J \sum_{r=1}^R \mathbf{s}_{i_r} \cdot \mathbf{S}_r. \quad (2.34)$$

$c_{i\sigma}$  annihilates an electron at site  $i = 1, \dots, L$  with spin projection  $\sigma = \uparrow, \downarrow$ , and  $\mathbf{s}_i = \frac{1}{2} \sum_{\sigma\sigma'} c_{i\sigma}^\dagger \boldsymbol{\sigma}_{\sigma\sigma'} c_{i\sigma'}$  is the local conduction-electron spin density at substrate site  $i$ , where  $\boldsymbol{\sigma}$  is the vector of Pauli matrices. Impurity spins  $\mathbf{S}_r$  ( $S = \frac{1}{2}$ ) couple antiferromagnetically ( $J > 0$ ) or ferromagnetically ( $J < 0$ ) to the local electron spins at the sites  $i_r$ , where  $r = 1, \dots, R$ . In case of Kondo models,  $N$  is the number of the itinerant and non-interacting conduction electrons.

The Hamiltonian of the multi-impurity Anderson model is given by [57]

$$H = -t \sum_{\langle i,j \rangle, \sigma} c_{i\sigma}^\dagger c_{j\sigma} + U \sum_{r=1}^R n_{r\uparrow}^f n_{r\downarrow}^f + \varepsilon_f \sum_{r=1}^R n_r^f \quad (2.35)$$

$$+ V \sum_{r=1}^R \sum_{\sigma} (f_{r\sigma}^\dagger c_{i_r\sigma} + \text{H.c.}) - \mu \left( \sum_{r=1}^R n_r^f + \sum_{i=1}^L n_i^c \right).$$

Here  $f_{r\sigma}^\dagger$  and  $c_{i\sigma}^\dagger$  create an electron with spin projection  $\sigma = \uparrow, \downarrow$  at impurity sites  $r = 1, 2, \dots, R$  and at substrate sites  $i = 1, 2, \dots, L$ , respectively.  $n_{r\sigma}^f = f_{r\sigma}^\dagger f_{r\sigma}$  and  $n_{i\sigma}^c = c_{i\sigma}^\dagger c_{i\sigma}$  denote the corresponding occupation-number operators. The spin-summed occupation at one of the impurity sites and at one of the substrate sites are given by  $n_r^f = n_{r\uparrow}^f + n_{r\downarrow}^f$  and  $n_i^c = n_{i\uparrow}^c + n_{i\downarrow}^c$ , respectively.  $V$  is the hybridisation between an impurity site  $r$  and the nearest-neighbour substrate lattice site  $i_r$ .  $U$  and  $\varepsilon_f$  are the on-site Hubbard interaction and the local on-site energy for the impurity sites, respectively.  $\mu$  is the chemical potential. In our calculations we consider the particle-hole symmetric case with  $\mu = 0$  and  $\varepsilon_f = -\frac{U}{2}$ , where the system is half filled, i.e. the average occupation numbers are given by  $\langle n_r^f \rangle = 1$  and  $\langle n_i^c \rangle = 1$  for all  $r$  and all  $i$ .

The magnetic properties of the system are best characterised by site-dependent local and nonlocal spin correlation functions and susceptibilities. We consider the impurity-

impurity susceptibility

$$\chi_{r,r'} = \left. \frac{\partial m_r^f}{\partial h_{r'}} \right|_{h_{r'}=0} = - \int_0^{1/T} d\tau \langle S_{r,z}^f(\tau) S_{r',z}^f(0) \rangle, \quad (2.36)$$

i.e., the local impurity susceptibilities  $\chi_{r,r}$  and the inter-impurity susceptibility  $\chi_{r,r'} = \chi_{r',r}$ . These provide information on the local impurity magnetic moment and, most important, on the indirect magnetic coupling. Further, we are interested in the linear magnetic response of the conduction-electron system which is accessible via the impurity-substrate susceptibilities

$$\chi_{i,r}^{\text{cond}} = \left. \frac{\partial m_i^c}{\partial h_r} \right|_{h_r=0} = - \int_0^{1/T} d\tau \langle s_{i,z}^c(\tau) S_{r,z}^f(0) \rangle. \quad (2.37)$$

Here  $m_r^f = \langle S_{r,z}^f \rangle$  and  $m_i^c = \langle s_{i,z}^c \rangle$ , with  $S_{r,z}^f = \frac{1}{2}(n_{r\uparrow}^f - n_{r\downarrow}^f)$  and  $s_{i,z}^c = \frac{1}{2}(n_{i\uparrow}^c - n_{i\downarrow}^c)$ , are magnetic moments at the impurity site  $r$  and at the substrate lattice site  $i$ , respectively. Note that we will sometimes omit  $c$  and  $f$  indices in cases where an identification is clear, e.g. due to the mapping of capital letters to impurity sites and small letters to substrate sites.

Furthermore, the imaginary-time dependence of an operator  $A$  is given by  $A(\tau) = e^{H\tau} A e^{-H\tau}$ . In our calculations the susceptibilities, Eqs. (2.36) and (2.37), are computed as a numerical derivative with respect to a local magnetic field of strength  $h_r$  coupling as  $H \rightarrow H - h_r S_{r,z}^f$  to the Hamiltonian. We use weak local magnetic fields with a strength  $h_r = 10^{-5}$  to  $10^{-2}$  at an impurity and look for the response at substrate site  $i$ . The linear-response regime is ensured by performing calculations with different  $h_r$ .

Finally, we remark that the conventional weak-coupling Kondo temperature (Eq. (2.23)) is denoted as  $T_K^0$  in the following. Since the Kondo temperature  $T_K$  is a function of  $L$ , we will sometimes also use the term  $T_K^{(\text{bulk})}$  for  $T_K$  in the bulk limit.

## 2.5 The Kondo box

After making familiar with the essential ideas in the field of single-impurity Kondo physics, we want to turn our attention to the basic questions of the present work. Experimental progress allows to construct nano-scale sized materials such as quantum chorals or ultra-small metallic grains (Sec. 1.1), which may exhibit a quite different physical behaviour as compared to bulk systems. In case of Kondo physics, the term "Kondo box" has been coined to emphasise the special properties of a single-impurity system in contact with a spatially confined conduction-electron system [19, 20, 69, 62].

Due to the finite size of the Kondo box, we must include a new energy scale into our considerations, namely the level spacing  $\Delta$  of the conduction-electron system.  $\Delta$

## 2 The Kondo Effect

acts as a cutoff in terms of RG, similar to a high temperature. It stops the RG flow for cutoff energy scales  $D$  smaller than  $\Delta$ ; excitations become impossible, since their energy is at least of the order  $\Delta$  (section 2.3). Consequently, we obtain no further contributions to the effective coupling  $J_{\text{eff}}$  for  $D < \Delta$ , compare Eq. (2.21). Most clearly, this circumstance is seen for  $\Delta = T_K$ , what occurs for an initial  $J_{\text{eff}}(D_0)$  with  $J_{\text{eff}}(D_0) = J_\Delta$  by definition. Keeping with Eq. (2.21), for  $J_{\text{eff}}(D_0) < J_\Delta$ , the system is not able to reach the strong-coupling fixed point in the course of the RG procedure. Thus, we may conclude that a crossover to the finite-size regime is expected at  $J_\Delta$ , which usually corresponds to weak couplings. Be aware that, again, we have to weaken the meaning of  $\Delta = T_K$  in the way that it represents a crossover region rather than a phase transition.

The conduction-electron spectrum of the Kondo box consists of a discrete set of delta peaks. However, finite-size effects occur for  $J < J_\Delta$ , while for  $J > J_\Delta$  we can think of the Kondo screening as being conducted by a collection of electrons in the energy interval  $T_K$ . This suggests averaging effects over several electron states, whereby their discrete nature becomes irrelevant, allowing to resort, in this case, to the bulk density of states for our argumentation purposes.

Let us translate our ideas into a real-space picture, as it provides a very intuitive way of understanding. The Kondo energy scale  $T_K$  corresponds to a characteristic length scale  $\xi_K \sim v_F/T_K$ , which defines the size of the "Kondo screening cloud". For low temperatures  $T \ll T_K$ , the impurity is screened by the Kondo effect and a Kondo cloud develops. The high-energy physics is that of an essentially free impurity and can be found at distances  $r \ll \xi_K$  from the impurity, i.e. within the cloud. On the other hand, for  $r \gg \xi_K$ , physics is governed by the low-energy Kondo physics, i.e. the strong-coupling fixed point, implying almost free electrons which experience a strong repulsion from the Kondo cloud sites.

If we choose  $\Delta > T_K$ , the strong-coupling fixed point cannot be reached, and hence the concept of the Kondo screening cloud collapses, with significant implications in particular for large distances and low temperatures. As outlined above, the RG flow is stopped in the vicinity of or at the starting point of the RG procedure which is the "local-moment fixed point" with an unscreened impurity. Since  $J_{\text{eff}}$  is prevented from diverging, we merely obtain residual couplings of the impurity to the conduction electrons, determined by the low-energy properties of the finite substrate. The residual interactions can be obtained perturbatively, just as in the case of high temperatures. Converting the condition  $\Delta > T_K$  into the real-space picture, we obtain the intuitive requirement that the bulk Kondo cloud does not match the system size, i.e.  $\xi_K > L$ .

We want to numerically check our ideas using a single-impurity Anderson model (SIAM). As known from section 2.2, the impurity is coupled by an effective antiferromagnetic exchange to the conduction electrons, resulting in screening of the impurity spin. A convenient measure for the Kondo cloud correlations is the integrated correlation func-

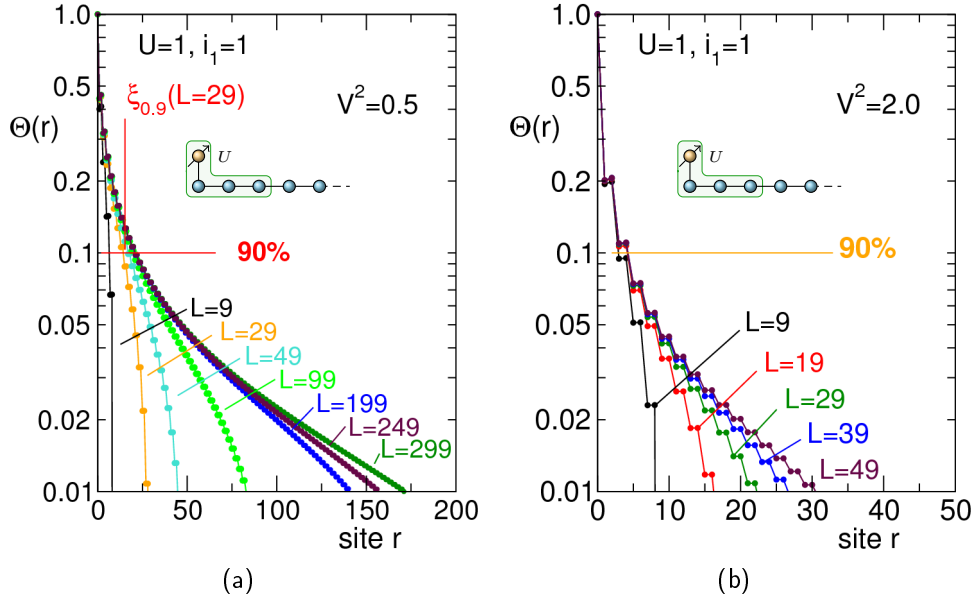


**Figure 2.6:** Integrated correlation functions  $\Theta(r)$ , as defined in the text (Eq. (2.38)), as functions of site  $r$  on a log scale. SIAM at  $U = 1$  with impurity at  $i_1 = 1$  and different system sizes  $L$  as indicated. Left:  $V^2 = \frac{1}{2}$ . Right:  $V^2 = 2$ .

tion [69]

$$\Theta(r) = 1 + \sum_{|i-i_1|<r} \frac{\langle \mathbf{S}_1 \mathbf{s}_i \rangle}{\langle \mathbf{S}_1 \mathbf{S}_1 \rangle}, \quad (2.38)$$

where  $\Theta(0) = 1$ .  $i_1$  denotes the site to which the impurity is coupled. With increasing distance  $r$  from the impurity more and more electron spins around  $i_1$  are included in the sum and  $\Theta(r)$  essentially decreases with  $r$ .  $\Theta = 0$  if all spins are included, signaling the complete screening of the impurity spin  $\mathbf{S}_1$ .  $\Theta(r)$  gives the fraction of the impurity spin that remains unscreened by the electrons up to distance  $r$  from  $i_1$ . A 90%-screening criterion, i.e.  $\Theta(\xi_{0.9}) = 0.1$ , for example, may be regarded as suitable to value the Kondo cloud size. For sufficiently large  $L$ ,  $\xi_{0.9}$  should give a good estimation of the bulk Kondo cloud size  $\xi_K$ .

An example for the typical shape of a Kondo cloud  $\Theta(r)$  is provided by a SIAM with  $L = 299$  (Fig. 2.6(a)). For decreasing  $L$ , the Kondo cloud shrinks, accommodating to the decreasing space. For large systems, this affects mostly the large distance behaviour, while for small systems  $L \lesssim 99$  we observe that also short-range details become influenced. The 90%-screening criterion for  $\Theta(r)$  suggests a Kondo cloud size of  $\xi_{0.9} = 20$  ( $L > 99$ ), where  $\xi_{0.9} \approx \xi_K$  due to  $\xi_K \gg L$ . Thus, for  $L = 9$  the condition  $\xi_K > L$  ( $\Delta > T_K$ ) is supposed to be fulfilled, and we enter the finite-size regime. Although the conventional Kondo cloud is not capable to develop, we

## 2 The Kondo Effect

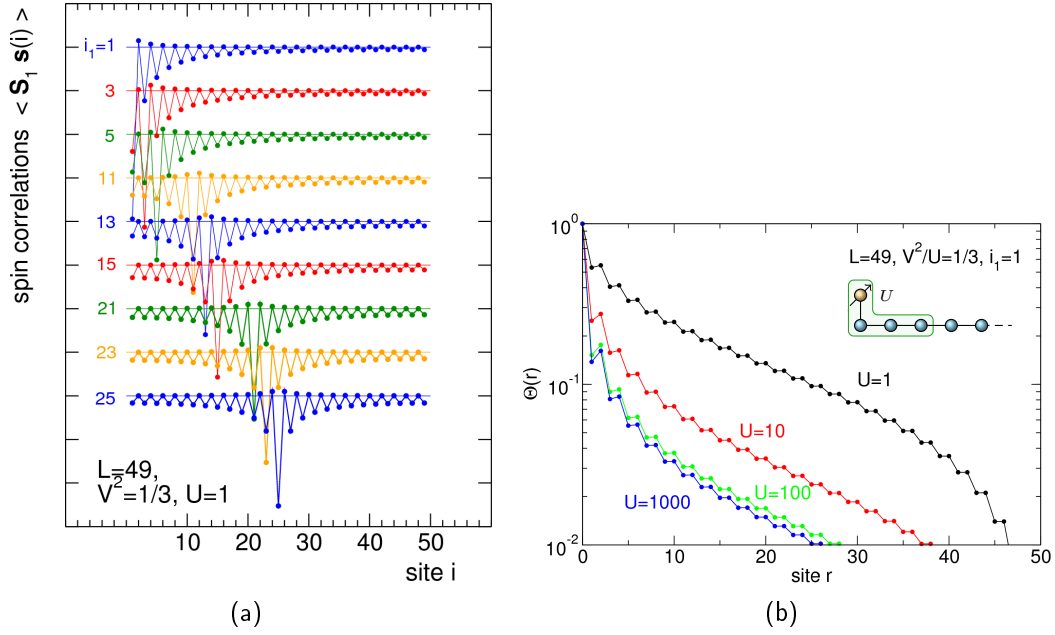


**Figure 2.7:** Left: spin correlations between impurity and conduction electrons  $\langle \mathbf{S}_1 \mathbf{s}_i \rangle$  as functions of site  $i$  for different impurity positions  $i_1$  as indicated. SIAM with  $V^2 = \frac{1}{3}$ ,  $U = 1$ , and system size  $L = 49$ . Lines have been shifted for better visibility. We do not show results in cases in which  $i_1$  is even due to the degeneracy of the ground state (see text). Right: integrated correlation functions  $\Theta(r)$ , as defined in the text (Eq. (2.38)), as functions of site  $r$  on a log scale. SIAM with  $i_1 = 1$  and  $L = 49$ . For different  $U$  as indicated, where  $V^2/U = \frac{1}{3}$  is kept fixed.

nonetheless obtain a singlet ground state and some sort of Kondo cloud. However,  $\Theta(r)$  has changed into an approximately linear function of  $r$ , indicating homogeneous spin correlations  $\langle \mathbf{S}_1 \mathbf{s}_i \rangle$  (visible in Fig. 2.8(a), black circles). We will have to figure out the reason for this observation (Sec. 5.2).

On the other hand, increasing  $V^2$  from  $V^2 = \frac{1}{2}$  in Fig. 2.6(a) to  $V^2 = 2$  in Fig. 2.6(b) obviously reduces the Kondo cloud size  $\xi_K$ . This leads to a faster convergence of  $\Theta(r)$  with respect to increasing  $L$ . In fact, by an appropriate data collapse of  $\Theta(r)$  for different  $V^2$ , one could find universal behaviour in terms of  $r/\xi_K$  [69].  $T_K \sim v_F/\xi_K$  is inferred to be larger for  $V^2 = 2$ , what is in line with the relations  $J = 8 \frac{V^2}{U}$  (Eq. (2.14)) and  $T_K \sim \exp(-\frac{1}{J})$  (Eq. (2.23)), provided we could ignore valence fluctuations on the impurity site.

When the impurity position  $i_1$  is varied, as done in Fig. 2.7(a), we observe that Kondo correlations  $\langle \mathbf{S}_1 \mathbf{s}_i \rangle$  are longer ranged if the impurity is at the chain center ( $i_1 = 25$ ) as compared to a position at the chain edges ( $i_1 = 1$ ). This circumstance rests on the fact that the local density of states experienced by the impurity is in fact not

equal for all sites in the electron system owing to the open boundaries, which induce Friedel oscillations [23]. Another peculiar finding is that an impurity, coupled to an even site  $i_1 = 2, 4, \dots$ , leads to a degenerate ground state spanned by states with total spin  $S_{\text{gs}} = 0$  and  $S_{\text{gs}} = 1$ . For  $V \rightarrow 0$ , we might understand this as effective decoupling of the impurity, i.e. vanishing residual couplings to the electron system for  $\Delta > T_K$ —despite the finite  $V$ . A similar effect is seen for Kondo boxes with an even number of conduction electrons (off-resonance case), where the chemical potential falls between two electron states. Hence, for  $\Delta > T_K$ , there are no states available which could couple to the impurity. Clearly, both observations deserve a deeper and more fundamental understanding and shall be regarded as starting points for the following investigations conducted in this work.

We briefly comment on the influence of charge fluctuations, which becomes apparent when we vary the local interaction  $U$  on the impurity site. Coming from  $U = 1$ , charge fluctuations become suppressed for increasing  $U$ , leading to a better defined impurity spin of almost  $S_1 = 0.5$  for  $U = 1000$ , in contrast to  $S_1 \approx 0.37$  for  $U = 1$  (based on  $\langle \mathbf{S}_1^2 \rangle = S_1(S_1 + 1)$ ). Likewise  $T_K$  rises for increasing  $U$  (keeping  $V^2/U$  fixed), visible from the stronger decrease of  $\Theta(r)$  in Fig. 2.7(b), what indicates a decreasing  $\xi_K$ . Apparently,  $T_K$  is also sensitive to the size  $S_1$  of the local moment.

The impurity-electron spin correlations  $\langle \mathbf{S}_1 \mathbf{s}_r \rangle$  in the interior and exterior regions of the Kondo cloud, shown in Fig. 2.8(a), are strongly governed by their different physical background. Following our above discussion, the impurity appears free at distances within the cloud  $r < \xi_K$ ; screening has not yet set in. We note that, in principle, we could also distinguish a characteristic length scale inside the cloud  $\xi_{\text{orb}} < \xi_K$ , below which the impurity moment is not yet formed due to pronounced charge fluctuations<sup>8</sup> ("free-orbital fixed point" [63, 8]). However, we find no indications for this scale in our results, as  $U$  is too large, i.e.  $\xi_{\text{orb}} \ll \xi_K$ .

Since the local moment has already formed, the local-moment regime allows for a perturbative treatment in the local exchange coupling  $J$ , yielding  $\langle \mathbf{S}_1 \mathbf{s}_r \rangle \sim (-1)^r / r^D$  in case of a  $D$ -dimensional lattices [70, 20]. Although the impurity spin  $\mathbf{S}_1$  is a conserved quantity within its lifetime  $\tau_K \sim 1/T_K$ , it decays for larger times owing to spin flips caused by the conduction electrons. Thus, for  $r \geq \xi_K$ , one expects an exponential dependency  $\langle \mathbf{S}_1 \mathbf{s}_r \rangle \sim \exp(-2r/\xi_K)$  [20], which is only hardly observable due to larger contributions from the following effect: for  $r \gg \xi_K$ , the impurity is completely screened and we obtain a Fermi liquid which feels the cloud as hardcore scatterer. This situation is accessible by perturbation theory in  $t/J$ , leading to  $\langle \mathbf{S}_1 \mathbf{s}_r \rangle \sim (-1)^r / r^{D+1}$  [70, 20].

<sup>8</sup>A. Mitchell et al demonstrate in Ref. [63] that a reliable, alternative method for the discrimination of the three regimes is to analyse  $|\Delta n(r)|$  as a function of distance  $r$  or temperature  $T$ .  $|\Delta n(r)|$  is the modulus of the excess charge density, i.e. of the difference between the conduction-electron density with and without impurity.

## 2 The Kondo Effect

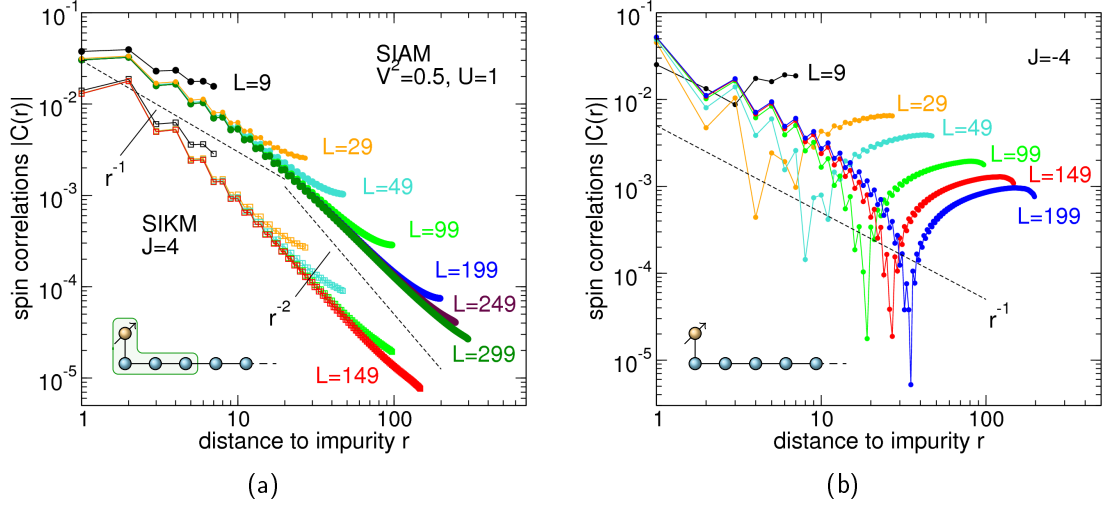


**Figure 2.8:** Two-site averaged Kondo cloud correlations  $|C(r)| = \frac{1}{2}|\langle \mathbf{S}_1 \mathbf{s}_{i_1+r} \rangle + \langle \mathbf{S}_1 \mathbf{s}_{i_1+r+1} \rangle|$  as functions of the distance  $r$  from the impurity on a double log scale. Different system sizes as indicated are considered. In all cases the impurity is coupled to a chain edge, i.e.  $i_1 = 1$ . For comparison, special distance dependencies are indicated as black dashed lines. Left: single-impurity Kondo model (SIKM) with antiferromagnetic  $J = 4$  (open squares) and single-impurity Anderson model (SIAM) with  $V^2 = \frac{1}{2}$  and  $U = 1$  (filled circles). Right: SIKM with ferromagnetic coupling  $J = -4$ . Note that there is a sign change manifesting as minimum in  $|C(r)|$ . For smaller distances than the position of the minimum, correlations are antiferromagnetic ( $C(r) < 0$ ), while they are ferromagnetic ( $C(r) > 0$ ) for larger distances.

In Fig. 2.8(a), we show the Kondo correlations  $\langle \mathbf{S}_1 \mathbf{s}_r \rangle$ , appropriately averaged, for a single-impurity Anderson model (upper lines with filled circles) for different system sizes  $L$ . For large  $L \gg \xi_K$ , one can clearly distinguish the local-moment regime and the strong-coupling regime by means of the different distance dependencies ( $\sim 1/r$  and  $\sim 1/r^2$ , respectively), indicating a crossover around  $\xi_K \approx 15 - 20$ . This is in agreement with the above value of  $\xi_{0.9}$  obtained from  $\Theta(r)$  (Fig. 2.6(a)). For small lattices with  $\xi_K \lesssim L$  (e.g.  $L = 29$ ), just the local-moment regime is retained, accompanied by a distance dependence  $\sim 1/r$  for almost all  $r$ . In the extreme limit  $\xi_K > L$ , where the system size cuts off the development of the Kondo cloud, the averaged Kondo correlations converge to a constant function of  $r$ , as already discussed above for  $L = 9$ .

In line with the previous results, a larger Kondo temperature  $T_K$  is obtained by suppressing charge fluctuations, what can be observed when we switch to a single-impurity Kondo model with perfect  $S_1 = \frac{1}{2}$  (lower lines with open squares in Fig. 2.8(a)). Choosing an equivalent coupling  $J = 4$  according to the relation  $J = 8 \frac{V^2}{U}$  (Eq. (2.23)), we find a large strong-coupling regime with a crossover at  $\xi_K \approx 10$ .



The results should be contrasted to those for a single-impurity model with ferromagnetic exchange coupling  $J < 0$  between impurity and conduction electrons (Fig. 2.8(b)), where we do not expect a crossover. As discussed in section 2.3, in the course of an RG procedure, the ferromagnetic  $J_{\text{eff}}$  decreases for decreasing cutoff energy scale and therefore the strong-coupling fixed point, which would correspond to a ferromagnetic Kondo effect, is not reached [8]. Interestingly, though we expectedly find a local-moment regime with  $1/r$  distance dependence, it is replaced at large distances by a regime with averaged spin correlations of opposite sign, resulting in a dip for the absolute values (Fig. 2.8(b)). As can be seen, the respective distance  $r$  for this sign change is, however, dependent on the system size  $L$ , signaling the finite-size origin of it.

## 2.6 Outlook

In the course of the numerical study of Kondo box models, we have recognised that finite-size effects may play a major role in determining the physics of the weak-coupling regime. This is the case when the finite-size gap  $\Delta$  of the conduction-electron system is larger than the Kondo energy scale  $\Delta > T_K$  or  $\xi_K > L$ , respectively. From the point of view of RG, the physics is settled: the system cannot reach the strong-coupling fixed point but remains trapped at the local-moment fixed point, where the impurity is unscreened. It means that the system size  $L$  may act as a cutoff energy scale comparable to a high temperature  $T \gg T_K$ , rendering perturbative approaches possible.

However, for our purposes we need to develop a much broader concept of finite-size effects than those currently available. We will have to analyse the effect of residual couplings to the electron system, which can result in completely different behaviour than in the conventional regime  $T_K > \Delta$ . Some important questions have been already raised: what happens at even sites, where the impurity appears to be decoupled for  $\Delta > T_K$ ? What is the origin of "Kondo clouds" of an impurity at odd sites for  $\Delta > T_K$ ? Which effects do mutual interactions with other impurities have in the finite-size regime? By means of perturbation theory and numerical techniques, we will elaborate a conclusive concept of finite-size effects in impurity systems, which allows to answer such questions.



## 3 Methods and theorems

### 3.1 Introduction

It is a well-known obstacle for numerical calculations that the Hilbert space of a quantum system scales exponentially with the system size, preventing the application of any exact diagonalisation approaches for system sizes significantly beyond  $L = 10 - 20$ , what is our intention in this work. Major alternative numerical methods have their own drawbacks: numerical RG (NRG [10]) is tailored for the investigation of Kondo models, however, typically only for a few impurities or orbitals. Dynamical mean-field theory (DMFT) [26, 71] may be plagued by the incomplete incorporation of nonlocal correlations due to its mean-field nature. On the other hand, quantum Monte Carlo techniques can have severe problems with low temperatures and the fermionic sign—especially in frustrated situations, e.g. in two dimensions [53]. Exact analytical results, even if they exist (e.g., on the basis of the Bethe approach [67]), may demand involving evaluations. An exception represents the general Lieb theorem (Sec. 3.5) which is applicable to systems of interest for us and delivers important, exact analytical results [47, 48, 72].

If we are interested in the ground-state properties of one-dimensional models, we may choose density-matrix renormalisation group [25] (DMRG, Sec. 3.3). It permits an efficient control over the number of numerical degrees of freedom and produces highly accurate, nonperturbative results without restriction to special model types. In this work we employ a DMRG variant which is based on matrix-product states (MPS). Standard DMRG is basically a zero-temperature technique.

However, its power is limited to one-dimensional models, as we will explain below. For this reason, we will also work with a real-space variant of dynamical mean-field theory [27] (R-DMFT, Sec. 3.4) to be able to investigate higher-dimensional models (Sec. 11.5). This requires understanding of the reliability of R-DMFT, which will be discussed in chapters 4 and 11.

For clarity, all DMRG calculations for this work have been performed by the author, whereas the R-DMFT results have been obtained by Irakli Titvinidze. Both numerical methods are discussed in this chapter; with emphasis on DMRG as the main source for numerical results.

## 3.2 Origin of DMRG

We want to briefly present a survey of the historical background of DMRG. It was developed by Steven White in 1992 [25] as consequence of trying to formulate a real-space renormalisation group method, what turned out to be a difficult task. The problem can be traced back to the question as to what an appropriate approach for low-energy wave functions of a certain system is. Keeping in mind the necessary flow from small to large length scales, an intuitive but incomplete guess would be a product state of low-energy wave functions of two corresponding subsystems [73]. Individual boundary conditions of the subsystems then usually lead to the wrong ground state of the total system, since the true ground state is not subject to these constraints at the interface of the subsystems. However, White showed that the correct low-energy wave functions can be obtained if one introduces a bipartite structure of system and environment, which allows for fluctuations between both subsystems, and hence a larger class of possible ground states than just a product state. This is indicative of entangled states (Eq. (3.20)), which are discussed below.

Later, one realised that DMRG is connected to matrix-product states: first, it was shown that the fixed-point state of a DMRG procedure in an infinite system attains the structure of matrix-product states. Then it became clear that the finite-system variant of DMRG is a variational treatment of MPS [74, 75].

A second, independent branch evolved from the study of certain models with ground states which have remarkable simple structure in form of MPS with small matrix dimensions. A prominent example is the one-dimensional Affleck-Kennedy-Lieb-Tasaki Hamiltonian (AKLT) [76, 75]

$$H = \sum_i \left( \mathbf{S}_i \mathbf{S}_{i+1} + \frac{1}{3} (\mathbf{S}_i \mathbf{S}_{i+1})^2 \right), \quad (3.1)$$

where, in this case,  $\mathbf{S}_i$  refer to  $S = 1$  spins. Its ground state ("AKLT state") belongs to the simplest, non-trivial MPS as it contains two-dimensional matrices. However, it also exhibits further fascinating properties. In the AKLT state, the  $S = 1$  spins at each site can be regarded as being decomposed into two single  $S = \frac{1}{2}$  which are linked across sites by singlet states, indicating a valence bond structure. Furthermore, it can be shown that spin correlations decrease exponentially in real space  $\langle S_i^z S_j^z \rangle \sim (-\frac{1}{3})^{i-j}$ . On the other hand the so-called "string correlator"  $\langle S_i^z \exp(i\pi \sum_{i < k < j} S_k^z) S_j^z \rangle = -\frac{4}{9}$  for  $j - i > 2$ , suggesting some kind of topological order.

## 3.3 Density-matrix renormalisation group

In the following, we want to present the basic elements of DMRG formulated with matrix-product states. Even though there are conceptual differences to original DMRG,

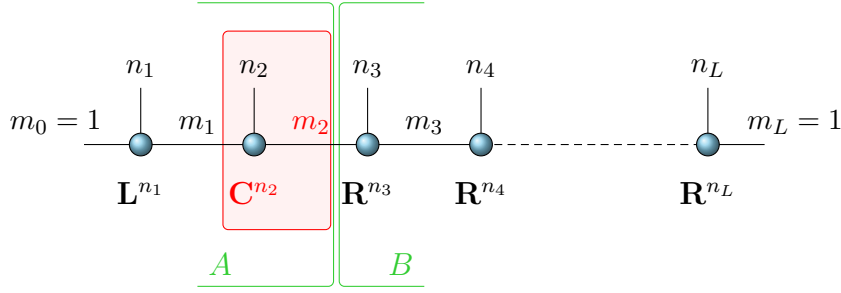


**Figure 3.1:** Network representation of a matrix-product state (MPS), which is an essential entity in MPS-based DMRG. The depicted MPS is local orthogonal with respect to the second site, which is currently dealt with by the algorithm (indicated by the red rectangle). The green lines indicate the respective bipartition into subsystem  $A$  and  $B$ . Blue circles symbolise local matrices, labeled below, which are connected with each other by "virtual bonds" (black lines).  $m_q$  denotes the corresponding matrix dimensions and  $n_q$  the local basis states at site  $q$ . In the course of one iteration step of a right-moving sweep, the solution of the local, effective eigenvalue problem, Eq. (3.7), gives new elements for  $C^{n_2}$ . Subsequently, we may adapt  $m_2$ , the size of  $C^{n_2}$ , by using the "mixed single-site approach", Eq. (3.13). The left-orthogonalisation of  $C^{n_2}$  (Eq. (3.3)) leaves remainder matrices which are multiplied to the right-orthogonal matrices  $R^{n_3}$  at site 3. The resulting  $C^{n_3}$  are the initial matrices for the next iteration step of the algorithm.

we will refer to it also as DMRG for simplicity. However, due to the wealth of fundamental aspects and implementation details, this overview cannot be complete. Instead, we want to focus more on the illustration of certain aspects which are essential for the numerical power of our specific implementation. Further detailed informations are compiled in Refs. [77], [78], and [68]. For general review papers, we refer for example to Refs. [79] and [75].

Our implementation is based on the premise to represent a state  $|\psi\rangle$ , usually the ground state, in form of a matrix-product state (MPS) [79, 75]

$$|\psi\rangle = \sum_{n_1, n_2, \dots, n_L} \mathbf{A}^{n_1} \mathbf{A}^{n_2} \dots \mathbf{A}^{n_L} |n_1\rangle |n_2\rangle \dots |n_L\rangle, \quad (3.2)$$

where  $|n_q\rangle$  are local basis states at site  $q$  (with dimension  $d_q$ ).<sup>1</sup>  $\mathbf{A}^{n_q}$  are  $m_{q-1} \times m_q$  matrices which contain the corresponding coefficients. These can be assumed to be real as we are just interested in the ground state. As we consider open boundary conditions,  $m_0 = 1$  and  $m_L = 1$ .

<sup>1</sup>However, "local" should not be taken to literally. Here, the choice of basis states is independent of any picture; we could alternatively use for example the momentum-space picture.

### 3 Methods and theorems

The MPS representation, Eq. (3.2), might appear as a severe approximation; however, it does not need to be an approximation at all, since one just needs to sufficiently increase the matrix dimensions to parameterise every state faithfully. On the other hand, we can also reverse this statement: by constraining the matrix dimensions to a numerically convenient size, we can find accurate approximations to the exact ground state. A rather extreme choice would be  $m_p = 1$  for all sites, resulting in  $1 \times 1$  matrices, i.e. scalars. Obviously, this represents a product state in real space, which neglects all nonlocal correlations.

Matrix-product states possess a gauge freedom (inserting  $\mathbf{X}\mathbf{X}^{-1} = \mathbf{1}$  into the MPS), which can be used to bring them into a locally orthogonalised form with respect to a particular site  $q$ . This will simplify the calculation of the effective Hamiltonian later on (Eq. (3.7)). We require

$$\sum_{n_p} \mathbf{L}^{n_p \dagger} \mathbf{L}^{n_p} = \mathbf{1} \quad (p < q) \quad (3.3)$$

$$\sum_{n_p} \mathbf{R}^{n_p} \mathbf{R}^{n_p \dagger} = \mathbf{1} \quad (p > q). \quad (3.4)$$

The matrices at site  $q$ ,  $\mathbf{C}^{n_q}$ , remain non-orthogonal. The MPS attains the following form

$$|\psi\rangle = \sum_{\substack{n_1, \dots, n_{q-1}, n_q, \\ n_{q+1}, \dots, n_L}} \mathbf{L}^{n_1} \dots \mathbf{L}^{n_{q-1}} \mathbf{C}^{n_q} \mathbf{R}^{n_{q+1}} \dots \mathbf{R}^{n_L} |n_1\rangle \dots |n_{q-1}\rangle |n_q\rangle |n_{q+1}\rangle \dots |n_L\rangle. \quad (3.5)$$

As a side product, we find the conditions that  $m_{p-1}d_p \geq m_p$  for  $p < q$  and  $m_p d_p \geq m_{p-1}$  for  $p > q$ . Replacing the inequality signs by equality signs, defines an MPS which is able to represent any state of the system, reflecting the exponential growth of the Hilbert space with increasing system size.

## Variational principle and sweeping

The matrix elements of an MPS can be regarded as variational parameters and the MPS itself as a trial wave function, subjected to a Ritz variational principle to obtain the ground state. Let us formulate how to choose the matrix elements which are best approximations for the ground state of a given Hamiltonian  $H$ . In principle, we could vary all matrix elements at the same time, but this would amount to some kind of exact diagonalisation algorithm. A more convenient way is to exploit the explicitly local representation of the MPS by varying only matrix elements at a particular site  $q$  and keeping matrix elements of all other sites fixed, i.e.

$$\frac{\langle \psi | H | \psi \rangle}{\langle \psi | \psi \rangle} = \text{minimal} \quad \text{for variations of } \mathbf{C}^{n_q}. \quad (3.6)$$

### 3.3 Density-matrix renormalisation group

In general, Eq.(3.6) can be formulated as generalised eigenvalue problem of the effective Hamiltonian  $\mathbf{K}$  (defined below). But since we require the MPS to be locally orthogonal (Eqs. (3.3) and (3.4)), it reduces to an ordinary eigenvalue problem with eigenvalue  $\lambda$

$$\sum_{ijn_q} K_{i'j'n'_q,ijn_q} C_{ij}^{n_q} = \lambda C_{i'j'}^{n'_q}. \quad (3.7)$$

In consequence of the locality of the problem to solve, the whole algorithm scales essentially linearly with the system size  $L$ , in contrast to exponential scaling in case of exact-diagonalisation routines.

To understand how  $K_{i'j'n'_q,ijn_q}$  is determined, we need to know how to conveniently handle operators in the MPS language. In a similar way as states, they are represented as matrix-product operators (MPO), e.g. the Hamiltonian  $H$

$$H = \sum_{n_1, n_2, \dots, n_L} \sum_{n'_1, n'_2, \dots, n'_L} \mathbf{H}^{n'_1 n_1} \mathbf{H}^{n'_2 n_2} \dots \mathbf{H}^{n'_L n_L} |n'_1\rangle \langle n_1| |n'_2\rangle \langle n_2| \dots |n'_L\rangle \langle n_L|. \quad (3.8)$$

$\mathbf{H}^{n'_q n_q}$  are  $M_{q-1} \times M_q$  matrices, where  $M_0 = 1$  and  $M_L = 1$ . An operator can have different faithful representations (also varying in matrix size), but schemes have been developed to generate matrices which are as small as possible and sparse [80, 81, 68]. Typically  $M_q$  is  $\mathcal{O}(10)$  in our calculations.

Furthermore, we recursively define two useful entities

$$\mathbf{E}_{\alpha_p}^p = \sum_{n_p n'_p} \sum_{\alpha_{p-1}} H_{\alpha_{p-1} \alpha_p}^{n'_p n_p} \mathbf{L}^{n'_p \dagger} \mathbf{E}_{\alpha_{p-1}}^{p-1} \mathbf{L}^{n_p} \quad (p < q) \quad (3.9)$$

$$\mathbf{F}_{\alpha_{p-1}}^{p\dagger} = \sum_{n_p n'_p} \sum_{\alpha_p} H_{\alpha_{p-1} \alpha_p}^{n'_p n_p} \mathbf{R}^{n_p} \mathbf{F}_{\alpha_p}^{p+1\dagger} \mathbf{R}^{n'_p \dagger} \quad (p > q), \quad (3.10)$$

where  $\mathbf{E}^0 = \mathbf{1}$  and  $\mathbf{F}^{L+1\dagger} = \mathbf{1}$ .  $\mathbf{1}$  denotes the unity matrix. One may notice that the recursive formulation of  $\mathbf{E}^p$  and  $\mathbf{F}^{p\dagger}$  permits an iterated update of both expressions when sweeping through the lattice site by site.

Now we can express the effective Hamiltonian  $K_{i'j'n'_q,ijn_q}$  in terms of known entities of site  $q$  and its adjacent sites  $q \pm 1$

$$K_{i'j'n'_q,ijn_q} = \sum_{\alpha_q \alpha_{q-1}} E_{\alpha_{q-1};i'i}^{q-1} H_{\alpha_{q-1} \alpha_q}^{n'_q n_q} F_{\alpha_q;j'j}^{q+1*}. \quad (3.11)$$

The corresponding sparse eigenvalue problem, Eq. (3.7), can be solved by efficient exact diagonalisation methods [82] such as the Lanczos method [83], the Davidson algorithm [84], or the Jacobi-Davidson algorithm, depending on the accuracy and convergence requirements. Regarding only the determination of the ground state, this is the most

### 3 Methods and theorems

time consuming part with an overall scaling of  $\mathcal{O}(\tilde{m}^3 \tilde{M}^2 d_q^2)$ .  $\tilde{m}$  denotes the order of magnitude of  $\mathbf{A}^{n_q}$  matrix dimensions and  $\tilde{M}$  those of  $\mathbf{H}^{n'_q n_q}$ .

We want to briefly describe the complete iteration procedure of our DMRG implementation (sketched in Fig. 3.1). According to previous considerations, a single iteration step contains only local updates. Thus, let us assume that the algorithm arrives at a specific site  $q$  and will deal with site  $q + 1$  in the next step, i.e. is right-moving. The optimal matrix elements of  $\mathbf{C}^{n_q}$  are obtained from the variational principle, Eq. (3.7). We have to take care that the matrices at site  $q$  are left orthogonal, i.e. obey Eq. (3.3). However, since this is not the case for  $\mathbf{C}^{n_q}$ , remainder matrices result from the left-orthogonalisation (e.g. singular value decomposition, SVD), which are multiplied to the matrices  $\mathbf{R}^{q+1}$  at site  $q + 1$  in a consistent way (wave-function transformation [85]). In consequence, we get a convenient initial guess for the variational treatment at the next site, reducing the number of necessary iterations. At the end, the  $\mathbf{E}^q$  matrices are updated using the recently obtained  $\mathbf{L}^{n_q}$  matrices according to Eq. (3.9), to ensure working with the correct effective Hamiltonian  $\mathbf{K}$  (Eq. (3.7)) in the next iteration step. When the right chain end is reached, the processing direction is changed to left, followed by analogue iteration steps. The outlined iteration scheme is performed until convergence is reached, what is usually the case after a few sweeps through the whole chain. A suitable exit criterion can be the convergence of the ground-state energy which has to decrease at each iteration towards the true ground-state energy. Alternatively, one can track the convergence of the overlap of the MPS before and after a complete sweep through the chain, what is a more demanding criterion as it captures also nonlocal aspects of the MPS convergence.

## Improvements and numerical details

A typical problem is that the algorithm can get stuck in a local energy minimum. In the original DMRG algorithm [25], such a situation is prevented by the two-site implementation, naturally introducing fluctuations from the second site. Another drawback of the pure single-site algorithm is that quantum numbers of the initial state do not change in the course of the calculation, constraining the convergence to the true ground state. For these purposes, White developed a "mixed single-site approach" [86, 81], applicable to single-site implementations, as discussed here. The idea is to weakly perturb the state; however, not randomly but in a physically consistent way. Based on the power method [86, 81], we may replace  $|\psi\rangle \rightarrow (1 + \varepsilon H)|\psi\rangle$ , where  $\varepsilon \ll 1$  and  $|\psi\rangle$  is the considered state. Note that this approach violates the variational property of the pure single-site variant, what may occasionally lead to a slight incline of the ground-state energy in the course of iterations.

A tractable implementation of this approach considers the reduced density matrix  $\rho$ . For an MPS  $|\psi\rangle$ ,  $\rho$  is obtained by carrying out the partial traces of the density matrix



### 3.3 Density-matrix renormalisation group

$|\psi\rangle\langle\psi|$ . For a right-moving algorithm, this means tracing out states from sites to the right of a particular site  $q$ , resulting in

$$\rho_{i_{q-1}n_q, i'_{q-1}n'_q} = (\mathbf{C}^{n_q} \mathbf{C}^{n'_q \dagger})_{i_{q-1}i'_{q-1}}. \quad (3.12)$$

For clarity,  $\boldsymbol{\rho}$  is a  $m_{q-1}d_q$  dimensional square matrix. We apply the perturbation in the following way

$$\boldsymbol{\rho} \rightarrow \boldsymbol{\rho} + \varepsilon \boldsymbol{\rho}' \quad (3.13)$$

$$\boldsymbol{\rho}' = \text{Tr}_R (H (\boldsymbol{\rho} \otimes \mathbf{1}_R) H^\dagger), \quad (3.14)$$

where  $\varepsilon$  is of the order  $10^{-2} - 10^{-3}$  in our calculations.  $\text{Tr}_R$  denotes the partial trace with respect to states to the right of  $q$  and  $\mathbf{1}_R$  the corresponding unity matrix.

After some algebra and using definitions Eqs. (3.9) and (3.10), one obtains

$$\rho'_{i_{q-1}n_q, i'_{q-1}n'_q} = \sum_{\substack{i'_{q-1}n'_q \\ i_{q-1}n_q}} \sum_{\substack{\alpha_{q-1}\alpha_q \\ \beta_{q-1}\beta_q}} \quad (3.15)$$

$$G_{\alpha_q\beta_q}^{q+1} H_{\alpha_{q-1}\alpha_q}^{n_q n_q} E_{\alpha_{q-1}, i_{q-1}i_{q-1}}^{q-1} \rho_{i_{q-1}n_q, i'_{q-1}n'_q} E_{\beta_{q-1}, i'_{q-1}i'_{q-1}}^{q-1 \dagger} H_{\beta_{q-1}\beta_q}^{n'_q n'_q *} \\ G_{\alpha_q\beta_q}^{q+1} = \text{Tr} \mathbf{F}_{\alpha_q}^{q+1 \dagger} \mathbf{F}_{\beta_q}^{q+1}. \quad (3.16)$$

Computing the elements of  $\boldsymbol{\rho}'$  this way is a quite demanding task and in principle not necessary, as our aim is to introduce only a small amount of physical fluctuations. Therefore, usually we use one of the two following simplified expressions in our calculations

$$\rho'_{n_q, n'_q} = \sum_{\alpha_{q-1}} \mathbf{E}_{\alpha_{q-1}}^{q-1} \boldsymbol{\rho}_{n_q, n'_q} \mathbf{E}_{\alpha_{q-1}}^{q-1 \dagger} \quad (3.17)$$

$$\rho'_{n_q, n'_q} = \sum_{n'_q n_q} \sum_{\alpha_{q-1}\alpha_q} H_{\alpha_{q-1}\alpha_q}^{n_q n_q} \mathbf{E}_{\alpha_{q-1}}^{q-1} \boldsymbol{\rho}_{n_q, n'_q} \mathbf{E}_{\alpha_{q-1}}^{q-1 \dagger} H_{\alpha_{q-1}\alpha_q}^{n'_q n'_q *}. \quad (3.18)$$

Another practical advantage of the introduction of fluctuations is that we can augment the pool of accessible states. We want to illustrate this issue by diagonalising the unperturbed reduced density matrix  $\boldsymbol{\rho}$  for a right-moving sweep at a particular site  $q$

$$\boldsymbol{\rho} = \mathbf{U} \mathbf{D} \mathbf{U}^\dagger, \quad (3.19)$$

where  $\mathbf{U} \mathbf{U}^\dagger = \mathbf{U}^\dagger \mathbf{U} = \mathbf{1}$ .  $\mathbf{D}$  is a diagonal matrix whose entries  $D_i$  add up to unity due to normalisation. Without fluctuations, as assumed so far, only  $m_q$  eigenvalues are permitted to be nonzero, preserving the matrix dimensions of  $\mathbf{C}^{n_q}$ . However, by incorporating  $\boldsymbol{\rho}'$  in general all  $m_q$  eigenvalues of  $\boldsymbol{\rho}$  are finite ( $m_{q-1}d_q \geq m_q$ ). Since the introduced perturbations are of physical origin, this circumstance can be exploited

### 3 Methods and theorems

to dynamically adjust matrix dimensions by a well-chosen criterion in the course of iterations. For example, we would increase matrix dimensions if the true ground state has an MPS representation with larger matrix dimensions, and conversely decrease matrix dimensions if they are not needed. Practically, we can define the maximal truncated weight which is the sum of eigenvalues  $D_i$  of discarded states. As we will see below, a reasonable approach is to discard states with the smallest eigenvalues  $D_i$ .

Besides the application of parallelisation techniques, further numerical optimisation is obtained by exploiting the two U(1) symmetries of impurity Hamiltonians corresponding to conservation of the total particle number and the  $z$  component of the total spin. However, it demands finer and more careful labeling and bookkeeping of states and operators. In our calculations, the matrix dimensions are of the order of  $m = 500$  in the largest invariant blocks of the  $A$  matrices, corresponding to a truncated weight of about  $10^{-8}$ .

A reliable error measure is the variance  $r = \langle \psi | (H - E)^2 | \psi \rangle$ , since it also captures the convergence of nonlocal parts of the ground state (opposed to the ground-state energy, which is related to the rather local Hamiltonian). It is easily accessible within an MPS-based implementation. For the two-impurity model calculations in chapter 4, we have checked that typically the standard deviation  $\sqrt{r} < 10^{-4}$ .

The MPO representation of the Hamiltonian allows us to easily consider different implementations of the Hamiltonian. For the case of a one-dimensional chain with  $R$  impurities, there are two possibilities to treat the impurities: (i) an impurity orbital  $r$  and the conduction-electron orbital  $i_r$  "below"  $r$  are treated as a single "site"  $q$  in the DMRG context. The disadvantage is that therewith the local Hilbert-space dimension at  $q$  is enlarged. (ii) The impurity orbitals  $r$  are treated as separate sites; i.e. a chain of length  $L + R$  is formed. This leaves the local Hilbert-space dimension constant but introduces next-nearest-neighbour hopping terms. In the case of the two-impurity models in chapter 4, we have tested both variants and found the differences in computational costs and accuracy to be marginal only. Mainly, variant (i) is employed.

## The success of DMRG

The reliability of DMRG for (most) one-dimensional systems rests on the scaling behaviour of an important quantity: the von Neumann entanglement entropy  $S_{A|B}$ , which measures the amount of entanglement between two subsystems<sup>2</sup>  $A$  and  $B$  in a pure state  $|\psi\rangle$  [75]. Here we consider the sites  $p \leq q$  as subsystem  $A$  and the sites  $p > q$  belong to subsystem  $B$  (Fig. 3.1).  $S_{A|B}$  is related to the eigenvalue spectrum of the

---

<sup>2</sup>Here, we concentrate on the entanglement properties and, thus, merely remark that there are deep connections to Schmidt decomposition and singular value decomposition (SVD). For details for example we refer to Ref. [75].

### 3.3 Density-matrix renormalisation group

reduced density matrix  $\rho_A = \text{Tr}_B |\psi\rangle\langle\psi|$  and  $\rho_B = \text{Tr}_A |\psi\rangle\langle\psi|$ , respectively,

$$S_{A|B} = -\text{Tr} \rho_A \log_2 \rho_A = -\text{Tr} \rho_B \log_2 \rho_B = - \sum_{a=1}^{m_{q-1} d_q} D_a \log_2 D_a, \quad (3.20)$$

where  $D_a$  is an eigenvalue of  $\rho$ .  $D_a$  is a nonnegative real number due to the corresponding Schmidt decomposition [75]. Obviously, a product state in real space gives  $S_{A|B} = 0$ , as there is just one finite  $D_a$ . On the other hand, if all  $D_a$  are equal, we obtain a maximally entangled situation.

The important aspect of Eq. (3.20) is that it relates  $S_{A|B}$  to the required matrix dimensions of an MPS (see also Eq. (3.19)) which faithfully represents the ground state. The matrix dimensions  $m_q$  can be read off from Eq. (3.20) as the number of nonzero eigenvalues  $D_a$ . Since the numerical costs increase with increasing matrix dimensions,  $S_{A|B}$  is a measure for the numerical requirements. Furthermore, it is illustrative for the compromise which DMRG achieves by truncating the reduced density matrix: the aim is to keep as much entanglement  $S_{A|B}$  between both subsystems as possible, while requiring that  $D_a$  is as small as possible. Consequently, when truncating  $\mathbf{C}^{n_q}$ , discarded eigenstates of  $\rho$  should have small or vanishing  $D_a$ .

In the thermodynamic limit, a generic state of a  $D$ -dimensional system possesses an entanglement entropy that is extensive, i.e. increases with the volume of the subsystems:  $S \sim L^D$ , where  $L$  is the linear size. However, an interesting exception represent states which obey the "area-law". Their entanglement entropy scales with the subsystem surface in leading order, i.e.,  $S \sim L^{D-1}$ . This is predicted to be the case for short-ranged Hamiltonians with an excitation gap, which induces a characteristic length scale and consequently a somehow localised form of entanglement. In such one-dimensional models, we thus obtain a constant entanglement entropy for area-law states, which is always tractable by an MPS with sufficiently large matrix dimensions, explaining the successful application of DMRG to a great number of one-dimensional models. However, already two-dimensional models would exhibit  $S \sim L$ , implying an unmanageable exponential increase of matrix dimensions for a suitable MPS with increasing  $L$ . Critical one-dimensional systems may be described by a conformal field theory (CFT) and exhibit  $S \sim c \log L$ , where  $c$  is the central charge of the CFT. Eq. (3.20) suggests that the matrix dimensions of a suitable MPS would increase linearly with  $L$  [75].

This issue can be also analysed from the perspective of real-space correlations. MPS are also known as finitely-correlated states, since they exhibit a specific behaviour for nonlocal correlations between an operator pair  $O_i O_j$  at sites  $i$  and  $j$  [75]. Assuming  $L \rightarrow \infty$ , one can derive ( $i < j$ )

$$\frac{\langle \psi | O_i O_j | \psi \rangle}{\langle \psi | \psi \rangle} = c_1 + \sum_{a=2}^{m^2} c_a \exp(-r/\xi_a), \quad (3.21)$$

### 3 Methods and theorems

where  $\xi_a = -1/\ln \lambda_a$  is the exponential decay length and  $\lambda_a$  ( $|\lambda_a| \leq 1$ ) an eigenvalue of a generalised  $\mathbf{E}$  matrix (here, however, for  $O$  and not for  $H$ ).  $m$  is the translational invariant  $A$  matrix dimension, and  $r = |j - i - 1|$ . The coefficients of the exponentials are denoted by  $c_a$ , where  $c_1$  belongs to eigenvalues  $\lambda_a$  of modulus 1. By a finite  $c_1$ , an MPS may mimic states with diverging correlation length. However, the more general situation is that the exponentials dominate the contributions to the MPS two-point correlations. In practice, an MPS may approximate true correlations by a superposition of these exponentials, what may be faithful for non-critical one-dimensional system. On the other hand, two-point correlations of critical one-dimensional systems obey power-law form (maybe with logarithmic corrections), which can be captured even by an MPS for short distances. However, at larger distances, the slowest exponential in Eq. (3.21) will start to dominate the MPS correlations, turning the correlations into a pure (incorrect) exponential [75].

In this context, it is important to notice that local (or almost local) quantities such as densities or ground-state energies of short-ranged Hamiltonians are reproduced very accurately. Nevertheless, one should always keep track of the convergence regarding the matrix dimensions  $m_q$ , to ensure that the MPS displays the correct long-range correlations.<sup>3</sup>

Extensions of DMRG tackle the discussed problems in different ways: tensor-network approaches such as projected entangled pair states (PEPS) or tensor-product states (TPS) try to reproduce higher-dimensional states (spatial dimensions  $D > 1$ ) obeying area laws [73]. The multi-scale entanglement renormalization ansatz (MERA) [89], on the other hand, emerged as a convenient tool to investigate critical systems. An intrinsic feature is the adding of an extra dimension representing the different energy scales at which the system is studied. Additionally, MERA sheds light on the recent promising claim of a correspondence between  $D + 1$ -dimensional conformal field theories and  $D$ -dimensional (classical) gravity theories in anti-de Sitter space (AdS/CFT, "holographic duality"), tracing back to the work of Juan Maldacena in 1997 [90].

## 3.4 Real-space dynamical mean-field theory

Dynamical mean-field theory (DMFT) [26, 71, 59] is a comprehensive, thermodynamically consistent, and nonperturbative approximation for correlated lattice-fermion models. It is based on the circumstance that the fermion self-energy, usually a nonlocal

---

<sup>3</sup>Refs. [87] and [88] discuss the reliability of finite-size scaling (i.e. increasing  $L$  for large but fixed matrix dimensions  $m \rightarrow \infty$ ) versus finite-entanglement scaling (varying  $m$ , keeping  $L$  fixed and large). This is especially interesting for critical systems, where both a finite  $L$  and a finite  $m$  may severely cut the long-range correlations by inducing artificial gaps and correlation lengths, respectively.

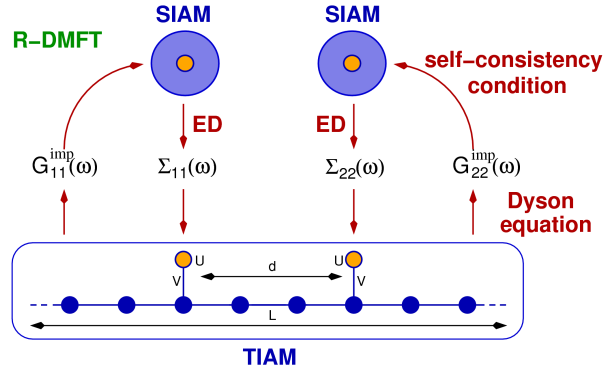


**Figure 3.2:** Schematic picture of real-space dynamical mean-field theory (R-DMFT) for the two-impurity Anderson model (TIAM). The system is given by two "magnetic" sites with strong Hubbard interaction  $U$  (orange) at a distance  $d$  coupled via a hybridisation term  $V$  to a one-dimensional conduction-electron system consisting of  $L$  non-interacting sites (blue). In the R-DMFT, the TIAM is self-consistently mapped onto two single-impurity Anderson models which are solved independently to get the local self-energies. These are used to set up the TIAM Dyson equation, which defines the parameters of the impurity models via the R-DMFT self-consistency equations (Eq. (3.25)). Figure is taken from Ref. [22].

quantity, becomes entirely local in the limit of infinite spatial dimensions (or infinite coordination number, respectively). Consequently, the Fourier transform of the self-energy is momentum independent. Nevertheless, it is still a function of frequency in this limit, what distinguishes DMFT from static mean-field approaches, because the problem retains its full local dynamics. An essential part of DMFT is that, starting from the limit of infinite dimensions, one can construct a mapping of a correlated fermionic lattice model to an effective single-site model which is embedded in the bath, constituted by the other fermions.

Applying DMFT in finite-dimensional lattices, therefore represents an approximation, which may be still remarkable reliable, even down to low-dimensional systems. However, this is highly dependent on the physical situation, as we will demonstrate in chapter 4 and 11. In case of multi-impurity models, DMFT is not able to incorporate the feedback of nonlocal inter-impurity correlations on the self-energy,<sup>4</sup> demanding a detailed check of its reliability. Our main goal is to apply DMFT to higher-dimensional impurity models which are beyond the applicability of DMRG (Sec. 11.5). For the purpose of determining the quality of DMFT, we will compare DMFT results for the two-impurity model in chapter 4 and for the multi-impurity model in chapter 11 with those obtained

<sup>4</sup>Nonlocal correlations may be taken into account to some extent by cluster extensions derivable from the "self-energy-functional approach" [91].

### 3 Methods and theorems

from numerically exact DMRG.

Here, the real-space DMFT (R-DMFT) is employed, which generalises DMFT to systems with missing or reduced translational symmetry [27]. This is achieved by mapping the original lattice model to a set of single-impurity Anderson models (SIAM), one for each of the geometrically or electronically inequivalent sites. R-DMFT has been applied for example to surface systems [92, 93], layered structures [94] as well as to ultracold atomic gases in optical lattices [95, 96].

We want to picture the general ideas of R-DMFT using the example of a multi-impurity Anderson model (illustrated in case of two impurities in Fig. 3.2). For further details of the two-impurity procedure we refer to Ref. [22]. Our goal is the computation of spin-dependent average occupation numbers  $\langle n_{i\sigma}^c \rangle$  and  $\langle n_{\alpha\sigma}^f \rangle$  for substrate and impurity sites, respectively. They are related to the local single-electron Green's functions

$$G_{\alpha\alpha,\sigma}^{\text{imp}}(i\omega_n) = \langle \langle f_{\alpha\sigma}; f_{\alpha\sigma}^\dagger \rangle \rangle_{\omega_n} \quad (3.22)$$

$$G_{ii,\sigma}^{\text{cond}}(i\omega_n) = \langle \langle c_{i\sigma}; c_{i\sigma}^\dagger \rangle \rangle_{\omega_n}, \quad (3.23)$$

given at the fermionic Matsubara energies  $\omega_n = (2n+1)\pi T$ . On the other hand, they are also diagonal elements of the Green's function matrix, which can be obtained from the real-space Dyson equation:

$$\hat{G}_\sigma^{-1}(i\omega_n) = (i\omega_n + \mu)\mathbf{1} - \hat{\varepsilon}_\sigma - \hat{\mathcal{T}} - \hat{\Sigma}_\sigma(i\omega_n), \quad (3.24)$$

where  $\mathbf{1}$  is the unity matrix,  $\hat{\varepsilon}_\sigma$  the diagonal local energy matrix, and  $\hat{\mathcal{T}}$  the hopping matrix.  $\hat{\varepsilon}_\sigma$  also includes magnetic field terms and is thus possibly spin dependent.  $\hat{\mathcal{T}}$  not only includes the hopping  $t$  between substrate sites but also hopping  $V$  between the substrate and impurity sites. For a system with  $L$  substrate sites and  $R$  impurities, the matrix dimension is  $L + R$  for each spin direction  $\sigma$ .

Within real-space DMFT, the self-energy is obtained by considering weak-coupling perturbation theory in  $U$  to all orders and by summing all local diagrams in the skeleton-diagram expansion of the self-energy,  $\hat{\Sigma} = \hat{\Sigma}[\hat{G}]$ . This implies that the resulting self-energy is local,  $\Sigma_{\alpha\beta,\sigma}(i\omega_n) = \delta_{\alpha\beta}\Sigma_{\alpha,\sigma}(i\omega_n)$ , but in general site dependent. As in the conventional DMFT, the local diagrams are not summed explicitly; the problem is rather reformulated by introducing a self-consistent mapping onto an effective single-impurity problem. In case of R-DMFT, a lattice model with  $R$  geometrically or electronically inequivalent sites is self-consistently mapped onto a set of  $R$  effective single-impurity models.

Knowing the self-energies  $\Sigma_{\alpha,\sigma}(i\omega_n)$  using Eq. (3.24), we can calculate the Green's function matrix  $\hat{G}(i\omega_n)$ , i.e. in particular the local Green's functions. The R-DMFT self-consistency conditions,

$$\frac{1}{\mathcal{G}_{\alpha,\sigma}^0(i\omega_n)} = \frac{1}{G_{\alpha\alpha,\sigma}^{\text{imp}}(i\omega_n)} + \Sigma_{\alpha,\sigma}(i\omega_n), \quad (3.25)$$

then provide us with the Weiss Green's functions  $\mathcal{G}_{\alpha,\sigma}^0(i\omega_n)$  for  $\alpha = 1, \dots, R$ , i.e., with the non-interacting Green's functions of the  $R$  effective impurity models. The one-particle parameters of each effective SIAM can be extracted from  $\mathcal{G}_{\alpha,\sigma}^0(i\omega_n)$ . The solutions of the effective models deliver the self-energies  $\Sigma_{\alpha,\sigma}(i\omega_n)$ , which are fed into Eq. (3.24), closing the self-consistency circle. In practice, the procedure starts with an initial guess of parameters of the effective SIAM, i.e. of the Weiss Green's functions  $\mathcal{G}_{\alpha,\sigma}^0(i\omega_n)$ , what allows to calculate the self-energies  $\Sigma_{\alpha,\sigma}(i\omega_n)$ .

In our calculations, we use exact-diagonalisation methods for the solution of the effective models [83, 82]. As we investigate systems at zero temperature, we introduce a low-frequency cutoff specified by the fictitious temperature  $\frac{T}{t} = 0.001$ , which allows to work in the finite-temperature Matsubara framework. A finite small number  $n_s - 1$  of auxiliary bath degrees of freedom in the effective SIAM is considered, typically  $n_s = 10$  for the Lanczos method. The computational effort of the R-DMFT scheme roughly scales linearly with the number of effective impurity models, i.e. with the number of inequivalent sites in the original system. However, for large  $(L + R)$  one has to take into account also the matrix inversion in Eq. (3.24).

If we replace the Anderson impurities (Eq. (2.35)) by Kondo impurities (Eq. (2.34)), we can still work with the presented R-DMFT scheme. The effective impurity problem in this case will be a single-impurity Kondo model. It consists of the local spin  $\mathbf{S}_r$ , the corresponding conduction-electron site  $i_r$ , to which the impurity is coupled, and the auxiliary bath sites.

## 3.5 Generalised Lieb theorem

Except of results from numerical calculations and insights from perturbation theory in the weak and strong-coupling regime, strict analytical results are available based on reflection positivity in spin space. Important applications concern the Hubbard model, as first was done by Lieb [47], and the Anderson and Kondo impurity model [48, 72, 97], which will be referred to in the following also as "generalised Lieb theorem". The theorem is of significance for our understanding of the physics at half-filling, in particular in checking and supporting our perturbative and numerical results, before extending them to models away of half-filling. It makes strict statements about the degeneracy of the ground state as well as about the total spin and the sign of spin correlation functions.

In this section we compactly outline the essential parts of the proof and its consequences for the Kondo impurity model, as presented by Shen [48]. A comparable proof can be given for a periodic Anderson impurity model [97]. First, we show the Hamiltonian of

### 3 Methods and theorems

the multi-impurity Kondo model with Hubbard- $U_i$  in the conduction-electron system

$$H = -t \sum_{\langle i,j \rangle \in \Lambda_{c,\sigma}} c_{i\sigma}^\dagger c_{j\sigma} + \sum_{i \in \Lambda_c} U_i \left( n_{i\uparrow}^c - \frac{1}{2} \right) \left( n_{i\downarrow}^c - \frac{1}{2} \right) + \sum_{r \in \Lambda_f} J s_{i_r}^c \mathbf{S}_r^f, \quad (3.26)$$

where  $\Lambda_{c,f}$  denote the subsets of c and f lattice sites, respectively.  $\mathbf{s}_i^c = \sum_{\sigma\sigma'} c_{i\sigma}^\dagger \boldsymbol{\sigma}_{\sigma\sigma'} c_{i\sigma'}$  is the electron spin at site  $i$  (Sec. 2.4). In the following, the impurity spin operators  $\mathbf{S}_r^f$  are represented as fermions, enforcing single occupancy at impurity sites. An essential assumption of the proof is that  $\Lambda_c$  is a bipartite lattice at half-filling. Thus, each site is occupied by one electron on average. The above Hamiltonian commutes with the  $z$  component of the total spin.

One may represent the ground state in terms of an orthonormal, real basis for  $N_0$  electrons of spin  $\sigma$  with elements  $\{|\psi_\alpha^\sigma\rangle\}$ , labeled by  $\alpha$ . We consider the following particle-hole transformation applied to the basis

$$\tilde{\mathbf{T}} = \prod_{i \in \Lambda_c} (c_{i\uparrow} - \varepsilon(i) c_{i\uparrow}^\dagger) \prod_{r \in \Lambda_f} \left( f_{i_r\uparrow} + \varepsilon(i_r) \frac{J}{|J|} f_{i_r\uparrow}^\dagger \right), \quad (3.27)$$

where  $\varepsilon(i) = 1$  if site  $i$  belongs to the A sublattice, and  $\varepsilon(i) = -1$  if it belongs to the B sublattice. Due to the properties of the transformation, the  $z$  component of the total spin for any vector  $\tilde{\mathbf{T}}|\psi_\alpha^\uparrow\rangle \otimes |\psi_\beta^\downarrow\rangle$  is  $S_{\text{gs}}^z = \frac{1}{2}(N_\Lambda - 2N_0)$ , where  $N_\Lambda$  is the number of lattice sites.

The variational wave function for the ground state of the subspace  $S^z = \frac{1}{2}(N_\Lambda - 2N_0)$  can be written as

$$|\psi(\mathbf{W})\rangle = \sum_{\alpha\beta} W_{\alpha\beta} \tilde{\mathbf{T}}|\psi_\alpha^\uparrow\rangle \otimes |\psi_\beta^\downarrow\rangle, \quad (3.28)$$

where  $\mathbf{W}$  is the matrix of coefficients.  $\mathbf{W}$  is Hermitian, since the Kondo model is spin up-down symmetric under the transformation  $\tilde{\mathbf{T}}$ —a necessary property for the theory of reflection positivity.

After some algebra, we are prepared to evaluate the variational energy of the lowest-energy state  $|\psi(\mathbf{W})\rangle$  in the subspace with  $S^z = \frac{1}{2}(N_\Lambda - 2N_0)$ . Since  $\mathbf{W}$  is Hermitian, it can be diagonalised:  $\mathbf{W} = \tilde{\mathbf{V}}^\dagger \tilde{\mathbf{D}} \tilde{\mathbf{V}}$ , where  $\tilde{\mathbf{D}}$  is a (real) diagonal matrix with diagonal entries  $\{\tilde{d}_\alpha\}$ . We can define a positive semidefinite matrix  $|\mathbf{W}| = \tilde{\mathbf{V}}^\dagger |\tilde{\mathbf{D}}| \tilde{\mathbf{V}}$ , where  $|\tilde{\mathbf{D}}| = \text{diag}(|\tilde{d}_1|, |\tilde{d}_2|, \dots)$ . For all  $U_i \geq 0$ , one can now estimate

$$E(\mathbf{W}) \geq E(|\mathbf{W}|). \quad (3.29)$$

This means,  $|\psi(|\mathbf{W}|)\rangle$  belongs to the ground-state manifold in the subspace with  $S^z = \frac{1}{2}(N_\Lambda - 2N_0)$ . In other words, one of the ground states (in case of degeneracy) can be identified as positive semidefinite (it has  $\tilde{d}_\alpha \geq 0$ ), i.e.,  $\mathbf{W} = |\mathbf{W}|$ . This



statement is independent of  $U_i$ .  $\mathbf{W} = |\mathbf{W}|$  is consequence of the reflection positivity in spin space.

It needs to be shown that the ground state in the subspace  $S^z = \frac{1}{2}(N_\Lambda - 2N_0)$  is nondegenerate for all  $U_i > 0$  and  $J \neq 0$ . This is done in a similar way as Lieb does in [47], amounting to the question whether  $\mathbf{W}$  is positive definite (all  $\tilde{d}_\alpha > 0$ ), what allows to apply some variant of the Perron-Frobenius positivity argument. Indeed, it turns out that  $|\mathbf{W}|$  is positive definite. Since one can also show that  $\mathbf{W} = \pm|\mathbf{W}|$ , i.e. that  $|\psi(\mathbf{W})\rangle$  and  $|\psi(|\mathbf{W}|)\rangle$  are equal except for a phase factor, the ground state is positive definite. This fact strictly excludes another orthogonal, positive definite ground state in the same basis. Summarising, when  $U_i > 0$  and  $|J| \neq 0$  the ground state is nondegenerate,<sup>5</sup> while for  $U_i \geq 0$  it is only known that  $|\psi\rangle$  (Eq. (3.28)) belongs to the ground-state manifold.

Already for the positive semidefinite ground state ( $U_i \geq 0$ ), we find that the overlap with the ground state of an exactly solvable Heisenberg model [98] is finite, permitting to calculate the total ground-state spin  $S_{\text{gs}} = \frac{1}{2}|N_{\tilde{A}} - N_{\tilde{B}}|$ .  $N_{\tilde{A}}$  and  $N_{\tilde{B}}$  denote the number of A and B sites of the two generalised sublattices, combining c and f sites. In consequence of the transformation  $\tilde{\mathbf{T}}$  (Eq. (3.27)), for  $J < 0$ , c and f orbital belong to the same generalised sublattice, while, for  $J > 0$ , they belong to different sublattices. One obtains

$$S_{\text{gs}} = \begin{cases} \frac{1}{2}(N_A + N_B^f - N_B - N_A^f), & \text{if } J > 0, \\ \frac{1}{2}(N_A + N_A^f - N_B - N_B^f), & \text{if } J < 0 \end{cases}, \quad (3.30)$$

where  $N_{A,B}$  gives the number of c sites belonging to a particular sublattice, while  $N_{A,B}^f$  gives the same number for the f sites. An important finding is that the total spin remains constant when changing  $J$  (keeping its sign fixed).

It is remarkable that even correlation functions can be obtained for all finite  $J$

$$\langle \psi | s_i^{c,+} s_j^{c,-} | \psi \rangle = \varepsilon(i) \varepsilon(j) C_{ij} \quad (3.31)$$

$$\langle \psi | S_r^{f,+} S_{r'}^{f,-} | \psi \rangle = \varepsilon(i_r) \varepsilon(i_{r'}) F_{rr'} \quad (3.32)$$

$$\langle \psi | s_i^{c,+} S_r^{f,-} | \psi \rangle = -\varepsilon(i) \varepsilon(i_r) \frac{J}{|J|} G_{ii_r}, \quad (3.33)$$

where  $C_{ij}$ ,  $F_{rr'}$ , and  $G_{ii_r} \geq 0$  if all  $U_i \geq 0$ , while they are strictly positive if all  $U_i > 0$ .

It can be noted that the sign of the correlation functions is not dependent on  $J$ . Purely staggered behaviour is found for  $\langle \psi | s_i^{c,+} s_j^{c,-} | \psi \rangle$  and  $\langle \psi | S_r^{f,+} S_{r'}^{f,-} | \psi \rangle$ , whereas  $\langle \psi | s_i^{c,+} S_r^{f,-} | \psi \rangle$  may have an extra sign due to the factor  $J/|J|$ .

<sup>5</sup>In Ref. [72] is shown that nondegeneracy is obtained already at  $U_i = 0$  for a dense Kondo lattice model, i.e.  $R = L$ .

### 3 *Methods and theorems*

Although the generalised Lieb theorem gives the sign of correlations as well as the total spin of the ground state, it says nothing about the amount of specific correlations. Specifically, we will realise in this work that these are generally quite different for  $J \rightarrow 0$  and  $J \rightarrow \infty$ . Questions, such as those related to spatial ordering of spins, cannot be satisfyingly answered by the theorem. In fact, the variety of different possible physical regimes is just the basic motivation for our work.

A crucial detail for our calculations is the situation when the ground state is not degenerate already for all  $U_i = 0$  but  $|J| \neq 0$  (e.g. due to the residual interactions for  $J < J_\Delta$ ). Then, one can imagine to turn on weak  $U_i$  (smaller than all other energy scales), what can be done adiabatically in a finite-size system. Thereby, the requirements for the generalised Lieb theorem are fulfilled and the same total ground-state spin is found for any other finite  $J'$ , too. Switching off the  $U_i$  at  $J'$  can be done again without changes in the total spin. Hence, we found that the ground state stays nondegenerate even for  $U_i = 0$ , when  $J$  is varied. In other words, the ground-state spin is preserved in this case for all finite couplings  $J$ .

## 4 Off-resonant models

### 4.1 Introduction

When impurities are low concentrated in metallic host materials, single-impurity concepts (chapter 2) can be easily applied. However, the larger this concentration becomes, the more important the mutual indirect interaction of impurities becomes [8]: impurities may locally polarise the conduction electrons and thereby affect impurity spins at other sites due to the itinerancy of the conduction electrons, constituting the Ruderman-Kittel-Kasuya-Yosida [12, 13, 14] (RKKY) exchange. This mechanism may lead to the breakdown of single-impurity concepts for larger impurity densities.

Indirect magnetic exchange between impurities can be derived perturbatively yielding the inter-impurity coupling  $J_{\text{RKKY}} \sim J^2$ . Doniach [45, 99] realised that this dependence on  $J$  will lead to a competition with the Kondo effect, which is related to an exponential scale  $T_K \sim \exp(-\frac{1}{J})$ : the weak-coupling regime  $J \ll 1$  is dominated by RKKY exchange, while the strong-coupling regime is governed by the Kondo effect, both being separated by a crossover (as in the finite systems in this work) or even a phase transition at  $J_D$  where  $|J_{\text{RKKY}}| = T_K$ .

This raises the obvious question what happens with this competition when we transfer the problem from an infinite conduction-electron system to a finite box. How and when do finite-size effects show up? In which fashion does the conventional physics change? These questions shall define the central objective for this and the following chapters 5-9.

In section 2.5 we have seen that the Kondo effect can be strongly affected by the presence of a finite level spacing  $\Delta$  in the conduction band, which, in our case, results from a spatially confined conduction-electron system (Kondo box [19, 20]). We realised that the typical spin correlations are cut off by the finite length of the system for  $\Delta > T_K$ , or equivalently,  $L < \xi_K$  [19, 20, 49, 100, 101, 102, 103, 104, 105]. From a renormalisation group (RG) perspective, the strong-coupling fixed point, describing the formation of the nonlocal Kondo singlet, is removed.

In this chapter, we want to start our study with the more "trivial" off-resonance case in which the chemical potential falls between empty and doubly-occupied conduction-electron states. Since there are no electron states available at energy scales lower than  $\Delta$ , not only the conventional Kondo effect is absent but also residual couplings of

#### 4 Off-resonant models

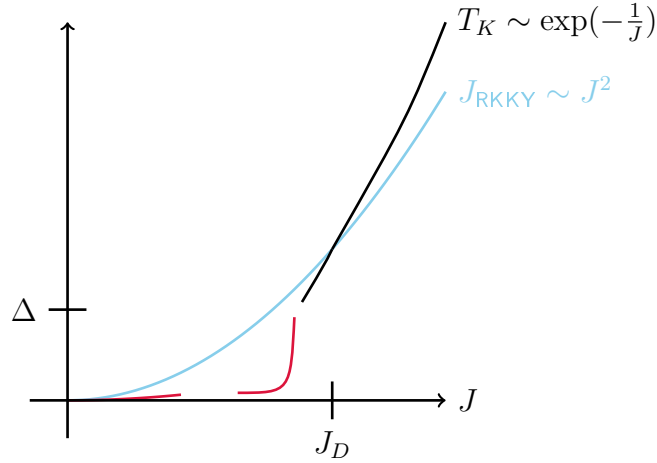


**Figure 4.1:** Competition between Kondo effect (black, green, and red) and RKKY interaction (blue) in an off-resonant impurity model for larger but finite lattices. The strong-coupling regime is ruled by the Kondo scale  $T_K$  (black) with a crossover to an RKKY regime below  $J_D$ . When  $T_K < \Delta$  or  $\xi_K > L$ , respectively, the Kondo cloud collapses. Since residual couplings between impurities and conduction electrons (red) vanish in off-resonance cases, this regime is entirely governed by the RKKY scale (blue). In the case in which the RKKY exchange leads to a finite total impurity spin  $S_{\text{tot}}$  (not shown here), corresponding Kondo correlations are already cut at  $J_{\Delta, \text{Rspins}}$ , i.e.  $\Delta = T_K^{(\text{Rspins})}$  where  $T_K^{(\text{Rspins})} < T_K^{(1\text{spin})}$  (Sec. 4.7).

impurities to the electrons (compare also the perturbative results in section 5.2). On the other hand, RKKY couplings remain qualitatively unchanged, and the conventional picture, which predicts an RKKY regime for  $J < J_D$ , is consequently unchanged (illustrated in Fig. 4.1). This is shown here using the example of a two-impurity model, which is off-resonant according to our conventions.

The clarity of the two-impurity model represents also a good occasion to analyse how the presence of another impurity influences the traditional single-impurity picture and how effects from the finite system and its boundaries come into play. Another purpose is to check how valid mean-field approaches, such as R-DMFT (Sec. 3.4), are—with its application to higher-dimensional models in mind (Sec. 11.5). We also address the influence of charge fluctuations at impurity sites by using an Anderson model (Sec. 2.2).

Before analysing the numerical results, we want to proceed with the presentation of conventional considerations in section 4.2, yet, with focus on the rich interplay between Kondo effect and RKKY exchange.

## 4.2 Review of multi-impurity and two-impurity models in the literature

### Kondo lattice model

One of the early works studying the physics of multi-impurity models was by S. Doniach and co-workers. First by mean-field approaches [45] and later by means of numerical renormalisation group (NRG) [99], they investigated the competition between magnetic impurity order and the Kondo effect in the one-dimensional Kondo necklace model

$$H_{\text{necklace}} = J \sum_i \mathbf{S}_i \boldsymbol{\tau}_i + \tilde{W} \sum_i (\tau_i^x \tau_{i+1}^x + \tau_i^y \tau_{i+1}^y), \quad (4.1)$$

The Kondo necklace model captures the low-energy spin physics of the dense Kondo lattice model in which an impurity is coupled to each site of the conduction-electron system [45].

The RKKY exchange between impurities may drive the system at low energy scales to other infrared fixed-points, governed by magnetic correlations among the impurities, than the strong-coupling fixed-point with screened impurities, known from the single-impurity model. Essentially, this sets the stage for a competition with the individual Kondo effect in the weak-coupling regime.

One finds that the RKKY interaction, which is derived from second-order perturbation theory in the local coupling  $J$ , is oscillatory in sign  $\sim \cos(2k_F d)$ , when the distance between the impurities  $d$  is varied ( $k_F$  is the Fermi momentum). At half-filling ( $k_F = \frac{\pi}{2}$ ), we obtain an antiferromagnetic coupling for odd  $d$  and a ferromagnetic one at even  $d$ , defining "(anti)ferromagnetic distances". For the given Hamiltonian, the impurities consequently experience an antiferromagnetic pattern of RKKY couplings. Doniach and co-workers were able to detect a second-order phase transition or crossover, respectively,<sup>1</sup> separating the Kondo regime for strong  $J$  from a regime with antiferromagnetically correlated impurities without Kondo effect (local-moment fixed point with effective coupling  $J_{\text{eff}} = 0$ ) in the weak-coupling regime. For large  $J$ , the Kondo effect leads to individual Kondo singlets for each impurity ( $J_{\text{eff}} \rightarrow \infty$ ).

The transition is supported by simple scaling arguments: the transition point  $J_D$  is found at the particular coupling where the nonperturbative Kondo temperature  $T_K \sim$

---

<sup>1</sup>Due to the Mermin-Wagner theorem [106] there is no breaking of a continuous symmetry, such as spin rotation symmetry, in one dimension at finite temperatures. However, mean-field approaches may (possibly implicitly) assume broken symmetries, suggesting artificial phase transitions. In fact, at half-filling in one dimension, the Kondo lattice model exhibits a "spin liquid phase"—a quantum disordered phase with finite spin and charge gaps. In this regime, spin and charge correlations decay exponentially in space and time [97].

$\exp(-\frac{1}{J})$  equals the modulus of the RKKY energy scale  $J_{\text{RKKY}} \sim J^2$ . The transition is numerically found to take place at  $J_D/\tilde{W} = 0.411$  [99] for the one-dimensional necklace model, Eq. (4.1). Interestingly, our numerical results show that  $J_D$  is of the same order also in other one-dimensional two and three-impurity models (section 5.5 and chapter 9).

## Two-impurity Kondo model

However, Doniach's picture is oversimplified in that the large density of impurities makes it impossible to ensure independent Kondo clouds for each impurity even for large  $J$ . This became known as the famous Nozières exhaustion principle [107, 108]. As soon as the clouds sufficiently overlap, a new state of matter emerges: the heavy fermions. We will be occupied in more detail with this question in chapter 13 and therefore first restrict ourselves to the case of models with few impurities.

The two-impurity model is the most simple impurity model that extends the physics of the single-impurity model by the indirect (or direct) exchange between two impurities. An immediate consequence is that universality in terms of the Kondo temperature  $T_K$  is lost due to the presence of  $J_{\text{RKKY}}$ . The model is described by the following Hamiltonian

$$H = H_{\text{el}} - J(\mathbf{S}_1 \mathbf{s}_{i_1} + \mathbf{S}_2 \mathbf{s}_{i_2}), \quad (4.2)$$

where  $\mathbf{s}_i$  is the spin density of conduction electrons at site  $i$  and  $H_{\text{el}}$  the Hamiltonian of an half-filled non-interacting conduction-electron system.

The interplay of Kondo effect and exchange in this model has been treated by C. Jayaprakash et al in Ref. [46] by perturbative scaling techniques [9]. When the temperature  $T$  (or energy scale, respectively) is successively lowered, one may pass through several different regimes. Technically, these are described as effective Hamiltonians at energy scale  $D$  (where  $D_0$  is the bandwidth), obtained from "integrating out" high-energy conduction-electron states.

For high temperatures (above all Kondo temperatures in the system) the impurities will be essentially free and all interactions can be treated perturbatively; thus, we are in the "two local moments regime". When the temperature  $T$  is lowered, we may encounter Kondo effects as soon as  $T < T_K$ . In these regimes, the system obeys the usual perturbative flow equation for the effective coupling  $J_{\text{eff}}(D)$  (Eq. (2.21)).

As discussed above, if the single-impurity Kondo temperature  $T_K$  is the largest energy scale, i.e.  $T_K > |J_{\text{RKKY}}|$  (when, e.g., impurities are far away from each other), we will obtain separately screened impurities with vanishing interactions between them (strong-coupling fixed point). Certainly, more interesting are situations in which the impurities interact with each other, leading to substantial deviations from single-impurity results, hence we set  $J < J_D$  or  $T_K < |J_{\text{RKKY}}|$ , respectively.

## 4.2 Review of multi-impurity and two-impurity models in the literature

When  $J_{\text{RKKY}}$  is antiferromagnetic ( $J_{\text{RKKY}} < 0$ ), the two impurities are locked in a singlet state for energy scales below  $|J_{\text{RKKY}}|$ . This is a special situation, as there is no residual magnetic impurity moment to be screened by conduction electrons. Furthermore, by means of NRG, Jones et al [109, 51] found that the competition leads to a critical point at  $\frac{|J_{\text{RKKY}}|}{T_K} \approx 2.2$  in case of a special particle-hole symmetry of the conduction-electron screening channels [52]. At and around this point, the effective Hamiltonian cannot be formulated in terms of a Fermi liquid, indicated for example by a very small Wilson ratio<sup>2</sup>  $R \ll 1$  [109]. One may understand the result of this competition as transition between the physics of two Kondo clouds in the strong-coupling regime ("correlated Kondo fixed point") and the physics without any Kondo clouds, leading to an asymptotic zero phase shift ("local-moment singlet fixed point") in the weak-coupling regime. The critical point itself is characterised by a diverging impurity contribution to the staggered susceptibility and the inter-impurity correlation function approaching  $\langle \mathbf{S}_1 \mathbf{S}_2 \rangle = -\frac{1}{4}$ . It is emphasised that, in spite of the phase transition, away from the critical point inter-impurity correlations  $\langle \mathbf{S}_1 \mathbf{S}_2 \rangle$  persist in the strong-coupling regime and Kondo correlations are still present in the weak-coupling regime [109, 51]. The transition turns into a crossover if the particle-hole symmetry is absent [50]. We will examine it in more detail in section 9.1.

For a ferromagnetic  $J_{\text{RKKY}}$  ( $J_{\text{RKKY}} > 0$ ) the scenario is different. Just as above, for temperatures below  $J_{\text{RKKY}}$  the two impurities are in a triplet state,  $S_{\text{tot}} = 1$ , which turns out to be screened by the conduction electrons in a complex way. In the triplet subspace the Hamiltonian Eq. (4.2) can be rewritten so that

$$H_{\text{fm}} = H_{\text{el}}(D \approx J_{\text{RKKY}}) - J^*(\mathbf{s}_{i_1} + \mathbf{s}_{i_2})\mathbf{S}_{\text{tot}}, \quad (4.3)$$

where  $\mathbf{S}_{\text{tot}} = \mathbf{S}_1 + \mathbf{S}_2$  is the total impurity spin and  $J^* = J(D \approx J_{\text{RKKY}})$  is the effective local coupling at  $D \approx J_{\text{RKKY}}$ . At this point it is convenient to have a closer look on the inversion symmetry of the conduction-electron system with respect to the midpoint of the two impurities. It is natural to define two orthogonal conduction-electron channels, namely odd and even with  $\psi(x) = \mp \psi(-x)$  (where  $x$  is measured from the midpoint)

$$H_{\text{el}} = H_{\text{el,odd}} + H_{\text{el,even}} \quad (4.4)$$

$$\mathbf{s}_{i_1} + \mathbf{s}_{i_2} = 2 \sum_{kk'} (u_{\text{odd}}(k)u_{\text{odd}}(k')\mathbf{s}_{\text{odd},kk'} + u_{\text{even}}(k)u_{\text{even}}(k')\mathbf{s}_{\text{even},kk'}), \quad (4.5)$$

where  $\mathbf{s}_{\text{odd/even},kk'} = \frac{1}{2} \sum_{\sigma\sigma'} c_{\text{odd/even},k\sigma}^\dagger \boldsymbol{\sigma}_{\sigma\sigma'} c_{\text{odd/even},k'\sigma'}$  is the spin operator of odd and even conduction electrons for momenta  $k$  and  $k'$  with Fourier coefficients  $u_{\text{odd/even}}(k)$ .

---

<sup>2</sup>The Wilson ratio, defined as the ratio between the magnetic susceptibility and the linear specific heat with the corresponding value in a non-interacting system, takes the universal value  $W = 2$  at low energy scales, as shown by NRG and later explained using Nozières' strong-coupling picture [64]. Since  $W = 1$  for non-interacting electrons,  $W = 2$  is a direct signature of the single-impurity Kondo effect [8].

#### 4 Off-resonant models

Since the  $k$  dependence<sup>3</sup> of  $u_{\text{odd/even}}(k)$  is not of interest for our discussion, all associated quantities are taken at their low-energy value for  $k = k_F$ .

It follows that the Hamiltonian Eq. (4.2) in the subspace with  $S_{\text{tot}} = 1$ , can be rewritten

$$H_{\text{fm}} = H_{\text{el}}(D \approx J_{\text{RKKY}}) - (J_{\text{odd}}\mathbf{s}_{\text{odd}} + J_{\text{even}}\mathbf{s}_{\text{even}})\mathbf{S}_{\text{tot}}, \quad (4.6)$$

where  $J_{\text{odd/even}} = 2u_{\text{odd/even}}^2 J^*$ .

This is the Hamiltonian of a two-channel problem for the nonlocal spin  $\mathbf{S}_{\text{tot}}$ , which may be compensated in two stages. The corresponding Kondo scales  $T_{K,\text{odd/even}}$  are of the order  $|J_{\text{RKKY}}|(T_K/|J_{\text{RKKY}}|)^{1/u_{\text{odd/even}}^2}$ . Without loss of generality, let us assume that  $T_{K,\text{odd}}$  is the largest Kondo scale. When the temperature is lowered below  $T_{K,\text{odd}}$ , this effectively results in a complex  $S = \frac{1}{2}$  object  $\tau$ , described by the effective Hamiltonian

$$H_{\tau} = H_{\text{el}}(D \approx T_{K,\text{odd}}) - (J_F\mathbf{s}_{\text{odd}} - J_A\mathbf{s}_{\text{even}})\tau. \quad (4.7)$$

The residual coupling of  $\tau$  to the remaining odd electrons,  $J_F$ , is ferromagnetic. This can be inferred from the results of an NRG calculation for a  $S = 1$  single-impurity model [110, 107] whose spectrum at the fixed point is understood in terms of a decoupled  $S = \frac{1}{2}$  single-impurity model. Consequently, when the temperature is decreasing, this leads to a decrease of  $J_F$  towards the local-moment fixed point regarding  $\tau$  ( $J_F = 0$ , compare also Sec. 2.3).

Unlike  $J_F$ ,  $J_A$  is antiferromagnetic, allowing for an additional screening process of  $\tau$  by the even electrons below  $T_{K,A}$  (where  $J_A \sim J_{\text{even}}(D \approx T_{K,\text{odd}})$ ). Thus, the effective Hamiltonian below  $T_{K,A}$  describes a Fermi liquid with remaining self-interactions between even and odd electrons separately. This means in particular that the phase shift at this stable "correlated Kondo fixed point" is asymptotically  $\frac{\pi}{2}$  in both the even and the odd channel and  $\pi$  in total.

If one of the energy scales  $T_{K,\text{odd/even}}$  is not present, e.g. when the respective density of states is vanishing, one obtains an underscreening situation, in which the total impurity spin exceeds the number of screening channels  $2S_{\text{tot}} > N_{\text{channels}}$ . This concerns especially finite-size systems, as we will see in section 9.2.

---

<sup>3</sup>By requiring normalisation and anticommutator relations for odd and even conduction electrons (e.g.  $[c_{\text{even/odd},k}^\dagger, c_{\text{even/odd},k'}]_+ = \delta_{kk'}$ ), a one-dimensional electron system can be shown to have  $u_{\text{odd/even}}^2(k) = \frac{1}{2}(1 \mp \cos(kd))$ , where  $d$  is impurity distance. In the case of a three-dimensional electron system one has to reduce to an effective one-dimensional description at first (the connecting line between the two impurities) by integrating over all solid angles  $d\Omega$  in spherical coordinates. Then, the coefficients  $u_{\text{odd/even}}^2(k) = 1 \mp \frac{1}{kd} \sin(kd)$  where  $k = |\mathbf{k}|$ . In both cases, for  $d \rightarrow 0$  and fixed electron momentum  $k$ , the coefficient of the even channel outweighs the one of the odd channel, since the odd electron wave function at the midpoint  $x = 0$  is strictly zero.



### 4.3 Two-impurity models—effective RKKY models

Our numerical investigation starts with the two-impurity model, which is the simplest impurity model to capture the competition between Kondo effect and RKKY exchange. Furthermore, finite-size effects show up in a relatively simple way. In this chapter, we will employ a two-impurity Anderson impurity model (TIAM, see section 2.4), aiming also at effects stemming from the inclusion of charge fluctuations at impurity sites. We will closely follow the ideas and arguments given in our paper, Ref. [22].

The model consists of two magnetic Hubbard sites ("impurities") modeled by single nondegenerate orbitals hybridising with a non-interacting tight-binding chain ("substrate"). In the limit of a strong local Hubbard interaction  $U$  and weak hybridisation, the Schrieffer-Wolff transformation (Sec. 2.2) explains the formation of local magnetic moments with a local antiferromagnetic exchange  $J = 8\frac{V^2}{U}$  between impurities and conduction electrons. For antiferromagnetic distance  $d$  (as in most cases in this chapter), there is a crossover from local Kondo-singlet formation at strong hybridisations  $V$  to nonlocal RKKY coupling of the impurities for  $V \rightarrow 0$ , as can be seen in spin-correlation functions and susceptibilities [111, 22, 112].

The finiteness of the electron system even promotes the RKKY regime as the Kondo effect is cut by the finite-size gap  $\Delta$  (Fig. 4.1). Considering our conventions, the number of electrons  $N$  is even in two-impurity models. The chemical potential  $\mu$  lies between fully occupied and unoccupied conduction-electron eigenstates ("off-resonance", Fig. 2.5(b)). Following the conclusions for the single-impurity Kondo box (Sec. 2.5), the behaviour at  $J \rightarrow 0$  is predicted as follows: the impurities will not be able to couple to the conduction electrons due to the presence of the finite-size gap for  $T_K < \Delta$ . Because the Fermi sea is nondegenerate, the screening of an impurity spin by conduction electrons would need a finite energy  $\sim \Delta$ . Converting this into couplings, one can define a coupling strength  $J_\Delta$  at which the Kondo temperature  $T_K$  becomes comparable with the finite-size gap  $\Delta$  [19]. Thus, for  $J < J_\Delta$  the Kondo effect is absent and free moments are generated. The low-energy sector at  $J \rightarrow 0$  is exactly described by the effective RKKY two-spin model

$$H_{\text{RKKY}} = -J_{\text{RKKY}} \mathbf{S}_1 \mathbf{S}_2 \quad (4.8)$$

$$J_{\text{RKKY}} = J^2 \chi_{i_1, i_2}^{0, \text{cond}} \sim (-1)^{|i_1 - i_2|} \frac{J^2}{|i_1 - i_2|}, \quad (4.9)$$

where  $J_{\text{RKKY}}$  is given in terms of the static conduction-electron susceptibility at  $J = 0$ . Another issue to be treated in this chapter is the reliability of the picture of two independent Kondo clouds. For strong couplings, we assume local clouds which do not disturb each other, but in the weak-coupling regime with its spatially extended clouds this cannot be valid any longer. This circumstance touches also the topic of

how appropriate mean-field approaches, such as real-space dynamical mean-field theory (R-DMFT), are. Here, we want to compare magnetic susceptibilities (introduced in section 2.4) obtained from R-DMFT to numerically exact DMRG results.

## 4.4 Magnetic response and spin correlations

In Fig. 4.2 is shown the magnetic susceptibility  $\chi_{i,1}^{\text{cond}}$  for a TIAM with  $L = 50$ . Placing the impurities at odd distances leads to an antiferromagnetic RKKY coupling, and we want to focus first on distances  $d = 4m + 1$ , where  $m$  is an integer. For  $d = 49$  (lowest panel on the right in Fig. 4.2), the impurities are located at the edges of the substrate chain. As a consequence of the antiferromagnetic coupling of the impurities to the conduction-electron system, the response at the impurity site  $i_r$  is antiferromagnetic, i.e.,  $\chi_{i,1} < 0$ . The calculations have been done for  $U = 8$  and  $V^2 = 2$ , corresponding to an intermediate effective coupling strength  $J = 8\frac{V^2}{U} = 2$ , what is clearly beyond the Kondo limit  $J \rightarrow 0$ . However, charge fluctuations are still suppressed: we find an average double occupancy of  $\langle n_{1\uparrow}^f n_{1\downarrow}^f \rangle = 0.072$  at the impurity site, and the impurity local moment  $\langle \mathbf{S}_1^2 \rangle = 3(1 - 2\langle n_{1\uparrow}^f n_{1\downarrow}^f \rangle)/4 = 0.64$  is much closer to the localised-spin value  $3/4$  than to the free-fermion value  $3/8$ .

The response is oscillatory in the distance  $|i - i_1|$  to the first impurity corresponding to the  $2k_F = \pi$  nesting wave vector. Its modulus is maximal at  $i_1$ , decreases with increasing  $i$ , and almost saturates until there is a slight upturn for  $i \rightarrow i_2 = 50$  for  $d = 49$ , i.e. at the position of the second impurity. This is consistent with the  $2k_F$  oscillation so that  $\chi_{i,1}^{\text{cond}}$  is positive at  $i = i_2$ . Furthermore, it implies that there is an antiferromagnetic alignment of the two impurities due to the antiferromagnetic RKKY interaction.

When the distance  $d$  between the impurities is decreased ( $d$  odd), the picture is supposed to change gradually. However, the  $i$  dependence of the susceptibility becomes more complicated: as the impurities are more correlated due to a stronger RKKY coupling, the response below the second impurity (see the second maximum of  $|\chi_{i,1}^{\text{cond}}|$ ) becomes stronger and stronger. The response at substrate sites between the two impurities increases, and its modulus develops a pronounced minimum close to  $i_2$ , while the response beyond the second impurity, for  $i > i_2$ , becomes very weak. Furthermore, the susceptibility changes sign between nearest neighbours. Its two-site average is negative between the impurities and also beyond the first impurity for  $i < i_1$  but is found to be positive for  $i > i_2$ . Another subtle feature is the ferromagnetic response at the nearest neighbour to the right of  $i_1$ , which is larger than the one to the left of  $i_1$  for all distances except for  $d = 5$  and  $d = 9$ . The ratio  $\chi_{i_1+1,1}^{\text{cond}}/\chi_{i_1-1,1}^{\text{cond}}$  is decreasing with decreasing  $d$ , becomes smaller than unity for  $d = 5$  and  $d = 9$ , and larger than unity again for  $d = 1$ .

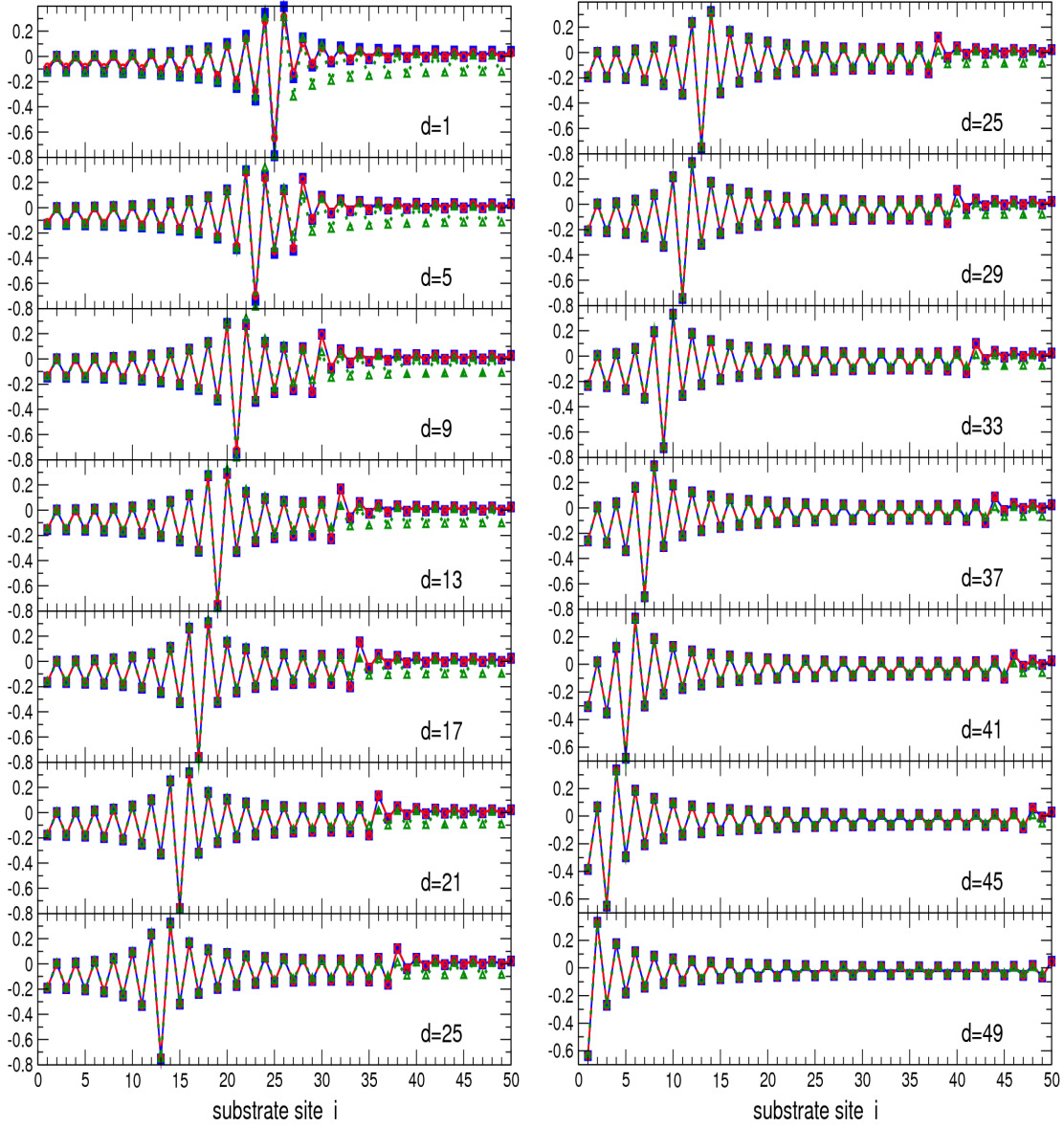


**Figure 4.2:** Static magnetic susceptibility  $\chi_{i,1}^{cond}$  at Hubbard interaction  $U = 8$  and hybridisation strength  $V = \sqrt{2}$  for a system with  $L = 50$  and two Anderson impurities at positions symmetric to the chain center and different distances  $d$  as indicated (taking into account the mirror symmetry).  $\chi_{i,1}^{cond}$  gives the linear response of the substrate at site  $i$  to a local magnetic field at the first (left) impurity. Blue lines with squares: results as obtained from real-space DMFT. Red dashed lines with circles: numerically exact solution as obtained from DMRG calculations. For comparison DMRG results for a system with  $L = 49$  sites and a single Anderson impurity are shown (dotted green line with triangles). Figures taken from Ref. [22].

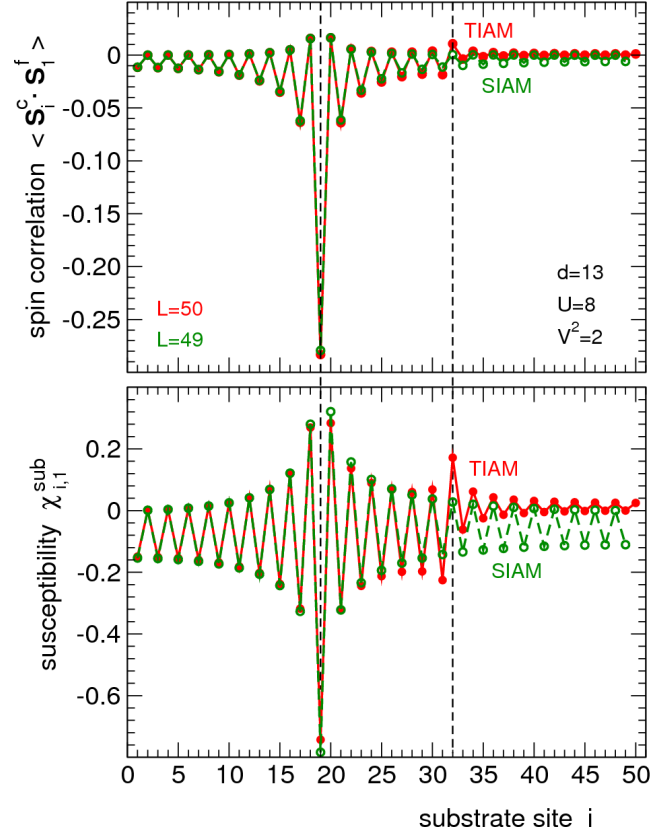


**Figure 4.3:** Spin-spin correlation function  $\langle \mathbf{S}_1 \mathbf{S}_i \rangle$  (upper panel) and magnetic susceptibility  $\chi_{i,1}^{\text{cond}}$  (lower panel) for  $U = 8$  and  $V = \sqrt{2}$  as obtained by DMRG for a system size  $L = 50$  ( $L = 49$ ) and two impurities (one impurity) as functions of site  $i$ . Red lines: results for two impurities and  $L = 50$  (TIAM). Green lines: results for  $L = 49$  and a single impurity at the same position as the left impurity in the two-impurity model (SIAM). The dashed lines indicate the positions  $i_1$  and  $i_2$  of the sites "below" the impurities. Figures taken from Ref. [22].

These non-trivial findings are perfectly captured by R-DMFT. This circumstance should not be regarded as obvious, because the nonlocal impurity-impurity susceptibility  $\chi_{2,1}$  is finite (Fig. 4.4(b)), and hence R-DMFT represents an approximation; even for  $d = L - 1$  (Sec. 3.4). And in fact, the mentioned features result from the effective impurity-impurity interaction, as can be concluded by comparing the TIAM results to results of a corresponding single-impurity Anderson model (SIAM, green lines in Fig. 4.2). To ensure a singlet ground state at half-filling, the system size of the SIAM is reduced by one site,  $L = 49$ . It can be seen that the differences between the single-impurity and the two-impurity results visible in the susceptibilities are most pronounced for  $i > i_2$  but also non-negligible for substrate sites between the two impurities.

In Fig. 4.3, we show  $\chi_{i,1}^{\text{cond}}$  and the equal-time spin-spin correlation function  $\langle \mathbf{S}_1 \mathbf{S}_i \rangle$

#### 4.4 Magnetic response and spin correlations

for  $d = 13$  on a larger scale in order to discuss its physics in detail. The response of the substrate to a static local field at the first impurity is governed by the low-energy excitations around the Fermi edge, i.e.,  $\omega = 0$ . Contrarily, the equal-time spin-spin correction function is obtained by a frequency integration of the dynamic (retarded) susceptibility  $\chi_{i1,1}^{\text{cond}}(\omega)$  and thus includes several energy scales. Nevertheless, the spin-spin correlation behaves qualitatively very similar to  $\chi_{i1,1}^{\text{cond}}$ , and we will refer to it on an equal footing with the susceptibility.

From the total ground-state spin  $S_{\text{gs}} = 0$ , one can directly find the following spin rule

$$\langle \mathbf{S}_1 \mathbf{S}_1 \rangle + \langle \mathbf{S}_1 \mathbf{S}_2 \rangle + \langle \mathbf{S}_1 \mathbf{s}_{\text{tot}} \rangle = 0, \quad (4.10)$$

where  $s_{\text{tot}} = \sum_{i=1}^L \mathbf{s}_i$  is the total spin in the conduction-electron system. Instead, we have for the single-impurity model

$$\langle \mathbf{S}_1 \mathbf{S}_1 \rangle + \langle \mathbf{S}_1 \mathbf{s}_{\text{tot}} \rangle = 0. \quad (4.11)$$

Keeping in mind that the inter-impurity correlations  $\langle \mathbf{S}_1 \mathbf{S}_2 \rangle$  are antiferromagnetic, it is clear that these will just compensate the impurity local moment; in the same way the Kondo correlations  $\langle \mathbf{S}_1 \mathbf{s}_{\text{tot}} \rangle$  do. For the two-impurity model at  $d = 13$ ,  $\langle \mathbf{S}_1 \mathbf{S}_2 \rangle$  is negative but its modulus is small compared to  $\langle \mathbf{S}_1 \mathbf{S}_1 \rangle$ . Looking at Eq. (4.10), the overall substrate response is thus still antiferromagnetic but somewhat reduced as compared to the single-impurity model.

Qualitatively, the same applies to the susceptibility as can be confirmed by the lower panel in Fig. 4.3. For any large but finite system with a nondegenerate singlet ground state, we again have a simple sum rule: a singlet ground state and a finite gap implies that the total magnetic moment must vanish for any  $h_1$  up to some finite critical field:  $\langle \mathbf{S}_{\text{gs}} \rangle = \langle \mathbf{S}_1 \rangle + \langle \mathbf{S}_2 \rangle + \langle \mathbf{s}_{\text{tot}} \rangle = 0$ . Taking the derivative with respect to  $h_1$  then yields

$$\chi_{1,1} + \chi_{2,1} + \sum_i \chi_{i,1}^{\text{cond}} = 0. \quad (4.12)$$

In the same way as above,  $\sum_i \chi_{i,1}^{\text{cond}} = -\chi_{1,1} < 0$  for a single impurity. For two impurities the total response of the substrate is still negative but slightly reduced in absolute values due to the presence of the second impurity, since  $\chi_{2,1} < 0$  at  $d = 13$ .

Pronounced effects due to the presence of the second impurity are observed directly below  $\mathbf{S}_2$ , at  $i_2$ , manifesting in a strong enhancement of  $\chi_{i_2,1}$ . The antiferromagnetic RKKY coupling then implies a singlet ground state. Thus, the substrate contribution to the magnetic moment induced by the magnetic field at the first impurity vanishes,  $\chi_1^{\text{cond}} = \sum_i \chi_{i,1}^{\text{cond}} = \frac{\partial}{\partial h_1} \langle s_{\text{tot},z} \rangle = 0$ . We can infer from Eq. (4.12) that in this case  $\chi_{1,1} + \chi_{2,1} = 0$ . Hence, applying a field  $h_1$  at the first impurity induces antiferromagnetically aligned magnetic impurities with the same absolute magnitude. For  $J$  beyond but close to the RKKY regime we expect the corresponding modulus of the substrate

## 4 Off-resonant models

response at sites at  $i_1$  and  $i_2$  as almost equal. For finite and actually intermediate  $J$ , see Fig. 4.3, the effect is strongly diminished but still clearly visible. Note that the above argumentation can analogously be given by referring to the spin-spin correlation.

Based on these conclusions, we can understand a reduction of the response of the substrate in the TIAM as compared to the SIAM. In Fig. 4.3 we see, however, that the reduction is not homogeneous: there is a comparatively strong reduction beyond the second impurity for  $i > i_2$ , while the response is nearly the same or even enhanced close to  $i_2$  for  $i < i_2$ , and there is almost no effect for  $i < i_1$ . However, large differences between TIAM and SIAM results are not expected close to the first impurity. This is understood from the extreme Kondo limit, where a picture of two separate Kondo clouds applies, leading to a magnetic response to a field at the first impurity similar to the one of a corresponding single-impurity model. According to the sum rule Eq. (4.12), we must then expect a weaker response away from  $i_1$ , i.e. for  $i > i_2$ .

We can use the sum rule Eq. (4.10) to roughly estimate the size of the individual "Kondo clouds" by working with the DMRG data for  $\langle \mathbf{S}_1 \mathbf{s}_i \rangle$  for the single-impurity model. We define the integrated spin-spin correlation function [69]

$$\Theta(r) = 1 + \sum_{|i-i_1|<r} \frac{\langle \mathbf{S}_1 \mathbf{s}_i \rangle}{\langle \mathbf{S}_1 \mathbf{S}_1 \rangle} \quad (4.13)$$

where  $\Theta(0) = 1$ . Like in section 2.5,  $\Theta(r)$  is the fraction of the impurity spin that remains unscreened by the conduction electrons up to distance  $r$  from  $i_1$ . Applying a 90%-screening criterion, the extent of the cloud amounts to  $\xi_K \approx 10 - 15$  lattice sites, consistent with the above discussion.

## 4.5 Distance dependence

The substrate susceptibility  $\chi_{i,1}^{\text{cond}}$  at the substrate site below the first impurity is shown in Fig. 4.4(a). The local impurity susceptibility  $\chi_{1,1}$  and the nonlocal impurity-impurity susceptibility  $\chi_{2,1}$  as functions of the distance  $d = 4m+1$  between the impurities (where  $m$  is an integer) are displayed in Fig. 4.4(b).

As a consequence of the intermediate effective coupling strength  $J = 2$ , the distance dependence of  $\chi_{2,1}$  cannot be explained by conventional RKKY theory. For  $J \rightarrow 0$ , the magnetic susceptibility is determined by the effective two-spin Heisenberg model Eq. (4.8) which yields  $\chi_{2,1} = -\chi_{1,1} \sim 1/J_{\text{RKKY}} \sim (-1)^d d = -d$  at odd distance  $d$ . Both the decreasing modulus of  $\chi_{2,1}$  with increasing  $d$  and the fact that  $\chi_{1,1} + \chi_{2,1} \neq 0$  are evidences that the RKKY regime has been left. Fulfilling the sum rule Eq. (4.12) amounts to a strong substrate contribution  $\sum_i \chi_{i,i}^{\text{cond}}$ .

Large  $d$  implies the applicability of the picture of two individual Kondo clouds. Thus,  $|\chi_{2,1}|$  is expected to decrease for growing  $d$ , whereas the behaviour of  $\chi_{1,1}$  is more

#### 4.5 Distance dependence

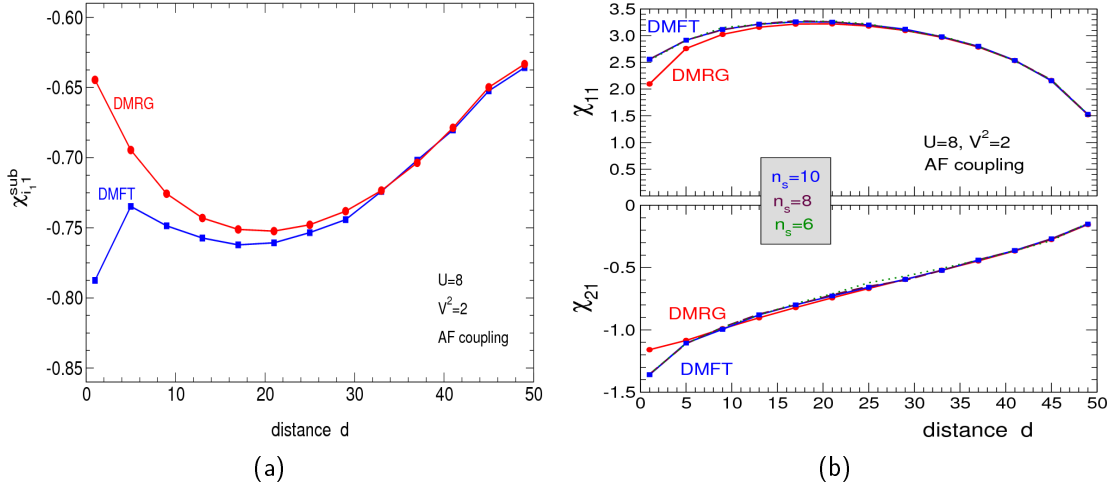


**Figure 4.4:** Left: susceptibility  $\chi_{i_1,1}^{\text{cond}}$  at lattice site  $i_1$  below the first impurity as a function of the impurity distance  $d = 4m + 1$  ( $m$  integer) for  $U = 8$ ,  $V = \sqrt{2}$ , and  $L = 50$  as obtained from R-DMFT (blue line) and DMRG (red line). Right: local impurity susceptibility  $\chi_{1,1}$  and nonlocal impurity-impurity susceptibility  $\chi_{2,1}$  as functions of the impurity distance  $d$  for  $U = 8$ ,  $V = \sqrt{2}$ , and  $L = 50$  as obtained from R-DMFT (blue line) and DMRG (red line). R-DMFT calculations are done with different numbers of bath orbitals in the effective single-impurity models:  $n_s = 6, 8, 10$ , as indicated. It shows that the R-DMFT results are converged with respect to  $n_s$ . Figures taken from Ref. [22].

interesting as it develops a maximum around  $d = 15 - 20$ . At short distances, the increase of  $\chi_{1,1}$  is due to the decreasing effective RKKY coupling. However, it is not the substrate contribution  $|\sum_i \chi_{i,1}^{\text{cond}}|$  that increases accordingly. The Kondo effect is only slightly influenced, since the density of states is roughly constant in the center of the chain. Hence,  $\chi_{1,1}$  increases, i.e. the magnetic moments tend to become free for increasing  $d$ . For large  $d$ , on the other hand, impurity-impurity interactions can be neglected completely, and one would naively expect a saturation of the local susceptibility at the inverse Kondo temperature since  $\chi_{1,1} \sim 1/T_K$  in a single-impurity model [10, 8]. However,  $\chi_{1,1}$  must decrease with increasing  $d$  at fixed  $L = 50$ , because the impurities move to the chain edges, where we have a site-dependent Kondo temperature.  $T_K$  increases with decreasing distance to the edge, since the non-interacting substrate local density of states at the Fermi energy is increasing. This observation has been already made in section 2.5 for the single-impurity Kondo box.

Our interpretation is supported by Fig. 4.5(a) which displays R-DMFT results for  $\chi_{1,1}$  and  $\chi_{2,1}$  for different system sizes  $L = 30$ ,  $L = 50$ , and  $L = 90$ . We find the same qualitative behaviour in all three cases. Quantitatively, however, there are sizable differences at inter-impurity distance  $d = 1$ , for example, which show that even

#### 4 Off-resonant models

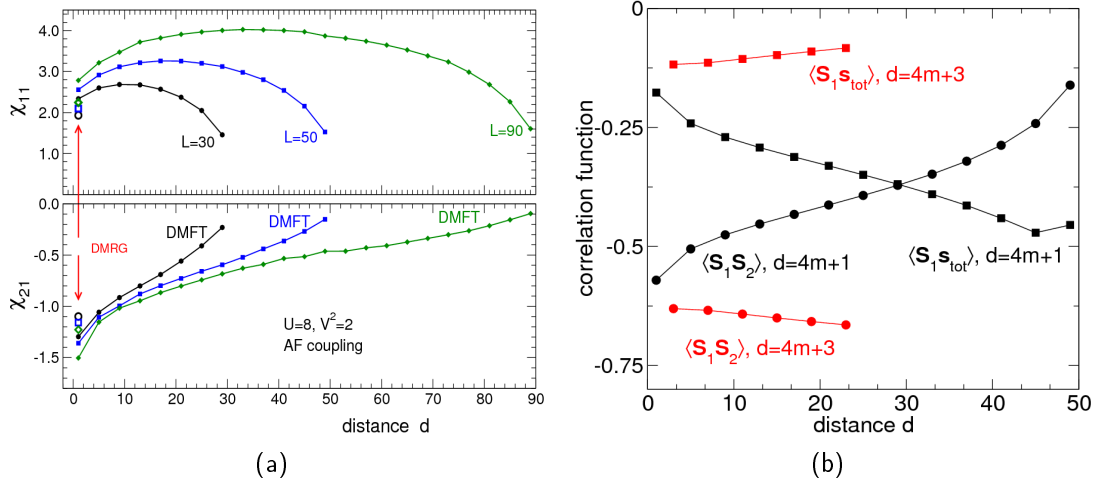


**Figure 4.5:** Left: local and nonlocal impurity susceptibilities  $\chi_{1,1}$  and  $\chi_{2,1}$  as functions of the impurity distance  $d$  for  $U = 8$ ,  $V = \sqrt{2}$ . R-DMFT calculations for different system sizes  $L$  as indicated. DMRG data are shown for comparison at nearest-neighbour distance  $d = 1$  only. Figure taken from Ref. [22]. Right: correlation functions of a TIAM at antiferromagnetic distance as functions of the impurity distance  $d$ . For the cases of  $d = 4m + 1$  (black symbols) and  $d = 4m + 3$  (red symbols), each with integer  $m$ .  $V^2/U = 0.1$  ( $U = 1000$ ) and  $L = 50$ . inter-impurity correlations  $\langle S_1 S_2 \rangle$  (circles) and correlations between impurity and conduction electrons  $\langle S_1 s_{\text{tot}} \rangle = \langle S_2 s_{\text{tot}} \rangle$  (squares) are shown.

with  $L = 90$  substrate sites the chain center cannot be regarded as bulk-like and that the center local density of states is still considerably dependent on  $L$ . On the other hand, the susceptibilities for  $d$  close to  $L$ , i.e. for systems with impurities located at or very close to the chain edges, are almost converged. Note that  $\chi_{1,1}$  for  $d = L - 1$  is almost the same for  $L = 50$  and  $L = 90$ . Again this shows that, at least for the larger systems, the magnetic response is dictated by the physics of the single-site Kondo effect. The presence of the second impurity has almost no effect on  $\chi_{1,1}$  and on the Kondo temperature of the first impurity. This does not exclude a finite magnetic interaction between the impurities and in fact a nonzero  $\chi_{2,1}$  for  $d = L - 1$  is found, which, in addition, also does not depend on  $L$  for the larger systems.

In Fig. 4.5(b), the spin correlation functions of a comparable TIAM, but with  $U = 1000$  and  $V^2/U = 0.1$ , are shown. Due to their rather special behaviour, we want to shift the discussion of the results for distances  $d = 4m + 3$  (red symbols) to section 4.7. We could repeat conclusions for the correlations  $\langle S_1 S_2 \rangle$ , based on those drawn from  $\chi_{2,1}$ . But we rather want to focus on the influence of charge fluctuations at the impurity sites, which become visible in the correlation function  $\langle S_i s_{\text{tot}} \rangle$ . For distances  $d = 4m + 1$ , the modulus of  $\langle S_i s_{\text{tot}} \rangle$  (black squares) increases for increasing  $d$ , starting



#### 4.6 Dependence on the local exchange coupling

from a small value of 0.18 at  $d = 1$ . Since  $\langle \mathbf{S}_1 \mathbf{S}_2 \rangle = -0.57$  for  $d = 1$  (black circles), these results are indeed dominated by the antiferromagnetic RKKY interaction, since a pure singlet-state would correspond to  $\langle \mathbf{S}_1 \mathbf{S}_2 \rangle = -\frac{3}{4}$ . On the other hand, for large  $d$  the Kondo effect becomes stronger and we could naively expect perfect Kondo singlets with  $\langle \mathbf{S}_i \mathbf{s}_{\text{tot}} \rangle \rightarrow -\frac{3}{4}$  which are not interfered by inter-impurity interactions. However,  $\langle \mathbf{S}_i \mathbf{s}_{\text{tot}} \rangle \rightarrow -\frac{3}{4}$  would be only possible in the Kondo limit, where the Anderson impurities become well-formed  $S = \frac{1}{2}$  impurities. Beyond this parameter regime, i.e. for intermediate and large  $V$ , charge fluctuations become important and we would rather expect values between  $-\frac{3}{4}$  (perfect Kondo singlets) and  $-\frac{3}{8}$  ( $V \rightarrow \infty$ ). This transition is clearly seen at  $d = 45$  as minimum in  $\langle \mathbf{S}_i \mathbf{s}_{\text{tot}} \rangle$  at  $\langle \mathbf{S}_i \mathbf{s}_{\text{tot}} \rangle = 0.45$  and shows that charge fluctuations are present even despite the extraordinary large  $U = 1000$ .

Let us also comment on another illustrative feature of the real-space interplay of the two Kondo clouds. As known from Sec. 2.5, inside of a single Kondo cloud and close to the impurity, i.e. in the "local-moment" region, the impurity appears essentially free since Kondo correlations due to the screening have not yet set in. Taking into account the extension of Kondo clouds using Eq. (4.13), this circumstance explains the above mentioned strange behaviour of  $\chi_{i_1+1,1}^{\text{cond}}/\chi_{i_1-1,1}^{\text{cond}}$  for  $d = 5$  and  $d = 9$  in Fig. 4.2. For these distances  $d < \xi_K \approx 10 - 15$  and in a naive picture both impurities are in the local-moment region of each other due to the antiferromagnetic impurity-impurity interaction. Thereby they can mutually screen the spin of each other, before screening by conduction electrons takes place on larger length scales, leading to smaller substrate response as compared to  $d > \xi_K$ .

In the strong-coupling limit  $J \rightarrow \infty$ , two Kondo impurities form perfectly local Kondo singlets which do not interact with each other. Let us consider a one-dimensional system of even length  $L$ , where the two impurities are coupled to the chain edges. State corrections in second-order perturbation theory in the electron hopping  $t$  result in inter-impurity correlations [113, 70, 114]

$$\langle \mathbf{S}_1 \mathbf{S}_2 \rangle = 12 \left( \frac{20}{9} \right)^2 \left( \frac{t}{J} \right)^4 \langle \text{FS}' | s_2^z s_{L-1}^z | \text{FS}' \rangle, \quad (4.14)$$

which are found to decay as  $1/d^2$ .  $|\text{FS}'\rangle$  denotes the conduction-electron Fermi sea with size  $L - 2$ , ranging from site 2 to  $L - 1$ . Eq. (4.14) can be interpreted as well as one impurity probing the spin correlations induced by the other impurity, i.e. correlations from the exterior region of the other Kondo cloud.

## 4.6 Dependence on the local exchange coupling

The crossover between the regime of individual Kondo clouds for large distances  $d$  and correlated impurities for small  $d$  can be converted to a crossover from strong

#### 4 Off-resonant models

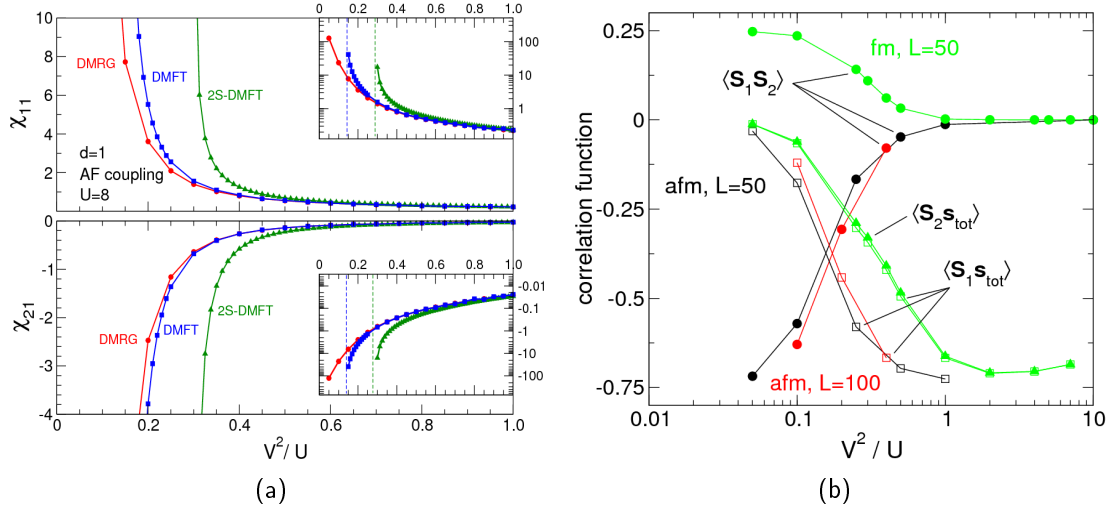


**Figure 4.6:** Left: local and nonlocal impurity susceptibilities  $\chi_{1,1}$  and  $\chi_{2,1}$  as functions of  $\frac{V^2}{U}$  for  $U = 8$  and  $d = 1$  as obtained by R-DMFT, real-space two-site DMFT (see Ref. [22] for details) and DMRG for a system with  $L = 50$ . Insets: Same quantities plotted on a logarithmic scale. Dashed lines indicate  $\frac{V^2}{U}$  where  $\chi_{1,1}$  and  $\chi_{2,1}$  diverge. Figure taken from Ref. [22]. Right: correlation functions of a TIAM at antiferromagnetic distance  $d = 1$  ("afm", black and red symbols) and at ferromagnetic distance  $d = 2$  ("fm", green symbols). Correlations are shown as functions of  $\frac{V^2}{U}$  ( $U = 1000$ ) on a log scale. Different system sizes  $L = 50$  (black and green symbols) and  $L = 100$  (red symbols) are considered. inter-impurity correlations  $\langle S_1 S_2 \rangle$  (circles) as well as  $\langle S_1 s_{tot} \rangle$  (squares) are displayed. Due to the unavoidable, asymmetric impurity positions for  $d = 2$ , we show in this case also  $\langle S_2 s_{tot} \rangle$  (triangles).

couplings to weak couplings. Fig. 4.6(a) shows the susceptibilities for  $d = 1$  as functions of  $V^2/U$ . For decreasing  $J$ , the system crosses over to a perfect RKKY model, accompanied by significant increasing deviations between R-DMFT and numerically exact DMRG data. Those can be noticed also in previous figures of this chapter for results at small distances (Figs. 4.4(b), 4.4(a), and 4.5(a)).

As long as  $V^2/U$  is large, the picture of two more or less separate Kondo clouds is maintained and correctly reproduced by R-DMFT. But as soon as  $V^2/U$  decreases, the mean-field approach, inherent in the method, breaks down completely. The screening of the magnetic moments is too weak to compensate the ordering tendencies induced by a comparatively strong inter-impurity interaction. The system becomes too susceptible to an artificial spontaneous symmetry breaking that is induced by the mean-field approximation itself. While the impurities' state is given by a  $SU(2)$  invariant singlet  $\frac{1}{\sqrt{2}}(|\uparrow\downarrow\rangle - |\downarrow\uparrow\rangle)$  for  $J \rightarrow 0$ , the mean-field theory predicts an incoherent mixture of degenerate ordered states  $|\uparrow\downarrow\rangle$  and  $|\downarrow\uparrow\rangle$ .

This qualitative failure is indicated by divergencies of  $\chi_{1,1}$  and  $\chi_{2,1}$  which take place at coupling strengths  $V^2/U$  which are somewhat smaller than those where first quantitative deviations from the exact data were found (see insets of Fig. 4.6(a)). This also implies that the mean-field approach is able to exhibit its limitations by itself before breaking down. One can find that the artificial transition occurs roughly at  $J = 8 \frac{V^2}{U} \approx 1$  for  $d = 1$ , i.e. in the intermediate  $J$  region.

Again, we want to compare our findings to  $\langle \mathbf{S}_1 \mathbf{S}_2 \rangle$  and  $\langle \mathbf{S}_i \mathbf{s}_{\text{tot}} \rangle$  in Fig. 4.6(b) for the TIAM with  $U = 1000$ .  $\langle \mathbf{S}_1 \mathbf{S}_2 \rangle$  (black circles) indicates the crossover from Kondo to RKKY regime by decreasing from almost vanishing values for strong  $V$  to perfect impurity singlet correlations  $-\frac{3}{4}$  for weak  $V$ . Complementary,  $\langle \mathbf{S}_i \mathbf{s}_{\text{tot}} \rangle$  (black squares) is large in absolute values and antiferromagnetic due to the Kondo effect for intermediate and strong couplings, while it is vanishing for weak  $V$  due to the disappearing Kondo effect for  $\Delta > T_K$ . For a larger system size  $L = 100$  (red symbols), the finite-size gap is approximately half as small. It is seen that this circumstance fosters the Kondo effect, since at weak but fixed  $V$  the modulus of  $\langle \mathbf{S}_1 \mathbf{S}_2 \rangle$  is decreasing for increasing  $L$ , whereas the modulus of  $\langle \mathbf{S}_i \mathbf{s}_{\text{tot}} \rangle$  is increasing.

## 4.7 Different distances between the impurities

So far we discussed the results for odd distances  $d = 4m + 1$  ( $m$  integer). Inspecting the relevant correlations for odd distances  $d = 4m + 3$  and fixed  $V$  and  $U$ , shown in Fig. 4.5(b) (red symbols), we observe that the distance dependence of local and nonlocal correlations is reversed: for increasing  $d$ , instead of vanishing, the inter-impurity correlation  $\langle \mathbf{S}_1 \mathbf{S}_2 \rangle$  even increases, while  $\langle \mathbf{S}_i \mathbf{s}_{\text{tot}} \rangle$  decreases. This pronounced odd-even effect is caused by the local density of states close to the Fermi energy, which is decreasing towards the chain edges for  $d = 4m + 3$ , while it is increasing for  $d = 4m + 1$ . It is a consequence of Friedel oscillations from the chain edges [23]. At the corresponding substrate sites  $i_1$  and  $i_2$  (symmetric to the chain center) we have a low weight  $|U_{ik_F}|^2$  of the highest (doubly) occupied one-particle energy eigenstate of the non-interacting substrate at the Fermi wave vector  $k_F$ , whereas  $|U_{ik_F}|^2$  is high for distances  $d = 4m + 1$ . The weight  $|U_{ik_F}|^2$  determines the local substrate density of states and thus the local Kondo temperature. Consequently, for increasing  $d = 4m + 3$ , the Kondo effect is more suppressed, resulting in more dominant RKKY exchange. At the edges ( $d = 47$ )  $|U_{ik_F}|^2$  is suppressed by more than a factor of 100 compared to the  $d = 4m + 1$  case ( $d = 49$ ), and the Kondo temperature is essentially vanishing.

Two-impurity models at ferromagnetic distances  $d = 2m$  are likewise interesting and far from trivial. In the Kondo limit the impurities become ferromagnetically correlated  $S = 1/2$  spins, leading to a triplet ground state. This is easily verified by means of DMRG calculations for  $L = 50$  (Fig. 4.6(b)):  $\langle \mathbf{S}_1 \mathbf{S}_2 \rangle \rightarrow \frac{1}{4}$  for  $V \rightarrow 0$  (green circles). The purely RKKY-ruled behaviour can be understood for  $J \rightarrow 0$  in the same way

## 4 Off-resonant models

as in the antiferromagnetic case as a cutoff of the Kondo effect by the finite system size. However, as discussed in section 4.2, the triplet formed by both impurities can be screened as a whole by the conduction electrons and thus be attributed an own Kondo temperature  $T_K^{(2\text{spins})}$ . Note that this screening can only take place for  $\Delta < T_K^{(2\text{spins})}$  (but  $J < J_D$ ). This is not in conflict with the adiabaticity of the ground state enforced by Lieb's theorem (Sec. 3.5), since, in the case of the screening, an additional triplet develops in the substrate, so that the total ground-state spin  $S_{\text{gs}} = 1$  is preserved. The physical background of this mechanism will occupy us in chapter 10. On the other hand, we know from section 4.2 that the Kondo temperatures of a two-impurity model at ferromagnetic distance may be much smaller than the one of a single-impurity model,  $T_K^{(2\text{spins})} < T_K^{(1\text{spin})}$ , resulting in  $J_{\Delta,1\text{spin}} < J_{\Delta,2\text{spins}}$ . This suggests that  $L = 50$  is far too small to accomodate the corresponding screening cloud. It is imaginable that this condition changes in larger systems, which will be explored in chapter 9.

The numerical results in Fig. 4.6(b) substantiate our considerations: over a large parameter region  $0.1 \leq V^2/U \leq 1$ , the correlation function  $\langle \mathbf{S}_1 \mathbf{S}_{\text{tot}} \rangle$  (green squares) remains weaker for fixed  $V$  than the corresponding results for  $d = 1$ . Consequently, the impurities are much more free and stronger governed by the ferromagnetic RKKY interaction. On the other hand, for large  $V^2/U$  charge fluctuations reduce the spin at the impurity sites.<sup>4</sup>

R-DMFT reproduces the spin-triplet ground state for small  $V^2/U$  by predicting, for infinitesimally small external magnetic field in the  $+z$  direction, a spontaneously symmetry-broken ferromagnetic state  $|\uparrow\uparrow\rangle$ . However, for increasing  $V$ ,  $\langle S_{\text{tot}}^z \rangle$  deviates from unity and even vanishes for  $V \rightarrow \infty$ .

## 4.8 Summary

We computed spin correlation functions and static spin susceptibilities of two-impurity Anderson models with finite  $L$ . Depending on the distance  $d$  between the two impurities and depending on the hybridisation strength  $V$ , we could classify the different features of the correlations as single-impurity effects or as resulting from the effective impurity-impurity interaction by comparing the TIAM results with those obtained from a corresponding single-impurity model. In this way, clear reminiscences of the RKKY interaction, i.e. of nonlocal singlet formation, are found to compete with the formation of individual Kondo clouds, i.e. screening of the impurity magnetic moments.

In addition, the correlations are strongly affected by the finiteness of the host system and by its boundaries. This results in effects from strong Friedel oscillations in the local

---

<sup>4</sup>This can be seen in Fig. 4.6(b) as the minimum of  $\langle \mathbf{S}_1 \mathbf{S}_{\text{tot}} \rangle$  (green squares) and  $\langle \mathbf{S}_2 \mathbf{S}_{\text{tot}} \rangle$  (green triangles) at  $\frac{V^2}{U} = 2$ .

density of states, especially if the impurities are in the vicinity of one of the chain edges. In this context, it is important to notice that due to the RKKY interaction, which may generate a new Kondo scale  $T_K^{(2\text{spins})} < T_K^{(1\text{spin})}$ , finite-size effects may be dominant over a much larger parameter range than in the single-impurity case, as observed in the TIAM at ferromagnetic distance.

Another aspect of our study was the reliability of real-space DMFT and it turned out that the aforementioned, complex interplay is almost perfectly recovered by R-DMFT. Qualitatively, the R-DMFT is reliable as long as the model parameters, in particular the local exchange coupling  $J \sim \frac{V^2}{U}$ , are in a regime well separated from the artificial symmetry-broken state. This parameter regime, where the impurity susceptibilities are not too large or where the magnetic moments are predominantly interacting with the conduction electrons rather than with each other, goes well beyond the extreme Kondo regime of non-overlapping Kondo clouds. The critical value of  $J = 8\frac{V^2}{U} \approx 1$  for  $d = 1$  gives an impression of a lower bound for the applicability of R-DMFT.

On the other hand, nonlocal effective interactions do not contribute to the single-particle self-energy on the DMFT level: the DMFT self-energy is just defined as the sum of the local skeleton diagrams only. This is a well-known shortcoming of mean-field theory, which gives rise to artifacts in the RKKY regime. Namely, for  $J \rightarrow 0$  the magnetic impurities are only weakly coupled to the host and thus become extremely susceptible. A tiny Weiss field within DMFT is then sufficient to drive the system to an artificial symmetry-broken state; i.e., a Néel-like state rather than a nonlocal singlet of the impurity magnetic moments is formed. Therefore, the physics of the RKKY regime in a two-impurity model is not accessible by DMFT.

However, an emerging question is how the total ground-state spin  $S_{\text{gs}}$  is maintained for all  $J$ . It was raised for a TIAM at ferromagnetic distance, where a triplet ground state is obtained for all finite  $V$  and  $U > 0$ . While we could easily identify the RKKY exchange as respective driving mechanism at weak  $J$ , it is not clear how a triplet builds up for strong  $J$ , where we find two paramagnetic Kondo clouds. This puzzle will be our inspiration to investigate in-depth the strong-coupling regime in chapter 10.

Considering effects from the finite chain size, the next logical step is to examine "on-resonance cases", which generate an even more interesting class of finite-size effects characterised by unconventional ground states. They will be discussed in the following chapters.



# 5 On-resonant models

## 5.1 Introduction

Unlike "off-resonance cases" (chapter 4), in "on-resonance cases" the highest occupied one-particle eigenenergy  $\varepsilon_{k_F}$  is singly occupied and thus the ground state of the non-interacting conduction-electron system is twofold Kramers degenerate [19, 20]. The essential difference is that when the standard Kondo cloud picture collapses ( $\Delta > T_K$ ), the  $k_F$  state may be subject to residual impurity couplings for  $\Delta > T_K$ , inducing a fundamentally different behaviour for  $J \rightarrow 0$ , as compared to off-resonance cases. This circumstance may result in an unconventional reentrant competition between RKKY exchange and Kondo effect where the ground state deviates from predictions of standard RKKY perturbation theory. This will constitute an important, if not the fundamental, cornerstone of our weak-coupling picture ( $|J| \ll t$ ).

In this chapter, we will see that the finite system size along with open boundary conditions causes an unconventional, spatially dependent competition with the RKKY interaction. As known from section 4.2, Doniach's scaling arguments predict that a multi-impurity system is dominated by the RKKY interaction for  $J < J_D$  or  $|J_{\text{RKKY}}| > T_K$ , respectively. It allows for magnetic ordering among the impurities, which then can be screened by the Kondo effect as a whole.

Cutting the nonperturbative Kondo effect at  $J_\Delta$  (where  $\Delta = T_K^{(1\text{spin})}$ ) implies that standard perturbation-theory in  $J$  is regularised. In on-resonance cases, our results show that screening of an impurity spin is possible for  $J \rightarrow 0$  but competes with the RKKY exchange. Our concept is summarised in Fig. 5.1. The corresponding linear-in- $J$  Kondo scale depends on the weight of the single-electron eigenstate at the Fermi edge at the substrate site "below" the impurity. Sites with finite weight are termed "good sites", whereas for "bad sites" the linear-in- $J$  contribution is vanishing and these sites are therefore subjected to RKKY coupling.

In the following we will show that these arguments give a complete qualitative picture of this physics, which is supported by numerical results obtained for a three-impurity Kondo using full diagonalisation, weak-coupling perturbation theory, and DMRG (Sec. 3.3). Note that in this and the following chapters we switch to Kondo impurity models, which neglect valence fluctuations at impurity sites, to concentrate on the spin exchange.

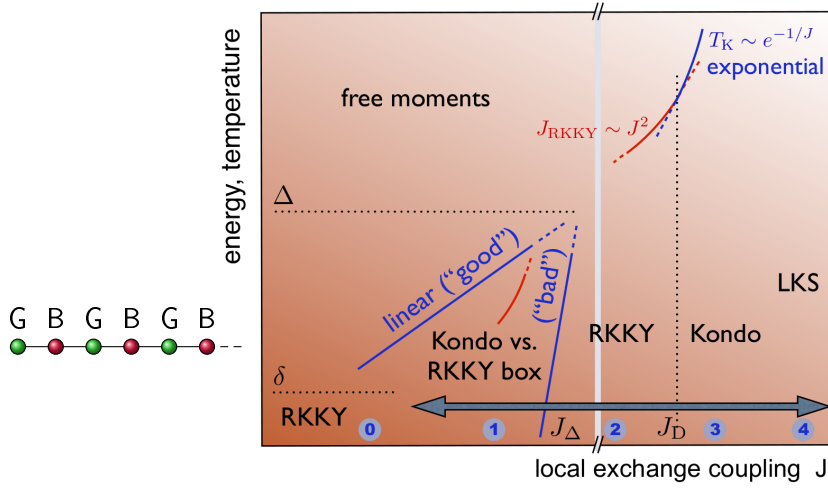


**Figure 5.1:** Competition between Kondo screening and RKKY interaction in an on-resonant quantum box. Local Kondo singlets (LKS) are formed for extremely strong  $J$  (regime 4). With decreasing  $J$ , the energy to break up a Kondo singlet becomes exponentially small (3). Below  $J_D$ , RKKY coupling is dominant (2). Finite-size effects set in for  $J < J_\Delta$ , defined as the point where the bulk Kondo temperature equals the finite-size gap,  $T_K = \Delta$ . If the system is sufficiently large, we have  $J_\Delta < J_D$ . The singlet-formation energy is linear in  $J$  for "good" and vanishes for "bad" sites (1): i.e., for sites where the  $k_F$  conduction-electron wave function has a finite (vanishing) weight, the Kondo effect "wins" (RKKY exchange wins). The remaining unscreened moments are subjected to nonlocal RKKY exchange subsequently. Simultaneously, RKKY exchange may generate a further Kondo scale  $T_K^{(Rspins)} < T_K^{(1spin)}$  (not shown here), whose Kondo correlations are cut at  $T_K^{(Rspins)} = \Delta$  (Sec. 5.4). As we will discuss in chapter 8, the coupling to the environment gives rise to an energy scale  $\delta$  [49, 115, 50], below which the reentrant competition breaks down and an exponentially small Kondo scale leads to an RKKY regime (0). The arrow marks the parameter range covered by the numerical calculations of Ref. [21]. Figure taken from Ref. [21]. The pictogram visualises the typical distribution of good (G) and bad sites (B) for sites  $i = 1, 2, 3, \dots$

To gain a deeper understanding, we start with the perturbation theory with respect to the local coupling  $J$  (Sec. 5.2), which aims at the derivation of an effective low-energy Hamiltonian for weak  $J$ . Additionally, as supplement, we specify the corresponding results for the "off-resonance case" (chapter 4). Subsequently, we apply the results to a particular three-impurity model which turns out to be a prime example as particular correlation functions reflect the dramatic impact of finite-size and boundary effects on the interplay between RKKY exchange and Kondo effect. However, we emphasise that



we choose the three-impurity model for the sake of simplicity. Similar results could be obtained also for other models if they are "on-resonant", e.g. two-impurity models with an odd number of conduction electrons. In the following, we will closely follow the arguments and explanations presented in our paper, Ref. [21].

## 5.2 Perturbation theory in the weak-coupling regime

Since the spectrum of a spatially confined host system is gapped by  $\Delta$ , Anderson's infrared orthogonality catastrophe will be prevented by removing the exponentially large number of possible excitations at the Fermi energy that are introduced by a single impurity (Sec. 2.3). Therefore, the overlap between the ground state without and with a single impurity will be finite, permitting an adiabatic connection of both situations by perturbation theory.

Thus, we can motivate the usefulness and reliability of perturbation theory in the finite-size regime where  $\Delta > T_K$ . Our intention is to understand the weak-coupling regime  $J \ll t$  in on-resonance cases as well as in off-resonance cases by deriving an effective low-energy Hamiltonian according to Ref. [116] (p. 39).

The multi-impurity Kondo model Hamiltonian Eq. (2.34) can be decomposed as  $H = H_0 + H_1$ , where

$$H_0 = -t \sum_{\langle i,j \rangle, \sigma} c_{i\sigma}^\dagger c_{j\sigma} \quad (5.1)$$

describes the system of non-interacting conduction electrons, and

$$H_1 = J \sum_{r=1}^R \mathbf{s}_{i_r} \cdot \mathbf{S}_r \quad (5.2)$$

is the local interaction between the conduction-electron spin at site  $i_r$  with the  $r$ -th impurity spin.

### The on-resonance case

In an on-resonance case the system's ground state

$$|\text{FS}, \mu\rangle \otimes |\mu_1\rangle \otimes \dots \otimes |\mu_R\rangle =: |\mu; \mu_1, \dots, \mu_R\rangle \quad (5.3)$$

is  $2^{R+1}$ -fold degenerate if there are  $R$  impurity spins.  $|\text{FS}, \mu\rangle$  represents the Fermi sea of an odd number  $N$  of conduction electrons with a net spin projection  $\mu = \pm \frac{1}{2}$  which

## 5 On-resonant models

is due to the  $z$ -component of the spin of the electron in the highest singly occupied one-particle state  $k_F$ .  $\mu_r = \pm \frac{1}{2}$  for  $r = 1, \dots, R$  is the magnetic quantum number of the localised spin  $\mathbf{S}_r$ , and  $|\mu_r\rangle$  the corresponding eigenstate of  $S_r^{(z)}$ .

Let  $P_0$  be the projector onto the subspace spanned by the degenerate ground states. Then, for finite  $J \neq 0$  and up to  $\mathcal{O}(J^2)$ , the interacting eigenenergies and eigenstates of  $H$  are obtained from the effective Hamiltonian

$$H_{\text{eff}} = P_0 H_1 P_0 + \sum_{m \neq 0} \frac{1}{E_0 - E_m} P_0 H_1 P_m H_1 P_0 \quad (5.4)$$

which is defined in the restricted Hilbert space corresponding to  $P_0$ . Here,  $m \neq 0$  labels the different subspaces spanned by non-interacting basis states with energy  $E_m$  orthogonal to the ground states with energy  $E_0$ . This is the standard expression obtained from degenerate second-order perturbation theory [116].

The linear-in- $J$  term is

$$P_0 H_1 P_0 = J \sum_{r=1}^R \sum_{\mu, \mu'} \sum_{\substack{\mu_1, \dots, \mu_R \\ \mu_1, \dots, \mu'_R}} |\mu; \mu_1, \dots, \mu_R\rangle \langle \mu; \mu_1, \dots, \mu_R | \mathbf{s}_{i_r} \mathbf{S}_r | \mu'; \mu'_1, \dots, \mu'_R \rangle \langle \mu'; \mu'_1, \dots, \mu'_R |. \quad (5.5)$$

Employing a unitary transformation of the one-particle basis,  $c_{i\sigma}^\dagger = \sum_k U_{ik} c_{k\sigma}^\dagger$ , which diagonalises the tight-binding part, the local spin of the conduction-electron system at site  $i_r$  can be written as:

$$\mathbf{s}_{i_r} = \frac{1}{2} \sum_{\sigma\sigma'} \sum_{kk'} U_{i_r k} c_{k\sigma}^\dagger \boldsymbol{\sigma}_{\sigma\sigma'} c_{k'\sigma'} U_{i_r k'}. \quad (5.6)$$

Therewith, the matrix element becomes

$$\begin{aligned} \langle \mu; \mu_1, \dots, \mu_R | \mathbf{s}_{i_r} \mathbf{S}_r | \mu'; \mu'_1, \dots, \mu'_R \rangle &= \frac{1}{2} \sum_{\sigma\sigma'} \sum_{kk'} U_{i_r k} U_{i_r k'} \langle \text{FS}, \mu | c_{k\sigma}^\dagger c_{k'\sigma'} | \text{FS}, \mu' \rangle \\ &\quad \times \boldsymbol{\sigma}_{\sigma\sigma'} \delta_{\mu_1 \mu'_1} \dots \langle \mu_r | \mathbf{S}_r | \mu'_r \rangle \dots \delta_{\mu_R \mu'_R}. \end{aligned} \quad (5.7)$$

Terms with  $k < k_F$  do not contribute, since  $\sum_{\sigma\sigma'} \boldsymbol{\sigma}_{\sigma\sigma'} \delta_{\sigma\sigma'} = 0$ . Therefore, we can assume  $k = k' = k_F$  and get  $\langle \mu | c_{k_F\sigma}^\dagger c_{k_F\sigma'} | \mu' \rangle = \delta_{\mu\sigma} \delta_{\mu'\sigma'}$ . Thus

$$\langle \mu; \mu_1, \dots, \mu_R | \mathbf{s}_{i_r} \mathbf{S}_r | \mu'; \mu'_1, \dots, \mu'_R \rangle = U_{k_F i_r}^2 \frac{1}{2} \boldsymbol{\sigma}_{\mu\mu'} \delta_{\mu_1 \mu'_1} \dots \langle \mu_r | \mathbf{S}_r | \mu'_r \rangle \dots \delta_{\mu_R \mu'_R}. \quad (5.8)$$

## 5.2 Perturbation theory in the weak-coupling regime

With the spin of the  $k_F$  electron,  $\mathbf{s}_F := \frac{1}{2} \sum_{\sigma\sigma'} c_{k_F\sigma}^\dagger \boldsymbol{\sigma}_{\sigma\sigma'} c_{k_F\sigma'}$ , we find

$$P_0 H_1 P_0 = P_0 \left( \sum_{r=1}^R J_r^{(1)} \mathbf{s}_r \mathbf{s}_F \right) P_0. \quad (5.9)$$

The effective linear-in- $J$  coupling is  $J_r^{(1)} := J U_{i_r k_F}^2$ .

In order  $J^2$  we obtain analogously

$$P_0 H_1 P_m H_1 P_0 = J^2 \sum_{r,r'} \sum_{\mu, \mu'} \sum_{\substack{\mu_1, \dots, \mu_R \\ \mu'_1, \dots, \mu'_R}} \quad (5.10)$$

$$|\mu; \mu_1, \dots, \mu_R\rangle \langle \mu; \mu_1, \dots, \mu_R | \mathbf{s}_{i_r} \mathbf{s}_r P_m \mathbf{s}_{i_{r'}} \mathbf{s}_{r'} | \mu'; \mu'_1, \dots, \mu'_R \rangle \langle \mu'; \mu'_1, \dots, \mu'_R|.$$

In the  $m$  sum only single-particle excitations  $(p, \sigma) \rightarrow (p', \sigma')$  with  $p \neq p'$  contribute:

$$P_{p,p',\sigma,\sigma'} = \sum_{\bar{\mu}; \nu_1, \dots, \nu_R} c_{p\sigma}^\dagger c_{p'\sigma'} |\bar{\mu}; \mu_1, \dots, \mu_R\rangle \langle \bar{\mu}; \mu_1, \dots, \mu_R | c_{p'\sigma'}^\dagger c_{p\sigma} \quad (5.11)$$

$$= \sum_{\bar{\mu}} c_{p\sigma}^\dagger c_{p'\sigma'} |\text{FS}, \bar{\mu}\rangle \langle \text{FS}, \bar{\mu} | c_{p'\sigma'}^\dagger c_{p\sigma}. \quad (5.12)$$

We insert this into the above equations, sum over  $p, p', \sigma, \sigma'$  ( $p \neq p'$ ), and employ the unitary transformation of  $\mathbf{s}_{i_r}$  and  $\mathbf{s}_{i_{r'}}$  to  $k$ -space. The resulting matrix elements factorise into matrix elements of impurity spins and matrix elements of conduction-electron degrees of freedom. The latter are of the form

$$\langle \mu | c_{k\sigma}^\dagger c_{k'\sigma'} c_{p\sigma''}^\dagger c_{p'\sigma'''} |\bar{\mu}\rangle = \langle 0 | c_{k_F\mu} c_{k\sigma}^\dagger c_{k'\sigma'} c_{p\sigma''}^\dagger c_{p'\sigma'''} c_{k_F\bar{\mu}}^\dagger | 0 \rangle \quad (5.13)$$

with the nondegenerate Fermi sea  $|0\rangle$  of  $N - 1$  conduction electrons, where  $N - 1$  is an even number. This matrix element is conveniently computed using Wick's theorem. After some straightforward algebra, we get

$$\begin{aligned} & \langle \mu; \mu_1, \dots, \mu_R | \sum_{m \neq 0} \frac{H_1 P_m H_1}{E_0 - E_m} | \mu'; \mu'_1, \dots, \mu'_R \rangle \quad (5.14) \\ &= \frac{J^2}{2} \sum_{r,r'} \sum_{\alpha, \beta \in \{x, y, z\}} \langle \mu_1, \dots, \mu_R | S_r^{(\alpha)} S_{r'}^{(\beta)} | \mu'_1, \dots, \mu'_R \rangle \\ & \quad \times \left[ \delta_{\alpha\beta} \delta_{\mu\mu'} \sum_{p < k_F, p' > k_F} \frac{1}{\varepsilon_p - \varepsilon_{p'}} U_{i_r p} U_{i_r p'} U_{i_{r'} p'} U_{i_{r'} p} \right. \\ & \quad + (\sigma^\alpha \sigma^\beta)_{\mu\mu'} U_{i_r k_F} U_{i_{r'} k_F} \sum_{p > k_F} \frac{1}{\varepsilon_{k_F} - \varepsilon_p} U_{i_r p} U_{i_{r'} p} \\ & \quad \left. - \left( (\sigma^\beta \sigma^\alpha)_{\mu\mu'} - 2\delta_{\alpha\beta} \delta_{\mu\mu'} \right) U_{i_r k_F} U_{i_{r'} k_F} \sum_{p < k_F} \frac{1}{\varepsilon_p - \varepsilon_{k_F}} U_{i_r p} U_{i_{r'} p} \right]. \end{aligned}$$

## 5 On-resonant models

We finally use the identity  $\sigma^\alpha \sigma^\beta = \delta_{\alpha\beta} + i \sum_\gamma \varepsilon_{\alpha\beta\gamma} \sigma^\gamma$  for the products of Pauli matrices, treat the terms  $r = r'$  and  $r \neq r'$  separately, and exploit particle-hole symmetry, i.e.,  $\sum_{p>k_F} \frac{1}{\varepsilon_{k_F} - \varepsilon_p} U_{irp} U_{i_r'p} = \sum_{p<k_F} \frac{1}{\varepsilon_p - \varepsilon_{k_F}} U_{irp} U_{i_r'p}$ . This yields

$$\sum_m \frac{1}{E_0 - E_m} P_0 H_1 P_m H_1 P_0 = P_0 \left( \sum_{r=1}^R J_r^{(2)} \mathbf{S}_r \mathbf{s}_F - \sum_{r,r'=1}^R J_{rr'} \mathbf{S}_r \mathbf{S}_{r'} \right) P_0, \quad (5.15)$$

where

$$J_{rr'} = \frac{J^2}{2} \sum_{\substack{p \leq k_F, p' \geq k_F \\ p \neq p'}} \frac{1}{\varepsilon_{p'} - \varepsilon_p} U_{irp} U_{irp'} U_{i_r'p'} U_{i_r'p} \quad (5.16)$$

and

$$J_r^{(2)} = 2J^2 U_{irk_F}^2 \sum_{p>k_F} \frac{1}{\varepsilon_p - \varepsilon_{k_F}} U_{irp}^2. \quad (5.17)$$

$J_{rr'}$  are the RKKY couplings, while  $J_r^{(2)}$  is the effective local Kondo coupling. Taking the limit  $L \rightarrow \infty$ ,  $J_r^{(2)}$  expectedly diverges (Sec. 2.3): it is roughly  $\sim \sum_p \frac{1}{\varepsilon_p} \sim \int dp \frac{1}{\varepsilon_p} \sim \ln L$ , where  $p$  denotes a conduction-electron momentum.

In general, without assuming particle-hole symmetry, we obtain

$$\begin{aligned} & \sum_m \frac{1}{E_0 - E_m} P_0 H_1 P_m H_1 P_0 \\ &= \frac{J^2}{2} P_0 \left[ 2 \sum_{r=1}^R |U_{irk_F}|^2 \left( \sum_{p>k_F} \frac{|U_{irp}|^2}{\varepsilon_p - \varepsilon_{k_F}} + \sum_{p<k_F} \frac{|U_{irp}|^2}{\varepsilon_{k_F} - \varepsilon_p} \right) \mathbf{S}_r \mathbf{s}_F \right. \\ & \quad \left. - \sum_{r,r'=1}^R \sum_{\substack{p \leq k_F, p' \geq k_F \\ p \neq p'}} \frac{U_{irp} U_{irp'} U_{i_r'p'} U_{i_r'p}}{\varepsilon_{p'} - \varepsilon_p} \mathbf{S}_r \mathbf{S}_{r'} \right] P_0. \end{aligned}$$

## The off-resonance case

For completeness, we now turn to the off-resonance cases, in which the total number of conduction electrons is even. The ground states are given by

$$|\text{FS}\rangle \otimes |\mu_1\rangle \otimes \dots \otimes |\mu_R\rangle =: |\mu_1, \dots, \mu_R\rangle, \quad (5.18)$$

where the degeneracy fully stems from the uncorrelated impurity spins.

## 5.2 Perturbation theory in the weak-coupling regime

Repeating our considerations for the linear-in- $J$  term,

$$P_0 H_1 P_0 = J \sum_{r=1}^R \sum_{\substack{\mu_1, \dots, \mu_R \\ \mu_1, \dots, \mu'_R}} |\mu_1, \dots, \mu_R\rangle \langle \mu_1, \dots, \mu_R | \mathbf{s}_{i_r} \mathbf{S}_r | \mu'_1, \dots, \mu'_R\rangle \langle \mu'_1, \dots, \mu'_R|, \quad (5.19)$$

we find that this term is vanishing, because there is no conduction-electron state at the chemical potential, and states below it ( $\varepsilon_k < \mu$ ) do not contribute.

The second-order contribution is

$$P_0 H_1 P_m H_1 P_0 = J^2 \sum_{r, r'} \sum_{\substack{\mu_1, \dots, \mu_R \\ \mu_1, \dots, \mu'_R}} |\mu_1, \dots, \mu_R\rangle \langle \mu_1, \dots, \mu_R | \mathbf{s}_{i_r} \mathbf{S}_r P_m \mathbf{s}_{i_{r'}} \mathbf{S}_{r'} | \mu'_1, \dots, \mu'_R\rangle \langle \mu'_1, \dots, \mu'_R|. \quad (5.20)$$

Again only single-particle excitations  $(p, \sigma) \rightarrow (p', \sigma')$  with  $p \neq p'$  give contributions:

$$P_{p, p', \sigma, \sigma'} = \sum_{\nu_1, \dots, \nu_R} c_{p\sigma}^\dagger c_{p'\sigma'} |\mu_1, \dots, \mu_R\rangle \langle \mu_1, \dots, \mu_R | c_{p'\sigma'}^\dagger c_{p\sigma} \quad (5.21)$$

$$= c_{p\sigma}^\dagger c_{p'\sigma'} |\text{FS}\rangle \langle \text{FS} | c_{p'\sigma'}^\dagger c_{p\sigma}. \quad (5.22)$$

One easily finds

$$\begin{aligned} \langle \mu_1, \dots, \mu_R | \sum_m^{m \neq 0} \frac{H_1 P_m H_1}{E_0 - E_m} | \mu'_1, \dots, \mu'_R \rangle \\ = \frac{J^2}{2} \sum_{r, r'} \sum_{\alpha, \beta \in \{x, y, z\}} \langle \mu_1, \dots, \mu_R | S_r^{(\alpha)} S_{r'}^{(\beta)} | \mu'_1, \dots, \mu'_R \rangle \\ \left[ \delta_{\alpha\beta} \delta_{\mu\mu'} \sum_{\varepsilon_p < \mu, \varepsilon_{p'} > \mu} \frac{1}{\varepsilon_p - \varepsilon_{p'}} U_{i_r p} U_{i_r p'} U_{i_{r'} p'} U_{i_{r'} p} \right], \end{aligned} \quad (5.23)$$

which gives a result comparable to the on-resonance case but without Kondo couplings

$$\sum_m^{m \neq 0} \frac{1}{E_0 - E_m} P_0 H_1 P_m H_1 P_0 = P_0 \left( - \sum_{r, r'=1}^R J'_{rr'} \mathbf{S}_r \mathbf{S}_{r'} \right) P_0 \quad (5.24)$$

$$J'_{rr'} = \frac{J^2}{2} \sum_{\varepsilon_p < \mu, \varepsilon_{p'} > \mu} \frac{1}{\varepsilon_{p'} - \varepsilon_p} U_{i_r p} U_{i_r p'} U_{i_{r'} p'} U_{i_{r'} p}. \quad (5.25)$$

## 5 On-resonant models

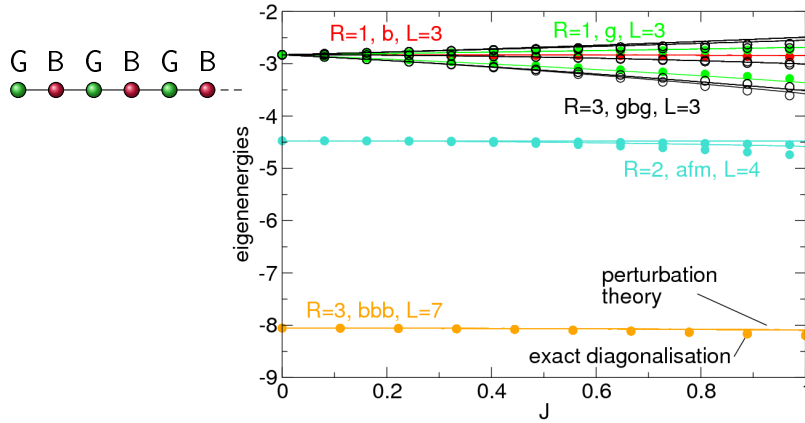


**Figure 5.2:** Eigenenergies of the effective low-energy model (solid lines, Eq. (5.26)), as functions of the local coupling  $J$ . Note that energies are shown only for states, arising from the subset of unperturbed conduction-electron states which are ground state(s) and thus separated from higher energy states by the finite-size gap  $\Delta$ . For comparison the corresponding eigenenergies of the original model for weak  $J$  are shown, as obtained from full diagonalisation (circles). Different impurity systems are considered with up to three impurities in on-resonance configurations as well as in off-resonance configurations. "g": single-impurity model with impurity at a good site (green), "b": single-impurity model with impurity at a bad site (red), "gbg": "good-bad-good" three-impurity configuration (black), "bbb": "bad-bad-bad" three-impurity configuration (orange), "afm": two-impurity model at antiferromagnetic distance  $d = 1$  (blue). The pictogram visualises the distribution of good (G) and bad sites (B) in a one-dimensional chain with open boundary conditions and an odd number of conduction electrons for sites  $i = 1, 2, 3, \dots$

## Comparison to full diagonalisation

In Fig. 5.2 the eigenenergies of several small impurity systems with up to three impurities (symbols) are compared with the eigenenergies of the corresponding low-energy effective models (lines), see Eq. (5.26). The perfect agreement for  $J \rightarrow 0$  is replaced by small deviations for intermediate  $J$ . These are mainly due to the formation of conventional Kondo singlets (i.e.  $\xi_K < L$ ), which give negative contributions  $\sim -\frac{3}{4}J$ . This is clearly not captured by the perturbation theory above where Kondo clouds (if present) are established only with the  $k_F$  electron and, thus, are of the size of the spatial extension of this state, i.e. generally  $\xi_K = L$ . Hence, the largest deviations are observed for off-resonance systems ( $R = 2$ , blue) or systems with impurities at bad sites (e.g.  $R = 1$  at a bad site, red) where Kondo clouds are absent for  $T_K < \Delta$ .

## Remarks

We want to shortly comment on the results. An on-resonance case is characterised by a finite-size system which sustains just a single conduction-electron state within  $\Delta$  to form a Kondo singlet—the  $k_F$  state. From Eq. (5.15) we can read off that the linear-in- $J$  contribution  $J_r^{(1)}$  is the leading order coupling at weak  $J$ . It depends on the weights of the  $k_F$  state at the impurity site (Sec. 2.4) and is finite in the models under consideration at odd sites  $i = 1, 3, \dots$  (Eq. (2.32)), whereas it vanishes at even sites  $i = 2, 4, \dots$  (see the pictogram in Fig. 5.2). The same scheme is found for the second-order local contribution  $J_r^{(2)}$ . However, the nonlocal RKKY couplings  $J_{rr'}$  are generally always finite. By contrast, in off-resonance cases (Eq. (5.24)) there is no electron state within  $\Delta$ , and hence only the RKKY interaction is retained. We emphasise that our results are not dependent on the dimensionality of the host system.

Our final remark picks up on the topic of a ferromagnetic  $J$ , for which our derivations are likewise valid. As known from section 2.3, a ferromagnetic Kondo effect cannot develop, because the ferromagnetic  $J_{\text{eff}}$  decreases in the course of an RG procedure. On the other hand, if  $J_{\text{eff}}$  is sufficiently small, we may apply our weak-coupling perturbation theory. This would occur at large distances  $r$ , which correspond to low cutoff energy scales in an RG treatment. Using the results above, we find that an impurity at a good site is then in a triplet state with the  $k_F$  conduction electron; what we could call a "ferromagnetic finite-size Kondo effect". Let us go back to Fig. 2.8(b) in section 2.5, where we showed spatially resolved impurity-electron spin correlation for a ferromagnetic single-impurity Kondo model. On the basis of our considerations, the large-distance regime is supposed to be governed by the finite-size Kondo effect. And indeed, we obtain ferromagnetic impurity-electron spin correlations there, which are almost constant as functions of  $r$  and decreasing for increasing  $L$ . This indicates that at these length scales the triplet is in fact made up with the  $k_F$  electron, which is homogeneously distributed among good sites, since  $U_{ik_F}^2 = \frac{2}{L+1}$  for good sites  $i$  (Eq. (2.32)).

## 5.3 The "bad-good-bad" configuration

Let us take a special representative of an on-resonant "Kondo-vs.-RKKY-exchange quantum box" and regard a model composed of three impurities coupled to adjacent sites of a chain. A naive argument based on Doniach's idea would consider the corresponding effective three-spin RKKY model with indirect antiferromagnetic couplings of the central with the adjacent spins and ferromagnetic coupling between the latter. The dominance of the RKKY exchange for weak couplings  $J$  would lead to a total impurity-spin doublet ground state, independent of the absolute magnitudes of the RKKY couplings.

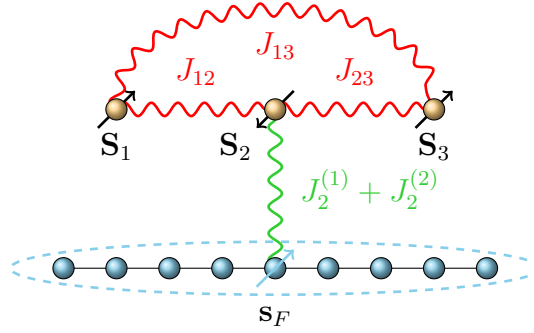


**Figure 5.3:** Effective low-energy model in the "bad-good-bad" configuration for  $\Delta > T_K$ : only the central impurity  $S_2$  is capable of forming a singlet state with the  $k_F$  conduction-electron spin  $s_F$  due to a finite  $U_{i_2 k_F} \neq 0$ . The effective local coupling of  $S_2$  to the conduction electrons has contributions both in first and second-order perturbation theory,  $J_2^{(1)} + J_2^{(2)}$ . Indirect RKKY exchange occurs in second-order perturbation theory in  $J$ , leading to antiferromagnetic couplings for adjacent impurities and ferromagnetic coupling otherwise.

However, it is in fact the Kondo effect that wins in this case: since the strong-coupling Kondo fixed point is cut off for  $J \rightarrow 0$  in a finite lattice, we find that perturbation theory is regularised and predicts that impurities couple to the conduction-electron system on a linear-in- $J$  scale (Sec. 5.2). There will be a finite weak  $J$  for which this scale is larger than the RKKY scale  $\sim J^2$  (sketched in Fig. 5.1). For couplings below this particular  $J$ , we expect the formation of a spin-singlet involving the conduction electrons. We will call this a "Kondo singlet" although  $T_K \sim J$  rather than being exponentially small. Additionally, as continuation of the Kondo cloud picture, one might think of this spin singlet as a "Kondo cloud" which spreads over the whole lattice (Sec. 2.5).

In understanding the consequences of this "finite-size Kondo effect"—as we will call this mechanism,—it is instructive to inspect the perturbative coupling of the impurity spin to the conduction-electron system. Whether or not there is this coupling depends on the weight factor  $U_{ik}$  at  $k = k_F$  which is the  $i$  component of the conduction-band one-particle energy eigenstate at  $\varepsilon_F$ :  $U_{ik_F} = \sqrt{\frac{2}{L+1}} \sin(ik_F)$ . For half-filling, where  $k_F = \frac{\pi}{2}$ , this quantity is finite at  $i = 1, 3, \dots, L-2, L$ , which we call "good" sites, opposed to "bad" sites at  $i = 2, 4, \dots, L-1$  with  $U_{ik_F} = 0$ .

In section 5.2, we derived the low-energy effective Hamiltonian up to order  $J^2$  (Eq. (5.15))

$$H_{\text{eff}} = \sum_{r=1}^R (J_r^{(1)} + J_r^{(2)}) \mathbf{S}_r \mathbf{s}_F - \sum_{r,r'=1}^R J_{rr'} \mathbf{S}_r \mathbf{S}_{r'}, \quad (5.26)$$

where  $\mathbf{s}_F$  is the spin of the delocalised  $k_F$  electron.



## 5.4 Uncovering the RKKY regime

The effective Hamiltonian inherits the symmetries of the full model such as total spin and particle conservation.  $H_{\text{eff}}$  can be verified by full diagonalisation for very small systems with  $L = 5$  and  $L = 9$  but also for larger chains with  $L = 21$  and  $L = 49$  using DMRG. The effective coupling constants depend on the weights  $U_{i_r k}$  and  $\varepsilon_k$  as follows for half-filling

$$J_r^{(1)} = J|U_{i_r k_F}|^2 \quad (5.27)$$

$$J_r^{(2)} = 2J^2|U_{i_r k_F}|^2 \sum_{p > k_F} \frac{|U_{i_r p}|^2}{\varepsilon_p - \varepsilon_{k_F}} \quad (5.28)$$

$$J_{rr'} = \frac{J^2}{2} \sum_{p \leq k_F, p' \geq k_F}^{p \neq p'} \frac{1}{\varepsilon_{p'} - \varepsilon_p} U_{i_r p} U_{i_r p'} U_{i_{r'} p'} U_{i_{r'} p}. \quad (5.29)$$

The ground-state properties now crucially depend on the position of the impurities.

In the following, we want to focus on the "bad-good-bad" configuration of the three impurities (illustrated in Fig. 5.3):  $\mathbf{S}_2$  is coupled to the good central site, and  $\mathbf{S}_1$  and  $\mathbf{S}_3$  are at the adjacent sites, which are bad sites. For small  $J$  and small  $L$  with  $T_K^{(\text{bulk})} < \Delta$ , the perturbative arguments given above apply; the Kondo scale is linear in  $J$  and  $\mathbf{S}_2$  is Kondo screened. The weaker ferromagnetic RKKY interaction then couples  $\mathbf{S}_1$  and  $\mathbf{S}_3$  to a nonlocal spin triplet. Thus we obtain a total ground-state spin  $S_{\text{gs}} = 1$ .

This is clearly reflected by several ground-state spin correlation functions (Fig. 5.4(a)): for  $L = 9$  at  $J \rightarrow 0$ , we find  $\langle \mathbf{S}_1 \mathbf{S}_3 \rangle \rightarrow \frac{1}{4}$  (red symbols), while  $\langle \mathbf{S}_1 \mathbf{S}_2 \rangle \rightarrow 0$  (blue symbols) and  $\langle \mathbf{S}_2 \mathbf{S}_3 \rangle \rightarrow 0$  by symmetry. The local correlations vanish  $\langle \mathbf{S}_1 \mathbf{s}_{i_1} \rangle \rightarrow 0$  at the bad sites (red symbols in Fig. 5.5(a)), but for the good one (green symbols)  $\langle \mathbf{S}_2 \mathbf{s}_{i_2} \rangle \rightarrow 0$  remains finite for  $J \rightarrow 0$ .

In the strong- $J$  limit  $J > J_\Delta$ , the distinction between good and bad sites becomes irrelevant, because the Kondo singlet is formed with conduction electrons in the energy range  $T_K$  measured from the Fermi energy  $\varepsilon_F$ , implying an effective averaging. Thus, all local spin correlation functions behave equally for strong  $J$ . That they tend to  $-3/4$ , indicates local Kondo-singlet formation, which is basically independent of the system size.

## 5.4 Uncovering the RKKY regime

At intermediate  $J$ , i.e.  $J_\Delta < J < J_D$ , the conventional interplay between Kondo screening and RKKY interaction is recovered and a domination of the RKKY interaction is expected. However, this crucially depends on the system size: for small systems, we rather have  $J_\Delta > J_D$ , and the intermediate- $J$  regime is skipped. This can be seen in Fig. 5.4(a) for  $L = 9$  and  $\langle \mathbf{S}_1 \mathbf{S}_2 \rangle$ , which stays close to zero in the entire  $J$

## 5 On-resonant models

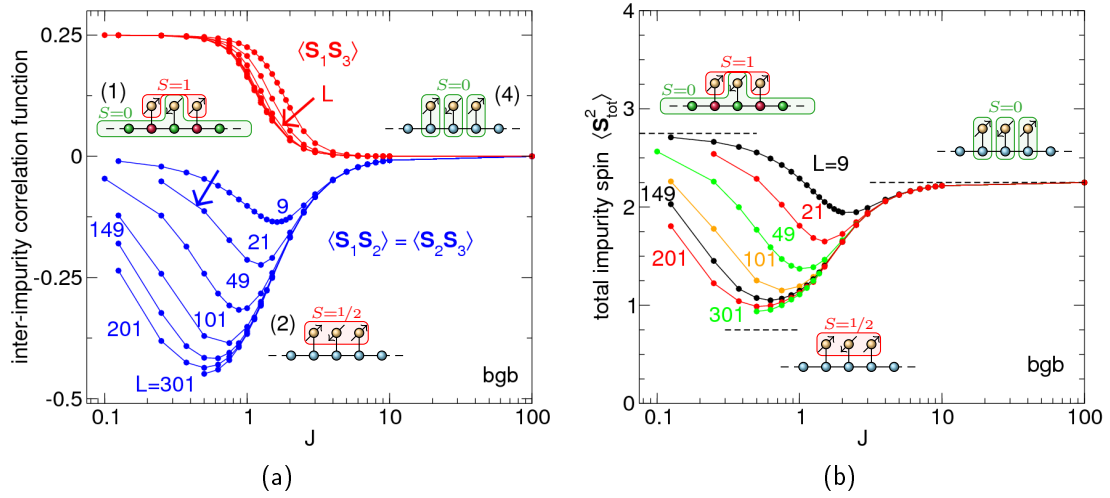


**Figure 5.4:** Left: inter-impurity spin correlations  $\langle \mathbf{S}_i \mathbf{S}_j \rangle$  showing reentrant competition between Kondo screening and RKKY coupling for the  $R = 3$  model ("bad-good-bad" as discussed in the text) with increasing system size up to  $L = 301$  sites. Note the log scale for  $J$ . With decreasing  $J$ , different regimes are found: (4) strong-coupling limit with local Kondo singlets. (3) Kondo screening dominates over RKKY interaction (shown in Fig. 5.5(a)). (2) RKKY interaction is the leading energy scale for large systems ( $J_D > J_\Delta$ ). (1) The linear Kondo scale dominates and leads to a screening of the central spin (at a good site), while in a second step RKKY exchange couples the remaining spins (at bad sites) to a nonlocal triplet. Right: respective total spin of the impurity system  $\langle \mathbf{S}_{\text{tot}}^2 \rangle = \sum_{ij} \langle \mathbf{S}_i \mathbf{S}_j \rangle$  as functions of  $J$  on a log scale. Dashed lines indicate the characteristic values in the different regimes as discussed in the text.

regime with an only shallow minimum around  $J = 1.5$ . In the strong-coupling limit the total impurity spin  $\langle \mathbf{S}_{\text{tot}}^2 \rangle = \sum_{ij} \langle \mathbf{S}_i \mathbf{S}_j \rangle$  is made up by three independent local moments  $S = 1/2$  with  $\langle \mathbf{S}_{\text{tot}}^2 \rangle = 3 \cdot \frac{3}{4}$ , while in the weak-coupling regime one determines  $\langle \mathbf{S}_{\text{tot}}^2 \rangle = 2 + \frac{3}{4}$  for the triplet of  $\mathbf{S}_1$  and  $\mathbf{S}_3$ , and  $\mathbf{S}_2$  being uncorrelated with  $\mathbf{S}_1$  and  $\mathbf{S}_3$ , see e.g. the results for  $L = 9$  in Fig. 5.4(b).

RKKY correlations among neighbouring impurity spins can develop only if the system is sufficiently large, namely if  $J_\Delta < J_D$ . In fact, for larger  $L$  the correlation function  $\langle \mathbf{S}_1 \mathbf{S}_2 \rangle \rightarrow -1/2$  in the intermediate- $J$  regime and  $\langle \mathbf{S}_1 \mathbf{S}_3 \rangle$  is close to  $1/4$ . These are the spin correlations of a three-spin system with ferromagnetic coupling between  $\mathbf{S}_1$  and  $\mathbf{S}_3$  and antiferromagnetic ones otherwise. Consequently, a more and more perfect  $S_{\text{tot}} \rightarrow \frac{1}{2}$  can develop for increasing  $L$ , confirmed by Fig. 5.4(b):  $\langle \mathbf{S}_{\text{tot}}^2 \rangle \rightarrow \frac{3}{4}$  for intermediate  $J$ , e.g. at  $J = 0.6$  for  $L = 149$ . With decreasing  $J$ , the system eventually crosses over to the perturbative finite-size Kondo regime at a  $J_\Delta$  which strongly decreases with decreasing  $L$ . From Fig. 5.4(b), one finds for example  $J_\Delta = 0.5$  for  $L = 149$ .

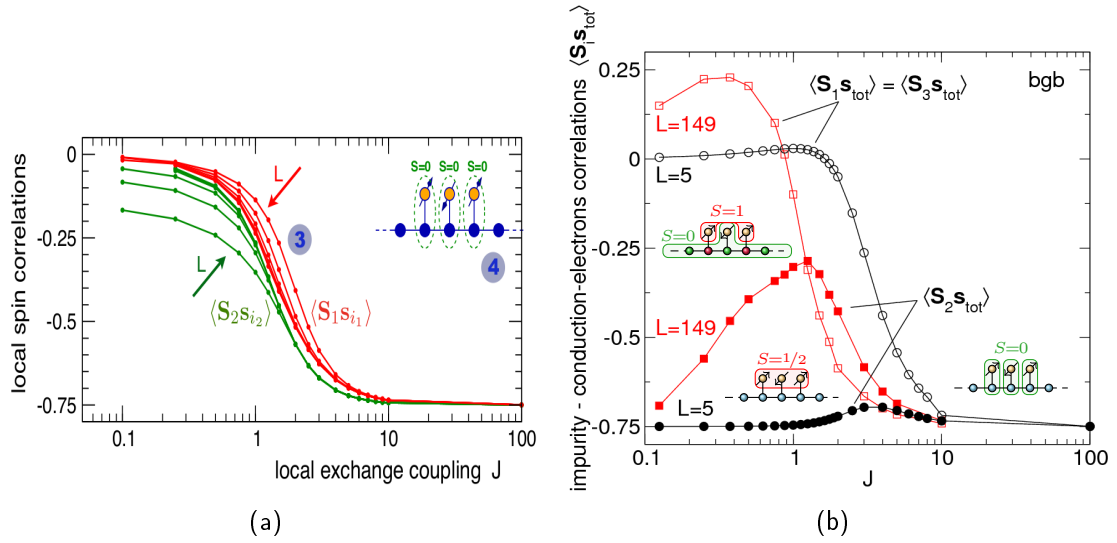


**Figure 5.5:** "Bad-good-bad" configuration as discussed in the text. Left: local spin correlations  $\langle S_r s_{i_r} \rangle$  as functions of  $J$  on a log scale. Figure taken from Ref. [21]. Right:  $\langle S_i s_{tot} \rangle$  as functions of  $J$  on a log scale. For  $L = 5$  (black circles) and  $L = 149$  (red squares). Open symbols:  $\langle S_1 s_{tot} \rangle = \langle S_3 s_{tot} \rangle$ , filled symbols:  $\langle S_2 s_{tot} \rangle$ .

Following the experiences with two-impurity models at ferromagnetic distance in section 4.7, one may speculate that the nonlocal impurity spin doublet, that is formed by the RKKY interaction in the intermediate- $J$  regime with  $\Delta < T_K^{(\text{bulk})} < |J_{\text{RKKY}}|$ , is Kondo screened in a subsequent step on a very small energy scale  $T_K^{(3\text{spins})} \ll T_K^{(\text{bulk})}$ .<sup>1</sup> A conventional Kondo effect would be obtained only if  $\Delta < T_K^{(3\text{spins})} \ll T_K^{(\text{bulk})} < |J_{\text{RKKY}}|$ , i.e. for very large systems. For intermediate  $L$  we rather expect  $T_K^{(3\text{spins})} < \Delta < T_K^{(\text{bulk})} < |J_{\text{RKKY}}|$ ; i.e. the corresponding Kondo correlations are again cut by the system size, which is responsible for the emergence of a new variant of the finite-size Kondo effect.

Can we numerically resolve the scale  $T_K^{(3\text{spins})}$ ? How does the screening of the three RKKY-correlated local moments takes place in detail?

<sup>1</sup>Remember from section 4.2 that the Kondo temperature of a two-impurity model at ferromagnetic distance is roughly of the order  $|J_{\text{RKKY}}|(T_K/|J_{\text{RKKY}}|)^{1/u_{\text{odd/even}}^2}$ , what may be estimated to be smaller than  $T_K$ . Moreover, in the presence of a symmetry between odd and even channel the Kondo temperature  $T_K^{(2\text{spins})} \sim \frac{(T_K^{(1\text{spin})})^2}{|J_{\text{RKKY}}|}$  due to  $u_{\text{odd}}^2 = u_{\text{even}}^2 = \frac{1}{2}$ . Hence  $\frac{T_K^{(2\text{spins})}}{|J_{\text{RKKY}}|} \sim \left(\frac{T_K}{|J_{\text{RKKY}}|}\right)^2 \xrightarrow{J \rightarrow 0} 0$  and  $\frac{T_K^{(2\text{spins})}}{T_K^{(1\text{spin})}} \sim \frac{T_K^{(1\text{spin})}}{|J_{\text{RKKY}}|} \xrightarrow{J \rightarrow 0} 0$  in the RKKY regime where  $T_K < |J_{\text{RKKY}}|$ .

## 5.5 The screening process

Notable insights can be obtained from analysing  $\langle \mathbf{S}_i \mathbf{s}_{\text{tot}} \rangle$  shown in Fig. 5.5(b). While for  $J \rightarrow \infty$  all local moments are equally and fully screened  $\langle \mathbf{S}_i \mathbf{s}_{\text{tot}} \rangle \rightarrow -\frac{3}{4}$ , for  $J \rightarrow 0$  only  $\mathbf{S}_2$  forms a singlet with the spin  $\mathbf{s}_F$  of the  $k_F$  electron, as it is coupled to a good site. Since  $\langle \mathbf{S}_i \mathbf{s}_{\text{tot}} \rangle \rightarrow \langle \mathbf{S}_i \mathbf{s}_F \rangle$  for  $J \rightarrow 0$  (Sec. 5.2), one finds  $\langle \mathbf{S}_2 \mathbf{s}_{\text{tot}} \rangle \rightarrow -\frac{3}{4}$  (filled circles), while  $\langle \mathbf{S}_1 \mathbf{s}_{\text{tot}} \rangle \rightarrow 0$  and  $\langle \mathbf{S}_3 \mathbf{s}_{\text{tot}} \rangle \rightarrow 0$  (open circles).

As shown above, a larger system size of, e.g.,  $L = 149$ , allows for a dominance of the RKKY interaction. We will see that this leads to two major deviations in  $\langle \mathbf{S}_i \mathbf{s}_{\text{tot}} \rangle$  as compared to those obtained for small system sizes (Fig. 5.5(b)). Unlike a system with  $L = 5$ ,  $\mathbf{S}_2$  is weaker correlated with  $\mathbf{s}_{\text{tot}}$  (filled red squares) for couplings  $J \gtrsim 2$  than its adjacent impurities (open red squares). This can be regarded as a consequence of the emerging RKKY correlations between the impurities, interfering with the (dominant) Kondo correlations of the impurities. Most easily, this circumstance is understood in the limit of the RKKY regime, as illustrated in Fig. 5.6(b): assume that the three impurities form a perfect  $S_{\text{tot}} = 1/2$ . Then the Kondo effect aligns the total conduction-electron spin  $\mathbf{s}_{\text{tot}}$  antiparallel to it, that is antiparallel to  $\mathbf{S}_1$  and  $\mathbf{S}_3$ , and parallel to  $\mathbf{S}_2$ . The tendency  $\langle \mathbf{S}_1 \mathbf{s}_{\text{tot}} \rangle < \langle \mathbf{S}_2 \mathbf{s}_{\text{tot}} \rangle$  is then continued into the Kondo regime  $J > J_D$ .

Fig. 5.5(b) also shows that  $\langle \mathbf{S}_i \mathbf{s}_{\text{tot}} \rangle$  decline in absolute magnitudes at decreasing but intermediate couplings around  $J = 1 - 3$ . This is a signature of the RKKY dominance, leading to a smaller total impurity spin  $S_{\text{tot}}$ , compare Fig. 5.4(b). We can think of the impurities partially screening themselves due to the antiferromagnetic pattern of the RKKY couplings. Thus, weaker screening by the conduction electrons is necessary.

Second, for  $J \leq 1$  the behaviour of  $\langle \mathbf{S}_i \mathbf{s}_{\text{tot}} \rangle$  is radically changed, and the roles of the impurities are reversed (Fig. 5.5(b)).  $\mathbf{S}_2$  becomes stronger antiferromagnetically correlated with the electrons when  $J$  decreases, while  $\mathbf{S}_1$  and  $\mathbf{S}_3$  exhibit strongly increasing ferromagnetic correlations with the conduction electrons. Note that in this parameter region, i.e.  $0.4 \geq J \geq 1$ , the total impurity spin doublet is still developing and  $S_{\text{tot}}$  is approaching  $\frac{1}{2}$ , see Fig. 5.4(b).

These are the characteristics of the parameter regime where the collective Kondo cloud of the RKKY-correlated impurities does not any longer match the system size, i.e.  $T_K^{(3\text{spins})} < \Delta$  ( $0.4 \geq J \geq 1$ ). To substantiate this conclusion, we can determine the residual couplings of the three RKKY-correlated impurities to the conduction electrons in analogy to the effective low-energy Hamiltonian (Eq. (5.26)), since perturbation theory in  $J$  is regularised by the finite  $\Delta$ . Keeping in mind that we are in the RKKY regime, it appears reasonable that the starting point of a suitable perturbation theory would be RKKY-correlated impurities—instead of uncorrelated impurities as in section 5.2. The contributions of their couplings with the conduction electrons are then analysed in orders of  $J$ , and we would find that the highest occupied one-particle state  $k_F$  has again a central status: only  $\mathbf{S}_2$  experiences a finite weight of the  $k_F$  state,  $U_{i_2 k_F} \neq 0$ ,

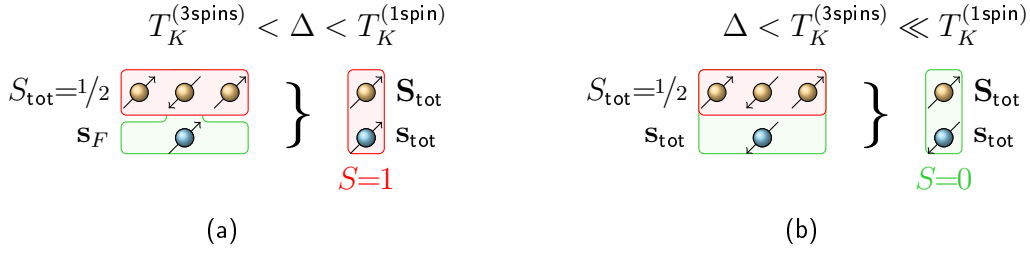


**Figure 5.6:** "Screening" of the total impurity spin in the "bad-good-bad" case within the RKKY regime.  $S_{\text{tot}} = \frac{1}{2}$  due to the antiferromagnetic RKKY couplings of adjacent impurities and ferromagnetic coupling between  $S_1$  and  $S_3$ . Left: only  $S_2$  can be screened by the  $k_F$  electron in the finite-size Kondo regime. However, RKKY correlations between  $S_2$  and its adjacent impurities are still dominant, leading to an effective ferromagnetic alignment of  $S_{\text{tot}}$  and  $s_F$ . Right: conventional screening process in which  $s_{\text{tot}}$  aligns antiferromagnetically to  $S_{\text{tot}}$ .

and hence exhibits antiferromagnetic correlations to the total conduction-electron spin  $s_{\text{tot}}$  (Fig. 5.6(a)). This is in contrast to  $J > 1$ , where  $s_{\text{tot}}$  displays an antiferromagnetic alignment to  $S_{\text{tot}}$  due to the conventional Kondo effect. Nevertheless, for  $0.4 < J < 1$ , we are in the RKKY regime and the antiferromagnetic RKKY couplings of  $S_2$  to  $S_1$  and  $S_3$  are dominant. This constellation leads to a ferromagnetic alignment of  $S_1$  and  $S_3$  to  $s_F$ , as seen in Fig. 5.5(b). At this point, it is emphasised that these ferromagnetic correlations  $\langle S_1 s_{\text{tot}} \rangle \rightarrow \frac{1}{4}$  are not due to some kind of ferromagnetic finite-size Kondo effect but a reasoned consequence of the vanishing  $U_{ik_F}$  at bad sites.

In the following, we will refer to the presented mechanism as "finite-size Kondo effect" of the RKKY-correlated impurities, based on the insight that it originates from a Kondo cloud which is cut off by the system size. This is similar as in the single-impurity finite-size Kondo effect occurring for  $\Delta > T_K^{(1\text{spin})}$ . However, we have to be cautious with the term "screening" in this regime, since  $S_{\text{gs}} \neq 0$ .

Below  $J = 0.4$ , the RKKY interaction gradually loses its dominance and the system is governed by the single-impurity finite-size Kondo effect with consequences discussed already above. Interestingly, the crossover is completed not before  $J$  becomes relatively small,  $J < 0.1$ , due to the tiny finite-size gap  $\Delta \approx 1/25$  ( $L = 149$ ). Note that for a small system of size  $L = 9$  ( $\Delta \approx 2/3$ ), this crossover occurs already at around  $J_\Delta \approx 1.5$  (Fig. 5.4(a)).

Is it also possible to estimate more accurately the crossover region between RKKY and Kondo regime? In this regard, a convenient strategy turns out to be the inspection of the total conduction-electron spin  $\langle s_{\text{tot}}^2 \rangle$ , since it (or at least parts of it) is exactly as large as necessary to screen the impurity spin. As it can be seen in Fig. 5.7(a), for a larger lattice of  $L = 149$ ,  $\langle s_{\text{tot}}^2 \rangle$  (red squares) develops an extended plateau at

## 5 On-resonant models

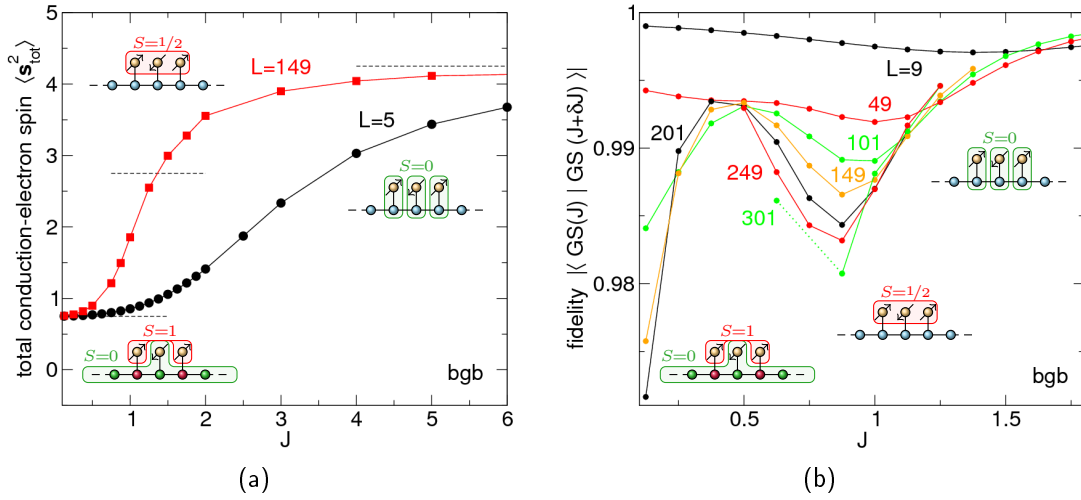


**Figure 5.7:** "Bad-good-bad" configuration as discussed in the text. Left: total conduction-electron spin  $\langle s_{\text{tot}}^2 \rangle$  as a function of  $J$ . For  $L = 5$  (black circles) and  $L = 149$  (red squares). The characteristic values in the discussed regimes are indicated as dashed horizontal lines. Right: ground-state fidelity  $F(J) = |\langle \text{GS}(J) | \text{GS}(J + \delta J) \rangle|$  for different system sizes  $L$  as indicated as functions of  $J$ , where  $\delta J = 1/8$ . For numerical convenience, the results for  $L = 249$  and  $L = 301$  are obtained in the  $M_{\text{tot}} = 1$  subspace.

$2 + 3 \cdot \frac{3}{4}$  in the strong-coupling regime (in comparison with  $L = 5$ , black circles) with three individually screened impurities.<sup>2</sup> Decreasing  $J$  leads to a smooth crossover at  $J_D \approx 1.75 - 2$ . The characteristic value in the RKKY regime, when the electrons screen an effective  $S_{\text{tot}} = \frac{1}{2}$ , is  $\langle s_{\text{tot}}^2 \rangle = 2 + \frac{3}{4}$  and is reached around  $J = 1.25 - 1.75$ . It has to be taken into account, however, that the total impurity spin is still larger than  $\frac{1}{2}$  (compare Fig. 5.4(b)). Hence, the screening has to be larger, giving rise to larger  $\langle s_{\text{tot}}^2 \rangle$  than  $2 + \frac{3}{4}$ . The corresponding intermediate plateau is supposed to stabilise and extend to smaller couplings  $J$  when  $L$  increases.<sup>3</sup> Nonetheless, it is interesting to recognise that  $J_D \approx 1.75$  is roughly in agreement with the value for the Kondo necklace model [99] which might be identified with  $J_D \approx 1.6$  (section 4.2). In line with our previous results, already for  $J \leq 1$ ,  $\langle s_{\text{tot}}^2 \rangle$  approaches  $\frac{3}{4}$  as expected from a finite-size Kondo effect either of the RKKY-correlated impurity compound or just of  $S_2$ .

<sup>2</sup>The adiabaticity of the ground state with total spin  $S_{\text{gs}} = 1$  (see section 3.5) implies the formation of a triplet somewhere in the conduction-electron system when the impurities are fully screened by the conventional Kondo effect. This is also the case for the correlated three spins in the RKKY regime as long as their collective Kondo cloud is not cut by the system size (see also Sec. 10.6).

<sup>3</sup>However, one has to keep in mind that  $T_K$  is an exponential energy scale as a function of  $J$ . That is why, meeting the condition  $\Delta = T_K$  means that for visible changes in  $J_\Delta$  we have to take exponentially increasing large system sizes  $L$ .

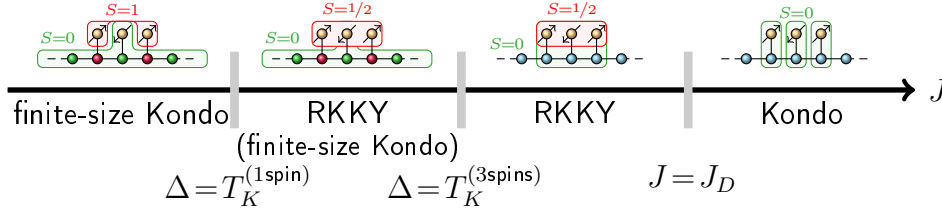


**Figure 5.8:** Full crossover scenario for the "bad-good-bad" case as a function of  $J$ . In the strong-coupling regime impurity spins are screened locally by the conduction electrons, while a decreasing  $J$  leads to growing Kondo clouds. Below  $J_D$ , the RKKY exchange is the leading energy scale, promoting antiferromagnetic order among the impurities. When further decreasing  $J$ , the perturbative regime is entered for  $T_K^{(3spins)} < \Delta$ . Hence, the Kondo effect of the three RKKY-correlated impurity spins develops a linear-scale, which is replaced by the finite-size Kondo effect of the central impurity for  $T_K^{(1spin)} < \Delta$ . Note that  $T_K^{(3spins)} < T_K^{(1spin)}$ .

Let us summarise our findings to get an impression of the manifold consequences of a finite  $\Delta$ . In this respect, an illustrative overview is provided by the ground-state fidelity  $F(J)$  (Fig. 5.7(b)). It is defined as the overlap between the ground states in the vicinity of a certain coupling  $J$ ,  $F(J) = |\langle \text{GS}(J) | \text{GS}(J + \delta J) \rangle|$ , and delivers a reliable measure for the changes in the ground-state correlations  $|\text{GS}(J)\rangle$  when varying  $J$ , especially at phase transitions and crossovers. Though the fidelity  $F(J)$  is entirely close to 1, it is still possible to identify the respective crossover regions by distinct dips, in particular the crossover to the finite-size Kondo regimes. On the one hand, for small systems, e.g.  $L = 9$ , there is just a smooth crossover between the strong-coupling regime dominated by the individual Kondo effects, and the weak-coupling regime governed by the finite-size Kondo effect. On the other hand, for larger system sizes, there is a first smooth crossover from the strong-coupling regime to the RKKY regime around  $J \approx 1.5 - 2$ . It marks the transition from separate Kondo clouds to an RKKY-correlated impurity system with total spin  $S_{\text{tot}} = \frac{1}{2}$ , again giving rise to a screening by the conduction electrons. When decreasing  $J$ , we meet the condition  $T_K^{(3spins)} < \Delta < T_K^{(\text{bulk})} < |J_{\text{RKKY}}|$ , i.e. the corresponding Kondo correlations are cut by the system size. Keeping with the previous findings, we expect to find a linear-in- $J$  3-spin Kondo scale below  $J = 1$  ( $L = 149$ ) which is visible in the dip at  $J = 0.875$ . Close to  $J = 0.4$ , we observe the crossover to the regime ruled by the finite-size Kondo effect of  $S_2$ , leading to a strong decrease of  $F(J)$  at  $J < 0.4$  ( $L = 149$ ). For increasing  $L$ , the finite-size induced crossover regions are shifted towards smaller  $J$ , in agreement with the condition  $\Delta = T_K$ .

## 5.6 Summary

While in two-impurity models there are no drastic influences due to the finite system size on the competition between Kondo effect and RKKY interaction, the most dramatic impacts are found in three-impurity models, which are on-resonant according to our conventions. Based on the effective low-energy Hamiltonian for weak  $J$ , derived from perturbation theory, we established the scheme of good and bad sites, which determines the residual couplings between an impurity and the  $k_F$  electron for  $J < J_\Delta$  ( $\Delta > T_K^{(1\text{spin})}$ ). The linear-in- $J$  Kondo scale is found to be finite at good sites and dominating RKKY couplings  $\sim J^2$  for  $J < J_\Delta$  ( $\Delta > T_K^{(1\text{spin})}$ ). This central insight allows us to understand the rich and remarkable consequences for the impurities and their correlations with each other and with conduction electrons. We observe a reentrant competition between Kondo effect and RKKY exchange, where the Kondo effect prevails for  $J \rightarrow 0$ —in contradiction to conventional expectations. While the impurities at bad sites are governed by the RKKY interaction, the Kondo effect leads to the screening of the central impurity of a "bad-good-bad" configuration (Fig. 5.8).

What happens for finite  $J$  when  $\Delta$  decreases, i.e. when the system size  $L$  increases? Clearly,  $J_\Delta$  declines, i.e. the range of applicability of our perturbation theory shrinks (Sec. 5.2). This is, however, superimposed by the RKKY interaction. On the one hand, small systems are clearly affected by strong finite-size effects, i.e.  $J_{\Delta,1\text{spin}} \gtrsim J_D$ . But even for systems with a few hundred substrate sites, a significant fraction of the standard weak-coupling physics is concealed by finite-size effects, since  $J_{\Delta,3\text{spins}} \lesssim J_D$ . This is just as in the two-impurity model at ferromagnetic distance (Sec. 4.7) where the Kondo temperature of the RKKY-correlated impurity compound may be much smaller than the single-impurity Kondo temperature. Thus, these Kondo clouds are much larger, requiring correspondingly much larger host systems for conventional screening.

Another nice example for how different the physics of finite-size systems can be, as compared to bulk systems, is the case of ferromagnetic  $J$ . Despite the nonexistence of an energy scale, comparable to  $T_K$ , for  $J < 0$ , we find triplet formation of the  $k_F$  electron and an impurity at a good site for a sufficiently small modulus of  $J$ . This could be regarded as "ferromagnetic finite-size Kondo effect" with a "cloud" of the scale of the system size.

In chapters 2 and 4, a couple of questions have been raised which could be answered in this chapter, constituting and underpinning our concept of finite-size effects. However, at the same time they raise new questions which will concern us in the next chapters: for one thing, what happens in on-resonant models with more than one impurity at good sites? In this case finite-size effects are responsible for the emergence of a special mechanism which generates correlations between impurities, which do not rely on indirect magnetic exchange.



## 6 Resonant enhancement

### 6.1 Introduction

In the previous chapter a rather special on-resonant impurity model was chosen to demonstrate the impressive impact of spatial confinement on the competition between RKKY exchange and Kondo effect. By means of the effective weak-coupling low-energy Hamiltonian, we determined the residual couplings between impurities and conduction electrons in case of  $\Delta > T_K$ , i.e. when the conventional Kondo cloud picture collapses. The residual couplings are regulated by the weights of the delocalised  $k_F$  conduction-electron state, resulting in a position-dependent (finite-size) Kondo effect in models with open boundaries.

Naively, one could ask which consequences follow for other impurity constellations? Following the aforementioned results, the most interesting case should be realised when all impurities are coupled to good sites. In this chapter, we will see that this setting results in unconventional ground states for  $\Delta > T_K$ , arising from the joint coupling of impurities to the spin  $s_F$  of the  $k_F$  electron. Such impurities are shown to display special correlations and enhanced interactions, what we refer to as "resonant enhancement". We want to work out the (in some cases) counterintuitive consequences step by step, because they manifest in several quantities in a sometimes not obvious way. Note that we concentrate, therefore, on the finite-size Kondo regime of single impurities, i.e.  $\Delta > T_K^{(1\text{spin})}$ .

Interestingly, the situation with all impurities coupled to the  $k_F$  electron could be regarded as the same occurring in multi-impurity systems in terms of Nozières' exhaustion problem [107, 108]. The dramatic consequences resulting in multi-impurity systems, explicated in chapter 13, underline the significance and urgency of the problem posed here: does the current picture of the finite-size Kondo effect and its unusual competition with the RKKY exchange remain valid in this case?

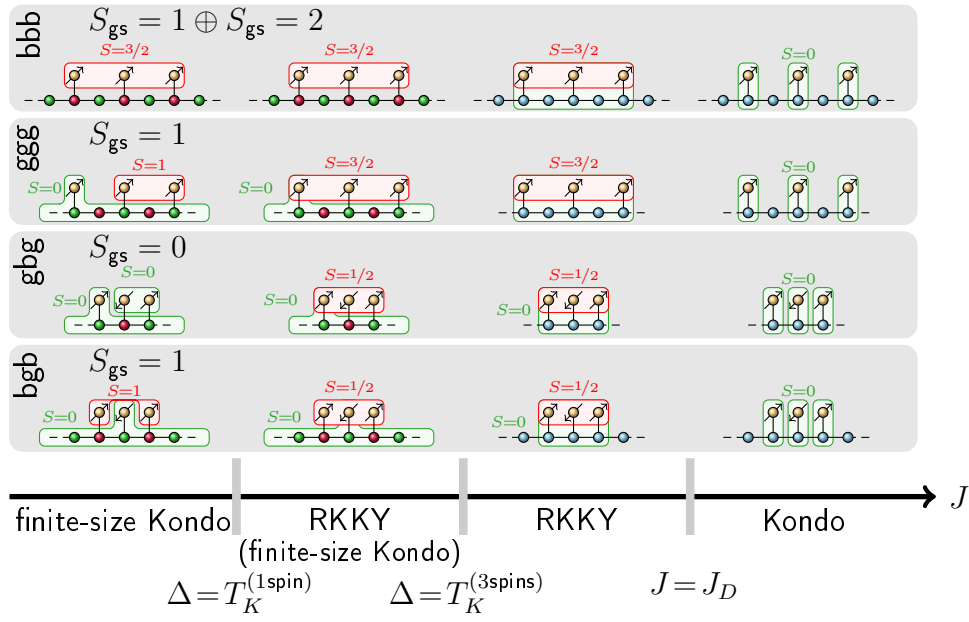


**Figure 6.1:** Complete overview of crossovers from the strong to the weak-coupling regime for the four possible configurations of three impurities according to the physical picture acquired in chapter 5 ("b": bad, "g": good). In the strong-coupling regime  $J > J_D$ , we find the dominance of the Kondo effect, which is replaced by the RKKY regime for intermediate  $J < J_D$  in larger conduction-electron systems. Depending on the distance  $d$  between next-neighbouring impurities,  $S_{tot} = 3/2$  is generated at ferromagnetic distance (even  $d$ ) and  $S_{tot} = 1/2$  at antiferromagnetic distance (odd  $d$ ). At smaller  $J$  ( $\Delta > T_K^{(3\text{spins})}$ ), the conventional Kondo correlations of the three RKKY-correlated impurities are cut off, while at even smaller  $J$  ( $\Delta > T_K^{(1\text{spin})}$ ) the system is governed by the finite-size Kondo effect of single impurities at good sites. Note that here and hereafter, in case of more than one impurity at good sites, only one combination of singlet formation with conduction electrons is shown as pictogram.

## 6.2 Apparent inconsistencies of the concept of the finite-size Kondo effect

Let us first go shortly through the remaining on-resonant three-impurity configurations for  $J \rightarrow 0$ , depicted in Fig. 6.1. Assume that  $L = 4n + 3$  with integer  $n$ ; i.e., the central site is bad: "good-bad-good". The physics of this system is thus dominated by Kondo screening of one of the two outer impurities at good sites. The remaining two impurities are subject to an antiferromagnetic coupling mediated by RKKY exchange, locking them into a spin singlet. Hence, the ground state is a Kondo singlet  $|KS_i\rangle$

## 6.2 Apparent inconsistencies of the concept of the finite-size Kondo effect

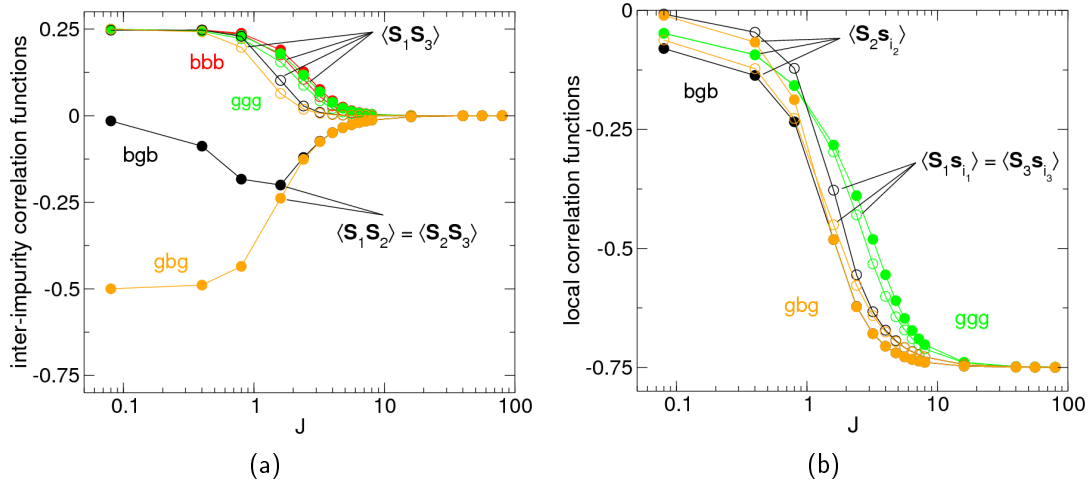


**Figure 6.2:** Left: inter-impurity correlation functions  $\langle \mathbf{S}_i \mathbf{S}_j \rangle$  as functions of the local coupling  $J$  on a log scale. Filled symbols:  $\langle \mathbf{S}_1 \mathbf{S}_2 \rangle = \langle \mathbf{S}_2 \mathbf{S}_3 \rangle$ , open symbols:  $\langle \mathbf{S}_1 \mathbf{S}_3 \rangle$ . All possible configurations of three impurities (at smallest possible distance) are considered: "bad-good-bad" (black symbols,  $L = 21$ ), "good-good-good" (green symbols,  $L = 21$ ), "bad-bad-bad" (red symbols,  $L = 19$ ), and "good-bad-good" (orange symbols,  $L = 19$ ). Right: local correlation functions  $\langle \mathbf{S}_r \mathbf{s}_{i_r} \rangle$  for the same configurations. Open symbols:  $\langle \mathbf{S}_1 \mathbf{s}_{i_1} \rangle = \langle \mathbf{S}_3 \mathbf{s}_{i_3} \rangle$ , filled symbols:  $\langle \mathbf{S}_2 \mathbf{s}_{i_2} \rangle$ . Due to the spin degeneracy in the "bad-bad-bad" case ( $S_{gs} = 1$  or  $S_{gs} = 2$ ), only the corresponding inter-impurity correlations can be shown, because they are the same in both total spin subspaces. This is not the case for  $\langle \mathbf{S}_r \mathbf{s}_{i_r} \rangle$ , which is therefore not shown.

entangled with an RKKY singlet

$$|\text{GS}\rangle = |\text{KS}_1\rangle \otimes |\text{RKKY}_{23}\rangle - |\text{RKKY}_{12}\rangle \otimes |\text{KS}_3\rangle \quad (6.1)$$

with total spin  $S_{gs} = 0$ .

Placing the three impurities at bad sites, we expect no Kondo effect. Due to the even impurity distance  $d = 2, 4, \dots$ , the RKKY interaction is ferromagnetic and leads to a total impurity spin  $S_{\text{tot}} = 3/2$ . The impurity spin does not couple to the total conduction-electron spin  $s_{\text{tot}} = 1/2$  for  $J \rightarrow 0$ . Hence, the total spin  $S_{gs} = 1$  or  $S_{gs} = 2$ ; the ground state is eightfold degenerate.

If the three impurities are on the other hand coupled only to good sites, the finite-size Kondo effect will allow one impurity spin to be screened by conduction electrons. Numerical calculations and the generalised Lieb theorem (Sec. 3.5) show that the ground state is a triplet for all finite  $J$ . But how can the three impurities be ferromagnetically correlated, when for  $\Delta > T_K$  the linear-in- $J$  Kondo scale is the leading energy scale?

In order to find a conclusive answer for this question, we have to make the role of finite-size effects transparent. Thus, we calculate the impurity spin correlations (Figs.

6.2(a) and 6.2(b)) for three-impurity models with system sizes which are relatively small ( $L \ll 150$ ) and produce an expanded finite-size regime (in terms of  $J$ ). As already known from the previous chapters, the strong-coupling regime is unaffected by finite-size effects, and so we focus on the weak-coupling regime. In line with the results of chapter 5, local spin correlations  $\langle \mathbf{S}_r \mathbf{s}_{i_r} \rangle$  of impurities  $\mathbf{S}_r$  at bad sites vanish for  $J \rightarrow 0$  and those of impurities at good sites remain finite, see Fig. 6.2(b). Furthermore, all good sites of a particular configuration show equal  $\langle \mathbf{S}_r \mathbf{s}_{i_r} \rangle$  for  $J \rightarrow 0$ , what is a result of the homogeneity of  $U_{ik_F}^2$  at half-filling:  $U_{ik_F}^2 = \frac{2}{L+1}$  at all good sites, see Eq. (2.32). Consequently, the dominating linear-in- $J$  coupling  $J_r^{(1)}$  is equal at all good sites. The convergence of local correlations for  $J \rightarrow 0$  are best seen in the "good-good-good" case in Fig. 6.2(b) (green symbols).

Let us turn to the inter-impurity correlations  $\langle \mathbf{S}_i \mathbf{S}_j \rangle$ , shown in Fig. 6.2(a). Due to the absence of the finite-size Kondo effect,  $\langle \mathbf{S}_i \mathbf{S}_j \rangle \rightarrow \frac{1}{4}$  for  $J \rightarrow 0$  in the "bad-bad-bad" configuration (red symbols), as expected for the RKKY regime. Furthermore, we are also familiar with the unconventional crossover to the finite-size Kondo regime in the "bad-good-bad" case (black symbols, see chapter 5). However, it is rather unexpected that  $\langle \mathbf{S}_1 \mathbf{S}_2 \rangle \rightarrow -\frac{1}{2}$  and  $\langle \mathbf{S}_1 \mathbf{S}_3 \rangle \rightarrow \frac{1}{4}$  in the "good-bad-good" case (filled orange circles) and  $\langle \mathbf{S}_i \mathbf{S}_j \rangle \rightarrow \frac{1}{4}$  in the "good-good-good" case (green circles) for  $J \rightarrow 0$ . These are the values which are usually attributed to the respective RKKY regimes. Surprisingly, there is no indication for the presence of the finite-size Kondo effect, even not in the "good-good-good" cases, where all impurities are involved in the finite-size Kondo effect.

In the previous section, it was shown that due to the finite-size Kondo effect an impurity at a good site has vanishing spin correlations with another one at a bad site, i.e.,  $\langle \mathbf{S}_{\text{good}} \mathbf{S}_{\text{bad}} \rangle \rightarrow 0$ . Thus, it might appear contradictory that there is no corresponding sign in  $\langle \mathbf{S}_1 \mathbf{S}_2 \rangle$  for  $J \rightarrow 0$  in the "good-bad-good" model. Instead, it rather exhibits inter-impurity correlations which are similar to the respective effective three-spin RKKY model (Sec. 5.4).

Another paradox is encountered when the RKKY couplings  $J_{rr'}$  of the effective weak-coupling Hamiltonian (Eq. (5.16)) are evaluated (shown in Fig. 6.3). For example in the "bad-bad-bad" case (red symbols) and the "bad-good-bad" case (black symbols) we can rediscover the common distance dependence of  $J_{rr'}$ , oscillating between antiferromagnetic (odd distances) and ferromagnetic (even distances) couplings, along with a decline for increasing distances. Surprisingly, for couplings only between good sites (open and filled green circles, open orange circles in Fig. 6.3) one observes a sign change at distances  $\gtrsim 4$  from ferromagnetic to antiferromagnetic ( $L \approx 49$ ). On the other hand, it is checked by DMRG calculations for a "good-good-good" model with  $L = 49$  and maximal impurity distance that there is no corresponding sign change in the inter-impurity correlation functions. Moreover, Fig. 6.3 shows that the moduli of RKKY couplings between good sites increase with increasing distance, contradicting

### 6.3 A mechanism generating ferromagnetically correlated impurities

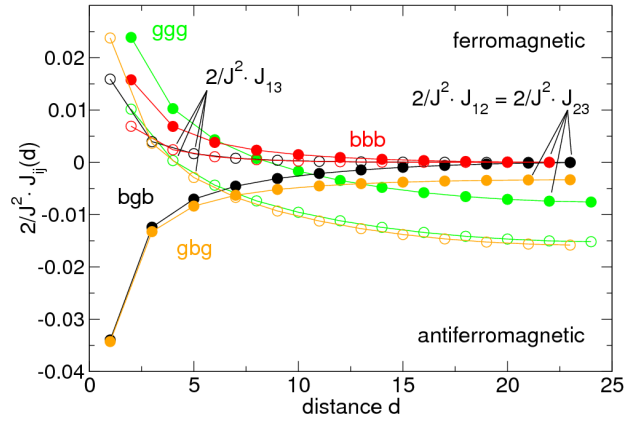


**Figure 6.3:** RKKY couplings  $\frac{2}{J^2} J_{rr'}$ , evaluated from perturbation theory (Eq. (5.29)), as functions of the distance  $d = |i_r - i_{r'}|$ . Filled symbols:  $\frac{2}{J^2} J_{12} = \frac{2}{J^2} J_{23}$ , open symbols:  $\frac{2}{J^2} J_{13}$ . For "bad-good-bad" (black symbols,  $L = 49$ ), "good-good-good" (green symbols,  $L = 49$ ), "bad-bad-bad" (red symbols,  $L = 47$ ), and "good-bad-good" configurations (orange symbols,  $L = 47$ ). Opposed to off-resonance cases and to couplings between bad sites,  $J_{rr'}$  can become antiferromagnetic for impurities at good sites, i.e. at ferromagnetic distances.

the usual RKKY distance dependence. We will have to come back to this problematic point later in this chapter (Sec. 6.4). Nevertheless, this finding again clarifies that correlations for  $J \rightarrow 0$  cannot be completely explained by RKKY dominance.

### 6.3 A mechanism generating ferromagnetically correlated impurities

The previous section leaves us behind in a contradictory situation regarding the "good-bad-good" and "good-good-good" configurations for  $J \rightarrow 0$ :  $\langle \mathbf{S}_r \mathbf{s}_{i_r} \rangle$  evidences the presence of the linear-in- $J$  Kondo scale which, however, has apparently no influence on  $\langle \mathbf{S}_i \mathbf{S}_j \rangle$ . On the other hand,  $\langle \mathbf{S}_i \mathbf{S}_j \rangle$  can be explained by the conventional RKKY distance dependence but not by the concrete RKKY couplings derived from perturbation theory in section 5.2. Coming back to the questions posed in the introduction of this chapter, we may state that a deeper understanding of our picture of finite-size effects is highly demanded to remove this controversy.

In the following, we want to explicate the reasons for the peculiar correlations of impurities at good sites. For this purpose, we restrict ourselves to a simpler system with only two impurities which are coupled to good sites  $i$  and  $j$ . The corresponding effective low-energy Hamiltonian (Eq. (5.26)) is readily diagonalised, and the normalised ground states  $|\text{GS}, M\rangle$  will be a linear combination of both possibilities to choose an impurity

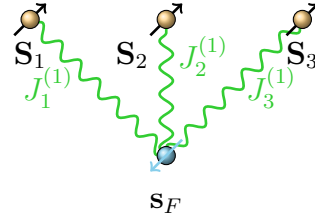


**Figure 6.4:** Effective low-energy model in the "good-good-good" case for  $\Delta > T_K$ : only the linear-in- $J$  coupling needs to be taken into account to explain the correlation functions for  $J \rightarrow 0$  (Figs. 6.2(a) and 6.6). This circumstance results in a starlike coupling geometry with a total spin  $S_{gs} = \frac{1}{2}(R-1) = 1$  ("central-spin model" [117]).

being in a singlet  $|KS_i\rangle$  with the  $k_F$  electron spin  $s_F$

$$|GS, M\rangle = \frac{1}{\sqrt{3}}(|KS_i\rangle \otimes |m_j\rangle + |m_i\rangle \otimes |KS_j\rangle). \quad (6.2)$$

$|m_i\rangle$  is the state of the unscreened impurity at site  $i$ . The total magnetisation  $M = m_i = m_j$ . Note that the structure of the ground state is completely unaffected by any RKKY interaction appearing in the effective Hamiltonian.

We are interested in the inter-impurity correlation function  $\langle \mathbf{S}_i \mathbf{S}_j \rangle$ :

$$\begin{aligned} \langle GS, M | \mathbf{S}_i \mathbf{S}_j | GS, M \rangle &= \frac{1}{3} \langle KS_i | \otimes \langle m_j | \mathbf{S}_i \mathbf{S}_j | KS_i \rangle \otimes |m_j\rangle + \frac{1}{3} \langle m_i | \otimes \langle KS_j | \mathbf{S}_i \mathbf{S}_j | m_i \rangle \otimes |KS_j\rangle \\ &+ \frac{1}{3} \langle KS_i | \otimes \langle m_j | \mathbf{S}_i \mathbf{S}_j | m_i \rangle \otimes |KS_j\rangle + \frac{1}{3} \langle m_i | \otimes \langle KS_j | \mathbf{S}_i \mathbf{S}_j | KS_i \rangle \otimes |m_j\rangle = \frac{1}{4}. \end{aligned} \quad (6.3)$$

Note that the same result would be obtained for a state in which the two impurities are in a mutual triplet state and uncoupled from  $s_F$ , resembling the situation in the RKKY regime. At half-filling, impurities at good sites are supposed to be at ferromagnetic distance in terms of the RKKY interaction due to an even distance  $d = 2, 4, \dots$ . Despite this coincidence which resolves the apparent contradictions in our concept, we already remarked that the above state, Eq. (6.2), is not influenced by RKKY exchange due to the dominant linear-in- $J$  Kondo scale. An intuitive view on this situation is rather that the impurities try to simultaneously align antiferromagnetically to  $s_F$  (although only one of them can be in a singlet with it), thereby becoming ferromagnetically correlated.

A comparable analysis becomes increasingly involved if more impurities at good sites are considered. Nonetheless, the ferromagnetic inter-impurity correlations can be confirmed by diagonalising an effective spin model with up to five impurities which are coupled only to  $s_F$  (this includes the "good-good-good" configuration, Fig. 6.4), and extracting  $\langle \mathbf{S}_i \mathbf{S}_j \rangle = \frac{1}{4}$ . The effective spin model is also known as "central-spin model" and is exactly solvable by a Bethe approach [117].

### 6.3 A mechanism generating ferromagnetically correlated impurities

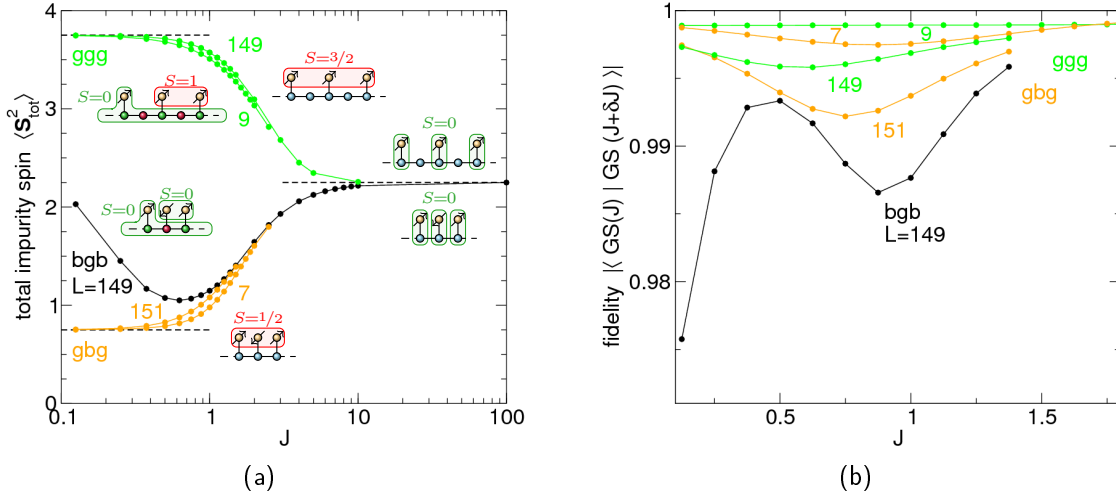


**Figure 6.5:** Results for the "good-good-good" (green symbols) and the "good-bad-good" (orange symbols) case (with smallest possible impurity distance). Different system sizes  $L$  as indicated are considered. For comparison the "bad-good-bad" results for a system size of  $L = 149$  (black symbols) are also shown. Left: total spin of the impurity system  $\langle S_{\text{tot}}^2 \rangle$  as a function of  $J$  on a log scale. Horizontal dashed lines show the characteristic values in the weak and strong-coupling regime as discussed in the text. Right: respective ground-state fidelities  $F(J) = |\langle \text{GS}(J) | \text{GS}(J + \delta J) \rangle|$  as functions of  $J$ , where  $\delta J = 1/8$ .

The total spin of the effective weak-coupling models with impurities only at good sites is numerically found to be  $S_{\text{gs}} = \frac{1}{2}(R - 1)$ , supported by the generalised Lieb theorem (Sec. 3.5). This confirms the idea that the ground state is indeed a linear combination of states, in which one impurity is screened by the  $k_F$  conduction electron and the other impurities are ferromagnetically correlated.<sup>1</sup> With this insight in mind, we can physically understand this situation as "resonant enhancement", as it originates from the special role of the  $k_F$  state and the joint coupling of impurities to it. However, we will see that the ferromagnetic inter-impurity corrections are not the only implications of it.

<sup>1</sup>Interestingly, the fact that  $S_{\text{gs}} = \frac{1}{2}(R - 1)$  gives rise to vague similarities to a spin-polaron picture, where ferromagnetically-correlated local moments are coupled to a single spin-down Bloch electron in an otherwise empty conduction band. The (under certain conditions) emerging polaron bound state is composed of the electron glued to the local moments by virtual magnon exchange [97, 61]. For our finite-size systems with impurities at good sites, the deviation of  $S = 1$  compared to a fully ferromagnetic state is spread homogeneously over the whole system; comparable to a magnon. Thus, the magnetisation of any impurity  $\langle S_i^z \rangle$  is smaller than  $\frac{1}{2}$  in the ground state with  $M_{\text{tot}} = S_{\text{gs}} = \frac{1}{2}(R - 1)$ . For example  $\langle S_i^z \rangle = \frac{5}{12}$  in the  $M_{\text{tot}} = 1$  ground state of the "good-good-good" configuration.

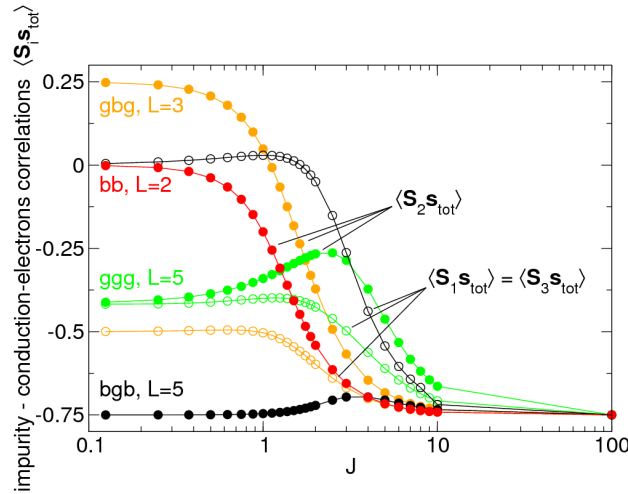


**Figure 6.6:**  $\langle S_i s_{\text{tot}} \rangle$  as functions of  $J$  on a log scale. For "bad-good-bad" (black symbols), "good-bad-good" (orange symbols), and "good-good-good" (green symbols) models with very small system sizes  $L$  as indicated. Open symbols:  $\langle S_1 s_{\text{tot}} \rangle = \langle S_3 s_{\text{tot}} \rangle$ , filled symbols:  $\langle S_2 s_{\text{tot}} \rangle$ . For comparison the two-impurity result ("bb", red) with  $L = 2$  is also shown as an example for an off-resonance case. The "bad-bad-bad" result is not shown due to the degeneracy of the ground state ( $S_{gs} = 1$  or  $S_{gs} = 2$ ).

Since the results of both the finite-size Kondo effect and the conventional RKKY theory more or less fall together, we cannot observe such pronounced dependencies of correlations (Fig. 6.5(a)) and fidelities (Fig. 6.5(b)) on the system size, as observed in the "bad-good-bad" case (black symbols, see chapter 5). The total impurity spin  $\langle S_{\text{tot}}^2 \rangle = \sum_{i,j=1}^R \langle S_i S_j \rangle$  (Fig. 6.5(a)) nicely reflect our conclusions. In the "good-good-good" case (green symbols), we obtain  $\langle S_{\text{tot}}^2 \rangle = \frac{3}{2} \frac{5}{2} = \frac{15}{4}$  for  $J \rightarrow 0$ , instead of  $\langle S_{\text{tot}}^2 \rangle = \frac{3}{4} + 2$  from a naive expectation of one screened impurity and one remaining triplet. In the "good-bad-good" case (orange symbols)  $\langle S_{\text{tot}}^2 \rangle = \frac{1}{2} \frac{3}{2} = \frac{3}{4}$ , as predicted by RKKY arguments.

For completeness, we want to analyse also the correlation function  $\langle S_i s_F \rangle$  describing the correlation of an impurity with the  $k_F$  electron in the state Eq. (6.2)

$$\begin{aligned}
 & \langle \text{GS}, M | S_i s_F | \text{GS}, M \rangle \\
 &= \frac{1}{3} \langle \text{KS}_i | \otimes \langle m_j | S_i s_F | \text{KS}_i \rangle \otimes | m_j \rangle + \frac{1}{3} \langle m_i | \otimes \langle \text{KS}_j | S_i s_F | m_i \rangle \otimes | \text{KS}_j \rangle \\
 &+ \frac{1}{3} \langle \text{KS}_i | \otimes \langle m_j | S_i s_F | m_i \rangle \otimes | \text{KS}_j \rangle + \frac{1}{3} \langle m_i | \otimes \langle \text{KS}_j | S_i s_F | \text{KS}_i \rangle \otimes | m_j \rangle = -\frac{1}{2}.
 \end{aligned} \tag{6.4}$$

While there is still an antiferromagnetic correlation, the deviation from the ideal single-impurity result  $\langle S_i s_F \rangle = -\frac{3}{4}$  comes from the joint coupling of both impurities to the  $s_F$ .



In Fig. 6.6 the correlation function  $\langle \mathbf{S}_i \mathbf{s}_{\text{tot}} \rangle$  is shown, which is supposed to coincide with the above discussed  $\langle \mathbf{S}_i \mathbf{s}_F \rangle$  for  $J \rightarrow 0$ . As shown in Eq. (6.4),  $\langle \mathbf{S}_1 \mathbf{s}_{\text{tot}} \rangle \rightarrow -\frac{1}{2}$  for  $J \rightarrow 0$  in the "good-bad-good" case (orange open circles). From an effective four-spin model (Fig. 6.4), one can also find that  $\langle \mathbf{S}_i \mathbf{s}_{\text{tot}} \rangle \rightarrow -\frac{5}{12}$  for  $J \rightarrow 0$  in the "good-good-good" case (open and filled green circles). Consequently, the more impurities are coupled to good sites, the lower is the magnitude of the respective  $\langle \mathbf{S}_i \mathbf{s}_{\text{tot}} \rangle$ .

Another interesting feature represents the correlations of  $\mathbf{S}_2$  with  $\mathbf{s}_{\text{tot}}$  in the "good-bad-good" case. While in the "bad-good-bad" case the impurities at bad sites do not show any correlations with the conduction electrons for  $J \rightarrow 0$ , in the "good-bad-good" case  $\mathbf{S}_2$  displays perfect ferromagnetic correlations  $\langle \mathbf{S}_2 \mathbf{s}_{\text{tot}} \rangle \rightarrow \frac{1}{4}$  (filled orange circles in Fig. 6.6). However, this is not caused by a ferromagnetic finite-size Kondo effect but by the RKKY interaction, which aligns  $\mathbf{S}_2$  always antiferromagnetic to the specific adjacent impurity spin which is not in a singlet-state with  $\mathbf{s}_F$ , leading to an overall ferromagnetic correlation of  $\mathbf{S}_2$  with  $\mathbf{s}_F$ .

## 6.4 Finite-size RKKY interaction

The last issue to be reconciled with our concept of finite-size effects is the strange distance dependence of the RKKY couplings between impurities at good sites, encountered in Fig. 6.3 (filled and open green circles, orange open circles), which is still missing a coherent explanation. The deviations from the standard RKKY behaviour have been listed above: the RKKY coupling exhibits an unconventional sign change from ferromagnetic to antiferromagnetic, and its modulus increases instead of decreasing for increasing distances between impurities.

The "wrong" sign is the most critical point. Were these antiferromagnetic couplings for impurities at even distances also present in the conventional RKKY regime, there would be a serious contradiction to the traditional distance dependence of the RKKY interaction  $\sim \cos(2k_F(i-j))/|i-j|$ , namely the pattern of antiferromagnetic (odd) and ferromagnetic (even) distances. In the RKKY regime, in a general consideration, signs of couplings translate (with exceptions) into signs of correlations. Then, on the level of correlations, the sign would be also in disagreement with the exact statements of the generalised Lieb theorem (section 3.5).

To figure out how to remove this discrepancy, we may let us guide by the fact that the "wrong sign" can be traced back to the contributions from the  $k_F$  state. This insight indicates that we must think of the RKKY interaction also as depend on the energy scale. The perturbative RKKY interaction in form of Eq. (5.29) is then only present in a finite-size regime in which the finite-size gap  $\Delta$  exceeds the RKKY energy scale  $\Delta > |J_{\text{RKKY}}|$ . This is akin to the finite-size Kondo regime ( $\Delta > T_K$ ) with its

## 6 Resonant enhancement

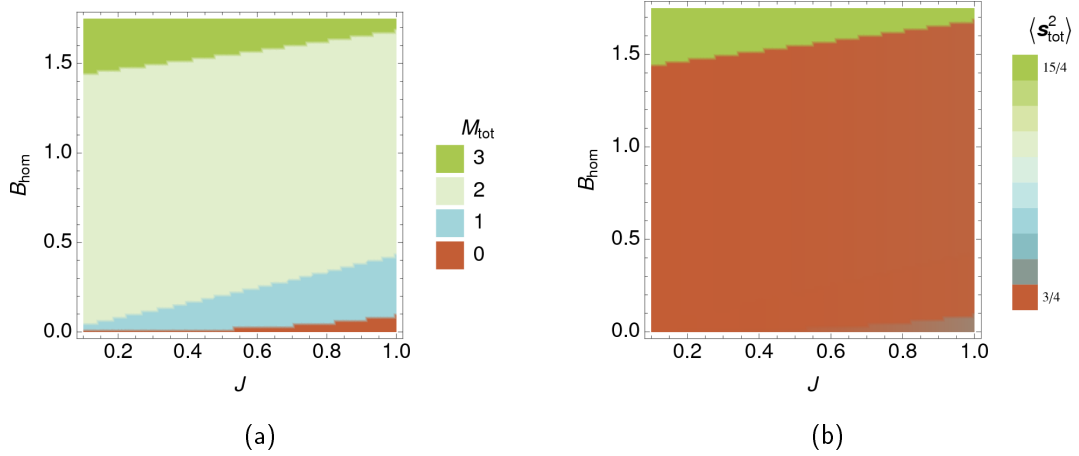


**Figure 6.7:** Ground-state correlations of a "good-bad-good" system of size  $L = 3$  for weak  $J$  in an homogeneous magnetic field  $B_{\text{hom}}$ , shown as functions of  $B_{\text{hom}}$  and  $J$ . Results have been obtained by full diagonalisation. For interpretation, see Fig. 6.8. Left: total magnetisation  $M_{\text{tot}}$ . Right: total conduction-electron spin  $\langle s_{\text{tot}}^2 \rangle$ .

special behaviour, which diverges from the conventional Kondo effect.<sup>2</sup> Thus, in the following we will refer to the RKKY interaction in form of Eq. (5.29) as "finite-size RKKY interaction". At energy scales larger than the finite-size gap, the aforementioned traditional dependence is recovered. Due to  $|J_{\text{RKKY}}| > T_K$  in the RKKY regime, the finite-size RKKY interaction can be found only within the single-impurity finite-size Kondo regime, where  $T_K < |J_{\text{RKKY}}| < \Delta$ .

Interestingly and in line with our above arguments (Sec. 6.3), RKKY couplings between impurities at good sites are irrelevant exactly in the finite-size regime; at least for the determination of correlation functions for  $J \rightarrow 0$  (they nonetheless give contributions to energy corrections). For this reason, the sign change cannot be observed by inspecting the inter-impurity correlation functions at weak  $J$ .

The enlarged RKKY interaction between impurities at good sites is another effect which only can be explained by the special conditions of the finite-size regime. It originates from the spatial dependence of the weight of the  $k_F$  conduction-electron state. At low energy scales, from the point of view of renormalisation group, small energy scales and differences can be resolved, which is especially important around the Fermi energy, where the largest contributions come from. If the distance between impurities is large and hence the conventional RKKY coupling small, then contributions in the finite-

<sup>2</sup>In contrast to the Kondo effect, where  $J_{\text{eff}} \rightarrow \infty$  at the strong-coupling fixed point, the RKKY couplings do not diverge when changing the energy scale (at least not up to second-order perturbation theory).

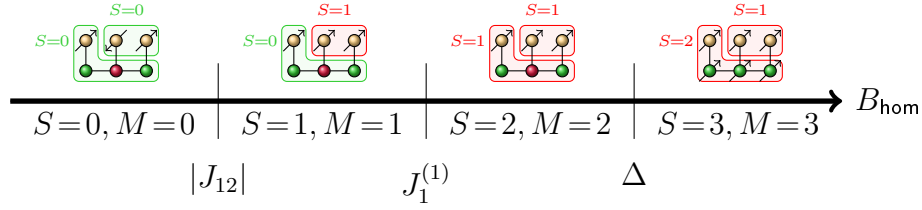


**Figure 6.8:** Visualisation of the dominant ground-state correlations of a "good-bad-good" system ( $L = 3$ ) for  $J \rightarrow 0$  in an homogeneous magnetic field  $B_{\text{hom}}$ . When  $B_{\text{hom}}$  is increased, one passes through the relevant energy scales, namely the RKKY scale  $J_{12} = J_{23}$  between impurities at good and bad sites, the linear Kondo scale  $J_1^{(1)}$ , and eventually the finite-size gap  $\Delta$ .

size RKKY couplings  $\sim U_{ik_F}$  (Eq. (5.29)) will become dominant. These special contributions benefit from two effects at good sites: a large density of states near  $\varepsilon_F$ , particularly at sites close to the chain edges, and an homogeneous distribution of weights of the  $k_F$  state  $U_{ik_F} = \pm \sqrt{\frac{2}{L+1}}$ . It is stressed that the "resonantly enhanced" RKKY couplings are likewise only present in the finite-size Kondo regime, where they have no effect on the impurity correlations.

## 6.5 Evidencing the different energy scales

Before concluding this chapter, we want to briefly demonstrate the presence of the relevant energy scales in finite-size systems in the weak-coupling regime, in particular the linear Kondo scale  $J^{(1)}$ . Additionally, this gives an idea of the typical structure of the energy spectrum in this regime and the correlations of low-energy excited states. In principle,  $J^{(1)}$  is directly obtainable from the eigenenergies of excited states as functions of  $J$  by using full diagonalisation or DMRG [68]. An alternative way, which is furthermore experimentally accessible, represent an homogeneous magnetic field applied to the system. Its coupling to the system is expressed by the additional Hamiltonian

$$H_B = -2B_{\text{hom}} \left( \sum_r S_r^z + \sum_i s_i^z \right). \quad (6.5)$$

For clarity, the  $z$  component of conduction-electron spin operators are defined as  $s_i^z = \frac{1}{2} (n_{i\uparrow} - n_{i\downarrow})$ .

Here, we consider a "good-bad-good" system of size  $L = 3$  as example. Since the ground state of this model is a singlet and all excited states have increasing  $S_{\text{gs}}$ , an increasing  $B_{\text{hom}}$  leads to subsequent level crossings of states with different total spin (Fig. 6.7(a)).

## 6 Resonant enhancement

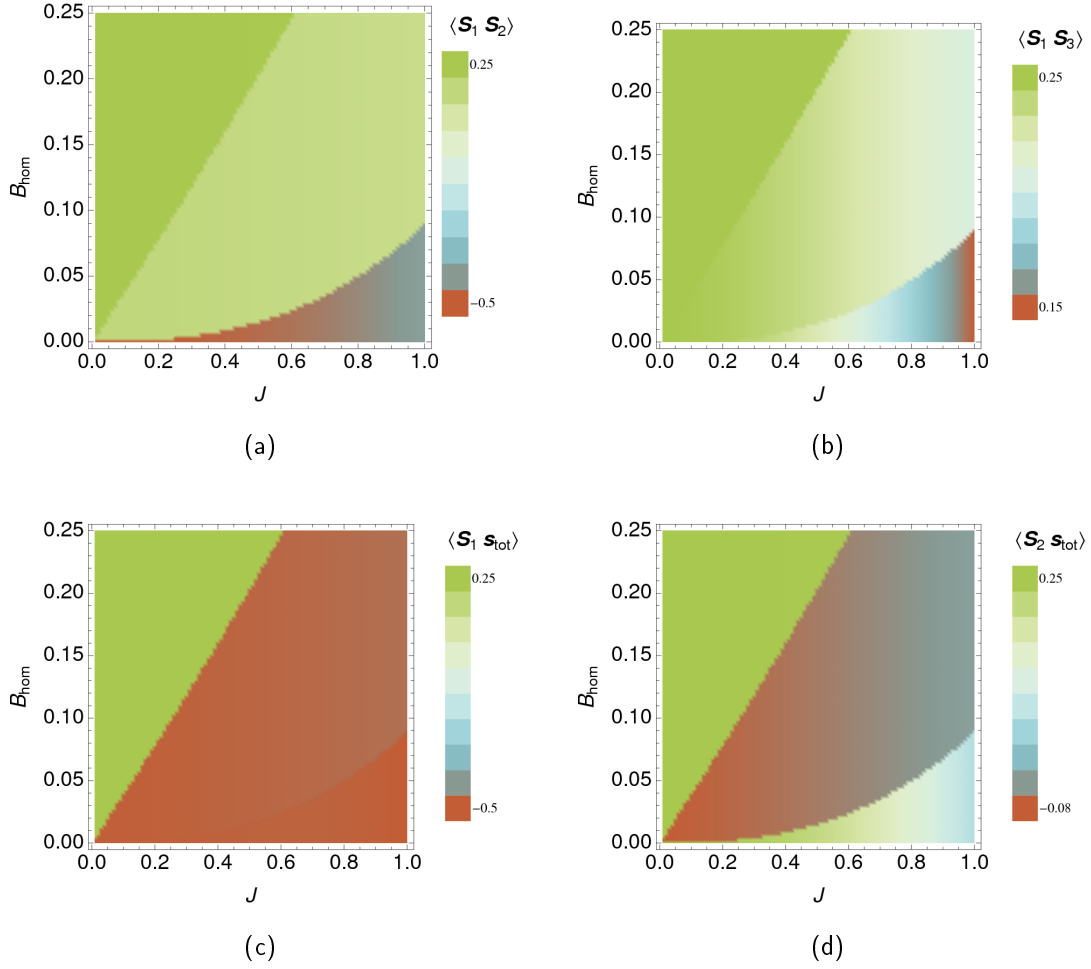


**Figure 6.9:** The same system as in Figs. 6.7(a) and 6.7(b). (a): inter-impurity correlation  $\langle \mathbf{S}_1 \mathbf{S}_2 \rangle = \langle \mathbf{S}_2 \mathbf{S}_3 \rangle$ , (b): inter-impurity correlation  $\langle \mathbf{S}_1 \mathbf{S}_3 \rangle$ , (c): impurity-electron correlations  $\langle \mathbf{S}_1 \mathbf{s}_{\text{tot}} \rangle = \langle \mathbf{S}_3 \mathbf{s}_{\text{tot}} \rangle$ , (d):  $\langle \mathbf{S}_2 \mathbf{s}_{\text{tot}} \rangle$ .

Fig. 6.8 illustrates the correlations in the different ground states which are obtained in the finite-size Kondo regime when  $B_{\text{hom}}$  increases. The smallest energy scale is the RKKY scale  $|J_{12}|$ , above which antiferromagnetic correlations between  $\mathbf{S}_2$  and its neighbouring impurities become ferromagnetic (Figs. 6.9(a) and 6.9(b)).  $|J_{12}|$  has a quadratic  $J$  dependence, as it is typical for the RKKY exchange. The next largest energy scale is the linear Kondo scale  $J_1^{(1)}$ , energetically separating states with Kondo singlets from those with "Kondo triplets" (Figs. 6.9(c) and 6.9(d)). Expectedly, the largest energy scale is the finite-size gap  $\Delta = \sqrt{2}$ . Above  $\Delta$ , the three conduction electrons become polarised (Fig. 6.7(b)), generating linear-in- $J$  scales for all impurities.

## 6.6 Summary

Although there is not such a compelling crossover, displayed in correlation functions and fidelity as functions of  $J$ , as in the "bad-good-bad" case, the investigation of models with more than one impurity at good sites proves the full validity and robustness of the picture of the finite-size Kondo effect, albeit with unexpected consequences.

If we let ourselves be guided by numerical results, e.g. for a model with three impurities at good sites, we could be convinced that the weak-coupling regime was governed by RKKY exchange—in contradiction to the picture developed in chapter 5 which claims the dominance of the finite-size Kondo effect. However, the resemblance to the RKKY regime is indeed just a coincidence, and the results can be conclusively reconciled with the finite-size Kondo regime at weak  $J$ . In fact, in chapter 12, we will show that away from half-filling the same mechanism is responsible for a magnetic "phase transition" at weak couplings  $J$ .

We termed the physical background of this regime "resonant enhancement": due to the fact that all impurities couple to the same  $k_F$  conduction-electron state, we obtain a special form of the finite-size Kondo effect where these impurities exhibit ferromagnetic inter-impurity correlations for  $\Delta > T_K$ . Furthermore, it is discussed that the finite-size picture includes a finite-size variant of the RKKY interaction, Eq. (5.29), which may exhibit a completely different distance dependence for impurities at good sites, as compared to the conventional RKKY couplings. This reflects again the joint coupling of these impurities to the  $k_F$  electron and leads to enhanced RKKY couplings which may show a sign change. Chapter 8 will demonstrate that "resonant enhancement" survives if the electron system is coupled to the environment.

In addition, it is discussed that the ground-state degeneracy at  $J = 0$  regarding the total impurity spin  $S_{\text{tot}}$  is lifted for impurities at bad sites in second-order perturbation theory in  $J$  by RKKY exchange. The same happens for impurities at good sites already in first order in  $J$ . Despite the strong similarities to the inter-impurity correlations in the RKKY regime, the mechanism goes back to the finite-size Kondo effect. This provides a novel mechanism to generate ferromagnetic correlations among impurities already linear in  $J$ , which do not rely on ferromagnetic indirect exchange  $\sim J^2$  and even dominate it for  $J \rightarrow 0$ .



## 7 Periodic chains

In the following chapter, we turn our attention to impurity models with a periodic conduction-electron system. Our intention is twofold: on the one hand, we have realised that system boundaries play a decisive role by inducing Friedel oscillations, which result in spatially varying finite-size effects. In this regard, it is generally interesting how these effects react to changes of the boundary conditions.

The second motivation comes from chapter 6, where we increased the number of impurities which couple jointly to the  $k_F$  electron. In consequence, we obtained a quite unexpected behaviour of impurity correlation functions. Here we want to pursue another strategy: instead of increasing the number of impurities, we increase the number of  $k_F$  electrons which are accessible for screening ("screening channels", see also Sec. 9.2). Namely, a periodic one-dimensional non-interacting conduction-electron system usually has got two Fermi levels which potentially establish a two-channel situation in the weak-coupling regime. This circumstance may lead to hitherto unknown effects, e.g. the simultaneous screening of two impurities for  $J \rightarrow 0$ .

Our focus is on the modifications of the weak-coupling regime  $\Delta > T_K^{(1\text{spin})}$ , as the strong-coupling regime is not expected to encounter any drastic changes regarding the impurity screening. However, we remark that an intermediate RKKY regime may appear for larger system sizes and  $J < J_D$ , in which two separate screening channels possibly become accessible. This is in contrast to the usual situation for open boundaries. The complete screening of the total impurity spin  $S_{\text{tot}} = 1$  for example should be possible for a two-impurity model at ferromagnetic distance [46] (Sec. 4.2).

In this chapter, we will primarily take small system sizes  $L < 10$  to achieve a largely extended finite-size Kondo regime. But also for another reason: While exact diagonalisation methods can easily manage the switching to periodic boundary conditions, for standard real-space DMRG they come along with long-range hopping from one chain edge to the other one. This directly introduces long-range entanglement, which is a severe obstacle for the application of DMRG to systems even with moderate system sizes. Nonetheless, there are extensions to genuine momentum-space formulations of DMRG [75] as well as work-arounds with convenient arrangements of interactions. However, R-DMFT results [112] will be also employed, as it easily allows us to investigate systems of larger size.

The discrete energy levels of a non-interacting periodic conduction-electron system of

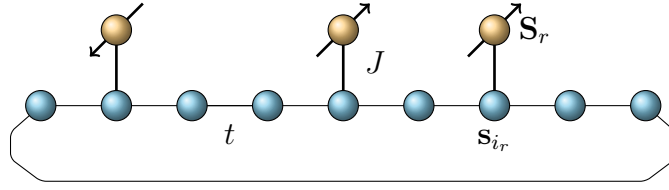


**Figure 7.1:** Impurity model discussed in chapter 7. The impurities are coupled to the conduction electrons as in the preceding chapters, but here the conduction-electron system is periodic, providing in most cases two Fermi levels. Two electrons at the Fermi energy can act as separate screening channels in the weak-coupling regime.

even size  $L$  are given by

$$\varepsilon_k = -2t \cos(k) \quad (7.1)$$

$$\exp(ikL) \stackrel{!}{=} 1 \rightarrow k_n L = 2\pi n \quad (7.2)$$

$$n = -L/2 + 1, \dots, -1, 0, 1, \dots, L/2 \quad (7.3)$$

$$U_{jk} = \frac{1}{\sqrt{L}} \exp(ikj). \quad (7.4)$$

In a periodic conduction-electron system, either the system is off-resonant or all sites are good due to the translational invariance, what is reflected by weights of a certain one-particle level  $k$ , which are equal for all sites  $i$

$$|U_{ik}|^2 = \frac{1}{L} \quad \forall i. \quad (7.5)$$

In Figs. 7.2(a) and 7.2(b), one can recognize that energy levels are generally twofold degenerate (aside from the usual spin degeneracy) except at the band edges. On-resonance situations occur when one, two (Fig. 7.2(a)), or three electrons occupy the one-particle states at  $\varepsilon_F$ . On the other hand, in an off-resonance case as depicted in Fig. 7.2(b), the chemical potential  $\mu$  falls in the finite-size gap between fully occupied levels and empty levels.

For the following discussion, it will be convenient to exploit the degeneracy of the levels  $k$  and  $-k$  and to transform the weights  $U_{ik}$  within the degenerate subspace to a basis with real coefficients

$$U_{jk,1} = \frac{1}{2}(U_{jk} + U_{j-k}) = \frac{1}{\sqrt{L}} \cos(kj) \quad (7.6)$$

$$U_{jk,2} = \frac{1}{2i}(U_{jk} - U_{j-k}) = \frac{1}{\sqrt{L}} \sin(kj). \quad (7.7)$$

These expressions are quite similar to the definitions of odd and even channels introduced in section 4.2. Here, even and odd parity is defined with respect to the site  $i$ ; channel 1 may then be identified with the even channel and channel 2 with the odd channel.



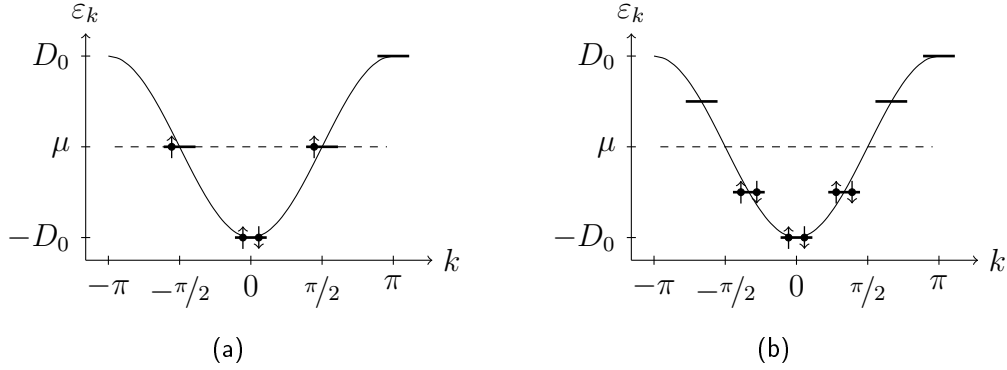


**Figure 7.2:** Energy levels  $\varepsilon_k$  of the non-interacting one-dimensional conduction-electron system with periodic boundary conditions ( $J = 0$ ) as functions of the momentum  $k$ . Note the twofold degeneracy of nearly all levels (aside from the usual twofold spin degeneracy). Solid lines: the electronic dispersion for  $L \rightarrow \infty$ .  $\pm D_0$  denote the band edges. Left: "on-resonance" case ( $L = 4$ ): if  $L = 4m$ , two electrons reside at the Fermi energy, leading to a sixfold ground-state degeneracy. They can be either in a non-magnetic configuration if one Fermi level is doubly occupied and the other one is empty. Alternatively, they can be in a magnetic configuration (as shown in the left figure), in which both levels are singly occupied. Right: for  $L = 4m + 2$  we obtain an "off-resonance" case (here  $L = 6$ ), i.e. the chemical potential  $\mu$  lies within the finite-size gap between doubly occupied and empty levels.

## 7.1 Off-resonant models

Recalling the results of chapter 4, it is clear right from the start that in off-resonance situations (Fig. 7.2(b)), i.e.  $L = 4m + 2 = 2, 6, 10, \dots$ , we expect no finite-size Kondo effect and instead an RKKY regime when  $J < J_\Delta$ . This conclusion can be confirmed by the results of two-impurity models with  $L = 6$  (Figs. 7.3(a) and 7.3(b)), where, for  $J \rightarrow 0$ ,  $\langle \mathbf{S}_i \mathbf{S}_{\text{tot}} \rangle \rightarrow 0$ , and  $\langle \mathbf{S}_1 \mathbf{S}_2 \rangle \rightarrow \frac{1}{4}$  for ferromagnetic distance (red circles) and  $\langle \mathbf{S}_1 \mathbf{S}_2 \rangle \rightarrow -\frac{3}{4}$  for antiferromagnetic distance (green circles). Also the ground-state spin can be derived from RKKY arguments alone, i.e.  $S = 0$  for antiferromagnetic distance and  $S = 1$  for ferromagnetic distance, see Tab. 7.1.

Similar conclusions have been drawn by I. Titvinidze et al in Ref. [112] where a periodic two-impurity Anderson model at antiferromagnetic distance and of size  $L = 50$  is studied by R-DMFT (Figs. 7.4(a) and 7.4(b)). As it is characteristic for the RKKY regime, the nonlocal susceptibility  $|\chi_{2,1}|$  of both impurities for small  $V^2/U = 0.25$  (green symbols in Fig. 7.4(a)) turns out to be large compared to the corresponding values for  $V^2/U \geq 0.5$  [112]. It can even be shown that  $\chi_{1,1} + \chi_{2,1} \approx 0$  approximately holds at  $V^2/U = 0.25$  (green symbols in Fig. 7.4(a)), what is a clear signature of the RKKY regime or at least of its proximity (Sec. 4.4). Consequently,  $|\chi_{2,1}|$  increases

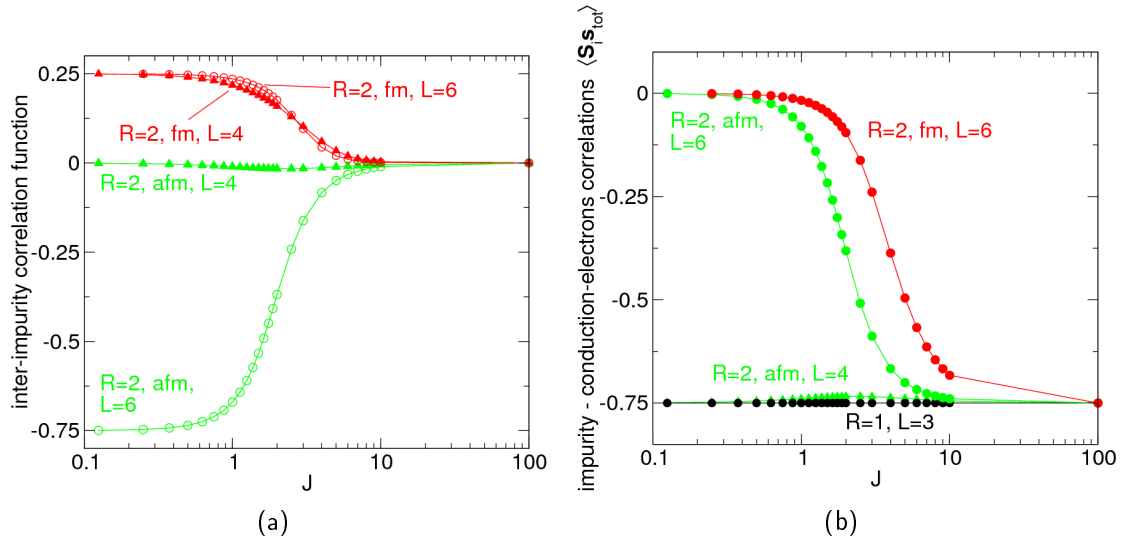


**Figure 7.3:** Impurity correlation functions for impurity models with periodic conduction-electron system as functions of the local coupling  $J$  on a log scale. For the single-impurity model  $R = 1$  ( $L = 3$ , black symbols) and two-impurity models ( $R = 2$ ) at antiferromagnetic distance  $d = 1$  ("afm", green symbols) and ferromagnetic distance  $d = 2$  ("fm", red symbols). Triangles:  $L = 4$ , circles:  $L = 6$ . Left: inter-impurity correlations  $\langle \mathbf{S}_i \mathbf{S}_j \rangle$ . Right: impurity-electron correlations  $\langle \mathbf{S}_i \mathbf{s}_{\text{tot}} \rangle$ . The two-impurity result with  $d = 2$  and  $L = 4$  is not shown due to the degeneracy of the ground state ( $S_{gs} = 0$  or  $S_{gs} = 1$ ) as discussed in the text.

with distance  $d$  between the impurities for  $V^2/U \leq 0.3$  (Figs. 7.4(a) and 7.4(b) for  $L = 50$ ), again corroborating the RKKY picture (Sec. 4.5).

## 7.2 On-resonant models

We do not intent to go into detail with the analytical treatment of on-resonance cases, especially because for a full picture we had to workout the perturbation theory in  $J$  up to second order in these two-Fermi-level systems. Our aim is rather to understand how the linear-in- $J$  coupling, which is the leading energy scale in on-resonant models at weak coupling strengths, lifts the degeneracy present for  $J = 0$ . To this end, we take a closer (yet more schematical) look on the first order of perturbation theory.

Let  $P_0$  be the projector to the ground-state subspace, and  $\mu$  denote the degrees of freedom of the non-interacting conduction-electron system (for details of notations see Sec. 5.2). The perturbation stems from  $H_1 = J \sum_{r=1}^R \mathbf{s}_{i_r} \cdot \mathbf{S}_r$ . Then the first-order

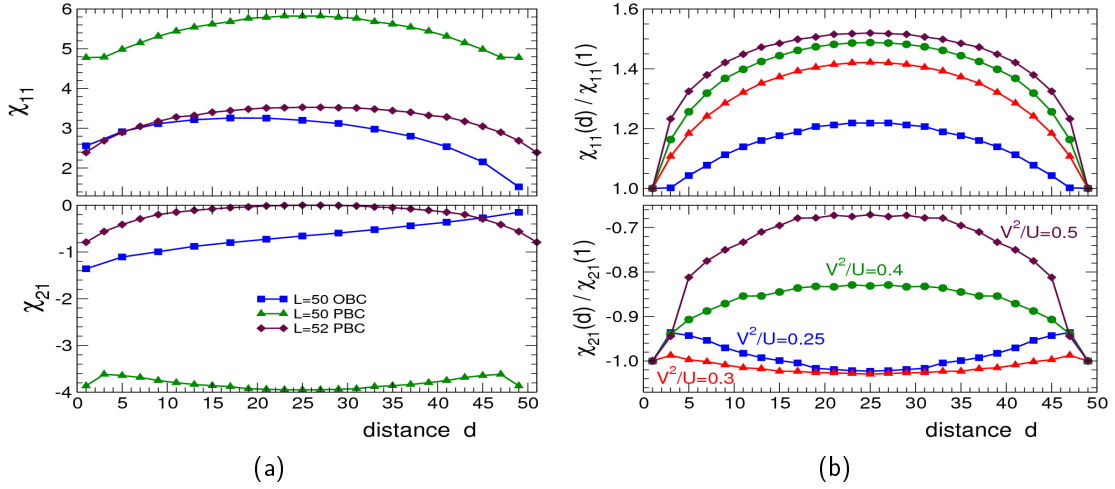


**Figure 7.4:** Local and nonlocal impurity susceptibilities  $\chi_{1,1}$  and  $\chi_{2,1}$  as functions of the distance  $d$  between adatoms for a TIAM at  $U = 8$ . Results have been obtained from  $R$ -DMFT. Left:  $L = 50$  and  $L = 52$  for periodic and for open boundary conditions.  $\frac{V^2}{U} = 0.25$ . Right: results for periodic boundary conditions, system size  $L = 50$ , and different  $\frac{V^2}{U}$  as indicated. Note that the susceptibilities are rescaled with their value for  $d = 1$ . Figures taken from Ref. [112].

contribution of degenerate perturbation theory [116] gives

$$P_0 H_1 P_0 = J \sum_{r=1}^R \sum_{\mu, \mu'} \sum_{\substack{\mu_1, \dots, \mu_R \\ \mu'_1, \dots, \mu'_R}} |\mu; \mu_1, \dots, \mu_R| \langle \mu; \mu_1, \dots, \mu_R | \mathbf{s}_{i_r} \mathbf{S}_r | \mu'; \mu'_1, \dots, \mu'_R \rangle \langle \mu'; \mu'_1, \dots, \mu'_R |, \quad (7.8)$$

where  $\mu_r = \pm \frac{1}{2}$  are the magnetic degrees of freedom of the impurities.

Similar to the treatment in section 5.2, expressions with  $|k| < k_F$  do not contribute, since these one-particle energy levels are fully occupied and  $\sum_{\sigma\sigma'} \sigma_{\sigma\sigma'} \delta_{\sigma\sigma'} = 0$ . So we can restrict ourselves to the computation of matrix elements for  $|k| = k_F$

$$\begin{aligned} \langle \mu; \mu_1, \dots, \mu_R | \mathbf{s}_{i_r} \mathbf{S}_r | \mu'; \mu'_1, \dots, \mu'_R \rangle &= \sum_{\mu, \mu'} \sum_{\sigma\sigma'} \sum_{\alpha, \alpha'=1,2} U_{i_r k_F, \alpha} U_{i_r k_F, \alpha'} \frac{1}{2} \sigma_{\sigma\sigma'} \quad (7.9) \\ &\times \langle \mu | c_{k_F, \alpha, \sigma}^\dagger c_{k_F, \alpha', \sigma'} | \mu' \rangle \delta_{\mu_1 \mu'_1} \dots \langle \mu_r | \mathbf{S}_r | \mu'_r \rangle \dots \delta_{\mu_R \mu'_R}, \end{aligned}$$

where  $c_{k_F, \alpha, \sigma}^\dagger$  creates an electron at the  $\alpha$ -th Fermi level with spin  $\sigma$ .

We do not want to calculate the matrix element  $\langle \mu | c_{k_F, \alpha, \sigma}^\dagger c_{k_F, \alpha', \sigma'} | \mu' \rangle$  but assume that in general it gives a certain non-vanishing value. Namely, more important are the products of weights of  $k_F$  states  $U_{i_r k_F, \alpha}^2$  and  $U_{i_r k_F, 1} U_{i_r k_F, 2}$ , respectively, since they directly govern whether or not impurities couple in linear order in  $J$  to electrons at  $\varepsilon_{k_F}$ .

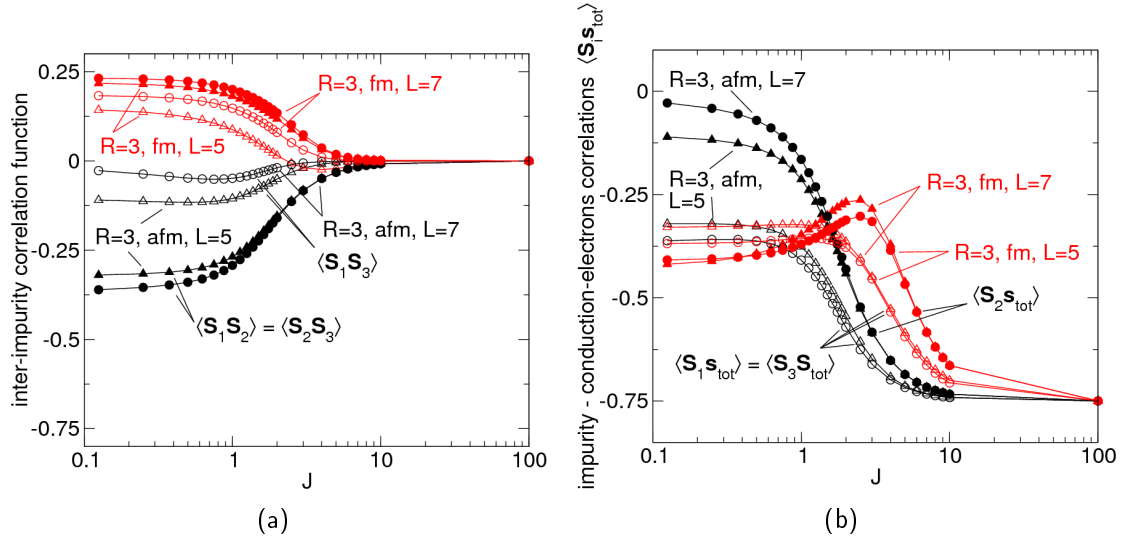


**Figure 7.5:** Impurity correlation functions for models with periodic boundary conditions as functions of  $J$  on a log scale. For three-impurity models  $R = 3$  where next-neighbouring impurities are positioned at antiferromagnetic distance  $d = 1$  ("afm", black symbols) and ferromagnetic distance  $d = 2$  ("fm", red symbols). Triangles:  $L = 5$ , circles:  $L = 7$ . Left: inter-impurity correlations  $\langle \mathbf{S}_i \mathbf{S}_j \rangle$ . Filled symbols:  $\langle \mathbf{S}_1 \mathbf{S}_2 \rangle = \langle \mathbf{S}_2 \mathbf{S}_3 \rangle$ , open symbols:  $\langle \mathbf{S}_1 \mathbf{S}_3 \rangle$ . Right: impurity-electron correlations  $\langle \mathbf{S}_i \mathbf{s}_{\text{tot}} \rangle$ . Open symbols:  $\langle \mathbf{S}_1 \mathbf{s}_{\text{tot}} \rangle = \langle \mathbf{S}_3 \mathbf{s}_{\text{tot}} \rangle$ , filled symbols:  $\langle \mathbf{S}_2 \mathbf{s}_{\text{tot}} \rangle$ .

## One-channel situations

Given one or three electrons occupying the levels at  $\varepsilon_{k_F}$ , then in general only one electron is effectively provided for screening when  $J \rightarrow 0$ . Already  $U_{i_r, k_F, \alpha}^2 \neq 0$  is sufficient that all impurities couple to this electron. Thus, for the single-impurity model (black symbols in Fig. 7.3(b)) and the three-impurity models ( $R = 3$ , Fig. 7.5(b)),  $\langle \mathbf{S}_i \mathbf{s}_{\text{tot}} \rangle \neq 0$  for  $J \rightarrow 0$ .

A surprising observation is that the weak-coupling inter-impurity correlations (Fig. 7.5(a)) behave qualitatively similar to those in the RKKY regime. From chapter 6 we know that if impurities jointly couple to one  $k_F$  electron, they exhibit ferromagnetic correlations  $\langle \mathbf{S}_i \mathbf{S}_j \rangle > 0$ . Here, however, such correlations are only found for  $R = 3$  models where next-neighbouring impurities are at ferromagnetic distance (red symbols in Fig. 7.5(a)). Conversely, antiferromagnetic inter-impurity correlations  $\langle \mathbf{S}_r \mathbf{S}_{r'} \rangle < 0$  emerge at weak  $J$  for all  $(r, r')$  pairs with odd  $|i_r - i_{r'}|$  (black symbols in Fig. 7.5(a)). This behaviour is also reflected by the ground-state spin as  $S_{\text{gs}} = 1$  in the first case and  $S_{\text{gs}} = 0$  in the latter case (Tab. 7.1). Our observation makes aware that a complete perturbative treatment is necessary to fully understand the correlation functions for  $J \rightarrow 0$ .

	$S_{\text{gs}}(L_1)$	$S_{\text{gs}}(L_2)$
$R = 1, L_1 = 3, L_2 = 5$	0	0
$R = 2, d = 1$ (antiferromagnetic), $L_1 = 4, L_2 = 6$	0	0
$R = 2, d = 2$ (ferromagnetic), $L_1 = 4, L_2 = 6$	$0 \oplus 1$	1
$R = 3, d = 1$ (antiferromagnetic), $L_1 = 5, L_2 = 7$	0	0
$R = 3, d = 2$ (ferromagnetic), $L_1 = 5, L_2 = 7$	1	1

**Table 7.1:** Total spin  $S_{\text{gs}}$  of the ground state(s) of several impurity models with periodic conduction-electron system for different system sizes  $L$ .  $d$  is the distance between next-neighbouring impurities. Results have been obtained by full diagonalisation.

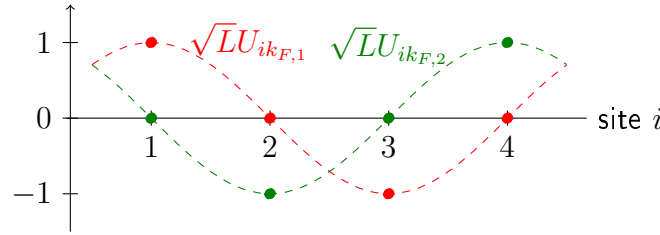


**Figure 7.6:** Site dependent weights  $U_{ik_F,1}$  and  $U_{ik_F,2}$  of the two linearly independent  $k_F$  states of the periodic non-interacting conduction-electron system with size  $L = 4$ . The dashed lines indicate the underlying functions, Eqs. (7.6) and (7.7).

## Two-channel situations

Nevertheless, strict statements are possible: a genuine two-channel situation can be found when two electrons reside at the Fermi levels, i.e.  $L = 4m = 4, 8, \dots$ . The ground-state degeneracy of the conduction-electron system at  $J = 0$  is sixfold: there are two non-magnetic configurations, in which two electrons occupy one Fermi level and the other one is empty. Conversely, when each Fermi level is singly occupied, magnetic states such as singlet and triplet states are possible (Fig. 7.2(a)). These will be of importance for us in the following.

One finds that  $U_{i_r k_F,1} U_{i_r k_F,2}$ , determining the strength of transitions of an electron from one Fermi level to another, always vanish (Fig. 7.6). Thus, the set of  $k_F$  states can simply be divided in two independent subsets with respect to the impurity couplings ("screening channels"). On the other hand,  $U_{i_r k_F, \alpha}^2 \neq 0$  but only for one of the two  $k_F$  states at a particular site  $i_r$ . Consequently, each impurity couples in linear order in  $J$  to only one of the two possible subsets of  $k_F$  states.

In the case of two impurities at ferromagnetic distance  $d = 2$ , depicted in Fig. 7.7(a), both impurities are only able to couple to the same  $k_F$  state for  $\Delta > T_K$ . This is known to lead to ferromagnetic correlations among them and antiferromagnetic correlations to the  $k_F$  electron (chapter 6), which is supported by Fig. 7.3(a) ( $L = 4$ ):  $\langle \mathbf{S}_1 \mathbf{S}_2 \rangle \rightarrow \frac{1}{4}$

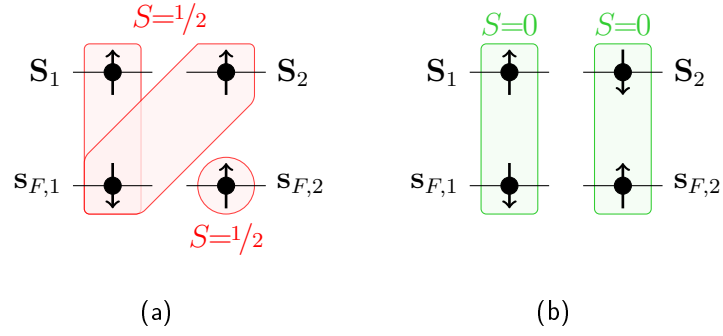


**Figure 7.7:** Effective weak-coupling low-energy models of periodic on-resonant two-impurity models with two electrons at the Fermi energy. Contributions are obtained when these two electrons are in a magnetic configuration (Fig. 7.2(a)).  $s_{F,1}$  and  $s_{F,2}$  denote the respective spins at Fermi level 1 and 2. Left: impurities at ferromagnetic distance. Both impurities experience the finite weights of the same  $k_F$  state. Right: impurities at antiferromagnetic distance. Both impurities couple to separate  $k_F$  states.

(red triangles) when  $J \rightarrow 0$ . Since the electron at the other Fermi level is left effectively uncoupled, one obtains a spin-degenerate ground-state manifold, spanned by states with  $S_{\text{gs}} = 0$  and  $S_{\text{gs}} = 1$ , compare Tab. 7.1.

A complete screening of both impurities using both screening channels is, however, possible if they are at antiferromagnetic distance, e.g.  $d = 1$  and  $L = 4$  (Fig. 7.7(b)). Then each impurity couples separately to a different subset of  $k_F$  states, leading to perfect screening of both impurities  $\langle \mathbf{S}_i \mathbf{S}_{\text{tot}} \rangle \rightarrow -\frac{3}{4}$  and vanishing inter-impurity correlations  $\langle \mathbf{S}_1 \mathbf{S}_2 \rangle \rightarrow 0$  for  $J \rightarrow 0$  (green triangles in Figs. 7.3(a) and 7.3(b)). This circumstance results in a total ground-state spin  $S_{\text{gs}} = 0$  (Tab. 7.1).

In Ref. [112] (Fig. 7.4(a)), a similar on-resonance situation with a periodic conduction-electron system of size  $L = 52$  is analysed using a TIAM at antiferromagnetic distance. For  $V^2/U = 0.25$ , a smaller nonlocal susceptibility  $|\chi_{2,1}|$  (maroon symbols) is found than for the off-resonant model with  $L = 50$  (green symbol). On the other hand,  $\chi_{1,1}$  (maroon symbols) is too large to disregard contributions from the conduction-electron system  $\sum_i \chi_{i,1}^{\text{cond}}$  to the sum rule

$$\chi_{1,1} + \chi_{2,1} + \sum_i \chi_{i,1}^{\text{cond}} = 0. \quad (7.10)$$

Therefore, larger Kondo correlations may be inferred for the on-resonant model with  $L = 52$  in comparison to the off-resonant model with  $L = 50$ . This conclusion is in agreement with the picture of a two-channel finite-size Kondo effect for  $J \rightarrow 0$ .

## 7.3 Summary

While the spatial variations of finite-size effects are lost in periodic conduction-electron systems due to translational invariance, our investigation reveals that a new class of effects emerges. We showed that periodic boundary conditions in one-dimensional systems usually result in two Fermi levels. Then two electrons in states at the Fermi energy  $\varepsilon_F$  can act as separate screening channels for  $\Delta > T_K$ , what we may call "multi-channel finite-size Kondo effect". Viewed from a wider perspective, this situation may be generally established when the electron system is subject to a larger symmetry group. Thus, periodic models may be regarded as representatives for the finite-size physics in higher dimensions, where the presence of a larger set of symmetries becomes possible and more impurities can be screened at weak coupling strengths  $J$ .

In a random or even realistic system the situation is rather more single-channel like, as several perturbations might break symmetries and leave behind only one level at  $\varepsilon_F$ . But when energy scales are properly chosen, even an approximate degeneracy around  $\varepsilon_F$  might be sufficient to ensure multi-channel physics for the finite-size Kondo effect. The investigation of these, including a fully-worked out perturbation theory may be considered worthy but is beyond the scope of this work and therefore left for future investigations. Nonetheless, the results presented here already give a fascinating foretaste for what is expected to occur in more symmetric or higher dimensional conduction-electron systems.





# 8 Coupling to the environment

## 8.1 Introduction

Encouraged by the convincing robustness of our picture of finite-size effects, we want to make contact to realistic situations and explore the consequences of a less perfect confinement of the Kondo box. In experiments, it is unavoidable that the box is at least weakly coupled to an environment. As a result, for example, the total spin  $S = 1$  of a "bad-good-bad" nano system can be screened by the lead spin degrees of freedom [115].

In the case of a perfect isolation of the Kondo box from the environment, the conduction-electron density of states consists of a set of delta peaks separated by the finite-size gap  $\Delta$  in the vicinity of the Fermi energy. However, a remaining coupling of the box to an environment will broaden these peaks with a characteristic width  $\delta \ll \Delta$  [118, 115, 50]: conduction-electron states acquire a finite lifetime, i.e. electrons are localised within the box only for a finite time  $\sim 1/\delta$ .

In the following, we want to describe in detail, how the environment exerts influence on both the Kondo effect and the RKKY exchange. As already indicated, the central quantity is again the local density of states  $\rho_i(E)$ , dictating the behaviour of both phenomena. We will demonstrate that the picture of finite-size effects acquired so far is continuous in terms of the weak environment coupling at energy scales above  $\delta$ . Remember that this conclusion has been already briefly mentioned in Fig. 5.1, where we summarised our picture of impurity physics.

Since details will rapidly become complicated, we need careful preparations. First of all, we determine the setting of the considered system (illustrated in Fig. 8.1). Though it is not possible with standard DMRG to use infinite conduction-electron systems in order to represent the environment, we can still approximate them by using large but finite chains, denoted here as "leads" despite their finite size. The system feels then two basically different types of finiteness:  $L_{\text{nano}}$ , beyond which the electrons penetrate the walls of the nano system, and the total system size  $L$ .

We will primarily consider a "bad-good-bad" three-impurity model, where the impurities are coupled accordingly to a  $L_{\text{nano}} = 5$  nano-sized conduction-electron system. That is,  $S_1$  and  $S_3$  are at bad sites of the nano system and  $S_2$  is at a good site. The nano system is itself symmetrically coupled by a hopping  $t' \ll t$  to the leads, which are of size

## 8 Coupling to the environment

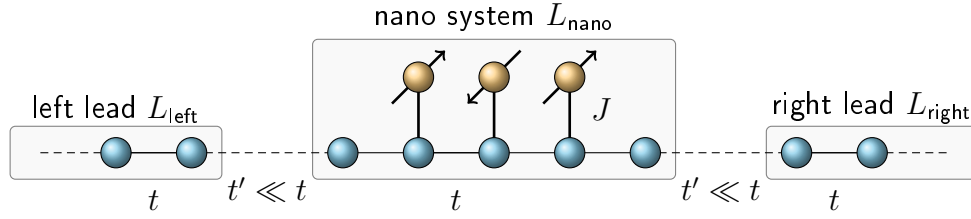


**Figure 8.1:** Impurity model discussed in chapter 8. The impurities are coupled to a small conduction-electron system of a few sites  $L_{\text{nano}}$  only, as shown here for the "bad-good-bad" case. The nano system is symmetrically coupled via a small hopping  $t' \ll t$  to two much larger subsystems of size  $L_{\text{leads}} \gg L_{\text{nano}}$ , denoted as "leads".

$L_{\text{left}}$  and  $L_{\text{right}}$ ; so  $L = L_{\text{left}} + L_{\text{nano}} + L_{\text{right}}$ . In order to fully account for consequences of finite-size effects, we consider three different configurations of  $\{L_{\text{left}}, L_{\text{right}}\}$  (Tab. 8.1). The corresponding Hamiltonian can be formulated as follows

$$\begin{aligned}
 H = & J \sum_{r=1}^3 \mathbf{s}_{i_r} \cdot \mathbf{S}_r - t \sum_{\alpha=\text{left}, \text{right}, \text{nano}} \sum_{\langle i,j \rangle \in \alpha, \sigma} c_{\alpha, i\sigma}^\dagger c_{\alpha, j\sigma} \\
 & - t' \sum_{\sigma} \left( c_{\text{left}, L_{\text{left}}, \sigma}^\dagger c_{\text{nano}, 1, \sigma} + c_{\text{nano}, 1, \sigma}^\dagger c_{\text{left}, L_{\text{left}}, \sigma} \right. \\
 & \quad \left. + c_{\text{right}, 1, \sigma}^\dagger c_{\text{nano}, L_{\text{nano}}, \sigma} + c_{\text{nano}, L_{\text{nano}}, \sigma}^\dagger c_{\text{right}, 1, \sigma} \right).
 \end{aligned} \tag{8.1}$$

## 8.2 Influence on the local density of states

The typical changes of the non-interacting conduction-electron spectrum induced by a finite  $t'$  are origin of several finite-size driven phenomena and have been discussed by P. Simon and I. Affleck in Ref. [118]. It turns out that, assuming  $t' \ll t$ ,  $\rho_i(E)$  at site  $i$  within the nano system can be well-approximated by a sum of slightly broadened Lorentzians located at the energies of the isolated nano system

$$\pi \rho_i(E) \approx \frac{2}{L_{\text{nano}}} \sum_{n=1}^{L_{\text{nano}}} \sin^2(ik_n) \frac{\delta_n}{(E - \varepsilon_n)^2 + \delta_n^2} \tag{8.2}$$

$$k_n \approx \pi \frac{n}{L_{\text{nano}} + 1} \tag{8.3}$$

$$\varepsilon_n = -2t \cos k_n \tag{8.4}$$

$$n = 1, 2, \dots, L_{\text{nano}}. \tag{8.5}$$

	$L_{\text{left}}$	$L_{\text{nano}}$	$L_{\text{right}}$	$L$
bgb, on-resonance	42	5	42	89
bgb, on-resonance	43	5	43	91
bgb, off-resonance	42	5	43	90

**Table 8.1:** Subsystem sizes  $L_{\text{left}}$ ,  $L_{\text{nano}}$ , and  $L_{\text{right}}$  of "bad-good-bad" configurations ("bgb") considered in the calculations.

Their widths are given by

$$\delta_n \approx \frac{2(t')^2 \sin^3(k_n)}{t(L_{\text{nano}} + 1)}. \quad (8.6)$$

In Fig. 8.2,  $\rho_i(E)$  according to Eq. (8.2) is displayed (solid lines) for  $i = i_1$  (bad site) and  $i = i_2$  (good site). Despite the broadening, the peaks retain their coarse structure known from the isolated "bad-good-bad" nano system. That is, gaps are approximately as large as respective finite-size gaps, e.g.  $\Delta_{\text{nano}} = 1$  at the Fermi energy for  $L_{\text{nano}} = 5$ . This circumstance already indicates that on energy scales larger than  $\delta_n$ , we may obtain essentially similar physics as in the isolated nano system.

From Eq. (8.6), it can be inferred that the peak widths  $\delta_n$  are maximal in on-resonant models at the Fermi level  $k_F = \pi/2$ , where  $\delta_F \approx \frac{2(t')^2}{t(L_{\text{nano}} + 1)}$ . For the here considered on-resonant configurations  $\delta_F \approx 0.03$  ( $t' = 0.1$ ). In the following, we will omit the index of  $\delta_F$  in situations in which it is clear that we refer to the broadening of the peak at the Fermi energy  $\varepsilon_F$ .

As seen from Fig. 8.2,  $\rho_i(E)$  according to Eq. (8.2), which is for  $L \rightarrow \infty$ , is a reliable approximation even for the exact weights  $U_{ik}^2$  of the considered finite-size systems as functions of the eigenenergy  $\varepsilon_k$ . Thus, we may employ  $\rho_i(E)$  to deduct conclusions also for the finite systems. However, we have to be careful, since on finer energy scales they are basically different, what is important for energy scales below the true finite-size gaps at  $\varepsilon_F$ ,  $\Delta_{\text{env}}$ , as already known from preceding chapters. Let us remark the observation that the gaps  $\Delta_{\text{env}}$  of the considered finite-size systems increase when  $t'$  increases.

It is understandable that the mentioned spectral differences near  $\varepsilon_F$  will provoke dramatically deviating behaviour for  $J \rightarrow 0$ , caused by the finite size of the leads. This is in particular the case when good (bad) sites of the full system are not good (bad) sites of the isolated nano system (here this concerns the models with  $L = 90$  and  $L = 91$ ). Effects can be also expected from the obviously strong dependence on  $t'$ , which is influencing the energy gaps around the Fermi energy as well as the strong increase (decrease) of the weights  $U_{ik}^2$  close to  $\varepsilon_F$  if there is a (no) peak.

## 8 Coupling to the environment

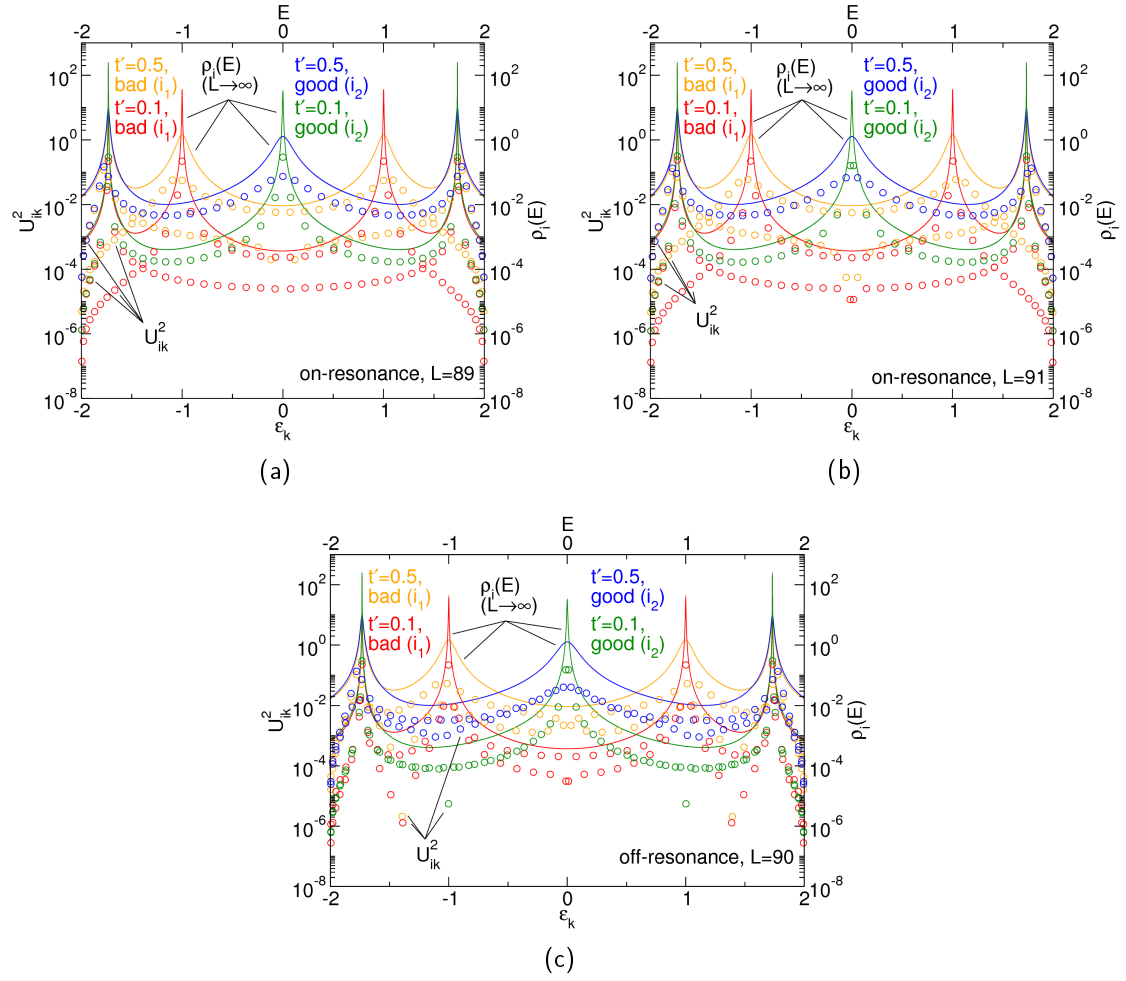


**Figure 8.2:** Exact weights  $U_{ik}^2$  of non-interacting conduction-electron states (left scale, circles) within the "bad-good-bad" nano conduction-electron system as functions of the eigenenergy  $\epsilon_k$ . For the systems discussed in the text (Tab. 8.1) with different hoppings  $t'$  as indicated. (a): on-resonance case with  $L = 89$ , (b): on-resonance case with  $L = 91$ , (c): off-resonance case with  $L = 90$ . In the on-resonance cases, we have  $U_{i_1k}^2 = U_{i_3k}^2$  due to mirror symmetry. Results for  $t' = 0.5$  at  $i_1$ : orange, for  $t' = 0.5$  at  $i_2$ : blue, for  $t' = 0.1$  at  $i_1$ : red, for  $t' = 0.1$  at  $i_2$ : green. For comparison, the local density of states  $\rho_i(E)$  according to Eq. (8.2) are shown as functions of the energy  $E$  (right scale, solid lines), see Ref. [118]. Note the log scale for  $\rho_i(E)$  and  $U_{ik}^2$ .

## 8.3 Influence on the Kondo physics

While the behaviour in the finite-size Kondo regime, i.e.  $T_K < \Delta_{\text{env}}$ , is determined by the mechanisms in-depth investigated in the previous chapters, the remaining question is which effect has the strongly energy dependent density of states, Eq. (8.2), outside

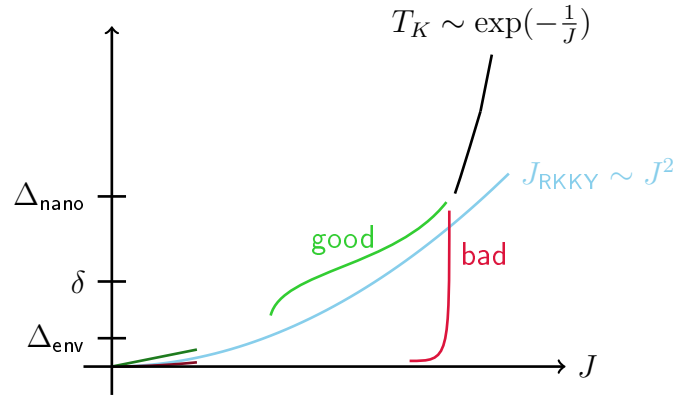


**Figure 8.3:** Competition between RKKY interaction (blue) and Kondo effect (black, green, and red) in a small quantum box coupled to finite but large leads by a small hopping  $t' \ll t$ . In the strong-coupling regime all impurities are separately screened by the conduction electrons due to a large Kondo scale  $T_K$  (black). For  $\xi_K > L_{\text{nano}}$  or, respectively,  $\Delta_{\text{nano}} > T_K$ , a crossover to the "lead Kondo effect" takes place, where Kondo clouds leak into the leads [118]. An intermediate RKKY regime is expected for larger nano systems sizes  $L_{\text{nano}}$  but is skipped here. At sites which correspond to good sites of the isolated nano system (green), the lead Kondo effect dominates the RKKY interaction, while it is exceeded by the RKKY interaction at bad sites (red). For large lead sizes  $L_{\text{left, right}}$ , the weights  $U_{ik}^2$  of electron states become approximately flat as functions of  $\varepsilon_k$  at small energy scales, i.e.,  $\varepsilon_k \ll \delta$ . This may give rise to an RKKY regime which is skipped here due to  $\Delta_{\text{env}} \approx \delta$ . Eventually, this regime may be replaced by the finite-size Kondo effect at very weak coupling strengths, when  $\Delta_{\text{env}} > T_K$ , where  $\Delta_{\text{env}}$  is the finite-size gap at the Fermi energy. If the finite-size Kondo effect is possible, the weights of the  $k_F$  state determine, whether a site is good (dark green) or bad (dark red).

this regime, i.e. for  $\Delta_{\text{env}} < T_K < \Delta_{\text{nano}}$ ? To find an answer, we restrict ourselves to the physics of a single impurity; tacitly assuming for a moment that the RKKY interaction is only marginally influenced. If we have a first look on the evolution of the Kondo energy scale  $T_K$  as function of  $J$ , sketched in Fig. 8.3, we find striking similarities to the situation in a finite system (Fig. 5.1). In the following, we want to explain why.

Let us first return to  $\rho_i(E)$ , which consists of broadened peaks at the energies of the nano system. Even in the finite systems discussed here, on energy scales larger than  $\delta$ , the local density of states appears approximately continuous since lots of states  $\sim \frac{L}{L_{\text{nano}}} \approx 18$  are collected within one broadened peak. This aspect makes it convenient to explore the effects on the Kondo effect from an RG perspective [118]. As known from Sec. 2.3, an iteration step within a perturbative RG treatment enhances the

## 8 Coupling to the environment

effective coupling  $J_{\text{eff}}$  by

$$J_{\text{eff}} \rightarrow J_{\text{eff}} + \frac{1}{2} J_{\text{eff}}^2 \left( \int_{-D}^{-D'} + \int_{D'}^D \right) dE \frac{\rho(E)}{E}, \quad (8.7)$$

where the effective band width is decreased from  $D$  to  $D' < D$ . In case of  $D, D' > \Delta_{\text{env}}$ , we can safely ignore the linear-in- $J$  contribution as it gives only marginal energy-scale independent contributions.

Due to averaging effects, the strong-coupling behaviour of the system is not dramatically changed by a finite  $\delta$ . However, when  $D' \lesssim \Delta_{\text{nano}}$ , the Kondo cloud leaks in the surrounding leads, i.e.,  $\xi_K > L_{\text{nano}}$ . We denote this regime as "lead Kondo regime", as it is established by the lead degrees of freedom, and to distinguish it from the finite-size Kondo effect. The behaviour of  $J_{\text{eff}}$  becomes strongly dependent on the fact whether an impurity is coupled to a good or a bad site in the original nano system. This is made clear by the flow equation, Eq. (8.7), for the case when  $\rho_i(E)$  contains a broadened peak at  $\varepsilon_F$  (that is for a good site  $i$ ). By taking just a single iteration step of Eq. (8.7) and lowering the energy scale from  $\Delta_{\text{nano}}$  to an energy scale  $\varepsilon_F < D' \ll \delta_F \ll \Delta_{\text{nano}}$ ,  $J_{\text{eff}}$  is then greatly enhanced as compared to a flat local density of states [118]

$$J_{\text{eff}}(D') \approx J_{\text{eff}}(\Delta_{\text{nano}}) + (J_{\text{eff}}(\Delta_{\text{nano}}))^2 \frac{2 \sin^2 k_F}{\pi L_{\text{nano}} \delta_F} \ln \left( \frac{\delta_F}{D'} \right). \quad (8.8)$$

The corresponding increase of  $J_{\text{eff}}$  at a bad site ( $i_1$  and  $i_3$  for the "bad-good-bad" configuration) is significantly smaller due to the low density of states  $\sim \frac{\delta}{\Delta_{\text{nano}}^2 L_{\text{nano}}}$ , stemming from tails of peaks in the vicinity of  $\varepsilon_F$ . Estimating the respective Kondo temperatures by the energy scale at which perturbation theory breaks down,  $J_{\text{eff}}(T_K) = \mathcal{O}(1)$ , and writing them as functions of the weak-coupling bulk Kondo temperature  $T_K^0$  (Eq. (2.23)), one obtains

$$T_K^{(\text{good})} \approx \delta \left( \frac{T_K^0}{D_0} \right)^{\left( \frac{t'}{t} \sin k_F \right)^2} \xrightarrow{t' \ll t} \delta \quad (8.9)$$

$$T_K^{(\text{bad})} \approx \Delta_{\text{nano}} \left( \frac{T_K^0}{D_0} \right)^{\left( \frac{t'}{t} \frac{1}{\sin k_F} \right)^2} \xrightarrow{t' \ll t} 0. \quad (8.10)$$

In Figs. 8.4(a) and 8.4(b), we show the evolution of  $T_K$ , according to Eqs. (8.2) and (8.7), as a function of  $T_K^0$  for a "bad-good-bad" nano system. As one can nicely observe by comparing with the results for a flat  $\rho_i(E)$  (black lines), finite-size effects set in for  $\Delta_{\text{nano}} \approx T_K$ : the energy scale  $D'$ , passing the broadened peaks of  $\rho_i(E)$ , leads to distinct steps of  $T_K$  (green and red lines). For  $\Delta_{\text{nano}} > T_K$ , one obtains the exponential slowing down of the decrease of  $T_K$  at a good site (green lines, Eq. (8.9)) and the rapid vanishing at a bad site (red lines, Eq. (8.10)).  $T_K^{(\text{good})}$  therefore

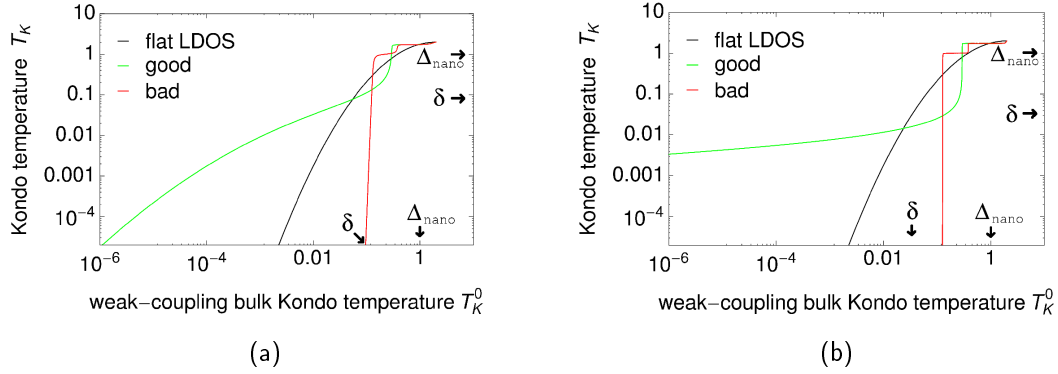


**Figure 8.4:** Single-impurity Kondo temperatures  $T_K$  as functions of the weak-coupling bulk Kondo temperature  $T_K^0 = D_0 \exp(-\frac{1}{\rho_0 J})$ , obtained from one iteration of Eq. (8.8) using the approximated  $\rho_i(E)$ , Eq. (8.2) [118]. For a "bad-good-bad" nano system of size  $L_{\text{nano}} = 5$ .  $T_K$  is defined here as the energy scale at which perturbation theory breaks down.  $\rho_0$  is the flat and hence featureless local density of states of the non-interacting conduction-electron system near  $\varepsilon_F$  and  $D_0 = 2t$ . For simplicity, we assume  $\rho_0 = \frac{1}{4t}$ .  $T_K$  is shown for  $i_2$ , a good site (green), and  $i_1$ , a bad site (red). For comparison, we show also results for a system with a flat local density of states (LDOS)  $\rho = \frac{1}{4t}$  (black). Note the double log scale. Left:  $t' = 0.5$ . Right:  $t' = 0.1$ .

plays the role of a replacement for the linear-in- $J$  coupling of a finite-size system, whereas impurities at bad sites are subject to RKKY exchange, again comparable to the situation in finite-size systems.

However, the rather constant behavior of  $T_K^{(\text{good})}$  must stop when we probe energy scales close to  $\varepsilon_F$  where  $\rho_i(E)$  becomes approximately flat. This circumstance recovers the exponential dependence of  $T_K^{(\text{good})}$  on  $J$  and may lead eventually to an RKKY regime according to scaling Doniach's arguments [45] (Sec. 4.2). In Fig. 8.4(a) one observes that, for  $t' = 0.5$ , this regime is realised at  $T_K^0 < 10^{-2} \approx \frac{1}{10}\delta$ , where  $T_K$  shows a decrease similar to the results for a flat density of states. On the other hand, regarding the finite systems discussed here, we find that  $\Delta_{\text{env}} \approx \delta$  (Fig. 8.2), which implies strong finite-size effects due to the finite leads, suggesting that the emergence of this RKKY regime is prevented.

When  $T_K < \Delta_{\text{env}}$ , as we already mentioned, the approximation of a continuous conduction-electron system loses its validity. Perturbation theory becomes reliable again, causing the emergence of the finite-size Kondo effect (if possible).

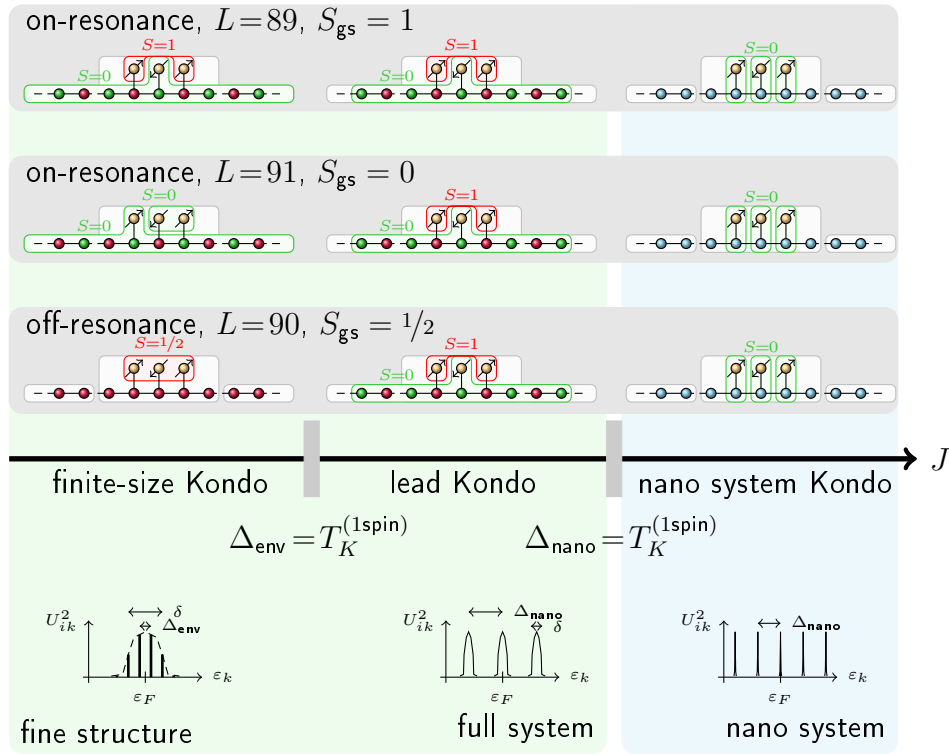


**Figure 8.5:** Crossover scenario as a function of  $J$ . For a "bad-good-bad" nano system coupled to larger finite leads by a hopping  $t' \ll t$ . For the discussion of the different regimes see Fig. 8.3 and the text. The upper panels illustrate the dominant ground-state spin correlations in the different regimes and considered configurations (Tab. 8.1). The lower panels display the relevant conduction-electron states in the different regimes in the case of a site, which is a good site of the isolated nano system, for an off-resonant model. Dashed lines indicate the local density of states at the same site ( $L \rightarrow \infty$ ).

## 8.4 How correlations change

With the above considerations, we are supplied with a coherent scenario of the competition between RKKY exchange and several finite-size shaped forms of the Kondo effect (summarised in Fig. 8.5). How are correlation functions affected by this interplay?

As is evident for inter-impurity correlation functions in Figs. 8.6(a), 8.6(b), and 8.6(c), the strong-coupling regime is determined by the physics of the "bad-good-bad" nano system, independently whether it is in total an on-resonance or an off-resonance situation. Due to the fact that the nano system is quite small  $L_{\text{nano}} = 5$ , we observe a direct crossover from the Kondo effect established by electrons localised within the nano system ("nano system Kondo effect") to the lead Kondo effect. It occurs in a



## 8.4 How correlations change

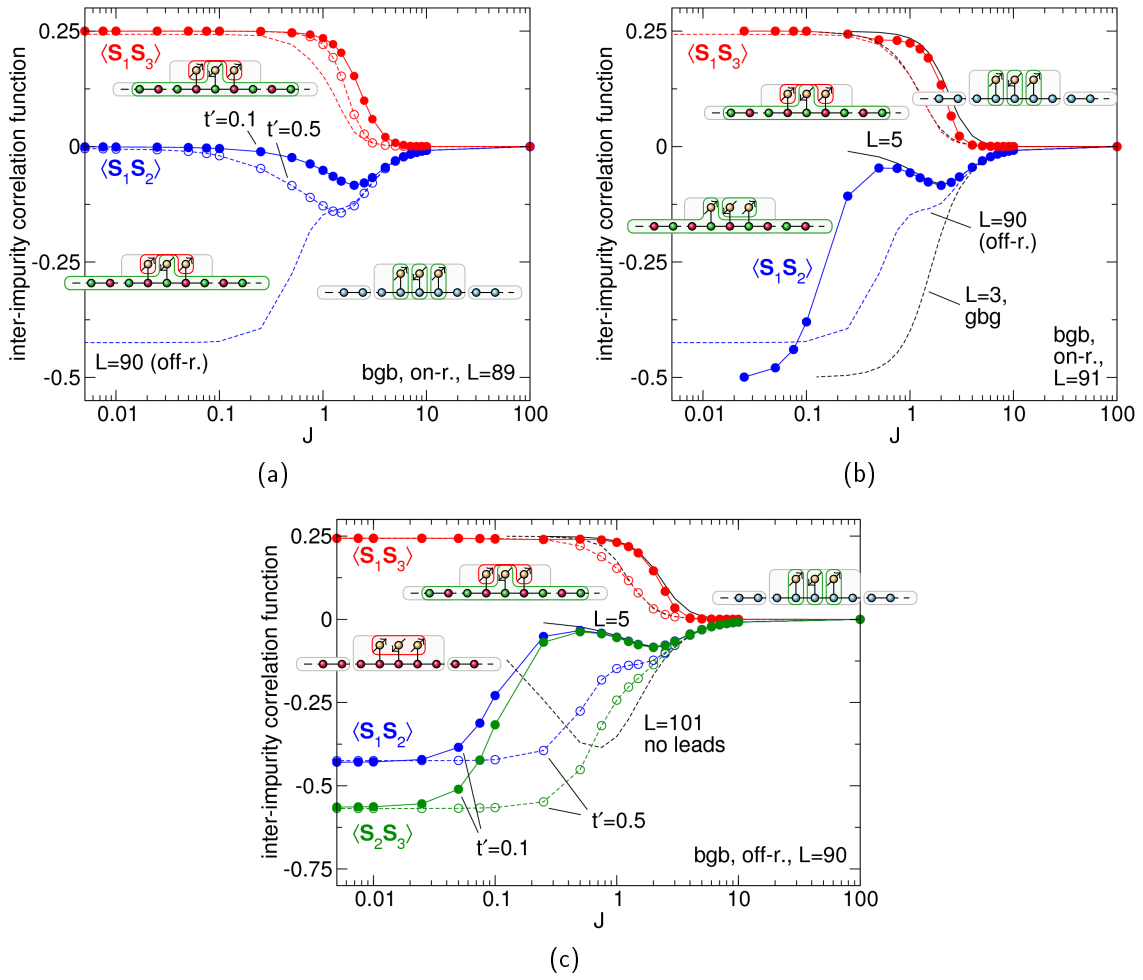


**Figure 8.6:** Inter-impurity correlations  $\langle S_1 S_2 \rangle$  (blue symbols) and  $\langle S_1 S_3 \rangle$  (red symbols) as functions of  $J$  on a log scale. For "bad-good-bad" nano systems and different couplings  $t'$  between leads and nano system:  $t' = 0.5$  (open symbols) and  $t' = 0.1$  (full symbols). (a): on-resonance configuration  $L = 89$ , (b): on-resonance configuration  $L = 91$ , (c): off-resonance case  $L = 90$ . Due to the asymmetric impurity positions in the off-resonance configuration, we also show in this case  $\langle S_2 S_3 \rangle$  (green symbols). For comparison, the results of the system with  $L = 90$  and  $t' = 0.5$  (blue dashed lines without symbols) are shown also in (a) and (c), the correlations of an isolated "bad-good-bad" nano system (black solid lines) in (a), (b), and (c) (in (a) symbols lie indistinguishably on those for  $t' = 0.1$ ), the correlations of an isolated "good-bad-good" nano system (black dashed lines without symbols) in (b), and the correlations of a "bad-good-bad" system without leads for  $L = 101$  (black dashed lines without symbols) in (c).

## 8 Coupling to the environment

similar way as the nano system without environment would cross over from the Kondo regime to the finite-size Kondo regime (note the solid black lines without symbols). This is clearly seen for  $t' = 0.1$ : there is the same pattern of good and bad sites which do or do not allow for Kondo effect at weak couplings  $0.75 < J < 2$ .  $\langle \mathbf{S}_1 \mathbf{S}_2 \rangle$  (blue symbols) displays just small antiferromagnetic correlations for intermediate  $J$ , before vanishing for decreasing  $J$  and  $\Delta_{\text{env}} < T_K < \Delta_{\text{nano}}$ . As already indicated above, the observed resemblance of nano system correlations for  $t' = 0$  ( $T_K < \Delta$ ) and  $t' \neq 0$  ( $\Delta_{\text{env}} < T_K < \Delta_{\text{nano}}$ ) is a consequence of the structure of the peaks in  $\rho_i(E)$  which appear effectively not broadened on energy scales larger than  $\delta$ . It underlines the deep relation between finite-size Kondo effect for  $T_K < \Delta$  and lead Kondo effect for  $\Delta_{\text{env}} < T_K < \Delta_{\text{nano}}$ . Let us also remark that larger nano systems would allow for an RKKY regime, accompanied by the emergence of respective finite-size effects (Sec. 5.5).

The agreement, however, expires for decreasing  $J$ , when the perturbative regime is restored for  $T_K < \Delta_{\text{env}}$ . The subsequent crossover takes place approximately at  $0.01 < J < 1$  for  $t' = 0.1$  and at larger couplings  $0.075 < J < 3$  for  $t' = 0.5$ . This shows that the gaps of the non-interacting electron system are generally dependent not only on  $L$  but also on  $t'$ , as recognised in section 8.2 (Figs. 8.2).

The crossover easily can be detected in the off-resonance case (Fig. 8.6(c)): for  $t' = 0.1$  and  $J < 1$ ,  $\langle \mathbf{S}_i \mathbf{S}_j \rangle$  depart from the corresponding nano system correlations. The final values for  $J \rightarrow 0$  can be understood from an effective three-spin model with unequal RKKY couplings  $J_{12} \neq J_{23}$ , causing imperfect  $\langle \mathbf{S}_1 \mathbf{S}_3 \rangle < \frac{1}{4}$  (red symbols) as well as asymmetric  $\langle \mathbf{S}_1 \mathbf{S}_2 \rangle \neq \langle \mathbf{S}_2 \mathbf{S}_3 \rangle$ , both about  $-\frac{1}{2}$  (blue and green symbols). In Fig. 8.7, it is also seen that all impurities become effectively decoupled from the electrons for  $J \rightarrow 0$  since  $\langle \mathbf{S}_i \mathbf{S}_{\text{tot}} \rangle \rightarrow 0$  (red symbols), as expected for an off-resonance case.

On the other hand, the  $L = 89$  system is in combination with the leads again a "bad-good-bad" system (Fig. 8.6(a)), while for  $L = 91$  we obtain in total a "good-bad-good" system (Fig. 8.6(b)). The drastic deviation from "bad-good-bad" physics for  $L = 91$  (Fig. 8.7) and  $J \rightarrow 0$  is reflected by  $\langle \mathbf{S}_1 \mathbf{S}_2 \rangle \rightarrow -\frac{1}{2}$  (instead of  $\langle \mathbf{S}_1 \mathbf{S}_2 \rangle \rightarrow 0$ ), and  $\langle \mathbf{S}_1 \mathbf{S}_{\text{tot}} \rangle \rightarrow -\frac{1}{2}$  (instead of  $\langle \mathbf{S}_1 \mathbf{S}_{\text{tot}} \rangle \rightarrow 0$ ).  $\mathbf{S}_2$  becomes effectively decoupled for  $J \rightarrow 0$ , since  $\langle \mathbf{S}_2 \mathbf{S}_{\text{tot}} \rangle \rightarrow 0$  (instead of  $\langle \mathbf{S}_2 \mathbf{S}_{\text{tot}} \rangle \rightarrow -\frac{3}{4}$ ).

Finally, let us note that there is no indication of an enhanced inter-impurity correlations  $\langle \mathbf{S}_i \mathbf{S}_j \rangle$ , which would evidence an intermediate RKKY regime as discussed above (Sec. 8.3). We may infer this from Fig. 8.6(c) where are additionally shown as a rough limit the correlations of a "bad-good-bad" system of size  $L = 101$  without leads (black dashed lines without symbols).

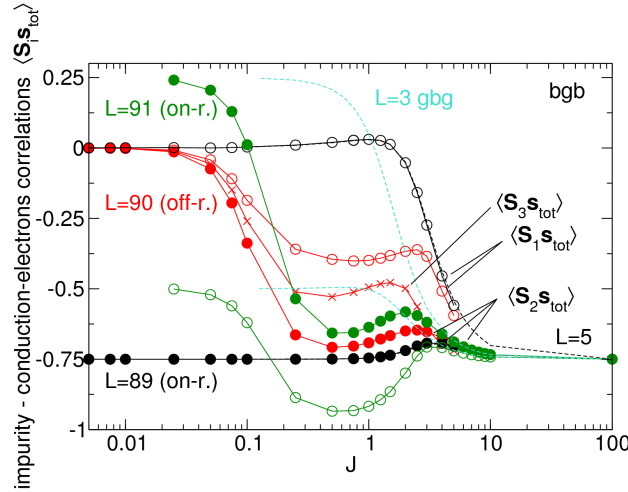


**Figure 8.7:** Impurity-electron correlations  $\langle S_i s_{tot} \rangle$  as functions of  $J$  on a log scale.  $\langle S_1 s_{tot} \rangle$ : open circles,  $\langle S_2 s_{tot} \rangle$ : filled circles. For different total system sizes and "bad-good-bad" nano systems with  $t' = 0.1$ . Off-resonance case  $L = 90$ : red symbols, on-resonance case  $L = 91$ : green symbols, on-resonance case  $L = 89$ : black symbols. Due to the asymmetric impurity positions in the off-resonance configuration, we also show in this case  $\langle S_3 s_{tot} \rangle$  (crosses). For comparison, the correlations of an isolated "bad-good-bad" (black dashed lines, nearly completely concealed by correlations of the model with  $L = 89$ ) and an isolated "good-bad-good" nano system (blue dashed lines) are shown.

## 8.5 Details of the screening process

How does the environment get involved in the screening processes in detail? For large  $J$ , Kondo clouds are well-localised within the nano system, whereas they leak into the environment for decreasing  $J$  as soon as  $T_K < \Delta_{\text{nano}}$ .

For  $T_K < \Delta_{\text{env}}$ , in the finite-size Kondo regime, the screening process is determined by the  $k_F$  state, which attains inhomogeneous weights  $U_{ik_F}$  for finite  $t'$  (Fig. 8.8(a)), what transfers to the shape of Kondo clouds for  $J \rightarrow 0$ . Let us begin with  $L = 89$ , which is an on-resonance case with a  $k_F$  wave function which is strongly localised within the nano system, see black symbols in Fig. 8.8(a). Therefore, the screening occurs mainly within the nano system and only for  $S_2$ , see black symbols in Fig. 8.8(b), e.g., at  $J = 0.05$ . Conversely, for  $L = 91$  we find an effective "good-bad-good" system for  $J \rightarrow 0$ , where only  $S_1$  and  $S_3$  can be screened (green symbols in Fig. 8.8(b)). Kondo correlations are concentrated in the two leads, since the  $k_F$  wave function is damped inside the nano system (red symbols in Fig. 8.8(a)). For  $L = 90$ , the Kondo correlations  $\langle S_i s_j \rangle$  (red symbols) expectedly vanish for  $J \rightarrow 0$ .

The situation is more delicate in the lead Kondo regime  $\Delta_{\text{env}} < T_K < \Delta_{\text{nano}}$  (e.g.

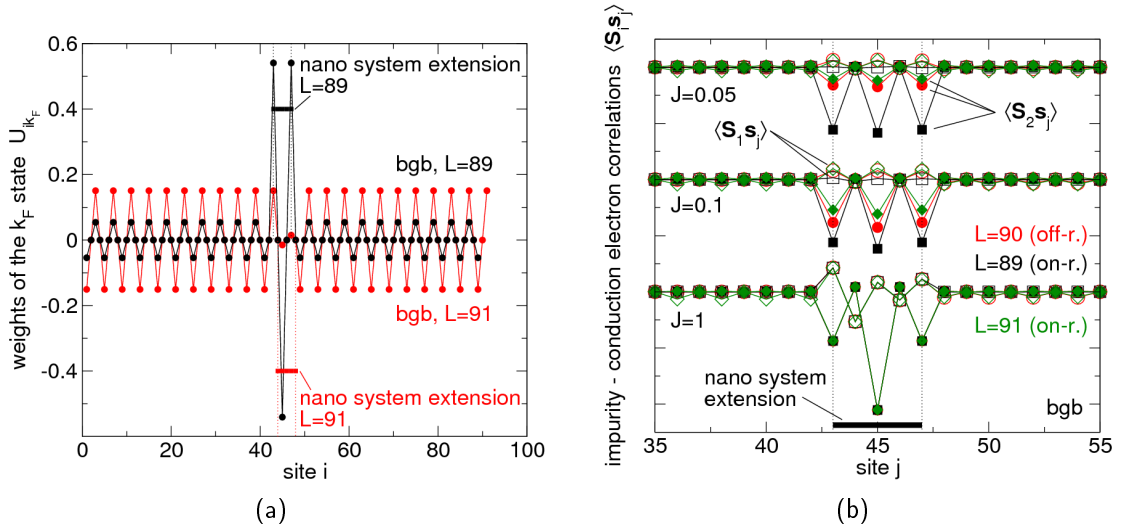


**Figure 8.8:** Left: weights  $U_{ik_F}$  of the exact  $k_F$  conduction-electron state for  $t' = 0.1$  in on-resonant configurations. For  $L = 89$ , the  $k_F$  state is strongly localised within the nano system; with large weights at sites which are good sites of the isolated nano system. On the other hand, for  $L = 91$  the state is strongly damped inside the nano system, possessing only small weights at sites which are bad in the isolated nano system. Right: spatially resolved impurity-electron correlations  $\langle S_i S_j \rangle$  ("Kondo clouds").  $\langle S_1 S_j \rangle$ : open symbols,  $\langle S_2 S_j \rangle$ : filled symbols. For different  $J$  as indicated and "bad-good-bad" nano systems. Off-resonance case  $L = 90$ : red symbols, on-resonance case  $L = 91$ : green symbols, on-resonance case  $L = 89$ : black symbols. In case of  $J = 0.05$ , the crossover to the finite-size Kondo regime is completed, while the system is within the crossover region for  $J = 0.1$ . For  $J = 1$ , the system is in the lead Kondo regime. For better visibility the lines have been shifted and are shown for sites  $j$  in the vicinity of the nano system.

$J = 1$  in Figs. 8.7 and 8.8(b)), where we observe the physics of a "bad-good-bad" system for all discussed configurations:  $S_1$  and  $S_3$  make up a triplet, while  $S_2$  is in a magnetically inert Kondo singlet.<sup>1</sup> The triplet may then be screened by the spin degrees of freedom of the leads, e.g. in case of  $L = 90$  by the right lead, which is composed of an odd number of lattice sites in our setup. Consequently, in Figs. 8.7 and 8.8(b) (red symbols, at  $J = 1$ ),  $\langle S_1 S_i \rangle \neq 0$  and  $\langle S_1 S_{\text{tot}} \rangle \neq 0$ , while  $\langle S_2 S_i \rangle \approx 0$  and  $\langle S_2 S_{\text{tot}} \rangle \approx 0$  for  $i$  in the right lead. One can even find that the triplet is screened asymmetrically  $\langle S_3 S_{\text{tot}} \rangle < \langle S_1 S_{\text{tot}} \rangle$  (Fig. 8.7). This persists down to small  $J \approx 1$

<sup>1</sup>Since this is not the finite-size Kondo regime, the Kondo singlet of  $S_2$  does not comprise only the  $k_F$  conduction electron but electrons within the whole broadened peak at  $\varepsilon_F$  in  $\rho_i(E)$ . Accordingly, the Kondo cloud size is not cut by the system size  $\xi_K < L$  but still  $\xi_K > L_{\text{nano}}$ .

and is due to the asymmetric geometry. Including the partial screening of the triplet, one obtains a total spin  $S_{\text{gs}} = 1/2$  for the whole system, compatible with the even total number of conduction electrons. We note that this situation might be viewed as underscreening of the nano system triplet.

For  $L = 89$ , the leads have an even size, and screening performed by them consequently is possible only for energy scales above  $\Delta_{\text{leads}} \sim 1/L_{\text{left, right}}$ . On the other hand, Lieb's theorem (Sec. 3.5) enforces  $S_{\text{gs}} = 1$ , suggesting that even if this screening takes place, it generates a new triplet somewhere in the leads. Fig. 8.8(b), however, shows that screening does not occur at  $J = 1$  (black symbols). When  $L = 91$  (green symbols), both leads are involved in the screening of the triplet (Fig. 8.8(b)), leading to large antiferromagnetic correlations  $\langle \mathbf{S}_{1\text{tot}} \rangle = \langle \mathbf{S}_{3\text{tot}} \rangle < -\frac{3}{4}$  (Fig. 8.7)), whereas  $\langle \mathbf{S}_{2\text{tot}} \rangle$  remains close to the correlations of the isolated nano system. Thus,  $S_{\text{gs}} = 0$ .

A "good-bad-good" nano system, which is a singlet for itself ( $t' = 0$ ), is not in need of any screening by the environment for  $\Delta_{\text{env}} < T_K < \Delta_{\text{nano}}$  (and similarly for  $\Delta_{\text{nano}} < T_K$ ). This can be seen in Fig. 8.9(b) (for e.g.  $J = 1$ ) by the observation that the correlations  $\langle \mathbf{S}_i \mathbf{S}_{\text{tot}} \rangle$  are equal to those of the isolated nano system (compare Fig. 6.6) for all considered configurations and large  $J > 0.75$ .

## 8.6 Influence on the RKKY physics

So far we neglected the influences on the RKKY interaction, but we already briefly indicated above that those modifications can be strong due to the energy dependent density of states close to  $\varepsilon_F$ . P. Simon found that for energy scales below the finite-size gap of the isolated nano system,  $D < \Delta_{\text{nano}}$ , intraresonance processes of the peak at  $\varepsilon_F$  in  $\rho_i(E)$  may change the sign of the RKKY coupling  $J_{\text{RKKY}}$ , and that  $|J_{\text{RKKY}}|$  may also encounter a strong enhancement at good sites of the isolated nano system due to the strong increase of  $\rho_i(E)$  at  $\varepsilon_F$  (visible in Fig. 8.2) [50]. Experimentally, such a strong enlargement of  $|J_{\text{RKKY}}|$  is also observed in quantum chorals [119, 100]. On the other hand, for energy scales  $D > \Delta_{\text{nano}}$  these effects are found to be absent and the traditional dependency  $J_{rr'} \sim J^2 \cos(2k_F(i_r - i_{r'}))/|i_r - i_{r'}|$  is recovered.

It is again intriguing but not unexpected to find here comparable "resonant enhancement" behaviour as for a system of finite size (Sec. 6.4). This is in close analogy to the relation of the finite-size Kondo effect to the lead Kondo effect. The broadening of peaks in  $\rho_i(E)$  is only relevant (and can be resolved) for energy scales  $D < \Delta_{\text{nano}}$ . Nevertheless, it is important to realise that the starting points of both results are basically different. In the case of Simon's work [50], one starts from  $L \rightarrow \infty$  and a continuous density of states, while in a finite-size system the conduction-electron spectrum is intrinsically discrete without the possibility of intraresonance processes.

For the following discussion, we switch to a "good-bad-good" nano system and examine

## 8 Coupling to the environment

	$\frac{2}{J^2} J_{12}$	$\frac{2}{J^2} J_{13}$
bgb, $L = 5$	-0.024	0.004
bgb, $t' = 0.1$ , on-resonance, $L = 89$	-0.024	0.004
bgb, $t' = 0.1$ , off-resonance, $L = 90$	-0.024	0.004
bgb, $t' = 0.1$ , on-resonance, $L = 91$	-0.025	0.004
gbg, $L = 3$	-0.044	-0.155
gbg, $t' = 0.1$ , on-resonance, $L = 89$	-0.044	1.295
gbg, $t' = 0.1$ , on-resonance, $L = 91$	-0.044	0.287
gbg, $t' = 0.1$ , off-resonance, $L = 92$	-0.046	1.773

**Table 8.2:** RKKY couplings  $J_{rr'}$  evaluated from Eq. (5.29). For configurations discussed in chapter 8 with "bad-good-bad" ("bgb",  $L_{\text{nano}} = 5$ ) or "good-bad-good" ("gbg",  $L_{\text{nano}} = 3$ ) nano system, respectively.

the behaviour of  $J_{13}$ , the RKKY coupling between sites which are good sites of the isolated nano system. We again consider an off-resonant model ( $L = 92$ ) and two on-resonant models ( $L = 89$ , an effective "bad-good-bad" system for  $T_K < \Delta_{\text{env}}$ ) and ( $L = 91$ ), to least constrain finite-size effects.

A first approach is to analyse RKKY couplings according to Eq. (5.29) for the considered models,<sup>2</sup> presented in Tab. 8.2. Indeed, a sign change for  $J_{13}$  as compared to  $t' = 0$  is found, albeit from antiferromagnetic to ferromagnetic coupling. Note that  $S_1$  and  $S_3$  are at ferromagnetic distance. This means that the "wrong" sign<sup>3</sup> of  $J_{13}$  for  $t' = 0$  (chapter 6) is "healed" by a finite  $t'$ . Interestingly, the sign change has no visible effects on the inter-impurity correlations: the "wrong" sign is concealed in the lead Kondo regime ( $0.75 < J < J_{\Delta_{\text{nano}}}$ ) by the special ferromagnetic correlations present between impurities at good sites (Sec. 6.3).

However, the enhancement of  $J_{13}$  has observable consequences. In section 6.4, we already found a similar enhancement of RKKY couplings in finite-size systems (see also Tab. 8.2), leading to distance dependencies which are inconsistent with the conventional RKKY interaction. Here, we find for  $t' = 0.1$  that the RKKY coupling  $|J_{13}|$  is enhanced by a factor of up to 10 as compared to  $t' = 0$ , while  $J_{12}$  is almost unaffected by changes in  $t'$ . Note that  $J_{13}$  is even a factor of up to 40 larger than  $J_{12}$  ( $t' = 0.1$ ).

We want to select just one example to illustrate the consequences: the off-resonance case ( $L = 92$ , red symbols in Figs. 8.9(a) and 8.9(b)) offers a good opportunity to

<sup>2</sup>As is well-known from section 6.4, the RKKY couplings according to Eq. (5.16) are applicable in the finite-size regime. That is why results for  $t' \neq 0$  are valid in the finite-size Kondo regime  $T_K < \Delta_{\text{env}}$  and results for  $t' = 0$  in the lead Kondo regime  $\Delta_{\text{env}} < T_K < \Delta_{\text{nano}}$ , where physics is similar to an isolated nano system in the finite-size Kondo regime  $T_K < \Delta$ .

<sup>3</sup>The opposite sign is due to contributions  $\sim U_{ik_F}$ —in the light of the work of Simon [50] an extreme analogue to the intraresonance processes.

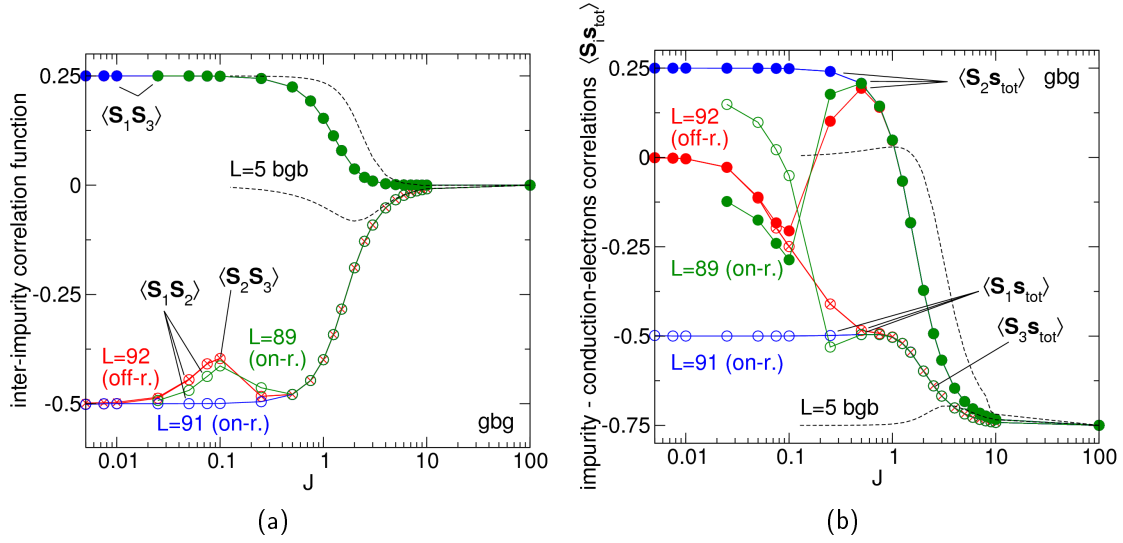


**Figure 8.9:** Correlation functions for "good-bad-good" nano systems ( $t' = 0.1$ ,  $L_{\text{nano}} = 3$ ) as functions of  $J$  on a log scale. Off-resonance configuration  $L = 92$ : red symbols, on-resonance configuration  $L = 89$ : green symbols, on-resonance configuration  $L = 91$ : black symbols. Left: inter-impurity correlations  $\langle \mathbf{S}_1 \mathbf{S}_2 \rangle$  (open circles) and  $\langle \mathbf{S}_1 \mathbf{S}_3 \rangle$  (filled circles). Note that results for  $\langle \mathbf{S}_1 \mathbf{S}_3 \rangle$  for all three configurations lie indistinguishably on each other. Right: impurity-electron correlations  $\langle \mathbf{S}_i \mathbf{s}_{\text{tot}} \rangle$ .  $\langle \mathbf{S}_1 \mathbf{s}_{\text{tot}} \rangle$ : open circle,  $\langle \mathbf{S}_2 \mathbf{s}_{\text{tot}} \rangle$ : filled circles. Due to the asymmetric impurity positions for  $L = 90$ , we show in this case also  $\langle \mathbf{S}_2 \mathbf{S}_3 \rangle$  and  $\langle \mathbf{S}_3 \mathbf{s}_{\text{tot}} \rangle$  (crosses). For comparison, the correlations of an isolated "bad-good-bad" nano system (black dashed lines) are shown. Note that results for the isolated "good-bad-good" nano system would lie indistinguishably on those for  $L = 91$ .

do that. When the RKKY regime is entered for  $\Delta_{\text{env}} > T_K$ , the off-resonant situation leads to  $\langle \mathbf{S}_i \mathbf{s}_{\text{tot}} \rangle \rightarrow 0$  for  $J < 0.1$  (red symbols in Fig. 8.9(b)).

On the one hand, the lead Kondo effect governs the correlations between  $\mathbf{S}_1$  and  $\mathbf{S}_3$  for  $\Delta_{\text{env}} < T_K < \Delta_{\text{nano}}$  ( $0.75 < J < J_{\Delta_{\text{nano}}}$ ), resulting in  $\langle \mathbf{S}_1 \mathbf{S}_3 \rangle \rightarrow \frac{1}{4}$ . On the other hand, the RKKY regime for  $J \rightarrow 0$  is effectively a simple three spin system with ferromagnetic  $J_{13}$  and antiferromagnetic but unequal couplings  $J_{12} \neq J_{23}$  (Tab. 8.2). However, due to the large coupling  $J_{13}$ ,  $\langle \mathbf{S}_1 \mathbf{S}_3 \rangle \rightarrow \frac{1}{4}$  (filled red circles in Fig. 8.9(a)) and  $\langle \mathbf{S}_1 \mathbf{S}_2 \rangle \rightarrow -\frac{1}{2}$  (open red circles) for  $J \rightarrow 0$ . The presence of an approximate mirror symmetry  $\langle \mathbf{S}_1 \mathbf{S}_2 \rangle \approx \langle \mathbf{S}_2 \mathbf{S}_3 \rangle$  for  $J \rightarrow 0$  (open red circles and red crosses, respectively) is another implication of the strongly enhanced  $J_{13}$ . This has to be contrasted with the asymmetric correlations, displayed in the "bad-good-bad" case (Sec. 8.3, Fig. 8.6(c)), likewise with an underlying asymmetric three-spin model. Furthermore, we may argue that weak  $|J_{12}|$  and  $|J_{23}|$  lead to stronger influences on  $\langle \mathbf{S}_1 \mathbf{S}_2 \rangle$  and  $\langle \mathbf{S}_2 \mathbf{S}_3 \rangle$  by residual couplings to the conduction electrons, which is visible as decrease of  $|\langle \mathbf{S}_1 \mathbf{S}_2 \rangle|$  and

$|\langle \mathbf{S}_2 \mathbf{S}_3 \rangle|$  in the intermediate crossover region (e.g. at  $J = 0.1$  in Fig. 8.9(a)).

## 8.7 Summary

In general, a small coupling between nano system and environment  $t' \ll t$  leads to a slight spectral broadening of the non-interacting electron states of the nano system. The broadening manifests in an emerging small energy scale  $\delta < \Delta_{\text{nano}}$  and triggers phenomena such as the leakage of the Kondo clouds into the environment ("lead Kondo regime", Secs. 8.3 and 8.5), the possible reappearance of the RKKY regime for  $J \rightarrow 0$  (Sec. 8.2), and particularly enhanced RKKY couplings between good sites of the isolated nano system (Sec. 8.6). Several predictions for the lead Kondo regime in Refs. [118] and [50] can be confirmed by numerical calculations. However, it must be noted that some results, such as the reappearance of the RKKY regime energy scales well below  $\delta$ , cannot be obtained owing to strong finite-size effects, i.e.,  $\delta \approx \Delta_{\text{env}}$ .

Furthermore, we concluded that correlations in the lead Kondo regime  $\Delta_{\text{env}} < T_K < \Delta_{\text{nano}}$  are compatible with the predictions of finite-size perturbation theory for  $T_K < \Delta$ . For example the novel mechanism described in chapter 6, which ferromagnetically correlates impurities at good sites of the isolated nano system for  $\Delta_{\text{env}} < T_K < \Delta$ , can be transferred to the lead Kondo regime: impurities align antiferromagnetically to the collection of electrons of the broadened peak at  $\varepsilon_F$  (instead of just to the  $k_F$  electron). The correspondence between both Kondo regimes follows from  $\delta$ , which should be irrelevant for energy scales larger than the broadening,  $D \gg \delta$ . However, the resemblance of the analytical results is remarkable, as the starting points are basically different for  $t' = 0$  and  $t' \neq 0$ . This gives us another view on the "resonant enhancement" of inter-impurity correlations and RKKY couplings between impurities at good sites (chapter 6) and furthermore confirms that our concept of finite-size effects is stable against weak interactions with the environment. However, the conventional Kondo cloud picture does not break down for  $\Delta_{\text{env}} < T_K < \Delta_{\text{nano}}$ .

From a wider perspective, the coupling  $t'$  can be viewed as a possibility to design density of states with non-flat features as a function of energy with corresponding consequences on Kondo effect and RKKY exchange in the weak-coupling regime. However, we may also understand our results in a more general way. On the one hand they are insensitive to a finite  $t' \ll t$ . On the other hand we may conclude that the energy gap  $\Delta$  at  $\varepsilon_F$ , which causes the finite-size Kondo effect, does not need to be consequence only of spatial confinement. It can also be effectively induced by suitable interactions, e.g. by localisation due to disorder or crystal defects (even on a mesoscopic scale). Additionally, it is vaguely imaginable that systems, which do not show a Kondo effect at energy scales above  $\Delta$  (e.g. due to anisotropies [43]), exhibit the same finite-size physics discussed in this work. Concluding, these considerations may indicate that prospects for experimental realisations are richer than maybe initially thought.



## 9 Large systems

After elaborating our picture of finite-size and boundary effects in detail with plenty of surprising consequences for the weak-coupling regime, we want to make contact to the old-established ideas about the screening process and the competition between Kondo effect and RKKY interaction [46, 51]. Following the results for large system size  $L$  in section 5.5, in which we recovered the RKKY regime of the "bad-good-bad" model, it should be possible to confirm conventional ideas also for other models. Here, we focus on two aspects: the phase transition expected for a two-impurity model at antiferromagnetic distance, which results in non-Fermi liquid physics [51] (Sec. 4.2), and multi-stage Kondo screening for models which exhibit a large total impurity spin  $S_{\text{tot}}$  in the RKKY regime [46].

### 9.1 Phase transition between Kondo and RKKY regime

As known from section 4.2, the low-energy sector of impurity models can serve as prototypes for non-Fermi liquid physics. One example represents the two-impurity Kondo model at antiferromagnetic distance, where Kondo screening by conduction electrons competes with self-screening of the impurities by antiferromagnetic RKKY exchange [51]. The model is known to exhibit such non-Fermi liquid properties at the phase transition between Kondo and RKKY regime emerging in the presence of a special particle-hole symmetry [52] which is deeply linked to the parity symmetry of conduction electrons. However, a phase transition is only possible for  $L \rightarrow \infty$  [44] and parity symmetry for the corresponding screening channel couplings is always broken, already due to the presence of open boundaries.<sup>1</sup> Nonetheless, remanant behaviour may be expected, especially for large lattices.

From our numerical results, the crossover can be suspected at  $J \approx 1.6$  (for  $L = 150$ ), based on the finding in Ref. [51] that at the critical point  $\langle \mathbf{S}_1 \mathbf{S}_2 \rangle = -0.25$ . According to the experience gained in previous chapters, it is clear that the corresponding tran-

---

<sup>1</sup>l. Affleck et al propose in Ref. [52] to place two impurities at antiferromagnetic distance with a direct ferromagnetic interaction in order to achieve this symmetric situation.

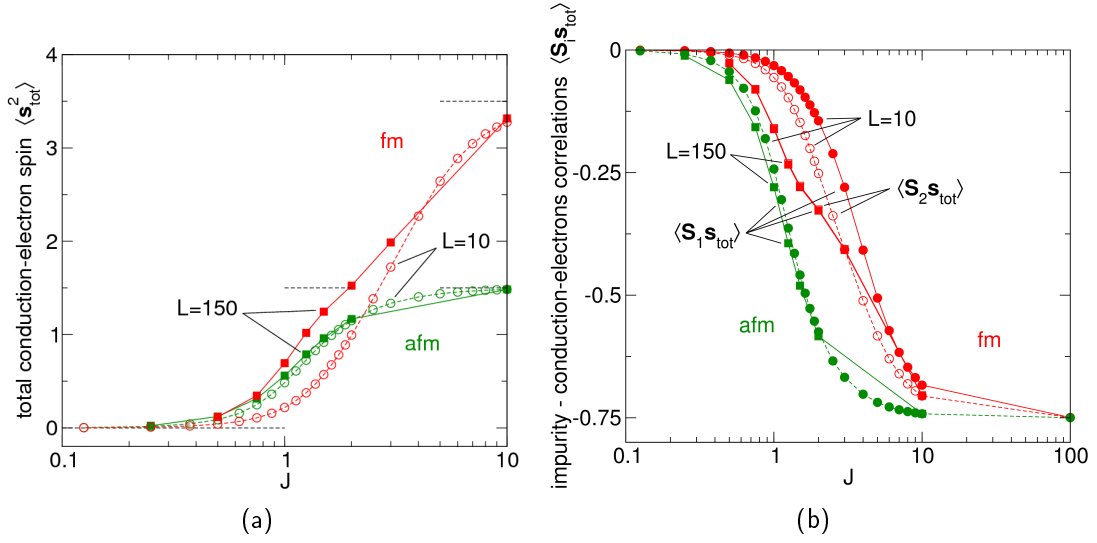


**Figure 9.1:** Correlation functions of two-impurity models at antiferromagnetic distance ( $d = 1$ , green symbols) and ferromagnetic distance ( $d = 2$ , red symbols) as functions of  $J$  on a log scale. For system sizes  $L = 10$  (filled and open circles) and  $L = 150$  (filled and open squares). Left: total conduction-electron spin  $\langle s_{\text{tot}}^2 \rangle$ . Horizontal dashed lines indicate the characteristic values, as discussed in the text, in the strong and weak-coupling regime, and for the ferromagnetic model also in the intermediate RKKY regime. Right: impurity-electron correlations  $\langle S_i s_{\text{tot}} \rangle$ .  $\langle S_1 s_{\text{tot}} \rangle$ : filled symbols. Due to asymmetric impurity positions for  $d = 2$ , we also show in this case  $\langle S_2 s_{\text{tot}} \rangle$  (open symbols). Note that, in case of  $L = 150$ ,  $\langle S_1 s_{\text{tot}} \rangle$  and  $\langle S_2 s_{\text{tot}} \rangle$  lie indistinguishably on each other.

sition region will be entirely hidden by finite-size effects for small system sizes such as  $L = 10$ . However, for  $L = 150$  we can expect the finite-size effects to be sufficiently repelled.

Nevertheless, the familiar correlations  $\langle s_{\text{tot}}^2 \rangle$  (green symbols in Fig. 9.1(a)) and  $\langle S_i s_{\text{tot}} \rangle$  (green symbols in Fig. 9.1(b)) do not seem to be suited to find evidences for the critical point. Increasing the system size from  $L = 10$  to  $L = 150$  obviously does not lead to the same fundamental changes as they are found in the "bad-good-bad" case in chapter 5.

However, a more convenient quantity in this regard represents the staggered impurity susceptibility  $\chi_{\text{stag}}^{\text{imp}}$ , which is expected to exhibit diverging behaviour at the transition point [51]. We obtain  $\chi_{\text{stag}}^{\text{imp}}$  as derivation of the magnetisation of one impurity with respect to a vanishing small, staggered magnetic field  $B_{\text{stag}}$ , i.e.  $\chi_{\text{stag}}^{\text{imp}} = \left. \frac{\partial \langle S_1^z \rangle}{\partial B_{\text{stag}}} \right|_{B_{\text{stag}} \rightarrow 0}$ .  $B_{\text{stag}}$  is of the order of  $10^{-4}$  in our numerical calculations and applied to the whole system.

### 9.1 Phase transition between Kondo and RKKY regime

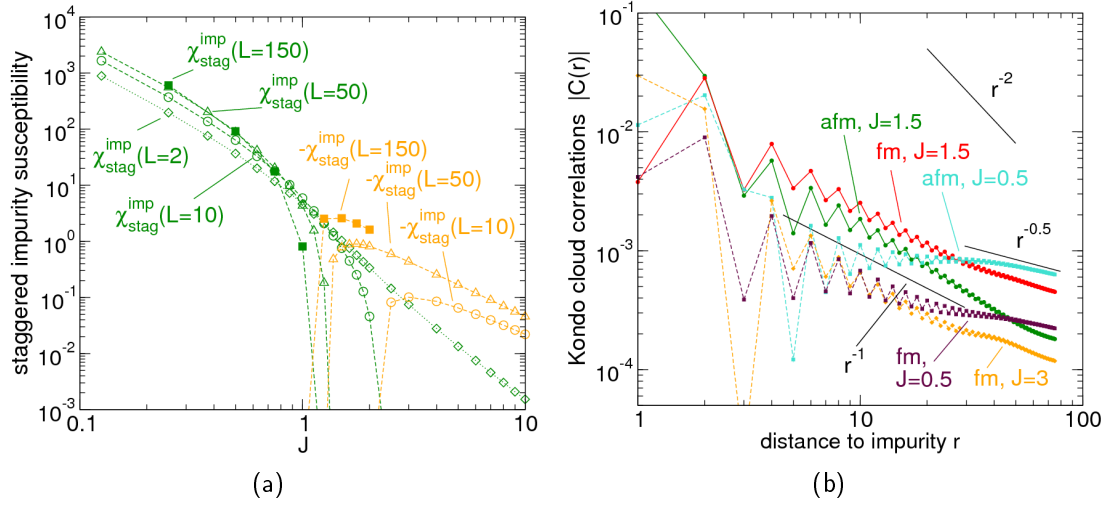


**Figure 9.2:** Left: staggered impurity susceptibility  $\chi_{\text{stag}}^{\text{imp}}$  (green symbols), as defined in the text, as functions of  $J$  on a double log scale. For a two-impurity model at antiferromagnetic distance  $d = 1$  and different system sizes  $L$ :  $L = 2$  (open diamonds),  $L = 10$  (open circles),  $L = 50$  (open triangles), and  $L = 150$  (filled squares). Due to a sign change of  $\chi_{\text{stag}}^{\text{imp}}$  for systems of size  $L > 2$ , we also show  $-\chi_{\text{stag}}^{\text{imp}}$  (orange symbols). Right: two-site averaged Kondo cloud correlations  $|C(r)| = \frac{1}{2}|\langle \mathbf{S}_1 \mathbf{S}_{i_1+r} \rangle + \langle \mathbf{S}_1 \mathbf{S}_{i_1+r+1} \rangle|$  as functions of the distance  $r$  from the first impurity. For two-impurity models at antiferromagnetic distance  $d = 1$  and couplings  $J = 0.5$  (blue symbols) and  $J = 1.5$  (green symbols), and for models at ferromagnetic distance  $d = 2$  and couplings  $J = 0.5$  (maroon symbols),  $J = 1.5$  (red symbols), and  $J = 3$  (orange symbols). System size  $L = 150$ . For comparison, special distance dependencies are indicated as black solid lines.

$\chi_{\text{stag}}^{\text{imp}}$  is displayed in Fig. 9.2(a) for different system sizes  $L$  (green symbols). Let us begin with an extremely small system of size  $L = 2$  (open diamonds). For strong couplings, the Kondo effect leads to vanishing  $\chi_{\text{stag}}^{\text{imp}}$ , since the Kondo cloud is essentially local. Only considering a local Kondo cloud,  $B_{\text{stag}}$  acts effectively as an homogeneous magnetic field, i.e.  $\chi_{\text{stag}}^{\text{imp}} \rightarrow 0$  for  $J \rightarrow \infty$ . On the other hand, for  $T_K < \Delta$ , the evolving nonlocal impurity singlet decouples from the conduction-electron system and is consequently very susceptible to staggered magnetic fields. Hence,  $\chi_{\text{stag}}^{\text{imp}} \rightarrow \infty$  for  $J \rightarrow 0$ .

Turning to a larger systems size of  $L = 150$  (filled squares), we find that the behaviour for  $J \rightarrow 0$  is unchanged, but in the intermediate-coupling regime we obtain a sign change of  $\chi_{\text{stag}}^{\text{imp}}$ . The negative  $\chi_{\text{stag}}^{\text{imp}}$  (orange symbols) is directly connected to the expanding Kondo clouds for finite but large  $J$ :  $B_{\text{stag}}$  matches exactly the  $2k_F$  oscillations within an extended Kondo cloud (Sec. 4.4). Since the spatial extension of the Kondo cloud is established by conduction electrons, they are therefore strongly polarised by

## 9 Large systems

$B_{\text{stag}}$ . On the other hand, the impurity is strongly bound antiferromagnetically to the electrons within the cloud. Thus, we can expect a negative effect on the orientation of the impurity spin for a positive  $B_{\text{stag}}$ , resulting in a negative  $\chi_{\text{stag}}^{\text{imp}}$ . This effect becomes strengthened for increasing system sizes  $L$  due to the increasing reachable Kondo cloud size.

For this reason, we may identify  $\chi_{\text{stag}}^{\text{imp}} < 0$  with the presence of individual, large Kondo clouds. The sign change in  $\chi_{\text{stag}}^{\text{imp}}$  might then be regarded as indication for both the crossover between Kondo regime and RKKY regime and the finite-size induced crossover to the RKKY regime for  $\Delta > T_K$ . However, the results displayed in Fig. 9.2(a) apparently favour the second possibility, since the  $J$  where the sign change occurs is shifted to smaller values for increasing  $L$ . Moreover, for  $L = 150$ , the corresponding coupling  $J \approx 1.0 - 1.25$  is (unexpectedly) close to  $J_{\Delta, 3\text{spins}} \approx 1$  from the "bad-good-bad" system of size  $L = 149$  (Sec. 5.5).

Furthermore, a small peak in  $-\chi_{\text{stag}}^{\text{imp}}$  may be spotted for  $J = 1.5$  ( $L = 150$ ), suggestive of marking the sought transition region between Kondo and RKKY regime. For smaller  $J$  than the peak position but still in its vicinity,  $\chi_{\text{stag}}^{\text{imp}}$  is still negative but with decreasing modulus (Fig. 9.2(a)), signaling the attenuation of individual Kondo effects in favor of the RKKY exchange. The peak is located close to the above discussed coupling of  $J \approx 1.6$  where  $\langle \mathbf{S}_1 \mathbf{S}_2 \rangle = -0.25$ .

## 9.2 Multi-stage Kondo screening

When RKKY couplings are ferromagnetic, a large nonlocal total impurity spin  $S_{\text{tot}}$  develops in the RKKY regime  $J_{\Delta, 1\text{spin}} < J < J_D$ . Unlike the antiferromagnetic model, RKKY interaction and Kondo effect may then act in a cooperative manner, since  $S_{\text{tot}}$  can be subject to a multi-stage Kondo effect, having in mind the discussion of the two-impurity Kondo model at ferromagnetic distance [46] (Sec. 4.2). As a function of decreasing temperature or energy scale, the total impurity spin is screened subsequently in steps of one half on (possibly) different energy scales  $T_K$  if no finite-size effects are present. However, a crucial issue in this discussion is the number of screening channels for  $J \rightarrow 0$ . Regarding a one-dimensional chain without orbital degeneracy, in general just one channel is present for  $J \rightarrow 0$ . This can be, however, circumvented by periodic boundary conditions and additional symmetries such as parity, which allows for an elegant transformation of the Hamiltonian of the non-interacting conduction-electron system. Finally, it can be revealed that, in case of the two-impurity model at ferromagnetic distance, two separate screening channels are provided, which permit to completely quench the total impurity triplet for sufficiently low temperatures [46] (Sec. 4.2).

One screening channel may only contribute  $\frac{1}{2}$  in the screening process, suggested by

the results of Ref. [110]. Below the corresponding Kondo temperature, the residual couplings to this channel usually turn out to be ferromagnetic, leading to an effective decoupling of the residual impurity spin from the channel. On the other hand, for  $J \rightarrow \infty$ , the number of screening channels in one-dimensional systems is one per impurity in form of localised electron states ( $J \gg t$ ).

We are already familiar with the fact that one property of finite-size effects for  $T_K < \Delta$  is to limit the number of available screening channels. For  $J \rightarrow 0$  there is no screening channel in off-resonance cases, whereas a single one is left over in on-resonance cases, namely the  $k_F$  conduction electron.

Consequently, large  $S_{\text{tot}}$  may establish underscreening situations, when the total impurity spin exceeds the number of screening channels  $2S_{\text{tot}} > N_{\text{channels}}$ . This is accompanied by interesting physics such as the "underscreening cloud", which has been found to emerge in a single-impurity model with impurity spin  $S = 1$  at energy scales below  $T_K$  (or length scales beyond  $\xi_K$ , respectively) [120], where a residual impurity spin is left over and governed by a ferromagnetic effective Kondo coupling. Therefore, the spin correlations outside of the underscreening cloud have special spatial dependencies, different from usual dependencies outside of a Kondo cloud. The low-energy properties of such an underscreening Kondo model can be described in terms of a so-called singular Fermi liquid, where the well-defined quasi-particles have a decay rate which vanishes with energy in a singular way near the Fermi energy [120].

Thus, in our setup we may expect in general one screening channel to be present in the RKKY regime, at most two in symmetrical configurations. Can we distinguish the different Kondo scales? At first glance, the answer appears to be negative, since the calculations are performed for zero temperature, and thus we will obtain the maximal screening. However, the finite-size Kondo effect helps to discriminate the different Kondo scales  $T_{K,i}$  (if present and taking part in the screening) since it translates them into sequences of  $J_{\Delta,i}$  defined by  $\Delta = T_{K,1}, \dots$ , where corresponding finite-size Kondo effects set in.

## Two-impurity model at ferromagnetic distance

Let us first turn to the two-impurity model at ferromagnetic distance. For  $T_K < \Delta$ , there is no screening channel available due to the off-resonance situation. For  $L = 10$  the impurity-electron correlations  $\langle \mathbf{S}_i \mathbf{s}_{\text{tot}} \rangle$  (red circles in Fig. 9.1(b)) are strongly dominated by finite-size effects with crossover from  $\langle \mathbf{S}_i \mathbf{s}_{\text{tot}} \rangle \rightarrow 0$  for  $J \rightarrow 0$  to  $\langle \mathbf{S}_i \mathbf{s}_{\text{tot}} \rangle \rightarrow -\frac{3}{4}$  for  $J \rightarrow \infty$ . This translates into a crossover for  $\langle \mathbf{s}_{\text{tot}}^2 \rangle$  (red circles in Fig. 9.1(a)) from 0 ( $J \rightarrow 0$ ) to  $2 + 2\frac{3}{4}$  ( $J \rightarrow \infty$ ).

On the other hand, for larger system sizes  $L$  at least one screening channel is expected to be available in the RKKY regime. For  $L = 150$ ,  $\langle \mathbf{S}_1 \mathbf{s}_{\text{tot}} \rangle$  and  $\langle \mathbf{S}_2 \mathbf{s}_{\text{tot}} \rangle$  (red squares in Fig. 9.1(b)) become similar due to less influences by Friedel oscillations. Furthermore,

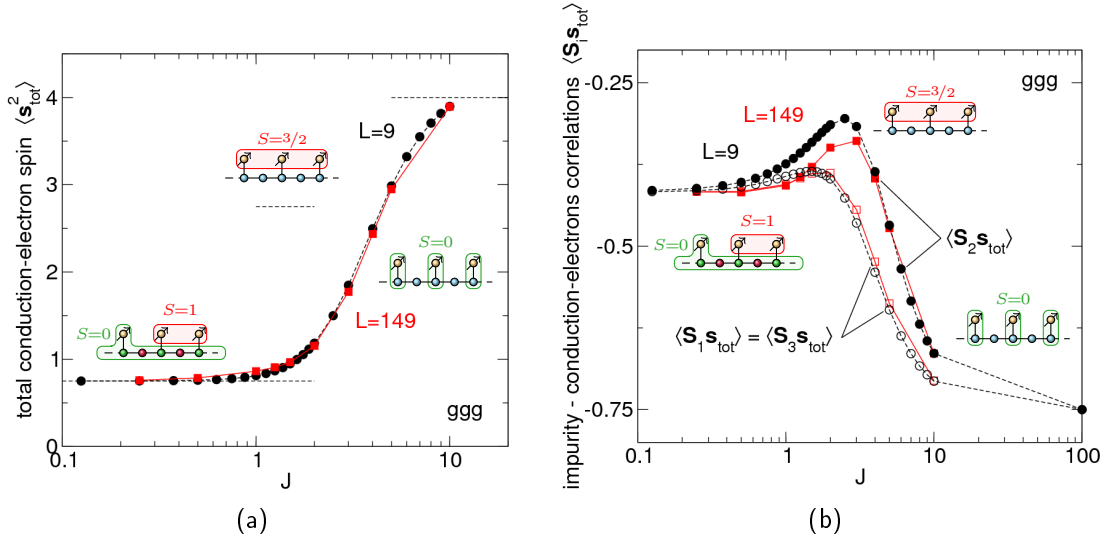


**Figure 9.3:** Correlation functions of three-impurity models in a "good-good-good" configuration with impurity distance  $d = 2$  as functions of  $J$  on a log scale. For system sizes  $L = 9$  (black circles) and  $L = 150$  (red squares). Left: total conduction-electron spin  $\langle s_{\text{tot}}^2 \rangle$ . Horizontal dashed lines indicate the characteristic values in the weak and strong-coupling regime as well the value corresponding to a possible screening of 1 of the total impurity spin in the intermediate RKKY regime. Right: impurity-electron correlations  $\langle \mathbf{S}_i \mathbf{s}_{\text{tot}} \rangle$ .  $\langle \mathbf{S}_1 \mathbf{s}_{\text{tot}} \rangle = \langle \mathbf{S}_3 \mathbf{s}_{\text{tot}} \rangle$ : open symbols,  $\langle \mathbf{S}_2 \mathbf{s}_{\text{tot}} \rangle$ : filled symbols.

stronger antiferromagnetic correlations  $\langle \mathbf{S}_i \mathbf{s}_{\text{tot}} \rangle$  are observed, hinting at a much more efficient screening process. This guess is confirmed by in Fig. 9.1(a) (red squares), since  $\langle s_{\text{tot}}^2 \rangle$  approaches  $2\frac{3}{4}$  (middle dashed line) for  $1.25 \leq J \leq 2$ . Note that the numerical results are cumulating below the middle dashed line, because the total impurity spin is not yet fully developed for these intermediate couplings, that is  $S_{\text{tot}} < 1$ .<sup>2</sup> However, our calculations give no evidence for the presence of a second screening channel due to symmetry arguments, since it would correspond to  $\langle s_{\text{tot}}^2 \rangle = 2 + 2$ . We note that the order of magnitude for the crossover between RKKY and Kondo regime is again in agreement with previous findings for  $J_D$  (e.g. Sec. 5.5).

<sup>2</sup>To ensure ground-state adiabaticity (Sec. 3.5), a rather interesting state develops: the screening of  $\frac{1}{2}$  of the impurity triplet leads to an additional  $\frac{1}{2}$  spin in the conduction-electron system, which builds up a triplet with the remaining impurity spin  $\frac{1}{2}$ .

## Kondo screening clouds

Both in the two-impurity model at ferromagnetic and antiferromagnetic distance we find traces of two interesting physical situations in the vicinity of  $J = 1.5$ , stemming from the competition between Kondo effect and RKKY exchange. Is this maybe reflected by the Kondo cloud correlations  $\sim \langle \mathbf{S}_1 \mathbf{s}_r \rangle$ , shown in Fig. 9.2(b)? Recalling chapter 4, such an analysis can be involving, so we just focus here on the long-range distance dependencies of  $\sim \langle \mathbf{S}_1 \mathbf{s}_r \rangle$ .

For the antiferromagnetic model at  $J = 1.5$  (green symbols), the typical RKKY distance dependence  $\sim 1/r$  inside of the Kondo cloud is obtained for almost all  $r$ , where  $r$  is the distance to the first impurity. Hence, we can think, in this case, of large Kondo clouds on the scale of the system size  $L$ . On the other hand, at  $J = 0.5$  (blue symbols) the cutoff of Kondo correlations for  $J < J_\Delta$  (and  $J < J_D$ , see Sec. 4.2) apparently leads to an anomalous, constant distance dependence for  $5 < r < 40$  and a  $1/r^{0.5}$  dependence for  $r > 40$ .

Interestingly, a comparable behaviour can also be found in the ferromagnetic model at  $J = 0.5$  (maroon symbols), i.e.  $J < J_{\Delta, 2\text{spins}}$ , and even at  $J = 1.5$  (red symbols), i.e.  $J \gtrsim J_{\Delta, 2\text{spins}}$ . Even more peculiarly, while at  $J = 10$  one can find an indication of the boundary of the Kondo cloud, signaled by a  $1/r^2$  power law, in both models (not shown in Fig. 9.2(b)), this is not the case at  $J = 0.5$ ,  $J = 1.5$ , and  $J = 3$  in the ferromagnetic model. Although it appears likely that the unusual distance dependency is a signature of the cutoff of Kondo correlations in finite systems, which can moreover be strongly influenced by RKKY physics, our finding shows that further research on it is needed.

## "Good-good-good" three-impurity model

In the "bad-good-bad" case only one channel is necessary to screen the  $S_{\text{tot}} = 1/2$ , while the "good-good-good" model develops a regular  $S_{\text{tot}} = 3/2$  total impurity spin in the RKKY regime due to the ferromagnetic impurity distance. One might suspect that, due to mirror symmetric positioning, the three impurities could access the two screening channels, provided by the odd and even conduction electrons (with respect to the center of the chain). This is in fact not found here: Fig. 9.3(a) displays  $\langle \mathbf{s}_{\text{tot}}^2 \rangle$ , crossing over from  $\frac{3}{4}$  for  $J \rightarrow 0$  (finite-size Kondo effect) to  $2 + 3\frac{3}{4}$  in the strong-coupling regime (Kondo effect) for  $L = 10$  (black symbols) as well as for  $L = 150$  (red symbols). The additional screening of more than  $\frac{1}{2}$  of the  $S_{\text{tot}} = \frac{3}{2}$ , which is anticipated at  $\langle \mathbf{s}_{\text{tot}}^2 \rangle = 2 + \frac{3}{4}$  (see middle dashed line), is obviously not realised.

The influence of finite-size effects in this underscreening situation (at weak  $J$ ) can be further characterised by  $\langle \mathbf{S}_i \mathbf{s}_{\text{tot}} \rangle$  (Fig. 9.3(b)). Its study is similar to previous ones (Sec. 5.5); however, correlations of the three impurities at weak  $J$  are determined by

position independent linear-in- $J$  Kondo couplings (chapter 6).

### 9.3 Summary

It requires already at least system sizes  $L = 149$  in the "bad-good-bad" case to reveal the conventional RKKY physics (chapter 5). In this light it might appear challenging to uncover with the help of DMRG the even smaller energy scales, caused by a two-stage Kondo effect for a "good-good-good" model or a two-impurity model at ferromagnetic distance [46], as well as the crossover between Kondo and RKKY regime in a two-impurity model at antiferromagnetic distance [51]. And in fact, it turns out that, in this regard, standard DMRG is pushed to its limits. The interesting physics is still influenced by finite-size effects or by the slightly broken symmetry between odd and even conduction-electron screening channel due to boundary effects.

Notwithstanding, it is notable that the general tendencies can be still be investigated, but we leave studies in this direction for further research. Such a program could include, e.g., the determination of critical exponents in the discussed antiferromagnetic model (Sec. 9.1). As examined in chapter 4, R-DMFT is applicable to these problems only in limited cases. Hence, considering models with a small number of impurities, it may be also more advantageous to choose other methods such as NRG [10], which deliver a considerably finer energy resolution than DMRG.

With this chapter we conclude our study of finite-size effects in impurity models. However, we will realise that the architecture of our picture of impurity physics is still incomplete, and thus we turn to a pressing question which arose several times in the course of this work: what remains less understood is the adiabaticity observed for the ground state of the discussed impurity models at half-filling. While finite-size effects modify large fractions of the weak-coupling regime, in the strong-coupling regime ( $J \gg t$ ) the conventional Kondo effect is the leading energy scale. Given the adiabaticity [47, 48, 72] (Sec. 3.5), where does the ground-state spin go in the strong-coupling regime in a large-spin model such as the "good-good-good" configuration? What is the mechanism which generates magnetism in this regime?



# 10 Strong-coupling regime

## 10.1 Introduction

The preceding chapters revolved around the strong influences of the finite size and the boundaries of the host system on the weak-coupling regime of an impurity system. In the course of our study, we employed an analytically proven adiabaticity for the ground state at half-filling [47, 48, 72] (Sec. 3.5), readily implying that magnetism may also be present in the Kondo regime ( $J \gg t$ ). This can be considered as the starting point for the current chapter, which asks how magnetism is generated in the strong-coupling regime of impurity models, where the magnetism of the impurities is quenched due to the Kondo effect. Here, we will follow ideas and conclusions of our papers Refs. [24] and [121].

We will reveal that magnetic couplings in the Kondo regime are due to a novel exchange mechanism, where the roles of conduction electrons and impurities are "inverted". The basic idea is as follows: for strong  $J$ , almost local Kondo singlets are formed, which act as hard scattering centers for the itinerant conduction electrons and may confine their motion, depending on the impurity position. In certain geometries, this tends to localise the conduction electrons and leads to the formation of local magnetic moments in the a priori uncorrelated conduction-electron system. The magnetic coupling between these moments is established via virtual excitations of the Kondo singlets. This exchange mechanism delivers a consistent physical explanation for the ground-state adiabaticity, observed at half-filling (Sec. 10.6) and ensured by exact results [48, 72] based on Lieb's concept of reflection positivity in spin space [47] (Sec. 3.5).

The resulting "inverse indirect magnetic exchange" (IIME) is studied by means of strong-coupling perturbation theory (Sec. 10.4). We derive an effective low-energy Hamiltonian for  $J \rightarrow \infty$ , containing magnetic and isospin exchange terms (see Sec. 10.3 for details) which govern the physics of the free electrons which are not trapped in Kondo singlets. In a sense, this may be regarded as a more detailed definition of Nozières' strong-coupling picture [64], describing in detail the weak interactions among the free "excess" electrons. A fascinating consequence of IIME are additional Kondo effects arising between excess electrons in different parts of the conduction-electron system.

Note that the strong-coupling regime itself is of physical interest, since the strong-

## 10 Strong-coupling regime

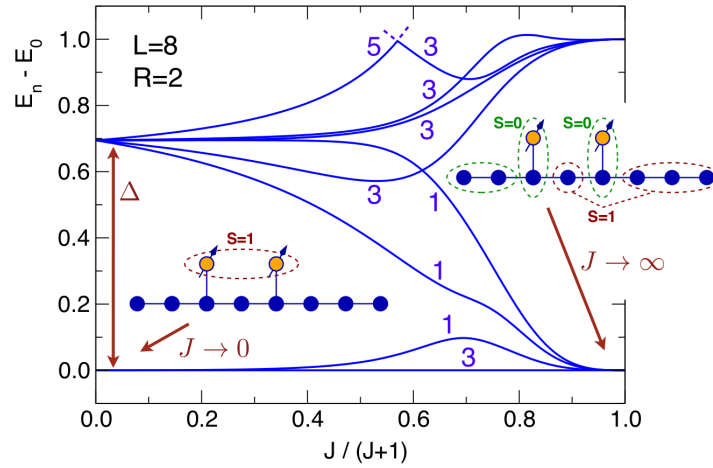


**Figure 10.1:** Inverse indirect magnetic exchange (IIME) mechanism. Lowest many-body eigenenergies  $E_n - E_0$  for  $n = 0, \dots, 7$  in the entire range  $0 < J < \infty$  (note the nonlinear scale) for the Kondo impurity model with  $L = 8$  host sites and  $R = 2$  impurity spins  $1/2$  at the sites  $i_1 = 3$  and  $i_2 = 5$ . Multiplicities are indicated by numbers. The system smoothly crosses over from conventional indirect RKKY exchange ( $J \rightarrow 0$ ) to a state for  $J \rightarrow \infty$  where two local Kondo singlets lead to the formation of two spins  $1/2$  in the host, which are coupled to a triplet via a magnetically inert Kondo singlet. The pictograms visualise the dominant spin correlations obtained numerically in both limits. Figure taken from Ref. [24].

coupling fixed point often describes low-energy properties of impurity models (chapter 2 and section 4.2). This fact also suggests that the locality of Kondo clouds is a rather flexible requirement for the IIME.

## 10.2 From RKKY to inverse exchange

The two-impurity model at ferromagnetic distance shall serve as an example for the crossover from the weak-coupling regime to the strong-coupling regime. The model is set with a small number of  $L = 8$  sites and impurities at  $i_1 = 3$  and  $i_2 = 5$ . Its eigenenergies are evaluated by full diagonalisation and shown in Fig. 10.1. As known from chapter 4, for  $J \rightarrow 0$ , the low-energy sector of  $H$  is exactly described by an effective RKKY two-spin model

$$H_{\text{RKKY}} = -J_{12} \mathbf{S}_1 \mathbf{S}_2 \quad (10.1)$$

$$J_{12} \sim (-1)^{|i_1 - i_2|} J^2 \frac{1}{|i_1 - i_2|}. \quad (10.2)$$

Due to the "ferromagnetic distance"  $|i_1 - i_2| = 2$ , the two impurity spins form a nonlocal triplet in the ground state for  $J \rightarrow 0$ .

As seen in Fig. 10.1, the ground state is unique (apart from the spin degeneracy) for any finite  $J \neq 0$ ,  $J \neq \infty$ . The generalised Lieb theorem (Sec. 3.5) enforces the absence of a ground-state level crossing at half-filling for a bipartite lattice. Therefore, the ground-state symmetry is preserved and the triplet remains intact for all couplings. However, its character must change. With increasing  $J$  the Kondo effect, cut by the finite size gap  $\Delta$  for  $J \rightarrow 0$ , sets in ( $T_K \sim \Delta$ ) and dominates for  $J \rightarrow \infty$ . The corresponding Kondo screening cloud is shrinking for increasing  $J$ , until it is essentially local. Hence, two completely local and magnetically inert "Kondo singlets" are obtained. Since the ground state must be a triplet, two spins  $S = \frac{1}{2}$  are formed in different parts of the conduction-electron system, which couple ferromagnetically. This is supported by numerical analysis of spin correlation functions.

While the magnetic coupling of impurity spins is mediated by the conduction electron of the metallic host for weak  $J$ , this type of interaction is mediated by local Kondo singlets (see pictograms in Fig. 10.1), thus representing an "inverse indirect magnetic exchange" (IIME).

## 10.3 Low-energy model

Before going into details with perturbation theory, we want to first discuss the general structure of the resulting effective low-energy Hamiltonian at strong couplings. Let us employ a modified version of the ferromagnetic two-impurity model of section 10.2 as example. To reduce complexity (and without changing the physics), we cut the system by two sites at the left chain edge and as well at the right chain edge (Fig. 10.2). Sites to which the impurities are coupled are denoted as B sites and the remaining sites as A sites.

In order to analyse the IIME mechanism, which obviously generates a ferromagnetic coupling between magnetic moments at both A sites  $i = 2$  and  $i = 4$ , we treat the hopping term  $\sim t$  perturbatively (while keeping  $J \rightarrow \infty$ ). This is compatible with the variation of  $J \gg t$  for fixed  $t$ , as done in our numerical calculations.

The starting point is the highly degenerate ground state of the  $t = 0$  model consisting of local Kondo singlets and an arbitrary electron configuration on A sites. As is shown in the next section in detail, a non-trivial effective model, capturing the low-energy sector of  $H$  in the limit  $0 < t \ll J$ , can be obtained at fourth order in  $t$  through processes, where e.g. an electron hops from  $i \in A$  and, again via  $B$ , back to  $i$ . The local Kondo singlet must be excited at an energy cost  $\sim J \gg t$  first and restored again on the way back, underlining that these processes must be indeed considered as virtual.

## 10 Strong-coupling regime

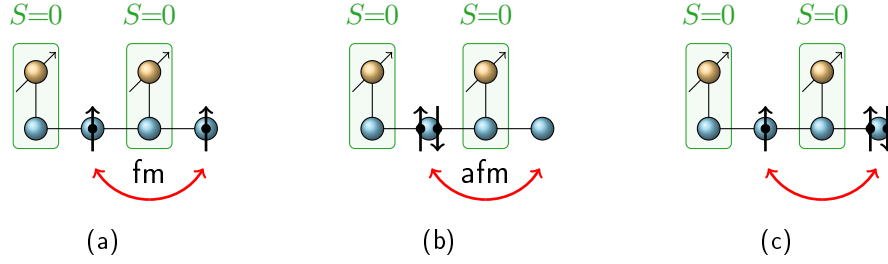


**Figure 10.2:** Contributions of nonlocal interactions to the effective low-energy model of the strong-coupling regime, Eq. (10.3): (a) ferromagnetic ("fm") spin exchange  $s_2 s_4$  for configurations in which sites 2 and 4 are singly occupied, (b) antiferromagnetic ("afm") isospin exchange  $t_2 t_4$  for doubly occupied or empty sites, and (c) correlated hopping between a site occupied by a spin and another one occupied by an isospin. In case of doubly occupied or empty sites we also find contributing terms which are Hubbard- $U$  like.

For  $J > 0$  and keeping terms up to  $\mathcal{O}(t^4/J^3)$ , we find

$$H_{\text{eff}} = -\tilde{\alpha}(s_2 s_4 - t_2 t_4) + \tilde{\alpha} \sum_{i \in A} \left( n_{i\uparrow} - \frac{1}{2} \right) \left( n_{i\downarrow} - \frac{1}{2} \right) \quad (10.3)$$

$$- \frac{1}{2} \tilde{\alpha} \sum_{\sigma} \left( c_{2\sigma}^{\dagger} c_{4\sigma} + \text{H.c.} \right) (1 - n_{2-\sigma} - n_{4-\sigma})$$

$$\tilde{\alpha} = \frac{64}{3} \frac{t^4}{J^3}. \quad (10.4)$$

The effective model is governed by a single energy scale  $\tilde{\alpha}$  and describes spin and charge degrees of freedom on A sites only. Degrees of freedom of local Kondo singlets do not appear in the effective Hamiltonian, as they are released only on large energy scales  $\sim J \gg t$ .

When analysing the effective Hamiltonian, Eq. (10.3), (illustrated in Fig. 10.2), we indeed find a ferromagnetic spin interaction (first term). A corresponding necessary local-moment formation is favoured by a repulsive Hubbard term (third term in Eq. (10.3)). This ferromagnetism competes with an antiferromagnetic exchange between local isospins (second term in Eq. (10.3)), defined by

$$\mathbf{t}_i = \frac{1}{2} \left( c_{i\uparrow}^{\dagger}, (-1)^i c_{i\downarrow} \right) \cdot \boldsymbol{\sigma} \cdot \left( c_{i\uparrow}, (-1)^i c_{i\downarrow}^{\dagger} \right)^T. \quad (10.5)$$

Isospins can be regarded as counterparts of spins: while spins  $\mathbf{s}$  are obtained at singly occupied sites, isospins  $\mathbf{t}$  are present if sites are empty (down isospin state) or doubly occupied (up isospin state). Note that the total isospin of the system and the total spin are the generators of the  $\text{SO}(4)$  symmetry group of the half-filled Kondo model

on the bipartite lattice [97]—and of the effective model as well. The fourth term in  $H_{\text{eff}}$  describes correlated hopping between spin and isospin-containing sites.

The effective model and thus the IIME concept is also valid for fillings  $n$  away from half-filling, as long as the local Kondo singlets in the  $t = 0$  ground state are unbroken, i.e. in this case for fillings  $1/2 \leq n \leq 3/2$ . In section 10.4, we show that in dimensions  $D > 1$  essentially the same effective model is obtained.

Before going into the details of the strong-coupling perturbation theory, let us figure out on general grounds why the isospin exchange must be antiferromagnetic and the spin exchange ferromagnetic (following Anderson's reasoning of antiferromagnetic spin exchange in the single-impurity model, Sec. 2.2). Our argumentation is illustrated in Figs. 10.3 and 10.4 and is based on the idea that hopping processes to and off a Kondo singlet, considered in a strong-coupling perturbation theory, do not change the total isospin or total spin of the system. Thus, isospin and spin symmetry are valid for the original model as well as for the effective model.

Therefore, all intermediate states will have the same total spin and total isospin as the unperturbed ground states which are connected to them by hopping processes. In perturbation theory one can then only expect hopping sequences which match the correct total isospin and total spin of states in the low-energy sector for finite  $t$ , in particular of the ground state. We may also invert this adiabatic statement: if it is possible to infer from intermediate states a definite total spin or total isospin, we can transfer the finding to, e.g., the ground state for finite  $t$ .

However, a few preparations are necessary. First we reduce to a simple toy system; a single-impurity model with  $L = 3$  and impurity at  $i_1 = 2$ . For  $t = 0$ , we have the sixfold ground-state degeneracy of spin and isospin states for the two electrons at A sites  $i = 1$  and  $i = 3$ . Second, as we will see in section 10.4, the essential contributions to the perturbation theory stem from the excitation of the Kondo singlet to a triplet, giving  $\sim -t^4/J^3$ . Furthermore, we emphasise that we just give here examples for motivation without claiming completeness, which will be provided in section 10.4 by conducting the complete perturbation theory up to fourth order in  $t$ .

We start with the isospin exchange (Fig. 10.3) by the investigation of a ground state for  $t = 0$  in which two independent isospins  $T_i = \frac{1}{2}$  of opposite orientation reside at the sites  $i = 1$  and  $i = 3$  next to the Kondo singlet, being in a superposition of  $T_{\text{tot},13} = 0$  and  $T_{\text{tot},13} = 1$  states (total isospin  $z$  component  $T_{\text{tot}}^z = 0$  due to half-filling). Since the Kondo singlet contains no isospins,  $T_{\text{KS}} = 0$ , the question is which state is the ground state for finite hopping  $t \neq 0$ :  $T_{\text{gs}} = 0$  or  $T_{\text{gs}} = 1$ ? When the system is perturbed as described above, we may reach the highest-excited state with a "Kondo triplet". Since we are interested in the isospin exchange, which is basically nonlocal, we need to move one electron by two hopping events from site  $i = 1$  to site  $i = 3$ . As can be seen in Fig. 10.3, the intermediate state contains no isospin at all; i.e. the total isospin  $T_{\text{sys}} = 0$ . Therefore, we conclude that the whole hopping sequence is

## 10 Strong-coupling regime

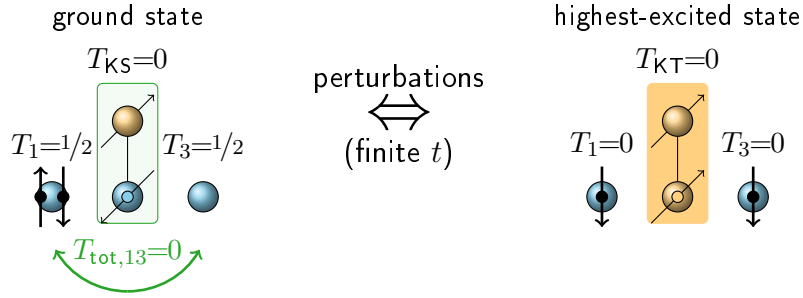


**Figure 10.3:** Antiferromagnetic isospin exchange in the strong-coupling regime of the single-impurity model for  $L = 3$ . The ground-state degeneracy of two independent isospins, prepared close to the Kondo singlet for  $t = 0$  (left panel), is lifted for finite  $t$  by antiferromagnetic isospin exchange, indicated by a green arrow in the left panel. The exchange is motivated here by perturbation theory in  $t$ , additionally using the fact that these hopping processes do not change the total isospin of the system  $T_{sys}$ . In fourth order of this perturbation theory, one may arrive at one of the highest-excited intermediate states with a "Kondo triplet" and two singly occupied sites next to it (right panel). Due to the total absence of isospins,  $T_{sys} = 0$  in the intermediate state. Hence,  $T_{tot,13} = 0$  for the two isospins in the ground state for finite  $t$ .

possible only for total  $T_{sys} = 0$  states. Since energy corrections of these sequences are negative  $\sim -\frac{t^4}{J^3}$  (fermionic signs due to the hopping cancel out),  $T_{sys} = 0$  states are energetically favoured for finite  $t$ . This means that the ground state for finite  $t$  is an isospin singlet and, thus, we find antiferromagnetic isospin exchange. It is obvious that a similar connection by hopping events between the  $T_{gs} = 1$  state and the intermediate Kondo-triplet state is not possible within fourth-order perturbation theory.

Proceeding with the spin exchange, we prepare a ground state for  $t = 0$  (depicted in Fig. 10.4) where two independent spins  $S_i = \frac{1}{2}$  are located at  $i = 1$  and  $i = 3$ , likewise in a superposition of  $S_{tot,13} = 0$  and  $S_{tot,13} = 1$  states ( $M_{tot} = 0$ ). Then, the intermediate Kondo-triplet state must contain two isospins, if we aim at nonlocal interactions again. Consequently, the intermediate state arising in perturbation theory is a total triplet state, whose total spin is determined by the Kondo triplet alone. With the same arguments as above, we may conclude that the ground state for finite  $t$  is also a total triplet state, generated by a ferromagnetic spin exchange.

## 10.4 Perturbation theory in the strong-coupling regime

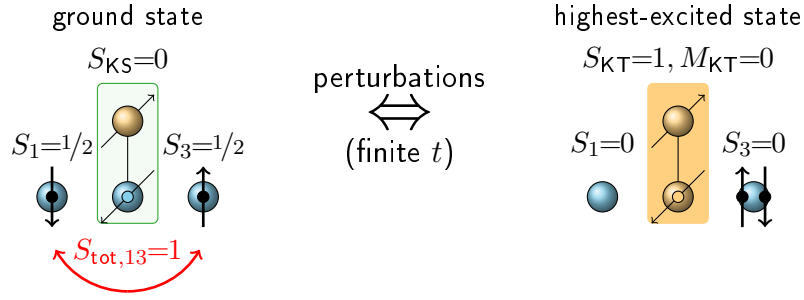


**Figure 10.4:** Ferromagnetic spin exchange in the strong-coupling regime of the single-impurity model for  $L = 3$ . The ground-state degeneracy of two independent spins, prepared close to the Kondo singlet for  $t = 0$  (left panel), is lifted for finite  $t$  by ferromagnetic spin exchange, indicated by a red arrow in the left panel. This is again motivated by intermediate states within perturbation theory in  $t$ , using the circumstance that these hopping processes do not change the total spin  $S_{sys}$ . In fourth order of this perturbation theory, one may arrive at one of the highest-excited intermediate states with a "Kondo triplet" in a  $M = 0$  state (right panel). Then the resulting isospins close to the triplet (doubly occupied and empty sites) carry no spin, hence  $S_{sys} = 1$  in the intermediate state. Consequently,  $S_{sys} = 1$  as well in the ground state for finite  $t$ .

## 10.4 Perturbation theory in the strong-coupling regime

In the following, the aim is to derive the effective low-energy Hamiltonian in the strong-coupling regime. However, this is conducted at a rather general level regarding the geometry, i.e. we allow for higher dimensionality and we allow that Kondo singlets confine spatially extended parts of the electron system for  $J \rightarrow \infty$ , which we will refer for simplicity to as "subsystems" hereafter (an example is shown in Fig. 10.9).

In order to keep the perturbation theory in the spirit of our calculations, which are performed at fixed  $t$  and varying  $J$ , the hopping  $t$  to and off a site  $i_r$  "below" an impurity  $r$  is considered as a perturbation to the situation when this site is part of a local Kondo singlet. Hence,  $J \rightarrow \infty$  corresponds to  $t \rightarrow 0$  for hopping processes to and off a local Kondo singlet. Note that for models with next-neighbouring impurities at distance  $d > 2$ , there is a clear difference in the unperturbed ground states between  $J \rightarrow \infty$  and all hopping amplitudes  $t = 0$ .

Again, we employ the perturbation theory presented in [116] (p. 39), applying it for the case of a small perturbation by  $t$ . In order to determine the effective low-energy

## 10 Strong-coupling regime

Hamiltonian, we consider

$$P_0 H_1 \sum_{k=0}^{\infty} (-t)^{k+1} \left( \sum_{m \ (m \neq 0)} \frac{P_m H_1}{E - E_m^{(0)}} \right)^k P_0 |\phi\rangle = (E - E_n^{(0)}) P_0 |\phi\rangle, \quad (10.6)$$

where  $H_1$  is the perturbation to the unperturbed Hamiltonian  $H_0$ , and  $H = H_0 - tH_1$ , and

$$E = E_n^{(0)} - tE_n^{(1)} + t^2 E_n^{(2)} - \dots \quad (10.7)$$

$|\phi\rangle$  denotes a state from the restricted Hilbert space corresponding to the ground-state manifold  $P_0$ .  $P_m$  is a projector of a subspace of the unperturbed model corresponding to the energy  $E_m^{(0)}$ .

The left-hand side of the above equation,

$$P_0 H_1 \sum_{k=0}^{\infty} (-t)^{k+1} \left( \sum_{m \ (m \neq n)} \frac{P_m H_1}{E - E_m^{(0)}} \right)^k P_0, \quad (10.8)$$

can be considered as an effective Hamiltonian in the subspace  $P_0$ . The  $E$  dependence may be regarded as harmless and can be eliminated for example by expanding in orders of  $t$  [122, 123].

## Hamiltonian and projection operators

For  $J \rightarrow \infty$ , we obtain a collection of local Kondo singlets. In order to reduce complexity, we first consider only cases with next-neighbouring impurities at distance  $d = 2$ . This results in a bipartite structure with Kondo singlets at B sites and free electrons residing at A sites  $i \in \mathcal{A}$ . At the end of this section, we return to the general case of  $d \geq 2$ .

For clarity, we repeat the general multi-impurity Kondo Hamiltonian ( $J > 0$ , Eq. (2.34))

$$H = -t \sum_{\langle i,j \rangle, \sigma} c_{i,\sigma}^\dagger c_{j,\sigma} + J \sum_{r=1}^R \mathbf{S}_r \mathbf{s}_{i_r}, \quad (10.9)$$

We assume that each impurity is in a Kondo singlet for  $J \rightarrow \infty$ , implying that the number of conduction electrons  $R \leq N \leq 2L - R$ .  $L$  is the number of sites in the conduction-electron system, i.e. in a one-dimensional system it is equal to the chain length.



#### 10.4 Perturbation theory in the strong-coupling regime

The starting point is the unperturbed Hamiltonian

$$H_0 = J \sum_{r=1}^R \mathbf{S}_r \mathbf{s}_{i_r}, \quad (10.10)$$

which contains the local exchange interaction terms.

The hopping to and off a site  $i_r$  below an impurity is considered as perturbation

$$H_1 = \sum_{r=1}^R H_1^r = \sum_{r=1}^R \sum_{\substack{\langle j, i_r \rangle \\ j \in \mathcal{A}}} \sum_{\sigma} (c_{i_r, \sigma}^\dagger c_{j, \sigma} + \text{H.c.}). \quad (10.11)$$

The excess electrons are confined on sites  $j \in \mathcal{A}$  by Kondo singlets (and by the boundaries in case of open boundary conditions), causing a large degeneracy. The subspace of unperturbed ground states (i.e. regarding  $H_0$  with  $J > 0$ ) is then spanned by the states

$$(|\psi_0\rangle)_{\{\alpha, \sigma\}} = \left( \prod_{r=1}^R |\text{KS}_r\rangle \right) \left( \prod_j c_{j, \sigma_j}^\dagger \right) |0\rangle, \quad (10.12)$$

where  $|0\rangle$  denotes the electron vacuum.  $|\text{KS}_r\rangle = \frac{1}{\sqrt{2}}(|\uparrow\downarrow\rangle - |\downarrow\uparrow\rangle)_r$  is a local Kondo singlet between impurity  $r$  and a single electron at site  $i_r \in \mathcal{B}$ .  $j \in \mathcal{A}$  and  $\sigma_j$  are the position and the spin of the  $j$ -th excess electron, respectively.

In the strong-coupling regime, the projectors of the unperturbed model have the general product form

$$P_m = \left( \prod_{r=1}^R P_{m_r}^r \right) \mathbf{1}^{\mathcal{A}}, \quad (10.13)$$

where  $P_{m_r}^r$  denotes the projector to the  $m_r$ -th subspace of the impurity  $r$  and the site  $i_r$  below it, and where  $\mathbf{1}^{\mathcal{A}}$  refers to  $\mathcal{A}$  sites.

Considering a single Kondo singlet  $r$ , the ground-state projector is

$$P_0^r = |\text{KS}_r\rangle \langle \text{KS}_r| \quad (10.14)$$

corresponding to the energy  $E_0 = -\frac{3}{4}J$ .

The high-energy subspaces of one local Kondo singlet are constituted by the "free impurity" states with an empty or doubly occupied site  $i_r$  below an impurity  $r$

$$P_1^r = \sum_s (|r, s; 0\rangle \langle r, s; 0| + |r, s; 2\rangle \langle r, s; 2|) \quad (10.15)$$

$$E_1 = 0 \quad (10.16)$$

## 10 Strong-coupling regime

and by the triplet states

$$P_2^r = |r, T, 0\rangle\langle r, T, 0| + \sum_s |r, T, z_s\rangle\langle r, T, z_s| \quad (10.17)$$

$$E_2 = \frac{1}{4}J. \quad (10.18)$$

$|r, s; 0\rangle$  ( $|r, s; 2\rangle$ ) represents the impurity  $r$  in state  $s$  with an empty (doubly occupied) site  $i_r$  below it. The triplet states are  $|r, T, 0\rangle = \frac{1}{\sqrt{2}}(|\uparrow\downarrow\rangle + |\downarrow\uparrow\rangle)_r$ , and  $|r, T, +1\rangle = |\uparrow\uparrow\rangle_r$ , and  $|r, T, -1\rangle = |\downarrow\downarrow\rangle_r$  (using the same order as for the Kondo singlet  $|KS\rangle_r$ ).

Consequently, high-energy subspaces of the full, unperturbed model  $H_0$  are made up by products of  $P_0^r, P_1^r, P_2^r$  for all impurities, excluding the ground-state subspace which is

$$P_0 = P_0^1 P_0^2 \dots P_0^R \quad (10.19)$$

with energy  $E_0^{(0)} = -R \cdot 3/4J$ .

One first observation is that  $P_0^r H_1^j P_0^r = 0 \ \forall j$  for a specific local Kondo singlet  $r$ , so we will only have to deal with even orders of perturbation theory. Furthermore,  $P_m^r H_1^r P_n^r = 0 \ \forall |m-n| \neq 1$ , and one readily concludes that in second order only terms involving one local Kondo singlet can contribute in Eq. (10.8) (Fig. 10.5)

$$P_0 H_1^r P_1^r H_1^r P_0 \quad (10.20)$$

$$P_1 = \sum_r P_1^r \prod_{r' \neq r} P_0^{r'}, \quad (10.21)$$

where  $P_1$  denotes the respective high-energy subspace. In fourth order, the relevant excitations can be subdivided in two groups. The first one,  $P_2$ , stems from the excitation of a specific singlet to a triplet via an intermediate "free impurity" state (Fig. 10.7)

$$P_0 H_1^r P_1^r H_1^r P_2^r H_1^r P_1^r H_1^r P_0 \quad (10.22)$$

$$P_2 = \sum_r P_2^r \prod_{r' \neq r} P_0^{r'}, \quad (10.23)$$

while the latter one,  $P_3$ , consists of states in which two singlets  $r$  and  $p$  are excited to "free impurity" states (Fig. 10.6)

$$P_0 H_1^r P_1^r P_0^p H_1^p P_1^p P_1^r H_1^r P_0^p P_1^p H_1^p P_0 \quad (10.24)$$

$$P_0 H_1^r P_1^r P_0^p H_1^p P_1^p P_1^r H_1^r P_0^p H_1^r P_0 \quad (10.25)$$

$$P_3 = \sum_{rp \ (r \neq p)} P_1^r P_1^p \prod_{r' \neq r, p} P_0^{r'}. \quad (10.26)$$

#### 10.4 Perturbation theory in the strong-coupling regime

The difference between the two processes (10.24) and (10.25) is the order in which the Kondo singlets are restored.

Processes such as

$$P_0 H_1^r P_1^r P_0^p H_1^r P_0^r P_0^p H_1^p P_0^r P_1^p H_1^p P_0, \quad (10.27)$$

where the two impurities are excited into a "free impurity" state one after another are not taken into account because the intermediate projector  $P_0^1 \dots P_0^r P_0^p \dots P_0^R$  is not orthogonal to the ground-state projector.

To shorten the subsequent derivation, we compute the following general matrix elements of  $c_{i_r\sigma}^{(\dagger)}$  and  $H_1$

$$\langle \text{KS}_r | H_1 | r, s, 2 \rangle = \frac{1}{\sqrt{2}} (\delta_{\sigma\uparrow} + \delta_{\sigma\downarrow}) \sum_{\substack{\langle j, i_r \rangle \\ j \in \mathcal{A}}} c_{i_r, \sigma}^\dagger \quad (10.28)$$

$$\langle \text{KS}_r | H_1 | r, s, 0 \rangle = \frac{1}{\sqrt{2}} z_s (\delta_{\sigma\downarrow} + \delta_{\sigma\uparrow}) \sum_{\substack{\langle j, i_r \rangle \\ j \in \mathcal{A}}} c_{i_r, \sigma} \quad (10.29)$$

$$\langle r, T, 0 | H_1 | r, s, 0 \rangle = \frac{1}{\sqrt{2}} \sum_{\substack{\langle j, i_r \rangle \\ j \in \mathcal{A}}} c_{j, -s} \quad (10.30)$$

$$\langle r, T, 0 | H_1 | r, s, 2 \rangle = -\frac{z_s}{\sqrt{2}} \sum_{\substack{\langle j, i_r \rangle \\ j \in \mathcal{A}}} c_{j, s}^\dagger \quad (10.31)$$

$$\langle r, T, \pm 1 | H_1 | r, s, 0 \rangle = \delta_{z_s, \pm 1} \sum_{\substack{\langle j, i_r \rangle \\ j \in \mathcal{A}}} c_{j, s} \quad (10.32)$$

$$\langle r, T, 0 | H_1 | r, s, 2 \rangle = z_s \delta_{z_s, \pm 1} \sum_{\substack{\langle j, i_r \rangle \\ j \in \mathcal{A}}} c_{j, -s}^\dagger, \quad (10.33)$$

where  $z_\uparrow = +1$  and  $z_\downarrow = -1$ .

To lift the full degeneracy, we will have to go at least to fourth order in perturbation theory and expect ground-state energy corrections in form of

$$E_0 = E_0^{(0)} - t E_0^{(1)} + t^2 E_0^{(2)} - t^3 E_0^{(3)} + t^4 E_0^{(4)}. \quad (10.34)$$

### Second order

An intermediate "free impurity" state (see Fig. 10.5 for an example) contributes as follows

## 10 Strong-coupling regime

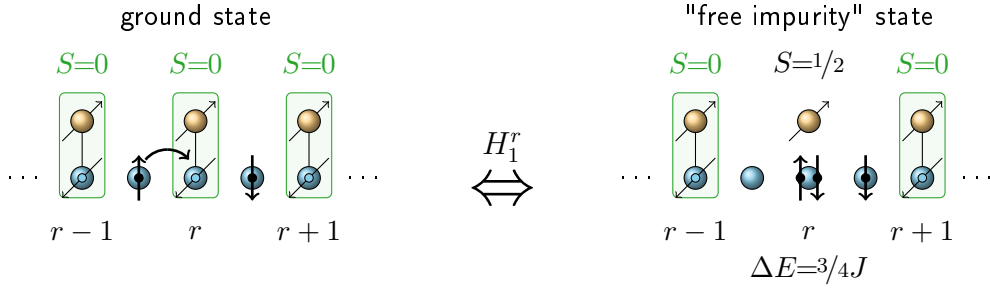


**Figure 10.5:** Second-order contribution to the strong-coupling perturbation theory of a one-dimensional impurity system. The Kondo singlet of impurity  $r$  is broken by an electron hopping to the site  $i_r$  below the impurity. It is restored in a subsequent step. The energy cost for one hopping process adds up to  $\Delta E = E_1 - E_0 = \frac{3}{4}J$ , where  $E_0$  is the ground-state energy and  $E_1$  the energy of the excited state.

$$\sum_{r=1}^R \frac{P_0 H_1^r P_1^r H_1^r P_0}{E - E_1^{(0)}} = \frac{t^2}{E + (R-1)^{3/4}J} \sum_{r=1}^R Z_{i_r} P_0, \quad (10.35)$$

where  $Z_{i_r}$  denotes the coordination number of site  $i_r$ , which is usually  $Z_{i_r} = 2$  in case of one-dimensional models.

### Fourth order: two-impurity contributions

Intermediate states in which two impurities are in a "free impurity" state (Fig. 10.6) only give constant terms in perturbation theory. We first consider variant (10.24)

$$\begin{aligned} & t^4 \sum_{r,p=1}^R \left( \frac{1}{E - E_1 - E_0 - (R-2)E_0} \right)^2 \frac{1}{E - 2E_1 - (R-2)E_0} \\ & \quad \times P_0 H_1^r P_1^r P_0^p H_1^p P_1^p P_0^p H_1^p P_0^p H_1^p P_0 \\ & = t^4 \left( \frac{1}{E + (R-1)^{3/4}J} \right)^2 \frac{1}{E + (R-2)^{3/4}J} \sum_{r,p=1}^R \left( -Z_{i_r} Z_{i_p} + \frac{1}{2} (Z_{r,p})^2 \right) P_0, \end{aligned} \quad (10.36)$$

where  $Z_{r,p} = \sum_{\alpha_1 \in \mathcal{A}} \langle \alpha_1, i_r \rangle \sum_{\alpha_2 \in \mathcal{A}} \langle \alpha_2, i_p \rangle \delta_{\alpha_1 \alpha_2}$  denotes the number of confined sites being neighbours of both the Kondo singlet  $r$  at site  $i_r$  and the Kondo singlet  $p$  at site  $i_p$ .

As one may have expected due to symmetry reasons, variant (10.25) amounts to a comparable result ( $r \neq p$ )

$$P_0 H_1^r P_1^r P_0^p H_1^p P_1^p P_0^p H_1^p P_0^p H_1^p P_0 = Z_{i_r} Z_{i_p} P_0. \quad (10.37)$$

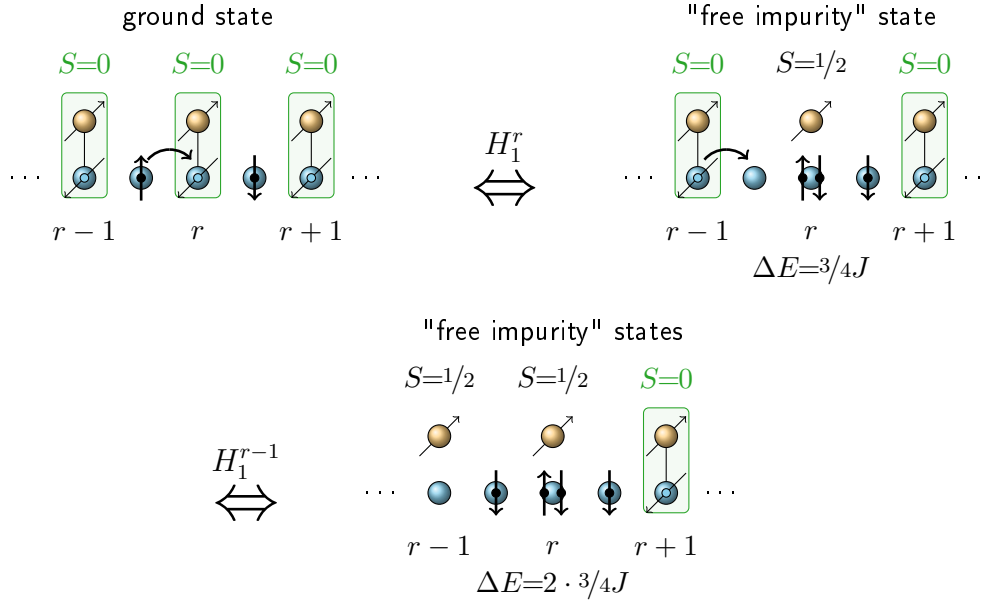


**Figure 10.6:** Fourth-order contribution to the strong-coupling perturbation theory of a one-dimensional impurity system which involves two neighbouring Kondo singlets. Successive electron hopping to the Kondo singlet of impurity  $r$  and off the Kondo singlet of impurity  $r-1$  leave two "free impurities" behind. Both singlets are restored in two subsequent steps. The energy cost of hopping to or off a Kondo singlet is  $\Delta E = E_1 - E_0 = \frac{3}{4}J$ .

## Fourth order: one-impurity contributions

The essential contributions to our perturbation theory stem from the excitation of a specific impurity to a triplet state via a "free impurity" state, illustrated in Fig. 10.7. After some algebra one obtains

$$\begin{aligned}
 & P_0^r H_1^r P_1^r H_1^r P_2^r H_1^r P_1^r H_1^r P_0^r \\
 &= 3 \sum_{\substack{\langle \alpha_1, i_r \rangle \\ \alpha_1 \in \mathcal{A}}} \sum_{\substack{\langle \alpha_2, i_r \rangle \\ \alpha_2 \in \mathcal{A}}} \sum_{\substack{\langle \alpha_3, i_r \rangle \\ \alpha_3 \in \mathcal{A}}} \sum_{\substack{\langle \alpha_4, i_r \rangle \\ \alpha_4 \in \mathcal{A}}} \sum_s |\text{KS}_r\rangle c_{\alpha_1, s}^\dagger c_{\alpha_2, -s} c_{\alpha_3, -s}^\dagger c_{\alpha_4, s} \langle \text{KS}_r|.
 \end{aligned} \tag{10.38}$$

We consider a geometry where Kondo singlets may be surrounded by as many subsys-

## 10 Strong-coupling regime

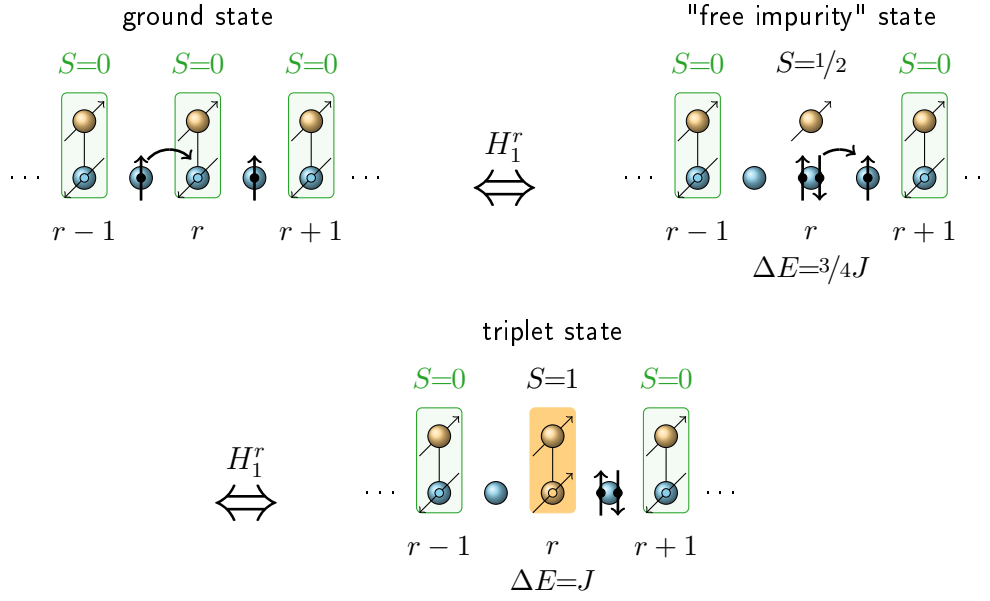


**Figure 10.7:** Fourth-order contribution to the strong-coupling perturbation theory of a one-dimensional impurity system, yielding the essential parts of the effective low-energy Hamiltonian Eq. (10.3). The Kondo singlet of impurity  $r$  is excited to the triplet state via a "free impurity" state (and restored afterwards). The energy difference between the triplet state and the ground state is  $\Delta E = E_2 - E_0 = J$ .

tems as desired, mimicking the situation in higher dimensions

$$\begin{aligned}
 & P_0^r H_1^r P_1^r H_1^r P_2^r H_1^r P_1^r H_1^r P_0^r \\
 &= 3 \sum_s |\text{KS}_r\rangle \left\{ \sum_{\substack{\langle \alpha_1, i_r \rangle \\ \alpha_1 \in \mathcal{A}}} (2n_{\alpha_1, s} - n_{\alpha_1, s} n_{\alpha_1, -s}) \right. \\
 &+ \sum_{\substack{\langle \alpha_1, i_r \rangle \\ \alpha_1 \in \mathcal{A}}} \sum_{\substack{\alpha_1 \neq \alpha_2 \\ \langle \alpha_2, i_r \rangle \\ \alpha_2 \in \mathcal{A}}} (c_{\alpha_1, s}^\dagger c_{\alpha_1, -s}^\dagger c_{\alpha_2, s} c_{\alpha_2, -s} + 2c_{\alpha_1, s}^\dagger c_{\alpha_2, s} (1 - n_{\alpha_1, -s} - n_{\alpha_2, -s}) \\
 &- n_{\alpha_1, s} n_{\alpha_2, -s} + c_{\alpha_1, s}^\dagger c_{\alpha_1, -s} c_{\alpha_2, -s}^\dagger c_{\alpha_2, s}) + \sum_{\substack{\text{all different} \\ \langle \alpha_1, i_r \rangle, \langle \alpha_2, i_r \rangle, \langle \alpha_3, i_r \rangle \\ \alpha_1, \alpha_2, \alpha_3 \in \mathcal{A}}} 2c_{\alpha_1, s}^\dagger c_{\alpha_2, s} \left( \frac{1}{2} - n_{\alpha_3, -s} \right) \\
 &- \sum_{\substack{\text{all different} \\ \langle \alpha_1, i_r \rangle, \langle \alpha_2, i_r \rangle, \langle \alpha_3, i_r \rangle \\ \alpha_1, \alpha_2, \alpha_3 \in \mathcal{A}}} (c_{\alpha_1, s}^\dagger c_{\alpha_2, s} + c_{\alpha_2, s}^\dagger c_{\alpha_1, s}) (c_{\alpha_1, -s}^\dagger c_{\alpha_3, -s} + c_{\alpha_3, -s}^\dagger c_{\alpha_1, -s}) \\
 &+ \sum_{\substack{\text{all different} \\ \langle \alpha_1, i_r \rangle, \langle \alpha_2, i_r \rangle, \langle \alpha_3, i_r \rangle, \langle \alpha_4, i_r \rangle \\ \alpha_1, \alpha_2, \alpha_3, \alpha_4 \in \mathcal{A}}} c_{\alpha_1, s}^\dagger c_{\alpha_2, -s} c_{\alpha_3, -s}^\dagger c_{\alpha_4, s} \left. \right\} \langle \text{KS}_r |.
 \end{aligned} \tag{10.39}$$

## 10.4 Perturbation theory in the strong-coupling regime

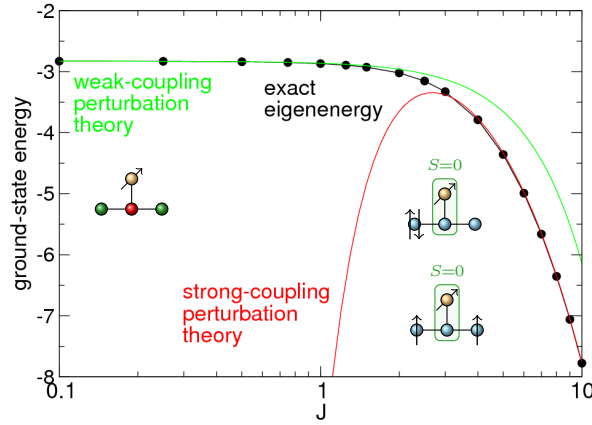


**Figure 10.8:** Exact ground-state energy (black line with filled circles) of a single-impurity model of size  $L = 3$ , where the impurity is coupled to  $i_1 = 2$ , as a function of  $J$  on a log scale. The ground-state energy is compared with the results of the weak-coupling perturbation theory of section 5.2 (green line) and with those of the strong-coupling perturbation theory presented here (red line).

Introducing spin operators  $\mathbf{s}_i$  and isospin operators  $\mathbf{t}_i$  (Eq. (10.5)), we find

$$\begin{aligned}
 P_0 H_1^r P_1^r H_1^r P_2^r H_1^r P_1^r H_1^r P_0 &= 6 \left\{ 1 + 2 \sum_{\substack{\langle \alpha, i_r \rangle \\ \alpha \in \mathcal{A}}}^{\beta < \alpha} \sum_{\substack{\langle \beta, i_r \rangle \\ \beta \in \mathcal{A}}} (\mathbf{s}_\alpha \mathbf{s}_\beta - \mathbf{t}_\alpha \mathbf{t}_\beta) \right. \\
 &\quad - \sum_{\substack{\langle \alpha, i_r \rangle \\ \alpha \in \mathcal{A}}} \left( n_{\alpha, \uparrow} - \frac{1}{2} \right) \left( n_{\alpha, \downarrow} - \frac{1}{2} \right) \\
 &\quad + \sum_s \sum_{\substack{\langle \alpha, i_r \rangle \\ \alpha \in \mathcal{A}}} \sum_{\substack{\langle \beta, i_r \rangle \\ \beta \in \mathcal{A}}}^{\beta < \alpha} (c_{\alpha, s}^\dagger c_{\beta, s} + c_{\beta, s}^\dagger c_{\alpha, s}) \left( \frac{1}{2} Z_{i_r} - \sum_{\substack{\langle \gamma, i_r \rangle \\ \gamma \in \mathcal{A}}} n_{\gamma, -s} \right) \\
 &\quad - \frac{1}{2} \sum_{\substack{\text{all different} \\ \langle \alpha_1, i_r \rangle, \langle \alpha_2, i_r \rangle, \langle \alpha_3, i_r \rangle \\ \alpha_1, \alpha_2, \alpha_3 \in \mathcal{A}}} (c_{\alpha_1, s}^\dagger c_{\alpha_2, s} + c_{\alpha_2, s}^\dagger c_{\alpha_1, s}) (c_{\alpha_1, -s}^\dagger c_{\alpha_3, -s} + c_{\alpha_3, -s}^\dagger c_{\alpha_1, -s}) \\
 &\quad \left. + \frac{1}{2} \sum_{\substack{\text{all different} \\ \langle \alpha_1, i_r \rangle, \langle \alpha_2, i_r \rangle, \langle \alpha_3, i_r \rangle, \langle \alpha_4, i_r \rangle \\ \alpha_1, \alpha_2, \alpha_3, \alpha_4 \in \mathcal{A}}} c_{\alpha_1, s}^\dagger c_{\alpha_2, -s} c_{\alpha_3, -s}^\dagger c_{\alpha_4, s} \right\} P_0.
 \end{aligned} \tag{10.40}$$

While the formulation of Eq. (10.40) in terms of  $\mathbf{s}_i$  is always possible, the isospin symmetry is only present for bipartite models [97]. However, this represents no general constraint since, first, we only treat bipartite models hereafter, and second one would otherwise replace  $\mathbf{t}_\alpha \mathbf{t}_\beta \rightarrow \frac{1}{2} (c_{\alpha, \uparrow}^\dagger c_{\alpha, \downarrow}^\dagger c_{\beta, \downarrow} c_{\beta, \uparrow} + c_{\alpha, \downarrow} c_{\alpha, \uparrow} c_{\beta, \uparrow}^\dagger c_{\beta, \downarrow}^\dagger) + \frac{1}{4} (n_\alpha - 1)(n_\beta - 1)$ .

## The final result

The last step is to adjust  $E$  by expanding our perturbative result up to fourth order in  $-t$  (Eq. (10.34)). We find

$$\begin{aligned}
E = & -R \frac{3}{4} J - \frac{4}{3} \frac{t^2}{J} \sum_{r=1}^R Z_{i_r} + \frac{32}{27} \frac{t^4}{J^3} \left( 2 \left( \sum_{r=1}^R Z_{i_r} \right)^2 - \frac{1}{2} \sum_{r,p=1}^R (Z_{r,p})^2 \right) \\
& + \frac{32}{3} \frac{t^4}{J^3} \sum_{r=1}^R \left\{ -1 + 2 \sum_{\substack{\langle \alpha, i_r \rangle \\ \alpha \in \mathcal{A}}} \sum_{\substack{\beta < \alpha \\ \langle \beta, i_r \rangle \\ \beta \in \mathcal{A}}} (\langle \mathbf{t}_\alpha \mathbf{t}_\beta \rangle_0 - \langle \mathbf{s}_\alpha \mathbf{s}_\beta \rangle_0) \right. \\
& + \sum_{\substack{\langle \alpha, i_r \rangle \\ \alpha \in \mathcal{A}}} \left\langle \left( n_{\alpha, \uparrow} - \frac{1}{2} \right) \left( n_{\alpha, \downarrow} - \frac{1}{2} \right) \right\rangle_0 \\
& - \sum_s \sum_{\substack{\langle \alpha, i_r \rangle \\ \alpha \in \mathcal{A}}} \sum_{\substack{\beta < \alpha \\ \langle \beta, i_r \rangle \\ \beta \in \mathcal{A}}} \left\langle \left( c_{\alpha, s}^\dagger c_{\beta, s} + c_{\beta, s}^\dagger c_{\alpha, s} \right) \left( \frac{1}{2} Z_{i_r} - \sum_{\substack{\langle \gamma, i_r \rangle \\ \gamma \in \mathcal{A}}} n_{\gamma, -s} \right) \right\rangle_0 \\
& + \frac{1}{2} \sum_{\substack{\langle \alpha_1, i_r \rangle, \langle \alpha_2, i_r \rangle, \langle \alpha_3, i_r \rangle \\ \alpha_1, \alpha_2, \alpha_3 \in \mathcal{A}}}^{\text{all different}} \left\langle \left( c_{\alpha_1, s}^\dagger c_{\alpha_2, s} + c_{\alpha_2, s}^\dagger c_{\alpha_1, s} \right) \left( c_{\alpha_1, -s}^\dagger c_{\alpha_3, -s} + c_{\alpha_3, -s}^\dagger c_{\alpha_1, -s} \right) \right\rangle_0 \\
& - \frac{1}{2} \sum_{\substack{\langle \alpha_1, i_r \rangle, \langle \alpha_2, i_r \rangle, \langle \alpha_3, i_r \rangle, \langle \alpha_4, i_r \rangle \\ \alpha_1, \alpha_2, \alpha_3, \alpha_4 \in \mathcal{A}}}^{\text{all different}} \left\langle c_{\alpha_1, s}^\dagger c_{\alpha_2, -s} c_{\alpha_3, -s}^\dagger c_{\alpha_4, s} \right\rangle_0 \Big\} + \mathcal{O}(t^6), \tag{10.41}
\end{aligned}$$

where  $\langle \dots \rangle_0$  denotes an expectation value taken in the ground-state manifold.

Let us check the reliability of our perturbation theory. As can be seen in Fig. 10.8, the perturbative results, Eq. (10.41), agree well with the exact eigenenergies of a single-impurity system in the strong-coupling regime ( $L = 3$ ,  $i_1 = 2$ ). Expectedly, deviations become large when  $J$  is of intermediate order (here  $J < 4$ ), since the Kondo cloud cannot any longer be assumed to be local or even existing.

## The general effective low-energy Hamiltonian

As promised, we want to extend our formalism to incorporate spatially extended subsystems which result from confinement by impurities in constellations where next neighbours are at distance  $d \geq 2$ . A typical one-dimensional example is depicted in Fig. 10.9. However, we have to adapt our labels to properly account for the inhomogeneity in the electron system, i.e. resolve specific sites in the extended subsystems. Subsystems are labeled by  $\alpha \in \mathcal{A}$ , where  $\mathcal{A}$  denotes the set of all substrate sites which are



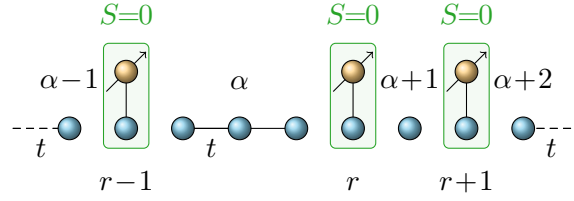


**Figure 10.9:** A generic one-dimensional impurity model in the ground state for  $J \rightarrow \infty$ .  $R$  Kondo singlets confine parts of the conduction-electron system, establishing independent electron subsystems  $\dots, \alpha - 1, \alpha, \alpha + 1, \dots$  for  $J \rightarrow \infty$ .

not connected to an impurity, while sites  $i \in \mathcal{B}$  are coupled to an impurity.  $\mathcal{A} \cup \mathcal{B}$  gives the set of all substrate sites.

Let us start with the unperturbed Hamiltonian

$$H_0 = J \sum_{r=1}^R \mathbf{S}_r \mathbf{s}_{i_r} - t \sum_{r=1}^R \sum_{\langle i,j \rangle \in \mathcal{A}} \sum_{\sigma} (c_{i,\sigma}^\dagger c_{j,\sigma} + \text{H.c.}). \quad (10.42)$$

It contains the local exchange interaction terms (first term) and the tight-binding Hamiltonian for sites which are not connected to an impurity (second term).

The hopping to and off a site  $i_r$  below an impurity is considered as perturbation

$$H_1 = \sum_{r=1}^R H_1^r = \sum_{r=1}^R \sum_{\substack{\langle j,i_r \rangle \\ j \in \mathcal{A}}} \sum_{\sigma} (c_{i_r,\sigma}^\dagger c_{j,\sigma} + \text{H.c.}) \quad (10.43)$$

$$= \sum_{r=1}^R \sum_{\alpha \in \mathcal{A}} \sum_{\substack{\langle j,i_r \rangle \\ j \in \alpha}} \sum_{\sigma} (c_{i_r,\sigma}^\dagger c_{\alpha,j,\sigma} + \text{H.c.}), \quad (10.44)$$

where we resolved explicitly the subsystem dependence of the conduction electrons in the last line.  $c_{\alpha,j,\sigma}$  annihilates an electron in subsystem  $\alpha$  at site  $j$  with spin  $\sigma$ .

Actually, it was necessary to repeat all calculations with the assumption that the unperturbed extended subsystems possess more than one one-particle state. Fortunately, this is not the case as we will see now.

The focus should be on the fourth-order one-impurity result (Eq. (10.40)) as it gives the essential contributions to the effective Hamiltonian. Since our derivation is correct up to fourth order in  $t$ , subsystem excitation energies  $\sim t$  will not appear in the energy denominators of the fourth-order result. This permits a tremendous simplification, since we are in the position to sum over all possible subsystem excitations, before calculating anything in detail. Employing completeness in the Hilbert space of a specific subsystem, this sum adds up to  $\sum_m P_m^{\mathcal{A}} = \mathbf{1}^{\mathcal{A}}$ . In the end, we obtain qualitatively the

## 10 Strong-coupling regime

same effective Hamiltonian as before. Keeping terms up to  $\mathcal{O}(t^4/J^3)$  and neglecting constant energy shifts, we find

$$\begin{aligned}
H_{\text{eff}} \sim & \frac{32}{3} \frac{t^4}{J^3} \sum_{r=1}^R \left\{ \sum_{\alpha \in \mathcal{A}} \sum_{\substack{\langle i, i_r \rangle \\ i \in \alpha}} \left( n_{\alpha, i, \uparrow} - \frac{1}{2} \right) \left( n_{\alpha, i, \downarrow} - \frac{1}{2} \right) \right. \\
& + 2 \sum_{\substack{\beta < \alpha \\ \alpha, \beta \in \mathcal{A}}} \sum_{\substack{\langle i, i_r \rangle, \langle j, i_r \rangle \\ i \in \alpha, j \in \beta}} (\mathbf{t}_{\alpha, i} \mathbf{t}_{\beta, j} - \mathbf{s}_{\alpha, i} \mathbf{s}_{\beta, j}) + 2 \sum_{\alpha \in \mathcal{A}} \sum_{\substack{i < j \\ \langle i, i_r \rangle, \langle j, i_r \rangle \\ i, j \in \alpha}} (\mathbf{t}_{\alpha, i} \mathbf{t}_{\alpha, j} - \mathbf{s}_{\alpha, i} \mathbf{s}_{\alpha, j}) \\
& - \sum_{\substack{\beta < \alpha \\ \alpha, \beta \in \mathcal{A}}} \sum_{\substack{\langle i, i_r \rangle, \langle j, i_r \rangle \\ i \in \alpha, j \in \beta}} \sum_s (c_{\alpha, i, s}^\dagger c_{\beta, j, s} + c_{\beta, j, s}^\dagger c_{\alpha, i, s}) \left( \frac{1}{2} Z_{i_r} - \sum_{\gamma \in \mathcal{A}} \sum_{\substack{\langle k, i_r \rangle \\ k \in \gamma}} n_{\gamma, k, -s} \right) \\
& - \sum_{\alpha \in \mathcal{A}} \sum_{\substack{i < j \\ \langle i, i_r \rangle, \langle j, i_r \rangle \\ i, j \in \alpha}} \sum_s (c_{\alpha, i, s}^\dagger c_{\alpha, j, s} + c_{\alpha, j, s}^\dagger c_{\alpha, i, s}) \left( \frac{1}{2} Z_{i_r} - \sum_{\gamma \in \mathcal{A}} \sum_{\substack{\langle k, i_r \rangle \\ k \in \gamma}} n_{\gamma, k, -s} \right) \\
& + \frac{1}{2} \sum_{\alpha_1, \alpha_2, \alpha_3 \in \mathcal{A}} \sum_{\substack{\text{all different} \\ \langle i, i_r \rangle, \langle j, i_r \rangle, \langle k, i_r \rangle \\ i \in \alpha_1, j \in \alpha_2, k \in \alpha_3}} (c_{\alpha_1, i, s}^\dagger c_{\alpha_2, j, s} + c_{\alpha_2, j, s}^\dagger c_{\alpha_1, i, s}) \\
& \quad \times (c_{\alpha_1, i, -s}^\dagger c_{\alpha_3, k, -s} + c_{\alpha_3, k, -s}^\dagger c_{\alpha_1, i, -s}) \\
& - \frac{1}{2} \sum_{\alpha_1, \alpha_2, \alpha_3, \alpha_4 \in \mathcal{A}} \sum_{\substack{\text{all different} \\ \langle i, i_r \rangle, \langle j, i_r \rangle, \langle k, i_r \rangle, \langle l, i_r \rangle \\ i \in \alpha_1, j \in \alpha_2, k \in \alpha_3, l \in \alpha_4}} c_{\alpha_1, i, s}^\dagger c_{\alpha_2, j, -s} c_{\alpha_3, k, -s}^\dagger c_{\alpha_4, l, s} \left. \right\}.
\end{aligned} \tag{10.45}$$

An important extension is the inclusion of interaction terms within a specific subsystem (third and fifth term), as a result of the fact that a particular Kondo singlet may have connections to different sites of the same subsystem.

## 10.5 Correlation functions and Kondo effects

In order to understand more deeply the implications of the effective low-energy strong-coupling Hamiltonian, Eq. (10.45), the correlations of two different families of impurity systems shall be investigated. The first part of this section centers around single-impurity systems ( $R = 1$ ), where, for  $J \rightarrow \infty$ , the Kondo singlet at  $i_1$  subdivides the substrate chain in two separate subsystems, what permits an unambiguous analysis of correlations. Another motivation comes from the observation that the subsystems can exhibit a magnetic or isospin Kondo effect due their mutual coupling by IIME. By contrast, multi-impurity models (second part) provide informations about the distribution of isospins. The following analysis and its conclusions are not specific to the

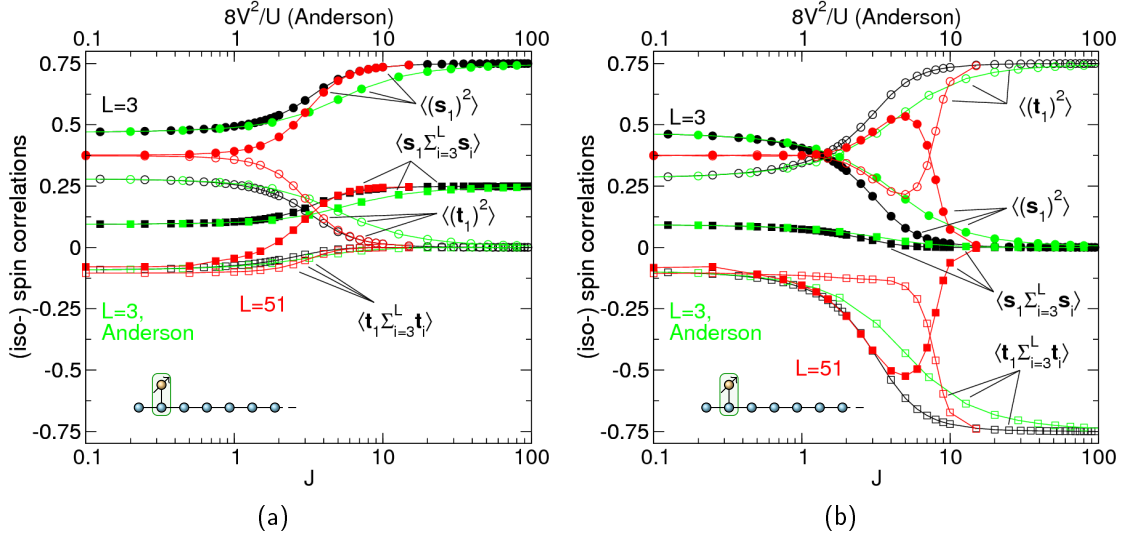


**Figure 10.10:** Spin and isospin correlations of single-impurity models in which the impurity is coupled to  $i_1 = 2$ . For an Anderson-type impurity model of system size  $L = 3$  (green symbols,  $U = 10$ ) and Kondo-type systems with  $L = 3$  (black symbols) and  $L = 51$  (red symbols). Local spin  $\langle s_1^2 \rangle$  (filled circles) and isospin  $\langle t_1^2 \rangle$  (open circles) are shown as functions of  $J$  on a log scale (lower horizontal axis) or, in case of an Anderson model, as functions of  $8V^2/U$  on a log scale (upper horizontal axis). Furthermore, the correlations between the two electron subsystems, which are formed for  $J \rightarrow \infty$ , are displayed, i.e.  $\langle s_1 \sum_{i=3}^L s_i \rangle$  (filled squares) and  $\langle t_1 \sum_{i=3}^L t_i \rangle$  (open squares). The inherent spin degeneracy of the ground state is lifted by an additional chemical potential for isospins  $\mu'_{iso}$ . Left:  $\mu'_{iso} = 10^{-2}$ . Right:  $\mu'_{iso} = -10^{-2}$ .

ground-state of the models under consideration but also give valuable impressions of the correlations of low-energy excited states of comparable systems at strong coupling strengths.

In case of  $R = 1$ , odd  $L$ , and  $i_1 = 2$ , we cannot apply Lieb's theorem (Sec. 3.5) since the ground state is degenerate, spanned by  $S_{gs} = 0$  and  $S_{gs} = 1$  states. For  $J \rightarrow 0$ , this is due to the effective decoupling of the impurity at a bad site (chapter 5). However, we also find the same ground-state degeneracy for  $J \rightarrow \infty$ , e.g. for system size  $L = 3$ : the  $S_{gs} = 0$  state is made up of isospins at the chain ends, whereas the  $S_{gs} = 1$  states contain ferromagnetically coupled spins there.

This circumstance allows us to easily switch between different types of ground states, since we can lift this degeneracy in a simple way for  $T_K > \Delta$ , i.e. in the presence of

## 10 Strong-coupling regime

the Kondo cloud. An additional, small<sup>1</sup> chemical potential  $\mu'_{\text{iso}}$  for isospins ( $|\mu'_{\text{iso}}| \ll 1$ ) can discriminate between states with different isospin number,

$$\mu'_{\text{iso}} \sum_i n_{i,\text{iso}} = \mu'_{\text{iso}} \sum_i ((1 - n_{i\uparrow})(1 - n_{i\downarrow}) + n_{i\uparrow}n_{i\downarrow}). \quad (10.46)$$

It favours ( $\mu'_{\text{iso}} < 0$ ) or repels ( $\mu'_{\text{iso}} > 0$ ) the development of isospins.<sup>2</sup> Supported by our numerical calculations, we will see that this treatment is successful for single-impurity models of size up to  $L = 51$  and for multi-impurity models with  $L = 47$  with impurities only at bad sites. However, the presence or absence of total subsystem isospins for models with impurities only at bad sites must be considered so far as not strictly proven but mainly motivated by numerical results.

Let us begin with the aforementioned single-impurity model (odd  $L$ ,  $i_1 = 2$ ), where, at strong  $J$ , the left substrate subsystem is just site 1, while the right subsystem is constituted by sites  $i = 3, 4, \dots, L$  (see pictogram in Fig. 10.10(a)). The results shown in Fig. 10.10(a) confirm that  $\mu'_{\text{iso}} > 0$  results in perfect spins in the two separate electron subsystems when  $J \rightarrow \infty$ : for  $L = 3$ ,  $\langle \mathbf{s}_1^2 \rangle = \langle \mathbf{s}_3^2 \rangle \rightarrow \frac{3}{4}$  (filled black circles) and  $\langle \mathbf{t}_1^2 \rangle = \langle \mathbf{t}_3^2 \rangle \rightarrow 0$  (black open circles). As expected from the magnetic coupling in the effective Hamiltonian, Eq. (10.45), the subsystem spins are ferromagnetically correlated  $\langle \mathbf{s}_1 \mathbf{s}_3 \rangle \rightarrow \frac{1}{4}$  (filled black squares). The same behaviour is observed for a larger system  $L = 51$  (red symbols) as well as for the correlations of an Anderson model of size  $L = 3$  (green symbols) at large  $V^2/U$ . However, the convergence of Anderson and Kondo-type models is not trivial due to strong charge fluctuations at the impurity site in case of the Anderson impurity. Nonetheless, a perturbation theory for Anderson impurities comparable to the one in section 10.4 could provide the understanding for it [121].

Decreasing  $J$  (or equivalently  $V^2/U$  for the Anderson-type model due to the Schrieffer-Wolff transformation, Sec. 2.2) permits the Kondo cloud to more and more delocalise. For  $\Delta > T_K$ , i.e. in the absence of the Kondo cloud, the IIME breaks down, and we may think of the conduction-electron system as a single standard Fermi sea at half-filling, since  $|\mu'_{\text{iso}}| \ll t$ . For larger system sizes ( $L = 51$ ) this implies for example short-range antiferromagnetic spin correlations, leading to  $\langle \mathbf{s}_1 \sum_{i=3}^L \mathbf{s}_i \rangle < 0$ . Furthermore, one finds an approximately equal density of spins and isospins at a particular site, i.e.  $\langle \mathbf{s}_i^2 \rangle \approx \langle \mathbf{t}_i^2 \rangle \approx \frac{1}{2} \frac{3}{4}$ . Apparently, it also leads to antiferromagnetic isospin correlations since  $\langle \mathbf{t}_1 \sum_{i=3}^L \mathbf{t}_i \rangle < 0$  (open squares). The  $L = 3$  systems converge to other values

<sup>1</sup>In general,  $|\mu'_{\text{iso}}|$  has to be balanced between  $|\mu'_{\text{iso}}| < \Delta$  to avoid additional formation of isospins, and  $|\mu'_{\text{iso}}| > \tilde{\alpha} = \frac{64}{3} \frac{t^4}{J^3}$  (Eq. (10.4)) to energetically separate low-energy states with and without total subsystem isospins. In case of models with impurities at bad sites, this simplifies to  $0 < |\mu'_{\text{iso}}| < \Delta$ .

<sup>2</sup>In practice, due to the special properties of "Kondo clouds" in the Anderson model for  $V \rightarrow \infty$ , in our calculations we used in this case an additional Hubbard- $U$  of the same size instead of  $\mu'_{\text{iso}}$ . This gives the same results for  $L = 3$  as is confirmed for Kondo-type models.

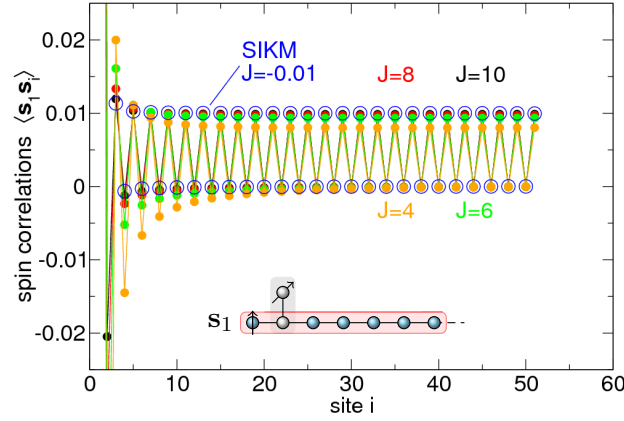


**Figure 10.11:** Spin correlations between the spin at the first chain site and sites  $i$  in the conduction-electron system  $\langle s_1 s_i \rangle$  for a single-impurity model with impurity at  $i_1 = 2$ . For  $L = 51$  and different local couplings  $J$  (as indicated). The spin degeneracy of the ground state is lifted by an additional chemical potential for isospins  $\mu'_{iso} = 10^{-2}$ . For comparison, we also show the same correlations (blue open circles) for a respective single-impurity Kondo model (SIKM,  $L = 49$ ,  $i_1 = 1$ ) with ferromagnetic  $J = -0.01$  (shifted by two sites to match the other correlation functions).

for  $J \rightarrow 0$  due to the strong discretisation.

A negative  $\mu'_{iso}$  generates the same ground-state correlations among the conduction electrons for  $J \rightarrow 0$ , as can be seen in Fig. 10.10(b). However, in the strong-coupling regime we obtain for all considered models a perfect isospin at the left chain end  $\langle t_1^2 \rangle \rightarrow \frac{3}{4}$  (open circles) and  $\langle s_1^2 \rangle \rightarrow 0$  (filled circles). The isospin is antiferromagnetically correlated with isospins of the right subsystem:  $\langle t_1 \sum_{i=3}^L t_i \rangle \rightarrow -\frac{3}{4}$  (open squares). In contrast to the case of a positive  $\mu'_{iso}$ , the crossover between the weak-coupling and the strong-coupling picture occurs already at larger  $J$  for  $L = 51$  and is much sharper:  $\langle t_1^2 \rangle$  decreases strongly for decreasing  $J$  around  $J \approx 10$ .

## Spin Kondo effect

The presence of a finite  $\mu'_{iso}$  slightly modifies the spectrum of the effective Hamiltonian for  $J \rightarrow \infty$  (Eq. (10.45)); with the intention to energetically separate ground states with and without total subsystem isospins. In the case of the above single-impurity model and  $\mu'_{iso} > 0$ , we consequently obtain the following "lowest-energy effective Hamiltonian"

$$H_{\text{eff}} \sim J' s_1 s_3, \quad (10.47)$$

where  $J'$  is ferromagnetic. Since the spin in the left subsystem  $\langle s_1^2 \rangle \approx \frac{3}{4}$  for  $J \gtrsim 5$  (see Fig. 10.10(a)), we can understand the original model in the lowest-energy sector

approximately as another single-impurity model of size  $L - 2$  where  $s_1$  plays the role of the magnetic impurity and couples ferromagnetically to the boundary of the right subsystem (sites 3 to  $L$ , see also pictogram in Fig. 10.11). Consequently, the spin correlations  $\langle s_1 s_i \rangle$  at  $i = 3, 4, \dots, L$ , shown in Fig. 10.11 for  $L = 51$ , can be explained as correlations of a ferromagnetic Kondo model.

The coupling  $J' \sim 64t^4/3J^3$  (Eq. (10.45)), increasing when  $J$  is decreased. Thus, the local parts of the spin correlations are supposed to become more dominant for decreasing but strong  $J$ . This is, however, not (or only slightly) observable. Instead, the correlations are almost homogeneous among the right subsystem, indicating a ferromagnetic finite-size Kondo effect, caused by the small subsystem size (Sec. 2.5). Our conclusions are corroborated by the comparison to the results of a corresponding single-impurity Kondo model ( $L = 49$ ,  $i_1 = 1$ ) with ferromagnetic  $J = -0.01$  (blue open circles), which approximately match those of  $J = 10$  ( $J' \approx 0.02$ ).

## Isospin Kondo effect

It becomes even more interesting when we analyse the ground state of the single-impurity model with  $\mu'_{\text{iso}} < 0$ . This setting favours a ground state for  $J \rightarrow \infty$  with antiferromagnetic coupling between isospins in the two subsystems, corresponding to the effective lowest-energy Hamiltonian

$$H_{\text{eff}} \sim J' \mathbf{t}_1 \mathbf{t}_3. \quad (10.48)$$

Since  $J'$  is antiferromagnetic,  $\mathbf{t}_1$  may be subject to Kondo screening by isospins of the right subsystem (see pictogram in Fig. 10.12(a)). This insight offers the exciting possibility of realising a Kondo effect without magnetic impurities (also known as "charge Kondo effect" [124]), based on valence fluctuations instead of spin fluctuations.

The charge Kondo effect has gained interest due to its low-temperature emergence in systems with strong electron-phonon interaction in  $C_{60}$  and  $C_{140}$  molecules, which gives rise to a negative Hubbard- $U$  ("bipolaronic state") [125]. If the molecule is attached to leads, isospin Kondo correlations develop. Another considered material is Tl-doped PbTe, which shows no magnetic moment but nevertheless a Kondo effect which is therefore assigned to the isospin degrees of freedom. The coupling of superconducting islands to non-superconducting leads may also give rise to such a Kondo effect [124]. The antiferromagnetic isospin Kondo effect here is caused by virtual excitations of the Kondo singlet.

With the preceding result for the spin Kondo effect in mind, which is strongly governed by finite-size effects, we want to roughly estimate the isospin Kondo scale  $\sim \exp(-\frac{1}{\rho J'})$ . Assuming a constant density of states  $\rho = \frac{1}{4}t$ , we find that even for larger system sizes and moderate  $J$  the condition for a finite-size Kondo effect,  $\Delta > T_K$ , is fulfilled: given  $J = 4$ , e.g., the subsystem size has to be of  $\mathcal{O}(10^5)$  to obtain  $\Delta = T_K$ . This

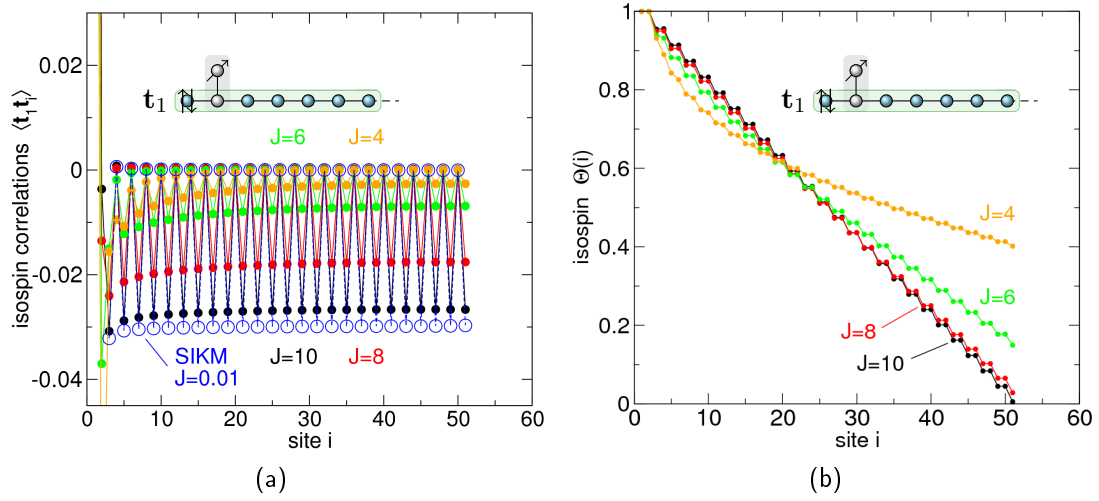


**Figure 10.12:** Left: isospin correlations between the isospin at the first chain site and sites  $i$  in the conduction-electron system  $\langle \mathbf{t}_1 \mathbf{t}_i \rangle$  for a single-impurity model with impurity at  $i_1 = 2$ . For  $L = 51$  and different local couplings  $J$  (as indicated). The spin degeneracy of the ground state is lifted by an additional chemical potential for isospins  $\mu'_{\text{iso}} = -10^{-2}$ . For comparison, we also show the same correlations (blue open circles) for a respective single-impurity Kondo model (SIKM,  $L = 49$ ,  $i_1 = 1$ ) with antiferromagnetic  $J = 0.01$  (shifted by two sites to match the other correlation functions). Right: the corresponding (integrated) correlation functions  $\Theta(i)$  (Eq. (10.49)) as functions of sites  $i$ .

result questions the applicability for standard DMRG if one aims at going beyond the finite-size regime.

Consequently, we can expect the isospin Kondo effect to be always cut by the subsystem size in our calculations. This is indeed seen in the isospin correlations between  $\mathbf{t}_1$  and the isospins  $\mathbf{t}_i$  of the right subsystem, displayed in Fig. 10.12(a) for a system size  $L = 51$ . For  $J = 10$ , but also for smaller couplings  $J$ , one finds a nearly homogeneous Kondo cloud, however, with decreasing modulus of correlations for decreasing  $J$  owing to the fast decay of  $\langle \mathbf{t}_1^2 \rangle$  (Fig. 10.10(b)).

For the same reason, the matching of results at  $J = 10$  to the correlations of an ordinary single-impurity model of size  $L - 2$  with antiferromagnetic  $J = 0.01$  is worse than in the case of positive  $\mu'_{\text{iso}}$ . It is also illuminating to have a look on the following the integrated correlation function (Fig. 10.12(b))

$$\Theta(i) = 1 + \sum_{j=3}^i \frac{\langle \mathbf{t}_1 \mathbf{t}_j \rangle}{\langle \mathbf{t}_1 \mathbf{t}_1 \rangle}. \quad (10.49)$$

It is formulated in analogy to the usual spin Kondo effect [69] (Eq. (2.38)).  $\Theta(i)$

gives the fraction of the isospin  $\mathbf{t}_1$  which is not screened by isospins at sites  $3, \dots, i$ . Our results show that, with decreasing  $J$ ,  $\Theta(i)$  is increasing for  $i > 20$  and conversely decreasing for  $i < 20$ . In spite of the growing  $J'$ , the screening becomes weaker: the right subsystem even cannot screen  $\mathbf{t}_1$  completely for  $J \lesssim 8$ , what can be inferred from  $\Theta(L) > 0$ . We also have to realise that for decreasing  $J$  the basic assumption of our perturbation theory, that the Kondo cloud of  $\mathbf{S}_1$  is local, becomes more and more unrealistic, leading to substantial deviations from the strong-coupling picture, e.g. in regard of the declining  $\langle \mathbf{t}_1^2 \rangle$ .

Obviously,  $\Theta(i)$  is almost a linear function of chain site  $i$  at  $J \gtrsim 6$ . However, a conventional Kondo effect is expected to show a stronger decay [69], as we have seen for an ordinary single-impurity model in section 2.5 (Fig. 2.6(a)). This fact is highlighting again the important role of finite-size effects for the "inverse-exchange" spin and isospin Kondo effect.

## Spatial distribution of the isospin pair

The presence of isospins in ground states of models in the strong-coupling regime may have attracted already interest as the foundation of an isospin Kondo effect. If we let us guide by our previous results, we can further ask how they are distributed and interacting with each other in the presence of a greater number of local Kondo singlets. It can be supposed for  $J \rightarrow \infty$  that, when impurities are coupled without exception to bad sites, the ground-state manifold contains states with total spin  $S_{\text{gs}} = \frac{1}{2}(R+1)$  and  $S_{\text{gs}} = \frac{1}{2}(R-1)$ . For small and moderately large single-impurity models, we already confirmed that this degeneracy translates to the absence or presence of an antiferromagnetically-coupled  $T = \frac{1}{2}$  isospin pair for  $J \rightarrow \infty$ , and can be lifted by an additional  $\mu'_{\text{iso}} \neq 0$ . Let us show the same for a multi-impurity model.

However, a crucial insight is that the collective Kondo energy scale  $T_K^{(\text{Rspins})} \ll T_K^{(\text{1spin})}$ , generated by the RKKY interaction, is cut by the rather small system size (Sec. 9.2), i.e.  $J_D \approx J_{\Delta, \text{Rspins}}$ . Taking  $J_D = 1 - 2$  from results of other models (Sec. 9.2), we would consequently not assume the presence of Kondo clouds below  $J_D$ , what is, on the other hand, the basic assumption for IIME. And indeed, our numerical results show no evidence for the isospin pair at  $J = 1.5$ .

We compare the results of three different multi-impurity models (shown as pictograms in Fig. 10.13(a)), where next-neighbouring impurities are at distance  $d = 2$ . The system with  $L = 49$  and  $R = 25$  contains no isospin for  $J \rightarrow \infty$  (all impurities are at good sites). This model and its properties will be inspected in more detail in the following chapters 11 and 12. For system size  $L = 47$  and  $R = 23$  (all impurities are at bad sites), the ground state is degenerate.

Fig. 10.13(a) displays the local isospin  $\langle \mathbf{t}_i^2 \rangle$  for all three considered models. While, expectedly, the isospin density is almost vanishing at  $J = 10$  for  $L = 49$  (black



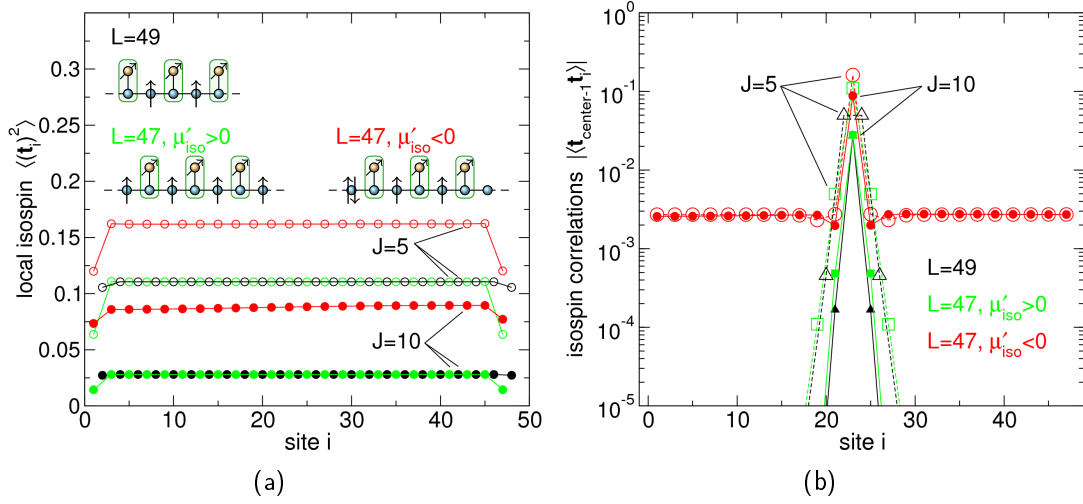


**Figure 10.13:** Results for multi-impurity Kondo models with distance  $d = 2$  between next-neighbouring impurities, as depicted in the left panel: for  $L = 49$  ( $R = 25$ , black symbols, results shifted for better visibility) and  $L = 47$  ( $R = 23$ ). In case of  $L = 47$ , we employ an additional chemical potential for isospins  $\mu'_{\text{iso}} = 10^{-4}$  (green symbols) or  $\mu'_{\text{iso}} = -10^{-4}$  (red symbols), respectively, to avoid a degenerate ground state. Left: local conduction-electron isospins  $\langle \mathbf{t}_i^2 \rangle$  as functions of sites  $i$  without Kondo singlet. Right: modulus of isospin correlations  $|\langle \mathbf{t}_{\text{center}-1} \mathbf{t}_i \rangle|$  on a log scale. We show the correlations between the site left to the central site and chain sites  $i$  without Kondo singlet. For  $J = 10$  (filled circles) and  $J = 5$  (open circles). Note that, except of  $\langle \mathbf{t}_{\text{center}-1} \mathbf{t}_{\text{center}-1} \rangle$ , the correlations  $\langle \mathbf{t}_{\text{center}-1} \mathbf{t}_i \rangle$  are negative (antiferromagnetic).

symbols) and  $L = 47$  with  $\mu'_{\text{iso}} > 0$  (green symbols), for the system with  $L = 47$  and  $\mu'_{\text{iso}} < 0$  (red symbols) we find that the isospin pair is smeared over the whole lattice (the slight spatial asymmetry is a harmless numerical artifact). It is even stable down to the coupling  $J = 5$ , since the excess isospin number, defined by

$$\Delta N_{\text{iso}} = \sum_i \left( \langle n_{i,\text{iso}} \rangle|_{\mu'_{\text{iso}} < 0} - \langle n_{i,\text{iso}} \rangle|_{\mu'_{\text{iso}} > 0} \right), \quad (10.50)$$

is computed to be  $\Delta N_{\text{iso}} \approx 1.66$  at  $J = 5$  (to be compared with  $\Delta N_{\text{iso}} \approx 1.92$  at  $J = 10$ ). This fact is reflected by  $\langle \mathbf{t}_i^2 \rangle$  which is obviously larger for  $\mu'_{\text{iso}} < 0$  than for  $\mu'_{\text{iso}} > 0$ . It should be realised that this observation is quite surprising as the large number of impurities may give rise to heavy-fermion physics at intermediate couplings, possibly interfering with the IIME (chapter 13).

The correlations between isospins at different sites vanish exponentially as functions of the distance for  $L = 49$  (black symbols) and  $L = 47$  with  $\mu'_{\text{iso}} > 0$  (green symbols), as can be seen in Fig. 10.13(b). It is clear that these isospins are essentially uncorrelated, reflecting that the excess electrons are non-interacting in this regard. This statement

## 10 Strong-coupling regime

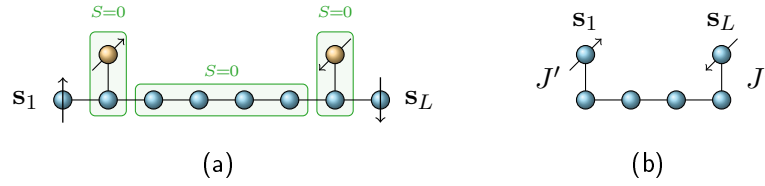


**Figure 10.14:** Left: two-impurity model at antiferromagnetic distance in the deep Kondo regime. Two  $S = \frac{1}{2}$  spins are confined at the chain ends for  $J \rightarrow \infty$  due to the formation of local Kondo clouds. Right: the corresponding effective low-energy model, describing the antiferromagnetic coupling of  $s_1$  and  $s_L$  as an "inverse RKKY exchange", mediated by electrons of the subsystem between both spins. The two local Kondo singlets (not shown) provide the effective exchange coupling  $J' \sim -\frac{t^4}{J^3}$  (IIME), which is ferromagnetic and locally couples  $s_1$  and  $s_L$  to the intermediate subsystem.

applies to  $J = 5$  as well as to the large coupling  $J = 10$ , albeit with differently strong decay rates in space. We need to contrast this finding with the correlations found in the model with  $L = 47$  and  $\mu'_{\text{iso}} < 0$  (red symbols): although it displays comparable short-range isospin correlations, for large distances from the central site we find small but constant long-range correlations for  $J = 5$  and  $J = 10$  due to the presence of the nonlocal isospin pair. It might be regarded as precursor of a transition to an antiferromagnetically isospin-ordered ground state, which, however, would be destroyed by order parameter fluctuations in this one-dimensional model due to the Mermin-Wagner theorem [106]. Hence, the long-range isospin correlations are constrained to a small value and vanish in the thermodynamic limit.

## 10.6 Indirect inverse exchange and adiabaticity

In section 10.2 we employed a two-impurity model to give an example for the adiabaticity between weak and strong-coupling regime, which is also enforced by Lieb's theorem under specific conditions (Sec. 3.5). However, the properties of more complex impurity models in the strong-coupling regime may not be directly obvious from our perturbative results (section 10.4). Take for example the two-impurity model at antiferromagnetic distance, depicted in Fig. 10.14(a), which has a singlet ground state. For  $J \rightarrow \infty$ , the two Kondo singlets at  $i_1 = 2$  and  $i_2 = L - 1$  produce two independent  $S = \frac{1}{2}$  spins at  $i = 1$  and  $i = L$ , and a non-magnetic subsystem in between them, i.e. comprising sites  $i = 3, \dots, L - 2$ . The absence of total subsystem isospins in the ground state manifold is a consequence of the Hubbard- $U$  like expressions in  $H_{\text{eff}}$ . We could diagonalise  $H_{\text{eff}}$  for the purpose of studying the ground state, which is, on the other hand, impossible for large  $L$ . Hence, we try an analytical approach: for  $J \rightarrow \infty$ , one could just calculate the energy corrections  $\langle H_{\text{eff}} \rangle_0$  as a rough approximation for  $t^4/J^3 \ll 1$  (Eq. (10.45)).

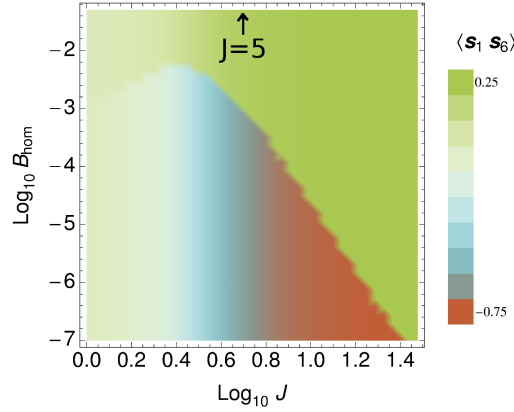


**Figure 10.15:** Ground-state correlations between  $\mathbf{s}_1$  and  $\mathbf{s}_L$  for a two-impurity model at antiferromagnetic distance (similar to Fig. 10.14(a)) in an homogeneous magnetic field  $B_{\text{hom}}$ . Correlations are shown as functions of  $J$  and  $B_{\text{hom}}$  on a double log scale. System size  $L = 6$ . Results have been obtained by full diagonalisation.

However, a piece is missing, because the degeneracy of both spins at  $i = 1$  and  $i = L$  is not lifted by  $\langle H_{\text{eff}} \rangle_0$ , since  $H_{\text{eff}}$  couples sites adjacent to a particular Kondo singlet. Fortunately, Fig. 10.14(a) is already suggestive of a resemblance to the ordinary two-impurity model at weak couplings but here with ferromagnetic local exchange coupling  $J'$ . We just need to conduct another perturbation theory, but for weak  $J' \sim \tilde{\alpha} \sim t^4/J^3$  and  $H_{\text{eff}}$ , i.e. within the low-energy sector of  $H$ . In second order,  $\mathbf{s}_1$  and  $\mathbf{s}_L$  are then antiferromagnetically coupled via an indirect inverse exchange, comparable to the RKKY exchange at weak  $J$  (Fig. 10.14(b)). This readily suggests the asymptotic form of the indirect coupling

$$J_{\text{IE}} \sim (J')^2 (-1)^{(d-2)}/(d-2), \quad (10.51)$$

where  $d$  denotes the impurity distance  $d = |i_1 - i_2|$ . An oscillatory distance dependence similar to the RKKY interaction is obtained, whereas the  $1/d$  dependence may be modified due to the strong Friedel oscillations present in the local density of states at the boundaries  $i = 3$  and  $i = L - 2$  of the intermediate subsystem, to which  $\mathbf{s}_1$  and  $\mathbf{s}_L$  are naturally coupled.

In order to observe the energy scale  $J_{\text{IE}}$ , we may precede in the same way as in our discussion of energy scales in the weak-coupling regime in section 6.5: an homogeneous magnetic field  $B_{\text{hom}}$  is applied to the system and its ground-state correlations are analysed (see section 6.5 for details). The  $J$  dependence of  $J_{\text{IE}}$  is evident from Fig. 10.15, where  $\langle \mathbf{s}_1 \mathbf{s}_L \rangle$  is shown for a two-impurity model at antiferromagnetic distance as a function of  $J$  and  $B_{\text{hom}}$ . Keeping  $J > 5$  fixed, the IIE energy scale  $J_{\text{IE}}$  is exceeded by  $B_{\text{hom}}$  precisely when  $\langle \mathbf{s}_1 \mathbf{s}_L \rangle$  turns ferromagnetic. From the slope of the transition line (Fig. 10.15), one infers that indeed  $J_{\text{IE}} \sim 1/J^6 = (J')^2$ .

## 10 Strong-coupling regime

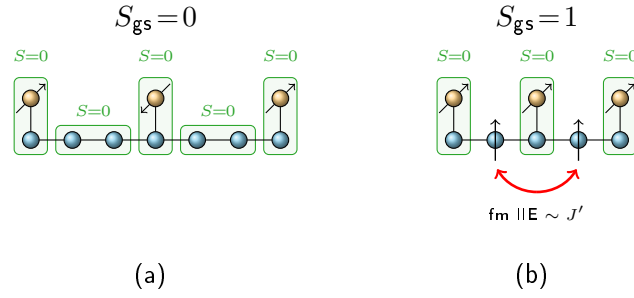


**Figure 10.16:** Three-impurity models in the deep Kondo regime. Left: "good-bad-good" case,  $L = 7$ . Singlet ground state. Right: "good-good-good" case,  $L = 5$ . Ferromagnetic spin exchange between spins, which are formed close to the central local Kondo cloud, leads to a triplet ground state.

Our analysis highlights the inverse nature of the indirect exchange: it shares interesting similarities to the weak-coupling RKKY theory, while the resulting effective Hamiltonian is formulated for conduction electrons instead of impurities. Let us additionally remark that in principle one may expect an exponential dependence of  $J_{\text{IE}}$  on the number of Kondo singlets between two sites [121].

Not only for the two-impurity model, the inverse exchange might be regarded as a consequence of the adiabaticity between weak and strong-coupling regime. In order to motivate this, we turn to the three-impurity models treated in chapter 6 (compare also Fig. 6.1).

In the "good-bad-good" case (Fig. 10.16(a)), all electron subsystems formed for  $J \rightarrow \infty$  have vanishing total spin, i.e. the ground state is a singlet state. By contrast, for a "good-good-good" configuration, shown in Fig. 10.16(b), ferromagnetically coupled spins develop next to the local Kondo singlet of impurity  $S_2$ , leading to  $S_{gs} = 1$ . In the "bad-good-bad" configuration, shown in Fig. 10.17(c), two spins are formed at the chain ends for  $J \rightarrow \infty$ , just as in the antiferromagnetic two-impurity model. However, due to the odd number of intermediate Kondo singlets these are ferromagnetically coupled. Therefore, a triplet ground state is obtained.

For all considered configurations, we obtain complete agreement with the total ground-state spin of the weak-coupling regime, rooted in the adiabatic ground-state property of these models at half-filling. But we can likewise exploit this circumstance to figure out how the same total spin develops in the RKKY regime, which has not been treated so far. Let us take the "bad-good-bad" configuration as example, where  $S_{gs} = 1$ , as we know for example from the weak-coupling regime (Fig. 10.17(a)). For  $J_{\Delta,1\text{spin}} < J < J_D$ , the three impurities are RKKY-coupled to a total impurity doublet, which may be screened conventionally by the conduction electrons if  $\Delta < T_K^{(3\text{spins})}$ , see Fig. 10.17(b). In this case, we must assume a triplet somewhere in the conduction-electron system,

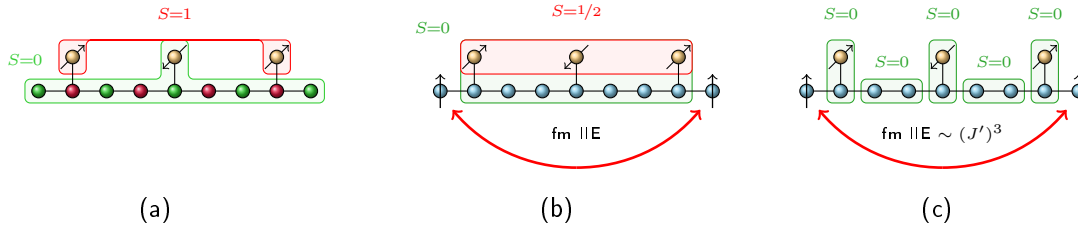


**Figure 10.17:** Ground-state adiabaticity in the "bad-good-bad" configuration, which has a triplet ground state for finite  $J$ . Left: finite-size Kondo regime ( $J < J_{\Delta,1spin}$ ). The triplet is formed between the impurities at bad sites. Middle: conventional RKKY regime ( $J_{\Delta,3spins} < J$ ). The impurity doublet  $S_{tot} = \frac{1}{2}$  is screened by conduction electrons, giving rise to two spins developing at the chain ends. Both spins are coupled by ferromagnetic spin exchange through the collective Kondo cloud. Right: deep Kondo regime. The triplet is again formed between spins at the chain ends, as discussed in the text.

which can only arise from ferromagnetically coupled spins formed at the chain ends due to symmetry. Hence, we can draw the remarkable conclusion that the inverse exchange mechanism is also valid with the same qualitative implications for more complex Kondo singlets, i.e. even in the RKKY regime with its collective screening cloud, and also for spatially extended Kondo singlets, as was already suggested in the introduction.

## 10.7 Summary

We have proposed an indirect magnetic exchange mechanism where confinement of conduction electrons due to scattering at Kondo singlets leads to local-moment formation at a priori uncorrelated sites. This IIME is "inverse" to the conventional RKKY coupling, as it describes weakly magnetic and isospin interactions among the not trapped electrons in the Kondo regime, mediated by virtual excitations of Kondo singlets. In complex impurity constellations, it is found to become oscillatory, depending on impurity distances and the number of intermediate Kondo singlets. Furthermore, by means of it, we are able to understand the ground-state adiabaticity at half-filling [47, 48, 72]. The IIME of a single Kondo singlet gives rise to ferromagnetic spin exchange as well as to antiferromagnetic isospin exchange, which can lead under specific conditions to an additional charge Kondo effect in the conduction-electron system with rather small  $T_K$ .

The question of magnetic ordering, e.g. due to RKKY exchange or IIME, has been excluded up to now. However, it shall lead over to the next chapter which is dedicated to the depleted Kondo lattice model in which impurities are located at every second

## *10 Strong-coupling regime*

site. At half-filling and for large  $L$ , we can thus expect to find a total impurity spin of macroscopic order; at weak couplings due to the ferromagnetic distance, whereas ferromagnetic order at strong couplings is provided by the excess electrons via IIME.

# 11 Depleted Kondo lattice model

## 11.1 Introduction

In the course of our study so far, we constructed a rich picture of impurity physics, which extends from the weak-coupling regime ( $|J| \ll t$ ) to the strong-coupling regime ( $J \gg t$ ). The weak-coupling regime is dominated by finite-size effects for  $T_K < \Delta$ , as discussed in chapters 4, 5, and 6. For  $T_K > \Delta$  but  $J < J_D$ , RKKY exchange wins the competition with the conventional Kondo effect, which, in return, governs the strong-coupling regime. As worked out in chapter 10, for strong  $J$ , local Kondo singlets provide the indirect inverse exchange for the remaining, not trapped conduction electrons. Furthermore, for certain geometries, the IIME can be understood as evolving by adiabatic connection from the standard RKKY coupling at weak  $J$ . This is ensured by (i) quantum confinement due to Kondo singlets and by (ii) exact results [48, 72] based on Lieb's concept of reflection positivity in spin space [47], which is applicable for Kondo systems on bipartite lattices at half-filling (Sec. 3.5).

At half-filling, the dense Kondo lattice model is always paramagnetic, while magnetic ordering may appear away from half-filling [97]. Another strategy to obtain magnetic ground states—which we will pursue in the following—is to deplete impurities, so that the excess conduction electrons at  $J \rightarrow \infty$  can magnetically order [53]. We will work with the depleted Kondo lattice model where we have an impurity only at every second site, leading to a large total spin.

The current chapter revolves around the emergence of magnetic order resulting from the different ordering mechanisms in the weak and strong-coupling regime, which becomes possible for  $L, R \rightarrow \infty$ . Especially in higher dimensions and away from half-filling (chapter 12), this is an important issue as, e.g., predictions of the ordering of the excess electrons at large coupling strengths become difficult.

The IIME shows an oscillatory distance dependence. For extended systems, it triggers long-range magnetic order, which is robust against charge fluctuations at impurity sites but sensitively depends on the quantum confinement of the conduction electrons, e.g., on the geometry of magnetic adatoms in an experimental setup using scanning-tunneling techniques. We study the magnetic order resulting from IIME by means of DMRG and R-DMFT which allows to investigate multi-impurity systems in higher dimensions, being relevant for experiments. Additionally, we will investigate properties

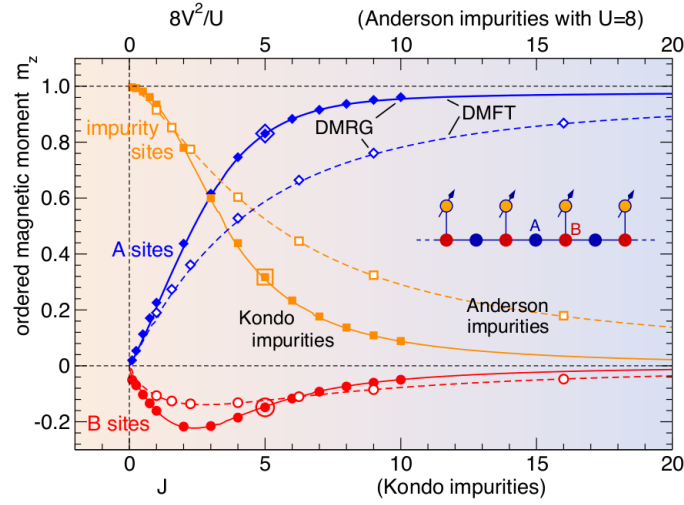


**Figure 11.1:** Crossover from the RKKY regime at weak coupling to the IIME regime at strong coupling. Calculated ordered magnetic moments on different sites of a tight-binding chain with  $\text{spin-}1/2$  Kondo impurities as functions of  $J$  (solid lines, filled symbols) and with Anderson impurities as functions of  $8\frac{V^2}{U}$  at Hubbard  $U = 8$  (dashed, open)—see pictogram for system geometry. Symbols: DMRG data for a system with  $L = 49$  uncorrelated sites (A and B),  $R = 25$  impurities (large symbols at  $J = 5$ :  $L = 89$ ,  $R = 45$ ), open boundary conditions. Lines: real-space dynamical mean-field theory (R-DMFT) for  $L = 100$ ,  $R = 50$ , periodic boundary conditions. Figure taken from Ref. [24].

of the low-energy excitations of the depleted Kondo lattice model. In doing so we will closely follow the argumentation and ideas given in our paper, Ref. [24].

## 11.2 Magnetic order

The emergence of magnetic order in condensed-matter systems has three necessary requirements (i) the existence or formation of local magnetic moments, (ii) a coupling mechanism favouring a certain alignment of the moments, e.g. ferro- or antiferromagnetically, and (iii) the stability of long-range magnetic order against different types of thermal or quantum fluctuations and as well against competing ordering phenomena such as superconductivity, charge or orbital order.

As we described in section 2.2, local-moment formation typically results from incompletely filled localised orbitals or from strong local correlations, and can be described in Hubbard-, Anderson-, or Kondo-type models [55, 126]. Coupling mechanisms can arise as consequence of different reasons: for example as direct Heisenberg exchange [127], as indirect Anderson super exchange [128, 129] or as other exchange mechanisms using



intermediate orbitals in insulators [130]. Another possibility is indirect RKKY exchange [12, 13, 14] in metallic host systems, which provides oscillatory, long-ranged couplings  $J_{\text{RKKY}} \sim \pm J^2/r^D$  between magnetic impurities in a system of dimensionality  $D$ .

While magnetic order at weak  $J$  due to RKKY exchange has been studied extensively, this is not the case for strong  $J$ . In the preceding chapter, we proposed the inverse indirect exchange mechanism (IIME) for the deep Kondo regime, where the roles of conduction electrons and impurities are "inverted". Referring to the requirements for magnetism listed above, we show that the Kondo effect helps (i) to form local moments, (ii) to couple the moments, and (iii) leads to magnetic order in certain nano-structured geometries.

We demonstrate that both exchange mechanisms indeed cause ferromagnetic order for large systems  $L, R \rightarrow \infty$ . As an example we choose a one-dimensional Kondo lattice model with a certain depletion scheme: impurities are coupled to sites  $i_r = 1, 3, \dots, L-2, L$  (B-sites, see inset of Fig. 11.1), i.e. at ferromagnetic distances. In the following, we numerically study this model for different  $L$  and  $R = \frac{1}{2}(L+1)$  impurities ( $R$  odd). At half-filling this model is known to exhibit a ferromagnetic ground state [48] and for the system shown in Fig. 11.1 ( $L = 49, R = 25$ ), in fact we find a large spin  $S_{\text{gs}} = \frac{1}{2}(R-1)$  in the entire  $J$  range.

In the same way as in section 10.2, one can understand the development of ferromagnetism for large systems. However, the adiabatic connection between RKKY exchange and IIME is more subtle in this case: in contrast to standard RKKY arguments, for  $J \rightarrow 0$  one impurity spin is screened by the single  $k_F$  conduction electron (see chapter 5 and Ref. [21]). This results in  $S_{\text{gs}} = \frac{1}{2}(R-1)$ . We find that the ground state for all (finite but large) systems studied here is a smooth function of  $J$ , and hence the total spin must be the same in both limits. For  $J \rightarrow \infty$  this large spin must be a consequence of the ferromagnetic coupling of local magnetic moments at the sites  $i = 2, 4, \dots, L-1$  (A-sites), which are formed as result of the increasing confinement of electrons due to the more and more local Kondo singlets at B-sites. This view is supported by the calculations yielding strong antiferromagnetic local spin correlations  $\langle \mathbf{s}_{i_r}, \mathbf{S}_r \rangle \rightarrow -\frac{3}{4}$ , vanishing RKKY correlations  $\langle \mathbf{S}_r, \mathbf{S}_{r'} \rangle \rightarrow 0$ , and local moment formation  $\langle \mathbf{s}_i^2 \rangle \rightarrow \frac{3}{4}$  at A-sites for  $J \rightarrow \infty$ .

Fig. 11.1 displays the ordered magnetic moments at special sites in the model system obtained from the ground state with maximum  $M_{\text{gs}} = S_{\text{gs}}$ : at the central impurity  $m_{\text{imp}} = 2\langle \mathbf{S}_{r,z} \rangle$ , at the B-site below this impurity  $m_B = \langle n_{i_r,\uparrow} - n_{i_r,\downarrow} \rangle$  and a neighbouring A-site  $m_A = \langle n_{i\uparrow} - n_{i\downarrow} \rangle$ . With increasing  $J$ , there is a clear crossover from the RKKY regime with  $m_{\text{imp}} \approx 1$  and  $m_A, m_B \rightarrow 0$ , to the IIME regime for  $J \rightarrow \infty$  where the magnetisation of the system results from ordered moments at A-sites. By comparing results for  $L = 49$  and  $L = 89$  (see large symbols at  $J = 5$  in Fig. 11.1), it is evident that the values are characteristic for the infinite system.

Employing the results of Sec. 10.4 which are based on treating the hopping term  $\sim t$

perturbatively, for  $J > 0$  and keeping terms up to  $\mathcal{O}(t^4/J^3)$ , we get

$$H_{\text{eff}} = -\tilde{\alpha} \sum_{\substack{i < j \in A \\ \langle i, j \rangle}} (\mathbf{s}_i \mathbf{s}_j - \mathbf{t}_i \mathbf{t}_j) + \tilde{\alpha} \sum_{i \in A} \left( n_{i\uparrow} - \frac{1}{2} \right) \left( n_{i\downarrow} - \frac{1}{2} \right) \quad (11.1)$$

$$- \frac{1}{2} \tilde{\alpha} \sum_{\substack{i < j \in A \\ \langle i, j \rangle}} \sum_{\sigma} \left( c_{i\sigma}^{\dagger} c_{j\sigma} + \text{H.c.} \right) (1 - n_{i-\sigma} - n_{j-\sigma})$$

$$\tilde{\alpha} = \frac{64}{3} \frac{t^4}{J^3}. \quad (11.2)$$

As discussed in chapter 10, we obtain ferromagnetic couplings between magnetic moments at next-nearest neighbouring A-sites  $i$  and  $j$  (first term), which explains the ferromagnetic nature of IIME through a local Kondo singlet. This ferromagnetism competes with the formation of a charge-density wave or  $\eta$  pairing [97], as favoured by the second term, which is written in terms of the local isospin (defined in Eq. (10.5)).

An important aspect is that the effective isospin interaction is antiferromagnetic. Thus, it is suppressed by thermal and quantum fluctuations of the order parameter for  $D = 1$  due to the Mermin-Wagner theorem [106]. This is opposed to ferromagnetic spin order at zero temperature. The necessary formation of local isospin moments in the ground state is suppressed anyway by the repulsive Hubbard term (third term in Eq. (11.1)), which favours formation of local magnetic moments.

Finally, there is a correlated hopping term in  $H_{\text{eff}}$  (fourth term), which is only active between a spin at  $i$  and an isospin at  $j$  or vice versa. It is interesting to recognise that under certain conditions it gives rise to an effective band picture [121]. The question arises for larger lattices if this situation in combination with the isospin interaction can be regarded as a seed for superconductivity, established by local Kondo singlets. This is an appealing idea due to the simultaneous presence of isospin and magnetic couplings of similar scale, suggesting resemblance to the situation in a great deal of unconventional superconductors [56, 97].

### 11.3 Charge fluctuations

As already suggested in section 10.5, the IIME mechanism is robust against charge fluctuations at the impurity sites, which shall be demonstrated here for the depleted Kondo lattice model. The spin- $\frac{1}{2}$  Kondo impurities are replaced by Anderson impurities, i.e. the coupling term in the Hamiltonian  $J \sum_{r=1}^R \mathbf{s}_{ir} \cdot \mathbf{S}_r$  is replaced by (Sec. 2.4)

$$U \sum_{r=1}^R \left( n_{r\uparrow} - \frac{1}{2} \right) \left( n_{r\downarrow} - \frac{1}{2} \right) + V \sum_{r=1}^R \sum_{\sigma} (d_{r\sigma}^{\dagger} c_{ir\sigma} + \text{H.c.}) \quad (11.3)$$

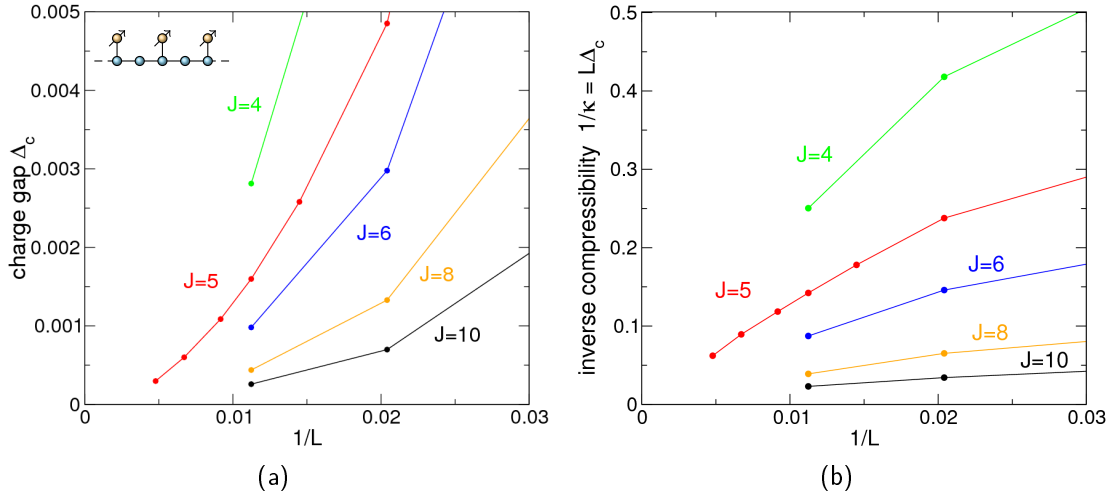


**Figure 11.2:** Left: charge gap  $\Delta_c$ , as defined in the text by Eq. (11.4), for the depicted depleted Kondo lattice model as functions of the inverse system size  $1/L$ . Calculated at half-filling for different couplings  $J$  as indicated. Right: the respective inverse compressibilities  $1/\kappa = L\Delta_c$  as functions of the inverse system size  $1/L$ .

$d_{r\sigma}^\dagger$  creates an electron at the  $r$ -th impurity site, namely a correlated site with Hubbard interaction  $U$  coupled to the conduction electrons by a hybridisation  $V$ .

The weak- $V$  limit is the Kondo limit with  $S = \frac{1}{2}$ -impurities at ferromagnetic distance, prescribed by the Schrieffer-Wolff transformation [58] (Sec. 2.2). It is indeed seen in Fig. 11.1 for  $8\frac{V^2}{U} = J \ll t$  and that the results of the Kondo model and the Anderson model (filled and open symbols) agree. Deviations are found beyond the Kondo limit and grow with increasing  $V$ , since the mapping is not any more reliable. However, both models show a crossover from RKKY-coupled magnetic moments at the impurity sites for weak  $V$  to IIME-coupled moments formed at the A-sites for strong  $V$ . For all finite couplings, the ground state is ferromagnetic. For Kondo impurities, the crossover takes place between  $J/t = 2$  and  $J/t = 4$ , while in the Anderson model it is located around  $V/t = 2$  for the respective  $D = 1$  models. In the Anderson model for strong  $V$ , confinement of A-site electrons is due to the formation of local and strongly bound states. The corresponding local states are equal mixtures of spin singlet and isospin singlet states, and hence display less magnetic correlations between impurity and B-site than Kondo singlets. It is remarkable that nevertheless we obtain the same physics as for Kondo impurities. We again note that a strong-coupling perturbation theory for Anderson impurities could support this conclusion [121].

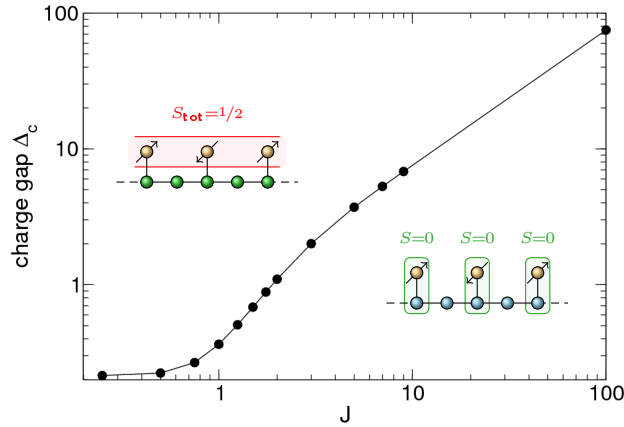


**Figure 11.3:** Charge gap  $\Delta_c$ , as defined in the text by Eq. (11.4), for the depleted Kondo lattice model discussed in this chapter. Calculated at quarter-filling for a system size  $L = 21$  and shown as a function of  $J$  on a double log scale.

## 11.4 Low-energy spin and charge excitations

The ferromagnetic state of the considered one-dimensional depleted Kondo lattice model represents a symmetry-broken state. Thus, its low-energy spin excitations are determined by magnons [61], whose dispersion relation vanishes for decreasing momenta [131]. Consequently, the spin gap between ground state and the respective one-magnon state vanishes for  $L \rightarrow \infty$ .

Furthermore, we find that the state is metallic. This is clear for the RKKY limit and easily verified in the intermediate and strong-coupling case by considering the charge gap

$$\Delta_c = \frac{1}{2}(E_0(N+2) + E_0(N-2) - 2E_0(N)), \quad (11.4)$$

where  $E_0(N)$  is the ground-state energy for  $N$  electrons in the  $M_{\text{tot}} = 0$  sector. We have calculated  $\Delta_c = \Delta_c(J, L)$  for different  $L = 49, 89, \dots$  (Fig. 11.2(a)) to get the charge susceptibility (compressibility)  $\kappa$  via  $\kappa^{-1} = L\Delta_c(J, L)$  (Fig. 11.2(b)) and extrapolated to the thermodynamic limit.  $\kappa$  is found to be finite in the entire  $J$  range, indicating metallic behaviour, but decreases with increasing  $J$ . For  $J = 5$  (red symbols), we can linearly extrapolate  $\frac{1}{\kappa} \rightarrow 0$  for  $\frac{1}{L} \rightarrow 0$ , what suggests strongly metallic behaviour. Mean-field calculations show that this is indeed due to a flat band mechanism [121]. The metallic behaviour is opposed to a "dense" Kondo lattice ( $R = L$ ) at half-filling, which is a spin-singlet Kondo insulator for any  $J$  (see Ref. [97]).

On the other hand, at quarter-filling  $N = R$  we find an insulator in the strong-coupling regime, since all conduction electrons are localised in Kondo singlets. This is seen in

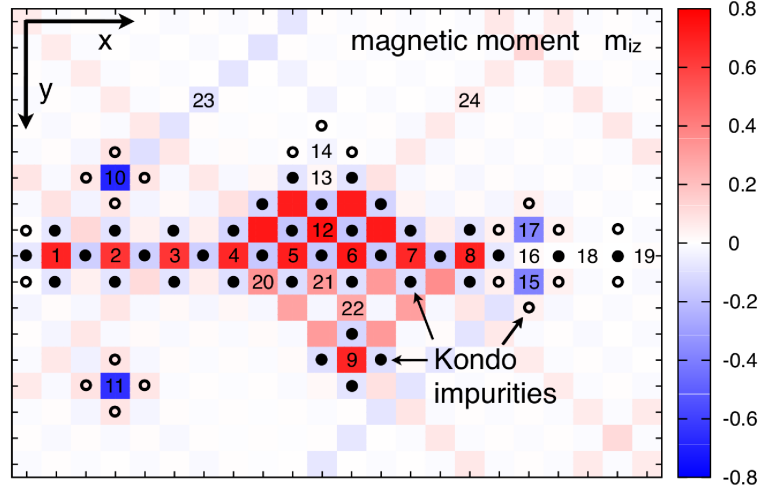


**Figure 11.4:** Magnetic structure of an IIME-coupled system in an artificial  $D = 2$  geometry.  $R = 57$  Kondo impurities (filled and open dots) are placed on an  $L = 22 \times 18$  array of uncorrelated sites and coupled locally ( $J = 5$ ). Real-space DMFT results for the ordered magnetic moments (color code) at sites in the uncorrelated layer. Periodic boundary conditions are used. Figure taken from Ref. [24].

Fig. 11.3, where, for  $J > 2$ , the charge gap  $\Delta_c$  becomes a linear function of  $J$ ; in order to obtain free electrons, one has to break a Kondo singlet at an energy cost of  $-\frac{3}{4}J$ . Contrasted with the metallic ground state at half-filling, one may consequently expect a metal-insulator phase transition as a function of  $N$  and more generally also as a function of  $J$  away from half-filling [53, 97].

## 11.5 Higher dimensions

From section 11.2 and Fig. 11.1 we can infer the magnetic ground state is accessible to a mean-field description. This is seen for the solid and dashed lines, which represent results of DMFT calculations for Kondo and Anderson impurities, respectively. As an impurity solver for DMFT (Sec. 3.4), we employ a standard implementation based on the Lanczos method [22]. In case of the depleted Kondo-lattice model the effective self-consistently determined impurity problem consists of the local spin  $S_r$ , the corresponding B-site and up to 8 bath sites. Up to 9 bath sites are used in the Anderson case. Almost perfect agreement with the DMRG data is found, see Fig. 11.1.

Let us remind ourselves of the R-DMFT results for the two-impurity model in chapter 4, which already showed the reliability of R-DMFT in the strong-coupling regime. The strongly nonlocal correlations of the metastable paramagnetic state for weak  $V$  are not accessible to DMFT [22] (Sec. 4.6). However, DMFT can describe the symmetry-

broken ferromagnetic state, which is weakly correlated for  $V \rightarrow 0$  (Sec. 4.7). On the other hand, for strong hybridisations  $V$ , the essential physics is dominated by local correlations. While the effective spin and isospin interactions in  $H_{\text{eff}}$  are nonlocal, they take place between degrees of freedom at the a priori uncorrelated A-sites. They are therefore expected to have a small feedback on the electron self-energy, which can be nonzero at the impurity sites only. This leads to a weakly  $\mathbf{k}$ -independent, i.e., almost local self-energy accessible to DMFT.

In contrast to standard DMRG, DMFT can easily be employed for calculations of magnetic properties of nanostructure of magnetic atoms on a  $D = 2$  metallic surface layer. Because of the agreement with DMRG for the symmetry-broken ground state of the  $D = 1$  bulk system, quantitatively reliable predictions are expected for  $D = 2$ . This can be checked to some extent in case of a bipartite structure, as the total spin quantum number is fixed by reflection symmetry in spin space [72, 48] (Sec. 3.5). An important aspect from a physical point of view, is to confine, with the help of the Kondo effect, conduction electrons in certain geometries to avoid a dissipation of the total spin into a large (bulk) layer.

In Fig. 11.4, the results of a  $D = 2$  calculation using R-DMFT are shown for the corresponding diluted Kondo lattice model in the symmetry-broken ground state. Electrons in the chain of A-sites 1, 2, ..., 8 with relative distance 2 are confined. Their moments in fact order ferromagnetically. A-site 9 resides at a distance 4 and is coupled ferromagnetically, while the local moments at sites 10 and 11 (with distance 3 and 5, respectively) couple antiferromagnetically to the chain. Note that the local moments at 10 and 11 are formed by confinement due to surrounding local Kondo singlets. If such local moments are weakly coupled to the rest of the system, a tiny Weiss field, produced by the chain, is sufficient to result in an almost full polarisation.  $|m_B|$  is in fact found to slightly increase with increasing distance from the chain. We conclude that the IIME is oscillatory and decreases with distance.

Further effects are found, caused by the IIME: neighbouring A-sites with larger effective coordination number mutually support magnetic polarisation, leading to slightly enhanced  $m_A$  at and around A-site 12. Confinement of an even number of electrons, however, results in no moment at sites 13 and 14, while the structure 15, 16, 17 is polarised due to an odd number of electrons. Confinement as such (with respect to all dimensions) is essential: electrons at 18 or 19 are not confined, no local moments are formed, and thus no polarisation is found. There is a proximity effect as can be seen at 20, 21, or 22. Furthermore, spin-dependent multiple scattering for electrons at the magnetic structures causes an interference pattern, see sites 23, 24, for example. R-DMFT is found to give quantitatively reliable results: summing up the local magnetic moments for the 396 uncorrelated sites and the 57 impurities, we find a ground-state spin moment of  $m_{\text{tot}} = 2S_{\text{tot},z} = 15.13$  which is, within numerical uncertainties, equal to the exact value  $m_{\text{tot}} = 36 - 21 = 15$  which can be obtained analytically [72, 48, 97] by counting the number of impurities on B (filled dots) and on A-sites (open dots).

# 12 Doped conduction-electron systems

## 12.1 Introduction

The adiabatic property of the ground state in terms of  $J$ , justified in section 3.5, is usually not present anymore in non-bipartite models or systems away from half-filling, rendering magnetic phase transitions (or level crossings, respectively) possible as functions of  $J$  or  $N$ .

Non-bipartite models can be easily achieved by introducing a next-nearest-neighbour hopping in the conduction-electron system or periodic boundary conditions for systems with odd  $L$ . Another class of models consists of systems where an impurity is coupled to more than one site, thus possibly breaking the bipartite structure.<sup>1</sup> Note that in non-bipartite models isospin symmetry is lost (Sec. 10.4). However, we will focus here on the case of models away from half-filling, i.e.,  $N \neq L$ , and leave the other mentioned cases for future research.

Considering an impurity model at fixed filling, we may expect two types of magnetic transitions as functions of  $J$  with basically different physical background. The first one is treated in section 12.2 and goes back to the discontinuity between finite-size Kondo regime and RKKY regime at weak couplings  $J$ . As known from chapter 6, impurities at good sites are ferromagnetically correlated for  $\Delta > T_K$  due to "resonant enhancement", but may be antiferromagnetically RKKY coupled for  $T_K > \Delta$  and  $J < J_D$ . The resulting magnetic "phase transitions" or level crossings, respectively, to the large-spin regime for  $J \rightarrow 0$  are of mesoscopic nature, triggered by the finite-size Kondo effect. Thus, they disappear in the thermodynamic limit. The second type is

---

<sup>1</sup>This is of relevance for experiments (and respective theoretical explanations), e.g. considering cobalt atoms deposited on copper surfaces [132]. Co atoms act effectively as  $S = \frac{1}{2}$  Kondo impurities with a sometimes complex coupling geometry. In this context, Ref. [132] reports the unexpected, non-monotone behaviour of the Kondo temperature  $T_K$  of a single Co atom with increasing number of surrounding Cu atoms. In this respect, it is helpful to see that the single-impurity RG flow equation (2.21) becomes in the most general case:  $dJ/d\ln D = -\frac{1}{2}(\rho'(-D) + \rho'(D))J^2(D)$ , where  $\rho'(E) = \sum_k \delta(E - (\varepsilon_k - \mu)) \sum_{mn} U_{mk} U_{nk}$  is the (non)local density of states of all substrate sites to which the impurity is coupled.

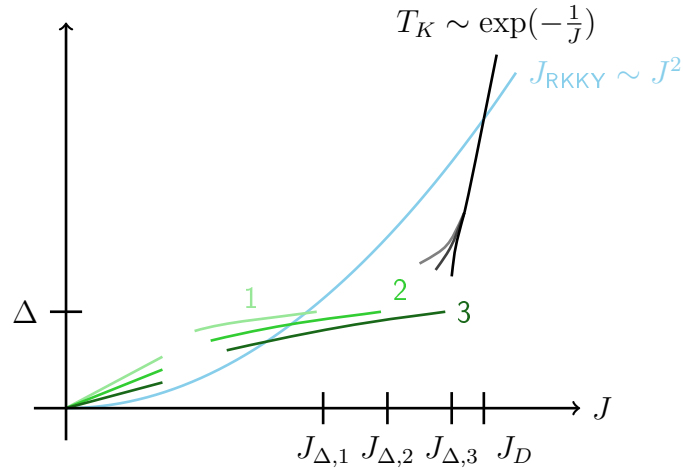


**Figure 12.1:** Inhomogeneous conduction-electron systems, e.g. due to open boundary conditions, may lead to spatially varying local densities of states and consequently to position dependent Kondo scales. This is indicated by the black, grey and light grey lines, showing  $T_{K,r}$  for three impurities at different sites. In the strong-coupling and intermediate-coupling regime, the usual competition between Kondo screening and RKKY interaction (blue) remains mostly unchanged. However, based on the condition  $\Delta = T_{K,r}$ , we obtain a different  $J_{\Delta,r}$  for each impurity  $r$ . Hence, for  $J \rightarrow 0$ , the perturbative regime sets in at different  $J_{\Delta,r}$ . Furthermore, away from half-filling (for odd  $N$ ), the weights of the  $k_F$  state attain non-trivial behaviour as functions of the position, too. Focusing on the case of impurities only at good sites, one obtains inhomogeneous linear-in- $J$  Kondo scales  $J_r^{(1)}$  (light green, green, dark green). For example, for  $J_{\Delta,1} < J < J_{\Delta,2}$  the impurities 2 and 3 are governed by the finite-size Kondo effect, exhibiting ferromagnetic correlations. On the other hand, impurity 1 is still dominated by the RKKY interaction.

the transition between RKKY and Kondo regime (Sec. 12.3), which is expected based on the knowledge that the strong-coupling regime of the dense Kondo lattice away from half-filling is ferromagnetically ordered, whereas the RKKY regime may exhibit paramagnetic behaviour [97].

We take the depleted Kondo lattice model introduced in chapter 11 as example here, for which we have shown in the previous chapter that it exhibits magnetic order at half-filling. Thus, it is an interesting question how this magnetic state extends to parameter regions away from half-filling. Our effective weak and strong-coupling theories along with numerical results will permit us to infer a qualitative ground-state "phase diagram" of this model as a function of  $J$  and  $N$  at the end of this chapter.



## 12.2 Transitions between finite-size Kondo and RKKY regime

As we will see in this section, the finite-size Kondo effect has fascinating implications away from half-filling, i.e., when the total conduction-electron number  $N \neq L$ . However,  $N$  should be odd to avoid "trivial" off-resonance situations. For the purpose of disentangling both aforementioned types of magnetic transitions, we concentrate in this section on quarter-filling, where only the first type is present.

The basic mechanism of the finite-size Kondo effect has been derived without special assumptions about the filling. Nonetheless, differences between the physics of systems with different  $N$  are expected, since bad sites become rare away from half-filling: e.g. at quarter-filling (here we take  $N = \frac{1}{2}(L + 1)$ ) only systems with  $L = 5, 13, 21, \dots$  have sites where exactly  $U_{ik_F} = 0$ . In the extreme case of just one conduction electron all sites are good.<sup>2</sup> Another characteristic feature is that, in contrast to half-filling,  $U_{ik_F}^2$  can be strongly inhomogeneous (Fig. 12.1).

In inhomogeneous systems—for example systems with open boundaries—the Kondo temperature is position dependent (as observed in Sec. 4.5). Based on  $\Delta = T_K$ , this circumstance leads to different  $J_{\Delta,r}$ , below which the finite-size Kondo effect sets in, for impurities at different sites. However,  $J_{\Delta,r}$  is also linked to  $U_{ik_F}^2$ , since it can be also regarded as the coupling where first and second order contributions of perturbation theory become of equal order of magnitude.

Let us for clarity assume that we choose a configuration in which all impurity sites are good. A particularly interesting situation arises when the RKKY interaction between good impurities is antiferromagnetic, in contrast to the usual ferromagnetic inter-impurity correlations due to "resonant enhancement" in the finite-size Kondo regime (chapter 6). Generally, this suggests a complex, multi-stage crossover at weak  $J$  away from half-filling. For  $J \rightarrow 0$ , one finds a large-spin regime with  $S_{\text{gs}} = \frac{1}{2}(R - 1)$ , governed by the finite-size Kondo effect. But when increasing  $J$ , as soon as  $J_{\Delta,r} < J < J_D$  for an impurity  $r$  with antiferromagnetic RKKY interaction, we will enter a regime with lower total spin  $S_{\text{gs}} < \frac{1}{2}(R - 1)$  (Fig. 12.1). It is emphasised that this is not possible at half-filling, where good sites are always at ferromagnetic distance ( $k_F = \frac{\pi}{2}$ ).

In Fig. 12.2 the numerical results of the depleted Kondo lattice model are shown for  $L = 9$  and quarter-filling  $N = R$  in the electron system. The filling implies

---

<sup>2</sup>This follows from simple geometric arguments. For open boundary conditions, the  $n$ -th conduction-electron state has  $n - 1$  nodes ( $n$  integer). Adding two sites, one at each chain end with an infinite on-site energy, is equivalent to these boundary conditions. If the distance between two nodes,  $(L + 1)/n$ , or a multiple of it coincides with a lattice site, a bad site is produced there. On the other hand, the filling determines the  $k_F$  state with  $k_F = \pi/(L + 1)n_F$  by  $N = 2(n_F - 1) + 1$ .

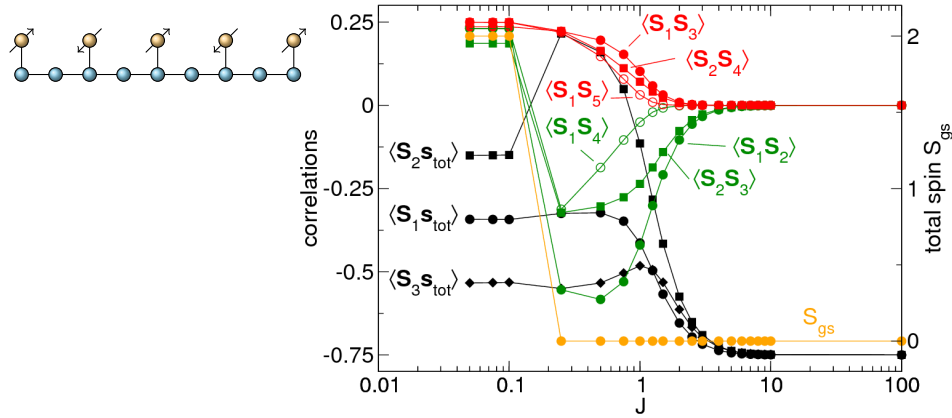


**Figure 12.2:** Results for a depleted Kondo lattice model with  $L = 9$ , as depicted in the pictogram, at quarter-filling.  $R = 5$  Kondo impurities are placed at sites  $i_r = 1, 3, 5, 7, 9$ . We show the total spin  $S_{gs}$  (orange symbols, right scale) and impurity-electron correlations (black symbols, left scale).  $\langle S_1 s_{tot} \rangle = \langle S_5 s_{tot} \rangle$ : circles,  $\langle S_2 s_{tot} \rangle = \langle S_4 s_{tot} \rangle$ : squares,  $\langle S_3 s_{tot} \rangle$ : diamonds. Inter-impurity correlation functions between impurities at distance  $d = 4, 8$  (red symbols, left scale):  $\langle S_1 S_3 \rangle = \langle S_3 S_5 \rangle$ : filled circles,  $\langle S_1 S_5 \rangle$ : open circles,  $\langle S_2 S_4 \rangle$ : filled squares. The same correlations for  $d = 2, 6$  (green symbols, left scale):  $\langle S_1 S_2 \rangle = \langle S_4 S_5 \rangle$ : filled circles,  $\langle S_1 S_4 \rangle = \langle S_2 S_5 \rangle$ : open circles,  $\langle S_2 S_3 \rangle = \langle S_3 S_4 \rangle$ : filled squares.

$k_F = \frac{\pi}{4}$ , which leads to ferromagnetic RKKY couplings for distances  $d = 4$  and  $d = 8$  (corresponding  $\langle S_i S_j \rangle$ : red symbols) and antiferromagnetic ones for distances  $d = 2$  and  $d = 6$  (corresponding  $\langle S_i S_j \rangle$ : green symbols). In total, we obtain an antiferromagnetic pattern for the correlated impurity system in the RKKY regime, resulting in a total impurity spin  $S_{tot} = \frac{1}{2}$ . Together with the Kondo effect, which screens the total impurity doublet for  $T_K^{1spin} > \Delta$ , one obtains a spin-singlet ground state,  $S_{gs} = 0$  (orange symbols). From  $\langle S_i S_j \rangle$ , it can be inferred that the RKKY regime is reached around  $J_D = 1 - 2$  and is immediately influenced by the finite-size Kondo effect due to the small system size, i.e.  $J_D \approx J_{\Delta, 5spins}$ . This is apparent for  $\langle S_2 s_{tot} \rangle$ , which exhibits a sign change for  $J_{\Delta, 2} < J < J_D$ . As consequence of the small residual couplings to the conduction electrons, i.e.,  $U_{i_2 k_F}^2 \ll U_{i_1 k_F}^2, U_{i_3 k_F}^2$ ,  $S_2$  (and  $S_4$ ) appears approximately as bad impurity.

However, when the finite-size Kondo regime is reached for all impurities at  $J < 0.25$ , we observe a sudden jump in the inter-impurity correlations for those correlations which change from antiferromagnetic to ferromagnetic values. Consequently, for  $J < 0.25$  the total spin increases to the expected value in the finite-size Kondo regime  $S_{gs} = \frac{1}{2}(R - 1) = 2$ . As is visible,  $\langle S_i S_j \rangle$  do not converge for  $J \rightarrow 0$  due to inhomogeneous  $J_r^{(1)}$  (Fig. 12.1).

Furthermore, all impurities have  $\langle S_i s_{tot} \rangle < 0$  (black symbols) for  $J < 0.25$ . Note

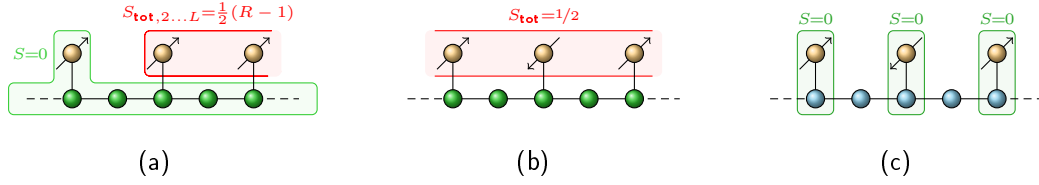


**Figure 12.3:** Depleted Kondo lattice model as discussed in chapter 11, where all impurities are at good sites for quarter-filling  $N = R$ . We show the different emerging regimes: (a) finite-size Kondo regime, resulting in a large  $S_{gs} = \frac{1}{2}(R - 1)$ . Subfigure (b) depicts the RKKY regime, where the antiferromagnetic pattern of inter-impurity couplings leads to a total impurity doublet. This is completely screened, either by  $s_F$  in case of intermediate system sizes ( $T_K^{(Rspins)} < \Delta < T_K^{(1spin)}$ ) or in a conventional way in case of larger system sizes ( $\Delta < T_K^{(Rspins)}$ ). In both cases, we find  $S_{gs} = 0$ . In the strong-coupling regime (c) all conduction electrons are trapped in local Kondo singlets and therefore  $S_{gs} = 0$ .

that this is not the case for  $S_2$  and  $S_4$  above this regime, i.e.,  $J \gtrsim 0.25$ , where  $\langle S_2 s_{tot} \rangle > 0$ . While one thus can easily read off  $J_{\Delta,2} = J_{\Delta,4} = 0.25$  from Fig. 12.2, it is difficult to infer from the displayed correlation functions on  $J_{\Delta,1} = J_{\Delta,5}$  and  $J_{\Delta,3}$ . Nevertheless, one may assume that they are considerably larger than  $J_{\Delta,2}$  since  $U_{i_2 k_F}^2 / U_{i_1 k_F}^2 \approx U_{i_2 k_F}^2 / U_{i_3 k_F}^2 \approx 1/10$ .

Except of the large-spin regime ( $T_K < \Delta$ , left panel in Fig. 12.3),  $S_{gs} = 0$  is obtained for all considered couplings  $J$  (blue symbols in Fig. 12.2). In the RKKY regime, this is caused by the antiferromagnetic pattern of couplings among the impurities in cooperation with the Kondo effect (middle panel in Fig. 12.3), while in the strong-coupling regime all conduction electrons are caught in Kondo singlets, leaving a vanishing ground-state spin (right panel in Fig. 12.3).

## 12.3 Transitions between RKKY and Kondo regime

Despite the failure of the generalised Lieb theorem (Sec. 3.5), the concept of inverse indirect magnetic exchange as well as the effective theories for the weak and intermediate-coupling regimes, presented in this work, remain valid also away from half-filling. Hence, we can apply them to understand the magnetic ground-state properties of the depleted Kondo lattice model, but for  $N < L$ . In Fig. 12.4, the total ground-state spin  $S_{gs}$  is shown as a function of  $J$  for different  $N$  and system size  $L = 49$ . Note that the large-spin regime, discussed in the previous section, is located at smaller  $J$  as compared to Fig. 12.2 due to the larger system size, and hence is not

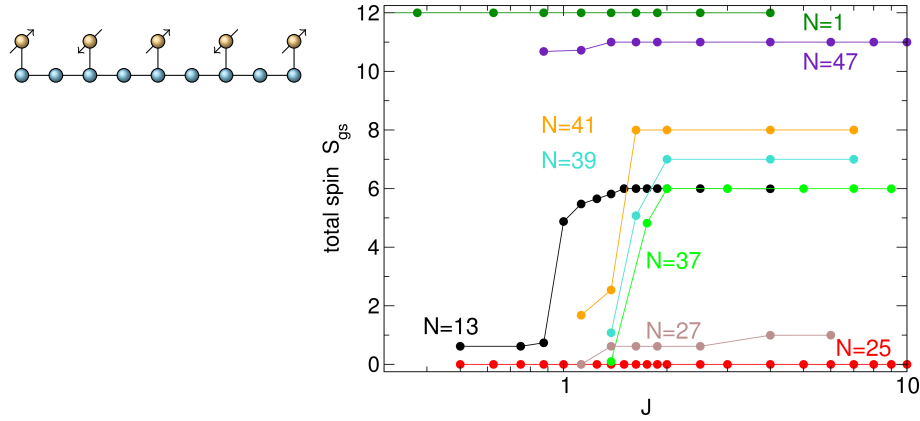


**Figure 12.4:** Total ground-state spin  $S_{gs}$  of the depleted Kondo lattice model depicted in the pictogram as functions of  $J$  on a log scale. Calculated for different fillings  $N$  as indicated. The system size is  $L = 49$  and the number of impurities  $R = 25$ . Note that non-integer values of  $S_{gs}$  may have several reasons: they may be due to a degenerate ground state or due to numerical inaccuracy of DMRG at crossovers.

visible in Fig. 12.4.

Based on the numerical results of Fig. 12.4, a qualitative "phase diagram"<sup>3</sup> as a function of  $N \leq L$  and  $J > 0$ , Fig. 12.5, can be constructed. Note that, according to our previous conclusions in section 12.2, the electron system with  $L = 49$  contains only good sites.

As a consequence of the special impurity depletion scheme, the phase diagram is approximately symmetric if mirrored at the line of quarter-filling  $N = R$ , for which we have discussed results above. At half-filling  $N = L$  (chapter 11), we observe the adiabatic behaviour of the ground state with a large spin of  $S_{gs} = \frac{1}{2}(R - 1)$  for all  $J$ , as enforced by the generalised Lieb theorem.

Furthermore, following the results of the previous section, a total spin of the same size could be found for all fillings  $N$  in the finite-size Kondo regime,  $T_K^{(1\text{spin})} < \Delta$ . On the other hand, only one electron prepared in the conduction-electron system ( $N = 1$ ) occupies the lowest one-particle state with finite weights  $U_{ik}$  at all sites. Therefore, it gives rise to ferromagnetic correlations among the impurities, since they are all interacting with the same electron ("spin-polaron" [97, 61]). Interestingly, this setting for  $N = 1$  at finite  $J$  shows basic similarities to the finite-size Kondo regime, where all impurities at good sites couple to the  $k_F$  electron, resulting in a large total spin, too.

Assuming continuity, in the RKKY regime  $S_{gs}$  is expected to decrease for increasing

<sup>3</sup>We only show the results for  $N \leq L$ , since, due to the bipartite lattice, the physics for  $N > L$  is the same as for  $N < L$  (particle-hole symmetry).

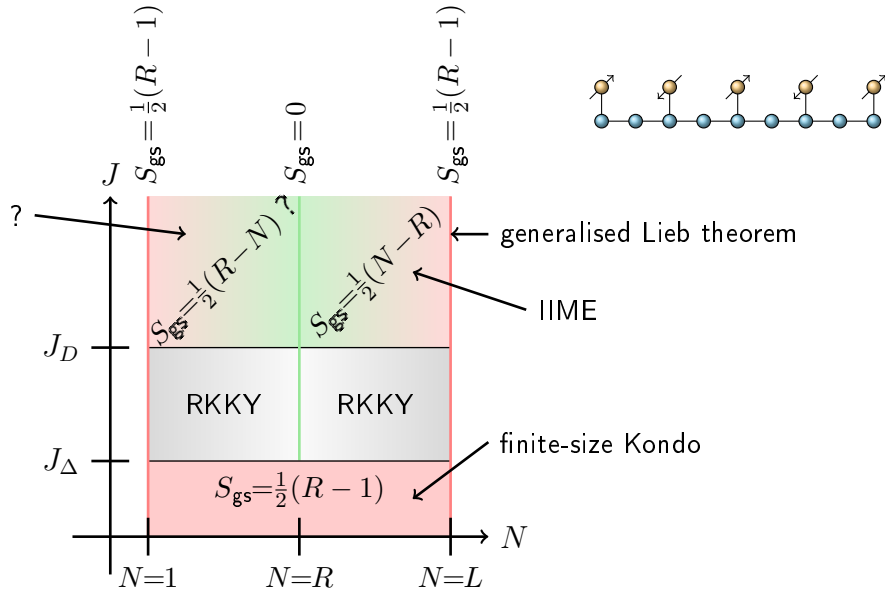


**Figure 12.5:** Qualitative ground-state "phase diagram" of the depleted Kondo lattice model depicted in the pictogram, as a function of  $J$  and the (odd) number of conduction electrons  $N \leq L$ . It is based on the conclusions for the weak and strong-coupling regime drawn in preceding chapters as well as on the numerical results shown in Fig. 12.4. For  $T_K < \Delta$  (i.e.  $J < J_\Delta$ ), a large-spin regime, where  $S_{gs} = \frac{1}{2}(R-1)$ , can be found in the weak-coupling regime for all fillings  $N$  (red lower area). On the other hand, for  $J_\Delta < J < J_D$  we expect an RKKY regime with filling dependent total ground-state spin (grey middle areas). In the strong-coupling regime,  $J > J_D$ , and above quarter-filling ( $L+R \geq N \geq R$ ) the inverse indirect magnetic exchange (IIME) leads to a magnetic ground state due to ferromagnetically-ordered conduction electrons (red-greenish upper right area). At half-filling  $N = L$ , we can apply the generalised Lieb theorem (Sec. 3.5, red right line). Note that in practice  $J_D$  and  $J_\Delta$  may be non-constant functions of  $N$ .

$N$ , until it is vanishing at quarter-filling due to the antiferromagnetic pattern of RKKY couplings ( $k_F = \frac{\pi}{4}$ ). Above quarter-filling, it increases towards the maximal value at half-filling. From the numerical results of Fig. 12.4, we find a large region, where RKKY exchange leads to a paramagnetic or low-spin ground state at weak and intermediate  $J$ , comparable to the situation in the dense Kondo lattice model. Due to the one-dimensionality of the substrate, one may think of the system as an "RKKY Tomonaga-Luttinger liquid" [97].

The strong-coupling regime above quarter-filling,  $L+R \geq N \geq R$  can be well-described by the IIME concept. Starting at quarter-filling with a vanishing number of excess conduction electrons, i.e. electrons which are not trapped in Kondo singlets, their

number grows with increasing  $N$ . Likewise increases the total spin  $S_{\text{gs}} = \frac{1}{2}(N - R)$ , since the excess electrons are ferromagnetically coupled through IIME. However, this needs analytical confirmation, as less polarised ground states appear also possible.

Further work is also demanded to clarify the precise reasons for the observed ferromagnetic ordering below quarter-filling for  $J > J_D$  (see e.g. results for  $N = 13$  at  $J \geq 2$  in Fig. 12.4), where correlations among unscreened impurities, i.e.  $\langle \mathbf{S}_i \mathbf{S}_j \rangle \neq 0$  for  $J \rightarrow \infty$ , are caused by an exchange mediated by holes instead of electrons. However, rough motivations for the ferromagnetic ground state can be drawn from results of the strong-coupling perturbation theory for the dense Kondo lattice model [97], based on a double-exchange like mechanism [130] which allows electrons to gain kinetic energy.

Although we obtained deep insights in the physics of this one-dimensional model, it will be also interesting to explore higher-dimensional variants of it, which allow for a larger set of emerging orders [106].

## 13 Exhaustion problem and heavy fermions

Before concluding our work, we want to resume the discussion about the number of screening channels, raised in chapter 9. While it is often obvious how large the number of channels is in the limits  $J \rightarrow 0$  and  $J \rightarrow \infty$ , for a large number of impurities, it becomes in general difficult to find enough screening channels to ensure separate screening of each impurity. For this problem, the term "exhaustion problem" has been coined [107, 108]. Within the energy range  $T_K$  one finds  $N_{\text{eff}} \approx \rho T_K$  electrons available for screening ( $\rho$  is the conduction-electron density of states).  $N_{\text{eff}}$  can be much smaller than the number of impurities  $R$ , leading to a potential underscreening situation if we assume a screening in a similar way as for a single impurity.

However, experiments on respective materials, such as intermetallic compounds containing rare-earth<sup>1</sup> (e.g.  $\text{CeAl}_3$ ,  $\text{CeCu}_2\text{Si}_2$ ,  $\text{CeCu}_6$ , ...) or actinide elements (e.g.  $\text{UPt}_3$ ,  $\text{U}_2\text{Zn}_{17}$ ,  $\text{UBe}_{13}$ , ...), reveal a (heavy) Fermi liquid state for low temperatures [8]. The corresponding small energy scale is reflected in the specific heat and the spin susceptibility [97]. In the following, we present some general ideas for dense impurity lattice models to illuminate this contradicting situation.

In contrast to materials with a dilute concentration of magnetic impurities, where the RKKY interaction may lead to frustrated, glassy states ("spin glass"), in dense Kondo lattice systems the RKKY exchange gives rise to magnetic order [56]. Even though the RKKY interaction may, as we know from preceding chapters, play an important role by correlating the impurities and thereby influencing the interplay with the Kondo effect, we will neglect it in our considerations to reduce complexity.

For strong exchange couplings, it becomes unrealistic, regarding typical materials, to exclude charge fluctuations from our considerations. Thus, let us concentrate on a periodic Anderson model ( $R = L$ ). Already for  $U = 0$ , one can study the major

---

<sup>1</sup>In "normal" rare earth compounds the f levels are strongly separated from the Fermi level, favouring the ferromagnetic direct exchange term of the Coulomb interaction between c and f electrons [8]. These materials may effectively be described by a Kondo lattice model with ferromagnetic exchange coupling [133, 18]. On the other hand, if the f levels lie nearer the Fermi energy, virtual excitations into the conduction band may result in a dominant antiferromagnetic exchange interaction (Sec. 2.2).

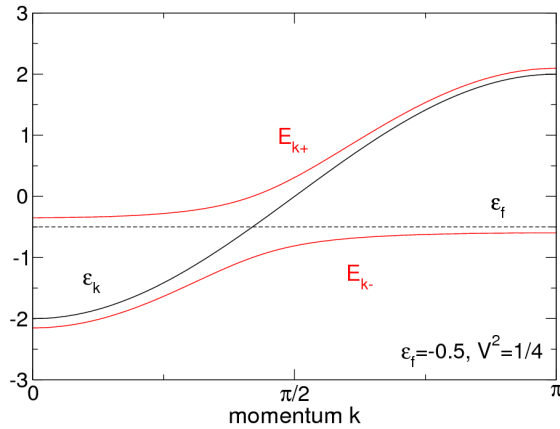


**Figure 13.1:** Heavy-fermion bands  $E_{k\pm}$  (red lines) according to Eq. (13.4) as functions of the momentum  $k$ . For a one-dimensional system,  $\varepsilon_f = -0.5$ , and  $V^2 = 0.25$ . The conduction-electron dispersion  $\varepsilon_k$  in the absence of impurities is shown as black line. The presence of impurities leads to a hybridisation gap between  $E_{k-}$  and  $E_{k+}$ , close to the atomic  $f$  levels  $\varepsilon_f$ .

effects due to the hybridisation of impurity subsystem ("f states") and conduction-electron subsystem by an analytical diagonalisation of the Hamiltonian. This results in a spectrum  $E_{k\pm}$  for quasi-particles defined by  $a_{k\sigma\pm}^\dagger$  with two separated hybridisation bands (Fig. 13.1)

$$a_{k\sigma+}^\dagger = u_k c_{k\sigma}^\dagger + v_k f_{k\sigma}^\dagger \quad (13.1)$$

$$a_{k\sigma-}^\dagger = -v_k c_{k\sigma}^\dagger + u_k f_{k\sigma}^\dagger \quad (13.2)$$

$$|u_k|^2 + |v_k|^2 = 1 \quad (13.3)$$

$$E_{k\pm} = \frac{1}{2} \left( \varepsilon_k + \varepsilon_f \pm \sqrt{(\varepsilon_k - \varepsilon_f)^2 + 4V^2} \right). \quad (13.4)$$

$\varepsilon_f$  is the on-site energy at impurity sites and  $\varepsilon_k$  the conduction-electron dispersion at  $V = 0$  with momentum  $\mathbf{k}$ . The gap between both bands is small and given by  $E_{0+} - E_{Q-}$ , where  $\mathbf{Q} = (\pi, \dots, \pi)$ . As is seen in Fig. 13.1, it is located close to  $\varepsilon_f$ .

When  $U$  becomes finite, two energy scales emerge: one is connected to charge degrees of freedom, which are high-energetic at large  $U$ . Another one is found at low energy scales and is due to the scattering of conduction electrons at impurity states. For temperatures above this small energy scale  $T^*$  the localised spins are only weakly coupled to the conduction electrons, to which they become strongly entangled for temperatures below this scale [97].

Diverse methods such as the Gutzwiller approach, slave boson methods, or the large- $N$  approximation have been developed to quantify effects from correlations arising from a finite  $U$ , usually based on renormalising the  $U = 0$  Anderson Hamiltonian



[97]. Of particular interest is the small energy scale  $T^*$ , which is related to the spin degrees of freedom. However, it has to be distinguished from the single-impurity Kondo temperature  $T_K$ , since it is rather associated to the physical picture of a collective Kondo effect. It is found that  $T^*$ , which is for a dense Kondo lattice model, is larger than the single-impurity  $T_K$  ("lattice enhancement") [97]. Another fundamental finding consists in a characteristically large density of states at the Fermi level, generated by the mixing of c states with f states

$$\rho_{\text{eff}}(\varepsilon_F) \sim \rho(\varepsilon_F) \frac{T_F}{T^*}, \quad (13.5)$$

where  $T_F$  is the Fermi temperature. Due to the large contributions of f states near the Fermi energy, the quasi-particles attain a strongly localised character. The effective mass  $m^*$  of these quasi-particles, compared with the bare mass  $m$ , is likewise quite large  $m^*/m = T_F/T^* \sim 1000$  [56]. Therefore, the term "heavy fermions" has been coined. Below the effective Fermi temperature, heavy-fermion systems display ordinary Fermi-liquid properties such as a sharply defined Fermi surface and small inverse quasi-particle lifetime.

Another astounding feature represents their large Fermi surface, which has been confirmed by experiments [56, 97]. We may employ the Luttinger sum rule, which states that the volume  $V_{\text{FS}}$ , enclosed by the Fermi surface, counts the number of fermions. At  $U = 0$  this is exactly the conduction electrons ( $N_c$ ) along with all electrons at impurity sites ( $N_f$ )

$$2 \frac{V_{\text{FS}}}{(2\pi)^3} = N_c + N_f. \quad (13.6)$$

When  $U$  becomes large, charge fluctuations at impurity sites become suppressed and local moments develop at impurity sites (Sec. 2.2), i.e.  $N_f \rightarrow R$  in Eq. (13.6). It implies that the large Fermi surface, build up by conduction electrons as well as localised moments, may also be found in Kondo impurity systems, as long as we can assume adiabatic connection to  $U = 0$ , i.e. provided that heavy fermions are stable. This is not the case, for example, when the system undergoes a magnetic phase transition at weak  $J$ , driven by the RKKY interaction.

Heavy-fermion materials may exhibit a plethora of fascinating states, such as antiferromagnetically ordered states, unconventional superconductivity, and Kondo insulators. The (tiny) excitation gaps (meV instead of eV) in Kondo insulators such as  $\text{YB}_{12}$ ,  $\text{CeNiSn}$ , or  $\text{Ce}_3\text{Bi}_4\text{Pt}_3$  are stabilised by the presence of impurities, since the electron system would be metallic if the local coupling vanished. A Kondo insulator arises for a half-filled Kondo lattice model, where the chemical potential lies within the hybridisation gap at finite  $J$  (Fig. 13.1). However, away from half-filling we usually find a metallic ground state, which has to be contrasted to the increasing resistance of a single-impurity model due to spin scattering at decreasing temperatures (Kondo effect,

chapter 2). Further interesting effects are caused by multi-orbital impurities, which may lead to a large impurity spin and additional orbital ordering mechanisms.

The discovery of superconductivity in heavy-fermion materials (Steglich et al in 1979 in  $\text{CeCu}_2\text{Si}_2$  [8]) was surprising, since superconductivity is highly sensitive to the presence of magnetic impurities, which break time-reversal symmetry, what is an essential ingredient for s-wave pairing [56]. Superconductivity appears in the vicinity of the critical point or crossover region, respectively, which separates the magnetic phase from the paramagnetic heavy fermion phase at low temperatures.

Furthermore, if the dense Kondo lattice model ( $R = L$ ) is studied by a mean-field approach, the resulting  $U(1)$  gauge invariance allows to discover a couple of close analogies between Cooper pairing in superconductivity and the Kondo effect [56]. However, while Cooper pairs are extended in space at a scale of  $\xi_C \sim v_F/T_C$  ( $T_C$ : critical temperature), the mean-field theory characterises the Kondo effect as local in space but highly nonlocal in time  $\tau_K \sim 1/T_K$ .

The underlying reason is that heavy fermions are explained in this approach as admixture of conduction-electrons with non-trivial, entirely local composite f electrons. The composite f electron is made of a localised conduction electron bound to a spin-flip of the local moment at the same site. It obtains contributions from high energy electron states instead of just from the low-energy electrons as in the single-impurity Kondo effect. In this manner, the exhaustion problem can be avoided, giving rise to a collective Kondo effect in form of the emerging heavy Fermi liquid at low energy scales.

However, many questions remain open: how does the heavy-fermion state arise in a finite-size system and in depleted impurity models? How does it compete or cooperate in this case with IIME (Sec. 10.5)? How robust is the large Fermi surface for intermediate and strong  $U$ , and in particular for Kondo impurity models ("Kondo breakdown" [134])? What happens at magnetic phase transitions, when, e.g., the RKKY exchange drives the system to magnetic order for decreasing  $J$ ? Do we obtain non-Fermi liquid physics when the heavy-fermion concept breaks down? These questions propose further investigations in this field, which could be addressed also in DMRG due to the local character of the Kondo interaction. However, non-local correlations, arising from the coherent scattering of composite f electrons and conduction electrons, can be a drawback. Informations about the heavy-fermion state can likewise be obtained by investigation of spectral properties of the considered model [135, 78].

# 14 Summary and outlook

## 14.1 Summary

Let us summarise the results of this work in which we put forward a rich and consistent concept of impurity physics in finite-size systems, which goes beyond existing works in this field.

We first turned to the obvious questions related to influences of finite-size effects. These result from a combination of spatial confinement of the conduction-electron system and Friedel oscillations due to open boundary conditions. An important result represents the conclusion that impurities can be correlated in the finite-size regime in basically different ways with each other and with the conduction electrons in a way that is different from customary belief. The renormalisation group (RG) methodology supplies us with an established framework to connect our results to conventional theories. As was pointed out in the introductory chapter 2, when the finite-size gap  $\Delta$  becomes the leading energy scale ( $\Delta > T_K$ ), the traditional Kondo cloud picture collapses, accompanied by a regularisation of the corresponding divergencies of the effective local Kondo coupling  $J_{\text{eff}}$  in terms of RG. In this situation, one may think of the system remaining at the local-moment fixed point and being described by residual impurity couplings to the conduction electrons and RKKY couplings between the impurities.

In "off-resonant models" (chapter 4) the chemical potential lies between empty and doubly-occupied conduction-electron states. For  $\Delta > T_K$ , we find that residual couplings of impurities to the electrons vanish and the system is governed by RKKY exchange. This is just as in the standard picture of the competition between Kondo effect and RKKY exchange for  $J < J_D$  [22].

On the other hand, in "on-resonant" one-dimensional models, a single electron resides in the highest occupied one-particle state  $\varepsilon_{k_F}$ . The central quantity turns out to be the residual coupling to this electron state, which is determined by its weight at a particular site. Thus, the set of sites in the electron system can be subdivided into good (finite weight) and bad sites (vanishing weight). As presented in-depth in chapter 5, this results in a subtle interplay between Kondo screening and RKKY exchange even in the limit  $J \rightarrow 0$ , where the symmetry of the ground state crucially depends on the geometrical position of the impurities. As demonstrated using the example of a "bad-good-bad" three-impurity model, for sufficiently large systems ( $J_D > J_\Delta$ ), an increasing

## 14 Summary and outlook

$J$  drives the system from Kondo screening on a linear-in- $J$  scale to conventional RKKY-coupled moments, until the Kondo effect takes over again for large  $J$  [21]. This scheme is confirmed by weak-coupling perturbation theory.

Further profound consequences are found for  $\Delta > T_K$  and models with a larger group of impurities at good sites, as they exhibit, e.g., ferromagnetic inter-impurity correlations and enhanced RKKY couplings, what we refer to as "resonant enhancement" (chapter 6). Though seemingly contradicting our previous considerations by suggesting an RKKY regime for  $J \rightarrow 0$ , these findings are inescapable implications of our concept of the "finite-size Kondo effect" and can be unambiguously explained by the joint coupling in linear order in  $J$  of multiple impurities to the  $k_F$  electron ("central-spin model"). We emphasise that the ferromagnetic inter-impurity correlations occur just due to the presence of this linear-in- $J$  scale without any need for an additional ferromagnetic exchange interaction.

Periodic systems (chapter 7) allowed us to clarify the decisive role of the boundaries which induce Friedel oscillations, regulating the spatial variation of finite-size effects. Additionally, the physics of models with higher-dimensional host systems became evident, as we could obtain two separate screening channels for the finite-size Kondo effect in a periodic one-dimensional substrate. This results in two fully compensated impurities for  $J \rightarrow 0$  if they are at odd distance ("multi-channel finite-size Kondo effect").

We motivated that our theory of finite-size effects is robust (chapter 8), if the system is weakly coupled to a larger environment. An interesting insight is that the standard Kondo cloud picture does not collapse for  $\Delta_{\text{nano}} > T_K$  (as in case of an isolated finite-size system), because the impurity is in this case strongly entangled with a collection of low-energy electrons penetrating the walls of the nano box. For  $J \rightarrow 0$ , the finite-size regime is replaced by an RKKY regime. The finite-size governed Kondo effect is experimentally accessible by studying magnetic field dependencies [43]. The relevant parameter range can be estimated roughly by setting  $T_K \sim \Delta \sim J_{\text{RKKY}}$ : RKKY couplings in the range of 0.1 – 10 meV correspond to Kondo temperatures of 1 – 100 K and, in a free-electron model [19], to system volumes of  $(11.6 \text{ nm})^3 - (2.5 \text{ nm})^3$ . However, we also stated that spatial confinement is merely one representative of an origin of the energy gap  $\Delta$  at the Fermi energy, which underlies the special physics. Conceivably, additional interactions among the conduction electrons may constitute it as well.

Returning to systems without environment, we gave an idea of how the system properties cross over to those conventionally expected, when the system size increases (chapter 9). This concerns, e.g., the number of screening channels in the weak-coupling regime as well as reminiscences of the phase transition between Kondo and RKKY regime for a two-impurity model at antiferromagnetic distance. However, we also realised that finite-size effects can be active over a considerable large parameter regime due to RKKY

interaction, which indirectly couples impurities and may lead to smaller Kondo temperatures for the resulting RKKY-correlated impurity compound. The corresponding Kondo cloud turns out to be much larger than the single-impurity Kondo cloud and is thus readily cut by the system size, i.e.,  $J_{\Delta, \text{RKKY}} \approx J_D$ . This circumstance can be an obstacle for recovering ordinary screening physics for systems of the order of  $L \approx 200$ . Likewise it may be regarded as a strong argument for the significance of finite-size related effects—also in experiments. In real materials the expansion of Kondo clouds is expected to be easily interfered for example with non-magnetic impurities, disorder, or even crystal defects.

Surprisingly, even the strong-coupling regime, in which traditional Kondo physics takes place, is influenced by finite-size effects which may cut the low-energy physics of the remaining weakly-interacting electrons. In chapter 10, we studied the case of strong  $J$ , in which local Kondo singlets evolve, allowing for a perturbative treatment in terms of small hopping amplitudes. This results in the novel "inverse indirect magnetic exchange" (IIME), which constitutes, among others, ferromagnetic magnetic coupling and antiferromagnetic isospin coupling between adjacent sites of a local Kondo singlet. These are mediated by virtual excitations of the magnetically inert Kondo singlet [24]. We may even understand IIME as complementary counterpart of the finite-size Kondo effect as it builds on the presence of Kondo clouds.

The developed seamless net of weak and strong-coupling results sparked the investigation of a depleted Kondo lattice model at half-filling in chapter 11, based on the idea that the normal state of the remaining conduction electrons in the strong-coupling regime is instable against ferromagnetic order due to IIME. One could have suspected this from the generalised Lieb theorem (Sec. 3.5), which enforces an adiabatic connection to the weak-coupling regime, in which impurity spins are (in this case) ferromagnetically ordered, driven by RKKY exchange. However, we could show that the same ordering mechanisms are present in host systems away from half-filling (chapter 12), where Lieb's theorem does not apply, and in higher-dimensional models. Our conclusions for the depleted Kondo lattice model have been condensed in a qualitative ground-state "phase diagram". Regarding multi-impurity systems, the question has been raised how IIME is influenced by heavy-fermion physics.

## 14.2 Outlook

Let us first turn to possible experimental exploration and application of the discussed impurity physics. We suggest to employ quantum-confined systems at surfaces by means of scanning-tunnelling techniques with the objective to construct nanospintronics devices bottom-up [42]. Confinement normal to the surface can be achieved, e.g., by insulating spacers [136], and lateral confinement will lead to strong variations in the local density of states as is known from quantum corrals, for example [137], but also

from non-magnetic adatoms, step edges, etc. Even if the confinement is not perfect, the strong spatial dependence of the Kondo temperature is sufficient, if combined with an atomically precise positioning of atoms, to utilise the Kondo-vs-RKKY physics in a quantum box. Different magnetic ground states for different spatial configurations of magnetic adatoms can be studied in real space as a function of an external magnetic field by means of single-atom magnetometry using spin-resolved scanning-tunnelling spectroscopy [43]. Regarding the inverse indirect exchange, the oscillatory distance dependence can be utilised to construct nanostructures with tailored magnetic properties, e.g., by placing magnetic atoms in certain geometries on a metallic layer, similar to RKKY-based artificial structures [42, 43]. Another promising field represent cold atom experiments which try to emulate impurity systems [138, 139, 140].

What is left to be done theoretically? At several occasions, we clarified that our concept is by no means finished and that open issues remain, directing the route for future research. Further attention may be attracted, e.g., by the emerging band picture for  $J \rightarrow \infty$  (Sec. 11.2), the strong-coupling perturbation theory for Anderson impurities (Sec. 10.5), and metal-insulator transitions as functions of  $J$  or  $N$  in the discussed depleted Kondo lattice model (Sec. 11.4). Furthermore, a great deal of extensions appears interesting, now that the basic principles of finite-size effects have been successfully put on a firm footing. Exploring the physics of higher dimensions just has been started in section 11.5 and in parts in chapter 7. However, two-dimensional systems and one-dimensional models with finite next-nearest neighbour hopping are also appealing due to the possibility of frustration at low temperatures [53], either due to RKKY exchange or IIME.

Future theoretical work may explore systems with correlated conduction electrons and preformed local moments, IIME in ferromagnetic ( $J < 0$ ) multi-impurity Kondo models, and in spin-only, e.g., Kondo necklace models. DMFT and DMRG studies of filling dependencies are accessible to quantum Monte-Carlo techniques on bipartite lattices at half-filling [53]. Another branch of activities could be constituted by the investigation of impurity models with correlated one-dimensional electron systems [114], which brings about the emergence of the Tomonaga-Luttinger liquid [4, 5]. The next step would be ferromagnetically ordered conduction-electron systems, what has been extensively discussed in the literature [141, 142, 143]. We may achieve this by introducing a finite next-nearest-neighbour hopping along with sufficiently strong local interactions [144, 77].

In recent years, the study of topologically ordered systems with impurities emerged as an very active field with promising prospects [145], which can be also brought in contact with our ideas.

The investigation of non-equilibrium physics is another interesting but demanding task due to the exponential nature of the Kondo energy scale. Modified mean-field approaches may be regarded as appropriate starting points for such discussions [97].

Aiming at realistic models and engineering spintronic devices, it appears necessary to gain more understanding of the interplay of the Kondo effect with orbital degrees of freedom which still represents in large parts an uncharted territory, e.g. in regard to local moment formation. Despite the heavy numerical requirements, Ref. [146] shows that this problem can be tackled successfully within sophisticated density-functional theory techniques.

Finally, let us pick up the introductory thoughts of our work and summarise that the vitality of condensed matter physics is proven by the exciting wealth of concepts and ideas along with their persistent renewal. As demonstrated in many different ways in this work, this important branch of physics is still open to novel discoveries. This even includes such established fields as impurity physics, where our work introduced a new perspective with fascinating possibilities of realisation.





# Bibliography

- [1] P. W. Anderson, *Science* **177**, 393 (1972).
- [2] P. W. Anderson, *More and Different: Notes from a Thoughtful Curmudgeon*, World Scientific, 2011.
- [3] T. S. Kuhn, *The structure of scientific revolutions*, University of Chicago Press, Chicago, 1970.
- [4] S.-i. Tomonaga, *Progress of Theoretical Physics* **5**, 544 (1950).
- [5] J. M. Luttinger, *Journal of Mathematical Physics* **4**, 1154 (1963).
- [6] R. B. Laughlin, *Phys. Rev. Lett.* **50**, 1395 (1983).
- [7] J. Bardeen, L. N. Cooper, and J. R. Schrieffer, *Phys. Rev.* **106**, 162 (1957).
- [8] A. Hewson, *The Kondo Problem to Heavy Fermions*, Cambridge University Press, New York, N.Y., 1993.
- [9] P. W. Anderson, *Journal of Physics C: Solid State Physics* **3**, 2436 (1970).
- [10] K. G. Wilson, *Rev. Mod. Phys.* **47**, 773 (1975).
- [11] J. Kondo, *Progress of Theoretical Physics* **32**, 37 (1964).
- [12] M. A. Ruderman and C. Kittel, *Phys. Rev.* **96**, 99 (1954).
- [13] T. Kasuya, *Progress of Theoretical Physics* **16**, 45 (1956).
- [14] K. Yosida, *Phys. Rev.* **106**, 893 (1957).
- [15] G. Binnig, H. Rohrer, C. Gerber, and E. Weibel, *Phys. Rev. Lett.* **49**, 57 (1982).
- [16] J. Li, W.-D. Schneider, R. Berndt, and B. Delley, *Phys. Rev. Lett.* **80**, 2893 (1998).
- [17] L. Zhou et al., *Nat Phys* **6**, 187 (2010).
- [18] W. Nolting and A. Ramakanth, *Quantum Theory of Magnetism*, Springer, 2009.
- [19] W. B. Thimm, J. Kroha, and J. von Delft, *Phys. Rev. Lett.* **82**, 2143 (1999).
- [20] T. Hand, J. Kroha, and H. Monien, *Phys. Rev. Lett.* **97**, 136604 (2006).
- [21] A. Schwabe, D. Gütersloh, and M. Potthoff, *Phys. Rev. Lett.* **109**, 257202 (2012).

## Bibliography

- [22] I. Titvinidze, A. Schwabe, N. Rother, and M. Potthoff, Phys. Rev. B **86**, 075141 (2012).
- [23] J. Friedel, Nuovo Cimento Suppl. **7**, 287 (1958).
- [24] A. Schwabe, I. Titvinidze, and M. Potthoff, Phys. Rev. B (R) **88**, 121107 (2013).
- [25] S. R. White, Phys. Rev. Lett. **69**, 2863 (1992).
- [26] A. Georges, G. Kotliar, W. Krauth, and M. J. Rozenberg, Rev. Mod. Phys. **68**, 13 (1996).
- [27] M. Potthoff and W. Nolting, Phys. Rev. B **59**, 2549 (1999).
- [28] D. C. Ralph, C. T. Black, and M. Tinkham, Phys. Rev. Lett. **74**, 3241 (1995).
- [29] D. C. Ralph, C. T. Black, and M. Tinkham, Phys. Rev. Lett. **78**, 4087 (1997).
- [30] C. H. Booth, M. D. Walter, M. Daniel, W. W. Lukens, and R. A. Andersen, Phys. Rev. Lett. **95**, 267202 (2005).
- [31] R. K. Kaul, G. Zaránd, S. Chandrasekharan, D. Ullmo, and H. U. Baranger, Phys. Rev. Lett. **96**, 176802 (2006).
- [32] T. W. Odom, J.-L. Huang, C. L. Cheung, and C. M. Lieber, Science **290**, 1549 (2000).
- [33] Y. Bomze et al., Phys. Rev. B **82**, 161411 (2010).
- [34] V. Madhavan, W. Chen, T. Jamneala, M. F. Crommie, and N. S. Wingreen, Science **280**, 567 (1998).
- [35] P. Wahl et al., Phys. Rev. Lett. **93**, 176603 (2004).
- [36] A. Yamasaki, W. Wulfskel, R. Hertel, S. Suga, and J. Kirschner, Phys. Rev. Lett. **91**, 127201 (2003).
- [37] M. Bode, O. Pietzsch, A. Kubetzka, and R. Wiesendanger, Phys. Rev. Lett. **92**, 067201 (2004).
- [38] H. J. Lee, W. Ho, and M. Persson, Phys. Rev. Lett. **92**, 186802 (2004).
- [39] C. F. Hirjibehedin, C. P. Lutz, and A. J. Heinrich, Science **312**, 1021 (2006).
- [40] D. Kitchen, A. Richardella, J.-M. Tang, M. E. Flatte, and A. Yazdani, Nature **442**, 436 (2006).
- [41] N. J. Craig et al., Science **304**, 565 (2004).
- [42] A. A. Khajetoorians, J. Wiebe, B. Chilian, and R. Wiesendanger, Science **332**, 1062 (2011).
- [43] A. A. Khajetoorians et al., Nat Phys **8**, 497 (2012).
- [44] P. Coleman, *Introduction to Many Body Physics*, Cambridge University Press,

2013.

- [45] S. Doniach, *Physica B+C* **91**, 231 (1977).
- [46] C. Jayaprakash, H. R. Krishna-murthy, and J. W. Wilkins, *Phys. Rev. Lett.* **47**, 737 (1981).
- [47] E. H. Lieb, *Phys. Rev. Lett.* **62**, 1201 (1989).
- [48] S.-Q. Shen, *Phys. Rev. B* **53**, 14252 (1996).
- [49] P. Simon and I. Affleck, *Phys. Rev. Lett.* **89**, 206602 (2002).
- [50] P. Simon, *Phys. Rev. B* **71**, 155319 (2005).
- [51] B. A. Jones and C. M. Varma, *Phys. Rev. B* **40**, 324 (1989).
- [52] I. Affleck, A. W. W. Ludwig, and B. A. Jones, *Phys. Rev. B* **52**, 9528 (1995).
- [53] F. F. Assaad, *Phys. Rev. B* **65**, 115104 (2002).
- [54] P. W. Anderson, *Phys. Rev. Lett.* **18**, 1049 (1967).
- [55] P. W. Anderson, *Phys. Rev.* **124**, 41 (1961).
- [56] P. Coleman, *AIP Conference Proceedings* **629**, 79 (2002).
- [57] S. Alexander and P. W. Anderson, *Phys. Rev.* **133**, A1594 (1964).
- [58] J. R. Schrieffer and P. A. Wolff, *Phys. Rev.* **149**, 491 (1966).
- [59] D. Vollhardt, *AIP Conference Proceedings* **1297**, 339 (2010).
- [60] N. Shannon, eprint arXiv:cond-mat/9910121 (1999).
- [61] W. Nolting, *Grundkurs Theoretische Physik 7: Viel-Teilchen-Theorie*, Springer-Lehrbuch, Springer, 2009.
- [62] I. Affleck, ArXiv e-prints 0911.2209 (2009).
- [63] A. K. Mitchell, M. Becker, and R. Bulla, *Phys. Rev. B* **84**, 115120 (2011).
- [64] P. Nozières, *Journal of Low Temperature Physics* **17**, 31 (1974).
- [65] I. Affleck, *Acta Phys. Polon. B* , 1869 (1995).
- [66] W. Metzner, M. Salmhofer, C. Honerkamp, V. Meden, and K. Schönhammer, *Rev. Mod. Phys.* **84**, 299 (2012).
- [67] N. Andrei, K. Furuya, and J. H. Lowenstein, *Rev. Mod. Phys.* **55**, 331 (1983).
- [68] D. Gütersloh, Kondo Screening versus Indirect Magnetic Exchange in a Kondo Quantum Box, Master's thesis, Universität Hamburg, 2012.
- [69] A. Holzner, I. P. McCulloch, U. Schollwöck, J. von Delft, and F. Heidrich-Meisner, *Phys. Rev. B* **80**, 205114 (2009).
- [70] E. S. Sørensen and I. Affleck, *Phys. Rev. B* **53**, 9153 (1996).

## Bibliography

- [71] W. Metzner and D. Vollhardt, Phys. Rev. Lett. **62**, 324 (1989).
- [72] H. Tsunetsugu, Phys. Rev. B **55**, 3042 (1997).
- [73] U. Schollwöck, Rev. Mod. Phys. **77**, 259 (2005).
- [74] S. Östlund and S. Rommer, Phys. Rev. Lett. **75**, 3537 (1995).
- [75] U. Schollwöck, Annals of Physics **326**, 96 (2011).
- [76] L. Affleck, Ian, Kennedy, Tom and Tasaki, Hal, Commun. Math. Phys. **115**, 477 (1988).
- [77] F. Zschocke, Ferromagnetism in Nano-Chains, Bachelor thesis, Universität Hamburg, 2010.
- [78] M. Lee, Krylov-Raum-Verfahren mit Matrixproduktzuständen, Master's thesis (Diplomarbeit), Universität Hamburg, 2011.
- [79] Verstraete, F., Murg, V., and Cirac, J. I., Advances in Physics **57**, 143 (2008).
- [80] F. Fröwis, V. Nebendahl, and W. Dür, Phys. Rev. A **81**, 062337 (2010).
- [81] I. P. McCulloch, Journal of Statistical Mechanics: Theory and Experiment **2007**, P10014 (2007).
- [82] H. Fehske, R. Schneider, and A. Weiße, *Computational Many-Particle Physics*, Lecture Notes in Physics, Springer, 2008.
- [83] C. Lanczos, Journal of Research of the National Bureau of Standards **45**, 255 (1950).
- [84] E. R. Davidson, Journal of Computational Physics **17**, 87 (1975).
- [85] S. R. White, Phys. Rev. Lett. **77**, 3633 (1996).
- [86] S. R. White, Phys. Rev. B **72**, 180403 (2005).
- [87] F. Pollmann, S. Mukerjee, A. M. Turner, and J. E. Moore, Phys. Rev. Lett. **102**, 255701 (2009).
- [88] B. Pirvu, G. Vidal, F. Verstraete, and L. Tagliacozzo, Phys. Rev. B **86**, 075117 (2012).
- [89] G. Evenbly and G. Vidal, ArXiv e-prints 1109.5334 (2011).
- [90] J. Maldacena, International Journal of Theoretical Physics **38**, 1113 (1999).
- [91] M. Potthoff, European Physical Journal B **32**, 429 (2003).
- [92] M. Potthoff and W. Nolting, Phys. Rev. B **60**, 7834 (1999).
- [93] H. Ishida and A. Liebsch, Phys. Rev. B **79**, 045130 (2009).
- [94] J. K. Freericks, Phys. Rev. B **70**, 195342 (2004).

- [95] R. W. Helmes, T. A. Costi, and A. Rosch, Phys. Rev. Lett. **100**, 056403 (2008).
- [96] M. Snoek, I. Titvinidze, C. Töke, K. Byczuk, and W. Hofstetter, New Journal of Physics **10**, 093008 (2008).
- [97] H. Tsunetsugu, M. Sigrist, and K. Ueda, Phys. Rev. B **47**, 8345 (1993).
- [98] E. Lieb and D. Mattis, Phys. Rev. **125**, 164 (1962).
- [99] R. Jullien, J. Fields, and S. Doniach, Phys. Rev. Lett. **38**, 1500 (1977).
- [100] K. Hallberg, A. A. Correa, and C. A. Balseiro, Phys. Rev. Lett. **88**, 066802 (2002).
- [101] P. Schlottmann, Phys. Rev. B **65**, 024431 (2001).
- [102] P. Schlottmann, Phys. Rev. B **65**, 174407 (2002).
- [103] P. S. Cornaglia and C. A. Balseiro, Phys. Rev. B **66**, 115303 (2002).
- [104] G. Franzese, R. Raimondi, and R. Fazio, EPL (Europhysics Letters) **62**, 264 (2003).
- [105] R. Bedrich, S. Burdin, and M. Hentschel, Phys. Rev. B **81**, 174406 (2010).
- [106] N. D. Mermin and H. Wagner, Phys. Rev. Lett. **17**, 1133 (1966).
- [107] Nozières, Ph. and Blandin, A., J. Phys. France **41**, 193 (1980).
- [108] P. Nozières, The European Physical Journal B - Condensed Matter and Complex Systems **6**, 447 (1998).
- [109] B. A. Jones, C. M. Varma, and J. W. Wilkins, Phys. Rev. Lett. **61**, 125 (1988).
- [110] D. M. Cragg and P. Lloyd, Journal of Physics C: Solid State Physics **12**, L215 (1979).
- [111] Y. Luo, C. Verdozzi, and N. Kioussis, Phys. Rev. B **71**, 033304 (2005).
- [112] I. Titvinidze and M. Potthoff, Journal of the Korean Physical Society **62**, 1434 (2013).
- [113] A. C. Tiegel, P. E. Dargel, K. A. Hallberg, H. Frahm, and T. Pruschke, Phys. Rev. B **87**, 075122 (2013).
- [114] K. Hallberg and R. Egger, Phys. Rev. B **55**, R8646 (1997).
- [115] S. Galkin, C.A. Balseiro, and M. Avignon, Eur. Phys. J. B **38**, 519 (2004).
- [116] F. H. L. Essler, H. Frahm, F. Göhmann, A. Klümper, and V. E. Korepin, *The One-Dimensional Hubbard Model*, Cambridge University Press, Cambridge, 2005.
- [117] Gaudin, M., J. Phys. France **37**, 1087 (1976).
- [118] P. Simon and I. Affleck, Phys. Rev. B **68**, 115304 (2003).

## *Bibliography*

- [119] A. Correa, K. Hallberg, and C. A. Balseiro, *EPL (Europhysics Letters)* **58**, 899 (2002).
- [120] L. Borda, M. Garst, and J. Kroha, *Phys. Rev. B* **79**, 100408 (2009).
- [121] I. Titvinidze, A. Schwabe, and M. Potthoff, unpublished (2013).
- [122] J. Kempe, A. Kitaev, and O. Regev, *SIAM J. Comput.* **35**, 1070 (2006).
- [123] S. Bravyi, D. P. DiVincenzo, and D. Loss, *Annals of Physics* **326**, 2793 (2011).
- [124] I. Garate, *Phys. Rev. B* **84**, 085121 (2011).
- [125] J. S. Lim, R. López, G. Platero, and P. Simon, *Phys. Rev. B* **81**, 165107 (2010).
- [126] J. Hubbard, *Proceedings of the Royal Society of London. Series A. Mathematical and Physical Sciences* **276**, 238 (1963).
- [127] W. Heisenberg, *Zeitschrift für Physik* **49**, 619 (1928).
- [128] H. Kramers, *Physica* **1**, 182 (1934).
- [129] P. W. Anderson, *Phys. Rev.* **79**, 350 (1950).
- [130] C. Zener, *Phys. Rev.* **82**, 403 (1951).
- [131] J. Goldstone, A. Salam, and S. Weinberg, *Phys. Rev.* **127**, 965 (1962).
- [132] N. Néel et al., *Phys. Rev. Lett.* **101**, 266803 (2008).
- [133] A. Schwabe and W. Nolting, *Phys. Rev. B* **80**, 214408 (2009).
- [134] Q. Si and F. Steglich, *Science* **329**, 1161 (2010).
- [135] P. E. Dargel et al., *Phys. Rev. B* **85**, 205119 (2012).
- [136] S.-J. Tang, T. Miller, and T.-C. Chiang, *Phys. Rev. Lett.* **96**, 036802 (2006).
- [137] M. F. Crommie, C. P. Lutz, D. M. Eigler, and E. J. Heller, *Surface Review and Letters* **02**, 127 (1995).
- [138] J. Bauer, C. Salomon, and E. Demler, *ArXiv e-prints* 1308.0603 (2013).
- [139] I. Bloch, J. Dalibard, and S. Nascimbene, *Nat Phys* **8**, 267 (2012).
- [140] D. Jaksch and P. Zoller, *Annals of Physics* **315**, 52 (2005), Special Issue.
- [141] M. Sindel et al., *Phys. Rev. B* **76**, 045321 (2007).
- [142] J. Martinek et al., *Phys. Rev. Lett.* **91**, 127203 (2003).
- [143] M. Gaass et al., *Phys. Rev. Lett.* **107**, 176808 (2011).
- [144] S. Daul and R. M. Noack, *Phys. Rev. B* **58**, 2635 (1998).
- [145] F. Goth, D. J. Luitz, and F. F. Assaad, *Phys. Rev. B* **88**, 075110 (2013).
- [146] B. Surer et al., *Phys. Rev. B* **85**, 085114 (2012).

# Eidesstattliche Erklärung

Die vorliegende Dissertation habe ich eigenhändig und ohne unerlaubte Hilfe angefertigt. Wörtlich oder inhaltlich aus anderen Quellen entnommene Stellen sind als solche kenntlich gemacht. Die Dissertation wurde in der vorgelegten oder in ähnlicher Form noch bei keiner anderen Institution eingereicht. Ich habe bisher keine Promotionsversuche anderwärts unternommen.

Andrej Schwabe

Hamburg, 19.11.2013





# Danksagungen

Eine Promotion gelingt nicht ohne die Unterstützung anderer Leute, denen ich an dieser Stelle danken möchte.

Michael Potthoff danke ich dafür, dass er mich in Kontakt mit der vielseitigen und immer noch sehr lebendigen Kondo-Physik und den damit verbundenen Forschungsfeldern gebracht hat, die Bestandteil dieser Arbeit geworden sind. Die wissenschaftlichen Freiheiten und die stetigen Anregungen zu konsequentem und kritischem Denken habe ich sehr genossen und geschätzt.

Meiner Arbeitsgruppe im Speziellen, inklusive der vielen ehemaligen Mitglieder, und den anderen Mitgliedern des I. Instituts der Uni Hamburg im Allgemeinen danke ich für die offene und konstruktive Atmosphäre, die ebenfalls maßgeblich zu den faszinierenden Resultaten beigetragen hat und darüber hinaus auch viel Gelegenheit zu persönlichen Kontakten gegeben hat. Den Gutachtern danke ich für die Flexibilität. Besondere Erwähnung sollten meine Bürokollegen Matthias Balzer und Maximilian Aulbach finden, die immer wieder als natürliche Ansprechpartner bei allen Arten von Problemen herhalten mussten.

Natürlich dürfen in dieser Aufzählung nicht diejenigen fehlen, die sich mit der Korrektur der frühen Textversionen herumgeschlagen haben und mir dabei geholfen haben, die Struktur und den Inhalt zu schärfen: Irakli Titvinidze, Daniel Gütersloh und Mohammad Sayad.

Und zuletzt danke ich meiner Familie und insbesondere Jeffi für die unschätzbare und nicht selbstverständliche Geduld und Ermutigung während der letzten Jahre.